Analyse expérimentale et modélisation multi-échelle du transfert de chaleur par convection dans les milieux poreux à l'appui des communautés de l'espace, du stockage de l'énergie et de la biomasse

Shaolin Liu

▶ **To cite this version:**

Shaolin Liu. Analyse expérimentale et modélisation multi-échelle du transfert de chaleur par convection dans les milieux poreux à l'appui des communautés de l'espace, du stockage de l'énergie et de la biomasse. Mécanique des fluides [physics.class-ph]. HESAM Université, 2023. Français. NNT : 2023HESAE061 . tel-04500039

HAL Id: tel-04500039
https://pastel.hal.science/tel-04500039

Submitted on 11 Mar 2024

HAL is a multi-disciplinary open access archive for the deposit and dissemination of scientific research documents, whether they are published or not. The documents may come from teaching and research institutions in France or abroad, or from public or private research centers.

L'archive ouverte pluridisciplinaire **HAL**, est destinée au dépôt et à la diffusion de documents scientifiques de niveau recherche, publiés ou non, émanant des établissements d'enseignement et de recherche français ou étrangers, des laboratoires publics ou privés.

HESAM UNIVERSITÉ

Arts et Métiers Sciences et Technologies

ÉCOLE DOCTORALE SCIENCES ET MÉTIERS DE L'INGÉNIEUR
[Laboratoire I2M - Campus de Bordeaux]

THÈSE

présentée par : **Shaolin LIU**
soutenue le : **10 October 2023**

pour obtenir le grade de : **Docteur d'HESAM Université**

préparée à : **École Nationale Supérieure d'Arts et Métiers**
Spécialité : **Mécanique des fluides**

Experimental analysis and multiscale modeling of convective heat transfer in porous media in support of the space, energy storage, and biomass communities

THÈSE dirigée par :
Mme Azita AHMADI-SENICHAULT

et co-encadrée par :
M. Jean LACHAUD

Jury

M. Abdelaziz OMARI	Professeur, ENSCBP Bordeaux	Président
M. Bruno DUBROCA	Directeur de recherche CEA, LCTS	Rapporteur
M. Frederic TOPIN	Maître de conférences HDR, Aix-Marseille Université	Rapporteur
M. Francesco PANERAI	Assistant professor, University of Illinois Urbana-Champaign	Examinateur
M. Michel QUINTARD	Directeur de recherche CNRS Emerite, IMFT	Examinateur
M. Victor POZZOBON	Ingénieur de recherche, CentraleSupélec	Examinateur
Mme Azita AHMADI	Professeur, ENSAM Bordeaux	Directrice de thèse
M. Jean LACHAUD	Maître de conférences, Université de Bordeaux	Co-encadrant de thèse
M. Cyril LEVET	Ingénieur de recherche, EPSYL-Groupe ALCEN	Invité
M. Thibaut ESENCE	Ingénieur de recherche, Eco-Tech Ceram	Invité

THÈSE

The ideals that have lighted my way, and time
after time have given me new courage to face
life cheerfully, have been Kindness, Beauty, and Truth.
(Albert Einstein)

Remerciements

First and foremost, I express my deepest gratitude to my advisors, Ms. Azita Ahmadi-Senichault and Mr. Jean Lachaud. Their professional expertise, endless patience, continuous guidance, and encouragement have been invaluable in the completion of this research. They have profoundly impacted me, not just acadically, but also personally.

I also extend my sincere thanks to my colleagues, including Hermes Scandelli, Jeremy Chevalier, Flora Lahouze, and Kanka Ghosh, whose suggestions, discussions, and support in the course of this research were invaluable.

Furthermore, I wish to acknowledge the financial support provided by the China Scholarship Council (CSC), which offered a precious opportunity for me to focus on my doctoral research.

Working in the I2M laboratory has been a significant part of my life, and I want to thank this team for not only offering top-tier facilities and resources but also for providing a friendly and motivational environment.

Last but not least, I would like to give special thanks to my girlfriend, Hui Yao. Her love, understanding, and continuous support have empowered me to face all difficulties and challenges. Her presence has been a significant force in the completion of this challenging task.

This work stands as a testament to the unwavering support from all of them, and it is an honor to have worked alongside these individuals.

Résumé

De nombreuses technologies émergentes reposent sur des milieux poreux, y compris des échangeurs de chaleur pour les concentrateurs solaires, les processus de production de biocarburants, les systèmes de stockage d'énergie de nouvelle génération tels que les piles à combustible et les supercondensateurs, et les boucliers thermiques pour les véhicules spatiaux, pour n'en nommer que quelques-uns. La modélisation du transport dans les milieux poreux nécessite de tenir compte des aspects multi-échelles inhérents à la structure des milieux poreux. Les problèmes typiques à plusieurs échelles peuvent impliquer plusieurs échelles successives ou au moins deux échelles généralement appelées micro-échelle ou échelle des pores et macro-échelle ou échelle de Darcy. Plusieurs méthodologies basées sur l'analyse théorique ont été développées pour mettre à l'échelle les équations de transport de la micro-échelle pour obtenir des modèles à l'échelle macro. Cette étude repose sur ces techniques de mise à l'échelle disponibles et utilise divers modèles à l'échelle macro pour étudier le transfert de chaleur par convection dans les milieux poreux. La précision de ces modèles à l'échelle macro est influencée par les propriétés de transport macroscopiques, à savoir la porosité, la perméabilité, le tenseur de Forchheimer, la conductivité thermique effective, le coefficient de transfert de chaleur volumique, etc. Bien que de nombreuses études aient été menées sur des propriétés de transport macroscopiques particulières, la complexité, abordée dans ce travail, provient du fait que ces paramètres sont interdépendants dans les équations de conservation couplées de la masse, de l'élan et de l'énergie.

L'objectif principal de cette thèse est de contribuer à la compréhension du transfert de chaleur par convection dans les milieux poreux grâce à des études expérimentales et numériques, pour donner un aperçu sur le choix des modèles macroscopiques pertinents à utiliser et sur la détermination des propriétés effectives ou macroscopiques inhérentes. Dans cette étude, les propriétés macroscopiques sont déterminées en utilisant deux approches. La première consiste en la résolution du problème inverse numérique-expérimental, tandis que la seconde est basée sur des simulations numériques directes à l'échelle micro. Dans la première approche, la technique transitoire à coup unique (TSBT) est utilisée pour réaliser des expériences sur deux installations, conçues spécifiquement pendant ce travail, avec différents diamètres de section d'essai de 1 cm et 20 cm. Nous étudions le transfert de chaleur par l'écoulement d'un gaz chaud à l'intérieur de trois différents types de milieux poreux : les feutres de fibres de carbone, utilisés dans les Systèmes de Protection Thermique (TPS), les lits de billes de verre, utilisés dans le Stockage d'Énergie Thermique (TES), et les lits de granulés et de copeaux de bois, utilisés comme biomasse dans la production d'énergie. Nous effectuons une analyse inverse numérique pour

estimer les quantités d'intérêt en utilisant la boîte à outils d'analyse de matériaux poreux basée sur OpenFoam (PATO) et le Kit d'analyse de conception pour l'optimisation et les applications à l'échelle Tera (DAKOTA). Dans la deuxième approche, la microstructure des milieux poreux est recherchée pour la simulation numérique directe de l'écoulement et du transfert de chaleur. Pour les applications TPS, le feutre de fibres de carbone est reconstruit à l'aide d'images tomographiques numérisées en 3D. La perméabilité et les tenseurs de Forchheimer sont ensuite calculés en résolvant les équations de Navier-Stokes à l'échelle micro. Pour les lits de billes de verre et de granulés de bois, un code de la méthode des éléments discrets (DEM) est utilisé pour générer des emballages de sphères et de cylindres. En résolvant les équations couplées de Navier-Stokes et d'énergie dans les phases fluides et solides, les coefficients de transfert de chaleur volumiques sont déterminés en fonction d'une méthode d'intégration.

Ce travail contribue à la compréhension et au développement de deux méthodes pour déterminer les propriétés de transport macroscopiques impliquées dans le modèle à l'échelle macro, permettant ainsi une étude plus précise des phénomènes de transfert de chaleur et de masse dans les milieux poreux. Les contributions numériques du travail de doctorat ont été implémentées dans PATO, qui a été diffusé en open source par la NASA.

Mots-clés : Simulations macroscopiques, Simulations microscopiques, Étude expérimentale, Coefficient de transfert thermique, Matériaux poreux.

Abstract

Numerous emerging technologies rely on porous media, including heat exchangers for solar concentrators, biofuel production processes, new-generation energy storage systems like fuel cells and supercapacitors, and heat shields for space vehicles, to name a few. Modeling transport in porous media requires accounting for the multiple-scale aspects inherent to the structure of porous media. Typical multiple-scale problems may involve several successive scales or at least two scales generally referred to as the micro-scale or pore-scale and the macro-scale or Darcy-scale. Several methodologies based on theoretical analysis have been developed to upscale transport equations from the micro-scale to obtain macro-scale models. This study is built upon these available upscaling techniques and uses various macro-scale models to investigate convective heat transfer in porous media. The accuracy of these macro-scale models is influenced by the macroscopic transport properties, namely porosity, permeability, Forchheimer tensor, effective thermal conductivity, volumetric heat transfer coefficient, etc. While many studies have been conducted on particular macroscopic transport properties, the complexity, addressed in this work, arises from the fact that these parameters are interrelated in the coupled conservation of mass, momentum, and energy equations.

The main objective of this thesis is to contribute to the understanding of convective heat transfer in porous media through experimental and numerical studies, to give insight on the choice of the relevant macroscopic models to use and on the determination of the inherent effective or macroscopic properties. In this study, the macroscopic properties are determined using two approaches. The first one consists of the experimental-numerical inverse problem resolution, while the second is based on direct micro-scale numerical simulations. In the first approach, the transient single-blow technique (TSBT) is used to perform experiments on two facilities, designed specifically during this work, with different test section diameters of 1 cm and 20 cm. We study heat transfer by the flow of a hot gas within three different types of porous media : carbon fiber felts, used in Thermal Protection Systems (TPS), packed beds of glass beads, used in Thermal Energy Storage (TES), and packed beds of wood pellets and chips, used as biomass in energy production. We perform a numerical inverse analysis to estimate the quantities of interest using the Porous material Analysis Toolbox based on OpenFoam (PATO) and the Design Analysis Kit for Optimization and Terascale Applications (DAKOTA). In the second approach, the microstructure of the porous media is sought for direct numerical simulation of the flow and heat transfer. For TPS applications, carbon fiber felt is reconstructed using 3D digitalized tomographic images. The permeability and the Forchheimer tensors are then computed by solving the

Navier-Stokes equations at the micro-scale. For packed beds of glass beads and wood pellets, a Discrete Element Method (DEM) code is used to generate packings of spheres and cylinders. By solving the coupled Navier-Stokes and energy equations in both fluid and solid phases, the volumetric heat transfer coefficients are determined based on an integration method.

This work contributes to the understanding and development of two methods for determining the macroscopic transport properties involved in the macro-scale model, thereby enabling a more accurate study of heat and mass transfer phenomena within porous media. The numerical contributions of the Ph.D. work have been implemented in PATO, which has been released as open source by NASA.

Keywords: Macroscopic simulations, Microscopic simulations, Experimental study, Heat exchange coefficient, Porous materials.

Nomenclature

Acronyms

CFD Computational Fluid Dynamics

CMT Computed Micro-Tomography

CSP Concentrated Solar Power

DAKOTA Design Analysis Kit for Optimi- zation and Terascale Applications

DEM Discrete Element Method

IP In Plane

LIGGGHTS Lammps Improved for General Granular and Granular Heat Transfer Simulations

LTE Local Thermal Equilibrium

LTNE Local Thermal Non-Equilibrium

NL2SOL Design Analysis Kit for Optimi- zation and Terascale Applications

PATO Porous material Analysis Toolbox based on OpenFOAM

PICA Phenolic Impregnated Carbon Ablator

REV Representative Element Volume

TES Thermal Energy Storage

TPS Thermal Protection Systems

TT Through Thickness

Greek symbols

α Forchheimer term, $\mathbf{F} \cdot \langle \mathbf{v_g} \rangle$, $\mathrm{m\,s^{-1}}$

ε_i volume fraction of the i-phase

μ_g dynamic viscosity of gas, $\mathrm{kg\,m^{-1}\,s^{-1}}$

ρ_i density of the i-phase, $\mathrm{kg\,m^{-3}}$

β Forchheimer coefficient scalar, $\mathrm{m^{-1}}$

β_0 Klinkenberg correction factor, m^{-1}

$\boldsymbol{\beta}$ Forchheimer coefficient tensor, m^{-1}

Latin symbols

a specific gas-solid surface area, m^{-1}

A_{sg} area of the s-g interface contained in the averaging volume, V, m^2

$\mathbf{A}$ the cross-section of the sample, m^2

$\mathbf{b_i}$ vector field that maps $\nabla \langle T_i \rangle^i$ onto $\tilde{T}_i$ in LTE model, $\tilde{T}_i$=$\mathbf{b_i} \cdot \nabla \langle T_i \rangle^i$

$\mathbf{b_{ii}}$ vector field that maps $\nabla \langle T_i \rangle^i$ onto $\tilde{T}_i$ in LTNE model

Bi Biot number

$c1 - c4$ coefficients associated with thermal conductivity

$c5, c6$ coefficients associated with thermal conductivity, $\mathrm{W\,m^{-1}\,K^{-1}}$

$c_{p,i}$ heat capacity of the i-phase, $\mathrm{J\,kg^{-1}\,K^{-1}}$

$\mathbf{C}$ product tensor, $\mathbf{K} \cdot \boldsymbol{\beta}$, m

d_{cl} cluster fiber diameter, m

d_f fiber diameter, m

d_{par} particle diameter, m

d_p pore diameter, m

$\mathbf{F}$ Forchheimer correction tensor

D tube diameter, m

f coefficients associated with Nusselt number

Fo Forchheimer number

h_s interstitial heat transfer coefficient, $\mathrm{W\,m^{-2}\,K^{-1}}$

h_v volumetric heat transfer coefficient, $\mathrm{W\,m^{-3}\,K^{-1}}$

H tube radius, m

$\mathbf{I}$ Identity tensor

k_t thermocouple or tube thermal conductivity, $\mathrm{W\,m^{-1}\,K^{-1}}$

k_i thermal conductivity of the i-phase, $\mathrm{W\,m^{-1}\,K^{-1}}$

$\mathbf{k_{i,eff}}$ effective thermal conductivity tensor of the i-phase, $\mathrm{W\,m^{-1}\,K^{-1}}$

K permeability scalar, m^2

$\mathbf{K}$	permeability tensor, m^2
K_{eff}	effective permeability scalar, m^2
$\mathbf{k_{eff}}$	effective thermal conductivity tensor, $\mathrm{W\,m^{-1}\,K^{-1}}$
$\mathbf{k_{dis}}$	dispersion term of the thermal conductivity, $\mathrm{W\,m^{-1}\,K^{-1}}$
$\mathbf{k_{tor}}$	tortuosity term of the thermal conductivity, $\mathrm{W\,m^{-1}\,K^{-1}}$
l_g	the size of the unit cell, m
L	sample length, m
M	gas molar mass, $\mathrm{kg\,mol^{-1}}$
$\mathbf{n_{gs}}$	outwardly directed unit normal vector pointing from the gas phase toward the solid phase, $\mathbf{n_{gs}}$=- $\mathbf{n_{sg}}$
Nu_s	Nusselt number based on h_s
Nu_v	Nusselt number based on h_v
p	gas pressure, $\mathrm{kg\,m^{-1}\,s^{-2}}$
$\mathbf{P}$	invertible matrix
$\langle p \rangle^g$	Intrinsic average pressure, $\mathrm{kg\,m^{-1}\,s^{-2}}$
Pe	Peclet number
Pr	Prandtl number
qm	gas mass-flow rate, $\mathrm{kg\,s^{-1}}$
qv	gas volume-flow rate, $\mathrm{m^3\,s^{-1}}$
Q	volumetric flow rate, $\mathrm{m^3\,s^{-1}}$
R	gas constant, $\mathrm{J\,K^{-1}\,mol^{-1}}$
Re_d	Reynolds number based on the pore diameter
s_i	scalar field used in LTNE model
T_i	point temperature in the i-phase, K
$\langle T_i \rangle^i$	initrinsic phase average temperature in the i-phase, K
$\tilde{T}_i$	the spatial deviation temperature in the i-phase, $\tilde{T}_i = T_i - \langle T_i \rangle^i$, K
$\langle T \rangle$	spatial average temperature in the LTE model, K
$\mathbf{u}$	Darcy velocity, $\varepsilon_g \langle \mathbf{v_g} \rangle^{\mathbf{g}}$, $\mathrm{m\,s^{-1}}$
u	magnitude of the Darcy velocity, $\mathrm{m\,s^{-1}}$
$\mathbf{v_g}$	velocity of the gas phase, $\mathrm{m\,s^{-1}}$

$\langle \mathbf{v_g} \rangle^{\mathbf{g}}$	intrinsic phase average velocity of the gas, $\mathrm{m\,s^{-1}}$
$\langle \mathbf{v_g} \rangle$	superficial average velocity, $\mathrm{m\,s^{-1}}$
$\tilde{\mathbf{v}}_{\mathbf{g}}$	the deviation of gas velocity, $\tilde{\mathbf{v}}_{\mathbf{g}} = \mathbf{v_g} - \langle \mathbf{v_g} \rangle^{\mathbf{g}}$, $\mathrm{m\,s^{-1}}$
V	averaging volume, $\mathrm{m^3}$
X, Y	variables associated with the Forchheimer equation

Subscripts

$\parallel$	horizontal flow directions
$\perp$	transverse flow directions
atm	atmosphere
con	conductivity
dg	diagnoal
dis	dispersion
eff	effective
g	gas
in	inlet
m	mixture of gas and solid phases
num	numerical result
out	outlet
s	solid
sta	static
t	thermocouple or tube
tor	tortuosity

Table des matières

Liste des tableaux

Table des figures

Chapitre 1

Introduction

Numerous technologies in development rely on porous materials: heat exchangers for solar concentrators [1], biofuel production processes [2], new generation energy storage such as fuel cells and supercapacitors [3], space vehicle heat shields [4], microfluidic sensors [5] etc . Chemical engineers and researchers at the forefront of their own fields and leading 21st century innovation would greatly benefit from fundamental developments in heat and mass transfer in porous media to reinforce application-specific phenomenological models. This work focuses on high-temperature flows in porous media, which have diverse applications ranging from the design of porous heat shields for space vehicles entering an atmosphere to the simulation of packed bed thermal energy storage (TES) systems. Although these applications may differ in their external conditions, from a physical point of view, the heat transfer phenomena occurring inside the materials are similar. Specifically, they involve heat exchanges between the solid structure of the porous material and the fluid flowing through its network of pores. Moreover, the conservation laws governing these materials' behavior remain consistent, with the mathematical models employing the same equations for mass, momentum, and energy. The study of high-temperature flows in porous materials holds significant relevance for various fields, particularly for space, energy storage, and biomass communities. To introduce the studied problem, let us start by presenting a brief introduction to the three communities and a review of their key strengths.

1.1 Context

In the space community, designing thermal protection systems (TPS) that can endure extreme temperatures is crucial for maintaining the safety and dependability of spacecraft and hypersonic vehicles [4]. To better comprehend and foresee the performance of TPS under diverse conditions, experts are striving to create novel materials and models. In the energy storage community, the shift toward renewable energy sources has necessitated the development of effective TES systems capable of storing and delivering energy as required, especially in relation to irregular energy sources like solar and wind power. While packed bed TES systems present a viable option, unraveling the intricate heat transfer and fluid dynamics within these systems continues to pose a considerable challenge. In the biomass community, effectively using biomass as an alternative energy source requires a comprehensive

understanding of the drying and pyrolysis processes that take place within wood particles. These processes are highly influenced by factors such as heat transfer, temperature, and the properties of the materials involved.

This research seeks to explore the intricacies of heat and mass transfer in porous materials, focusing on these three specific communities that exemplify the importance of understanding these phenomena in different communities. By delving into the complexities of each community, we seek to uncover fundamental insights into the heat and mass transfer processes occurring within porous materials, which will in turn inform the development of advanced materials and systems to tackle the growing global demand for energy and sustainability.

1.1.1 Heat and Mass Transfer in TPS Materials

TPS is essential for maintaining acceptable temperatures on the outer surface of spacecraft throughout all mission phases, particularly during atmospheric re-entry [6, 7, 8]. TPS materials are divided into two categories: ablative and non-ablative materials [9]. A common option for ablative TPS material is a porous, fibrous preform impregnated with a phenolic resin. NASA's Phenolic Impregnated Carbon Ablator (PICA) is an example of this class of material and has been successfully employed in various missions such as Stardust (NASA, 2006) [10, 11], Mars Science Laboratory (NASA, 2012) [12, 13], Mars 2020 (NASA, 2021) [14], and for the Dragon vehicles (SpaceX, since 2012) [15]. The European Space Agency and ArianeGroup have developed ASTERM [16], a low-density carbon/phenolic ablative material based on Calcarb, a carbon-fiber preform produced in Europe by Mersen. Ablative materials protect spacecraft by utilizing chemical reactions to reduce surface heat flux and minimize the conversion of kinetic energy to thermal energy. Since the 1950s, detailed TPS material response models have been developed, accounting for this complex physics, with significant progress made in the 1960s during the design of the Apollo heat shield [17, 18]. This complex material is also used in the Orion capsule, where it undergoes a phase of liquid ablation. It should be noted that no reliable model has been established for this process. Currently, there appear to be no ongoing research efforts on this particularly challenging subject. Active research communities continue to refine and adapt these models to new material generations to reduce design uncertainties [19, 20].

The widespread use of porous fibrous materials raises questions about the validity of inherited assumptions, such as the local thermal equilibrium (LTE) assumption, commonly used in TPS design. Heat transfer in porous materials can be studied under either LTE [4] or local thermal non-equilibrium (LTNE) [21, 22, 23, 24] assumptions. In LTE models, it is assumed that the average temperatures of the solid and gas phases are locally equal, that is, within a given representative elementary volume. Florio [25] and Puiroux [26, 27] demonstrated the validity of the local thermal equilibrium assumption for dense charring materials. However, Scoggins et al. [28] showed that the local thermal equilibrium assumption was invalid for PICA, using available literature correlations to estimate the heat transfer coefficient between the solid phase and the gas flowing through the pores [28]. Scandelli [29] proposed that the LTE hypothesis may be valid for typical entry conditions, as the thermal Peclet number within the pores remains small. However, the thermal Peclet number can become significant when pyrolysis gas velocities are high. In such cases, additional physical phenomena that are not considered in the

Peclet analysis, such as the change in enthalpy due to chemical reactions, can become non-negligible. Since correlations for materials similar to PICA were not available, Scoggins et al. [28] recommended conducting experiments to measure the heat transfer coefficient in low-density carbon fiber materials. The choice of a suitable macroscopic model to accurately describe coupled heat and mass transfer in TPS materials remains an open question.

1.1.2 Heat and Mass Transfer in packed bed TES systems

TES plays a vital role in harnessing renewable energy sources efficiently, as their intermittent nature poses challenges to consistent energy supply [30]. Concentrated solar power (CSP) plants, in particular, can greatly benefit from heat storage to reduce overall system costs [31]. Two main types of TES are sensible heat storage and latent heat storage [32]. Sensible heat storage increases the temperature of a solid medium, while latent heat storage involves a phase change in the storage material. Sensible TES can be further classified into two categories: direct storage of energy-carrying fluid and two-medium heat storage systems [30, 32]. Direct storage systems typically involve a single tank that maintains hot fluid above the cold fluid. In contrast, two-medium storage systems use a heat transfer fluid to carry heat and an additional solid or liquid for energy storage [33, 34]. Packed bed TES is a promising method for storing heat from solar radiation, utilizing air as the heat transfer fluid to convey heat to a solid packed bed.

As part of a numerical model comparison carried out in the packed bed TES [35] and summarized in Esence et al [30], four different groups of models were examined. These groups include the continuous solid phase models, which assume the solid behaves as a continuous medium rather than independent particles. Another group is Schumann's model, which neglects heat conduction in the radial direction within the solid phase, as well as heat conduction in the fluid and heat exchange between the particles. The single-phase model assumes that the solid and fluid phases have equal transient temperatures. Lastly, the concentric dispersion model considers a thermal gradient within the solid particles, with no inter-particle heat transfer, resulting in the temperature gradient at the particle surfaces being solely due to heat transfer between the fluid and the bed. The choice of bed material is critical to ensuring an efficient and cost-effective storage system. Various materials such as rocks [36], metals [37, 38], concrete [38], sand [39], and bricks [40] have been used depending on the application. Cast iron is popular for its high storage energy density, while stone or brick are more affordable options. Numerous studies have been conducted on packed bed heat transfer methods, considering factors such as void fraction, flow rate variations [35], wall thermal losses [33], particle size, packing material [41], and fluid inlet temperature [42].

To maximize the efficiency of these systems, energy analysis should be performed, which assesses the heat storage and the recovery process. Understanding the underlying principles of packed bed TES is essential for designing and implementing effective energy storage solutions to support the increasing use of renewable energy sources. By improving the performance of packed bed TES systems, it becomes possible to reduce the cost of renewable energy technologies and accelerate the transition to a more sustainable and environmentally friendly energy landscape.

1.1.3 Heat and Mass Transfer in biomass

Concerns regarding the reliance on fossil fuels and the impact of global warming have sparked increased interest in using renewable resources and waste streams for energy production [43]. Biomass presents an attractive option for renewable energy and carbon sequestration due to its sustainable nature [44]. Among biomass feedstocks, wood particles stand out as a favorable choice due to their widespread availability, cost-effectiveness, and carbon-neutral characteristics [45]. Heat transfer phenomena are inherent in multiple aspects of biomass utilization, including drying, pyrolysis, combustion, and gasification processes [46, 47, 48, 49]. For small quantities of biomass, particles can be heated directly with an electric heater placed inside the sample or by using an external furnace [45, 50]. However, in industrial settings, the heating of large quantities of biomass particles is required, necessitating alternative solutions such as heating particles in a container with a hot gas flow, typically in the form of a packed bed system [47]. Gaining a deeper understanding of thermal conversion behavior is crucial not only for improving process efficiency but also for reducing pollutant emissions.

Researchers have investigated heat and mass transfer processes within a single biomass particle, successfully modeling the sequence of chemical processes, including drying, pyrolysis, combustion, and char gasification [50, 51, 52, 53, 54]. Biomass-packed bed systems have been be modeled using either homogeneous (one-equation) or heterogeneous (two-equation) approaches to model heat transfer [51, 55, 56]. The homogeneous model assumes identical temperatures for the gas and solid phases, applying a single energy conservation equation to the entire system [57]. The heterogeneous model, however, applies separate energy equations to each phase [58, 59] and is recommended for biomass-packed beds during drying, devolatilization, and char combustion. The thermodynamic processes involved in the biomass community applications differ from those of the TES community. Biomass undergoes intricate physical and chemical processes, such as heat transfer, moisture evaporation, and decomposition kinetics. Understanding and optimizing these reactions bring significant challenges [50].

In the context of wood particles in packed beds, pyrolysis is influenced not only by temperature but also by mass and heat transfer processes within the wood particle. The products of pyrolysis are generally classified into three categories: char, tar, and gas. Pyrolysis is conducted in an oxygen-free environment at temperatures ranging from 523 to 873 K, depending on the feedstock characteristics [60]. The primary goal of the biomass community is to develop a model that explains the drying and pyrolysis processes of wood particles. This model will help improve the efficiency and effectiveness of biomass feed-stock for renewable energy production. Bamford et al. [61] were the first to propose a thermal pyrolysis model, the pyrolysis process is modeled as a 1st order kinetic equation following an Arrhenius law. Over the past few decades, numerous pyrolysis models have been presented in the literature, as summarized by White et al. [62]. These models can be categorized into three main types: single-step global reaction models [63], multiple-step models [64], and semi-global models [65]. Single-step global reaction models provide an overview of the devolatilization rate from biomass substrates. Multiple-step models involve a series of consecutive reactions to capture the complex kinetics of biomass pyrolysis. Semi-global models simplify the analysis by grouping pyrolysis products into three fractions: volatiles, tars, and char.

In summary, the three discussed applications and processes involving porous materials address

different aspects of heat and mass transfer. The investigation of heat and mass transfer in TPS materials revolves around the selection of the macroscopic model. It is worth noting that the widely accepted assumption of local thermal equilibrium between the solid and gas phases in TPS design has recently been questioned by several researchers. To address this, both one-temperature (1T) and two-temperature (2T) models have been examined. On the other hand, the objective of studying heat and mass transfer in packed bed TES systems is to develop and validate a comprehensive two-equation model that incorporates mass and momentum conservation under high-temperature conditions. Additionally, determining the effective conductivities and heat transfer coefficients is crucial to inform the two-equation model. Furthermore, the investigation of heat and mass transfer in biomass highlights the complexities of biomass pyrolysis processes. In comparison to the previous two applications, it involves a local thermal non-equilibrium model with chemical reactions. Despite their distinct applications, these processes share the common feature of porous reactive materials subjected to high temperatures, which play a critical role in each case.

A classification framework for macroscopic models is displayed in Fig.1.1. It categorizes models into two groups: those without chemical reactions and those with chemical reactions. The former applies to non-ablative TPS and TES, while the latter applies to ablative TPS and Biomass. In models without chemical reactions, conservation of mass, momentum, and energy (LTE or LTNE) are considered for the gas phase. In models with chemical reactions, solid and species mass conservation needs to be included to account for drying, pyrolysis, and/or heterogeneous reactions. Hence, both mass conservation for the solid and species conservation need to be considered. Understanding the mechanisms of heat and mass transfer and the challenges posed by porous materials in these applications will contribute to assessing and modeling mass, momentum, and heat exchanges between an elastic and reactive solid structure interacting with a high-temperature environment.

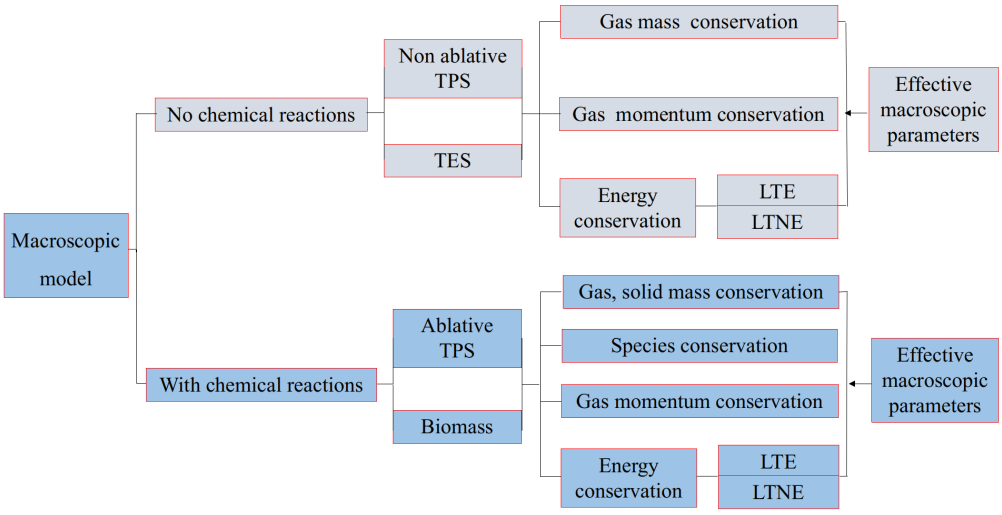

Figure 1.1 – Classification framework for numerical models

1.2 Modeling transport in porous media

Porous media can be simply defined as solid structures containing void spaces called pores. The interconnection of these pores allows for percolation, or the passage of a fluid through the material [21]. Porous architectures can take various forms, such as open or closed-cell foams, fiber felts, grain aggregates, and honeycombs. These materials can be found in nature (e.g., sponge, rock, wood) or be man-made (e.g., ceramics, carbon fiber composites). Man-made porous media can be inspired by natural materials or adopt radically different concepts to enhance their properties. For instance, the mechanical properties of carbon fiber composites greatly exceed those of wood. Fig. 1.2 illustrates four porous materials (carbon fiber felt, cork heat shield, wood, packed bed) at both micro and macro scale representations.

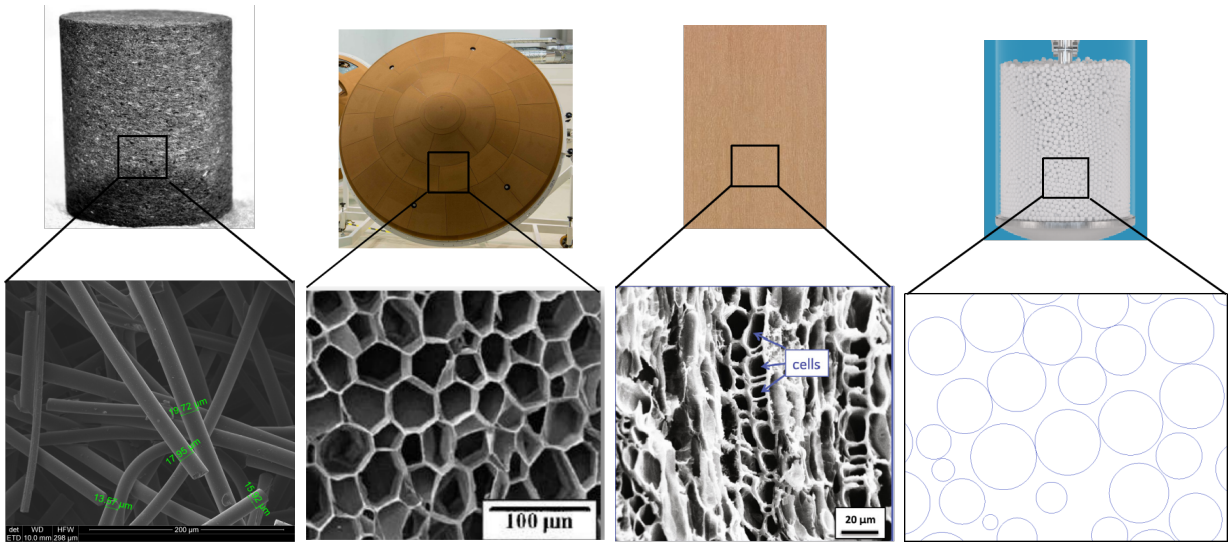

(a) carbon fiber felt (b) cork heat shield (c) wood (d) packed bed

Figure 1.2 – Micro scale and macro scale representations of the different porous materials

The macro-scale and micro-scale are two fundamental scales employed to describe porous media [66]. A representative multi-scale feature is shown in Fig. 1.3, where the top section illustrates the macro-scale and the bottom section depicts the micro-scale. At the micro-scale level, a separate continuum can be considered for different phases, with the solid and fluid phases typically represented by s and g, respectively. The characteristic lengths are expressed as l_s and l_g. On the macro scale, an effective representation is characterized by variable fluctuations at a scale of L. The relationship among scale levels can be described as $l_g << r_0 << L$, with r_0 representing the radius of the representative elementary volume (REV). The interactions between fluid and solid phases can be explained through classical fluid-solid mechanics and heat exchange at the micro-scale level. The micro-scale can be connected to the macro-scale via an upscaling procedure. In the following parts, we will discuss the mathematical equations governing the micro-scale and macro-scale to provide a deeper understanding of the processes occurring within porous media.

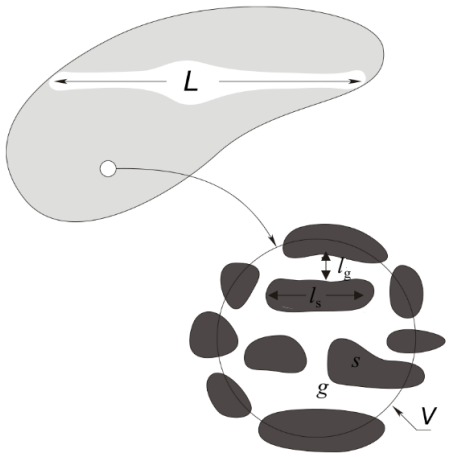

Figure 1.3 – Two-scale description of a porous medium

1.2.1 Transport problem at the micro-scale

At the microscopic scale, the description of the transport problem is provided by the Navier-Stokes equations (continuity and momentum conservation) and energy equations. These equations can be written in various forms, depending on the assumptions made [67, 68, 69]. To present these equations, we will categorize the system into three components: continuity, momentum, and energy. We will examine each of these components individually, presenting their final forms.

The single-phase flow of an incompressible Newtonian fluid g is considered in a macroscopic region of a rigid porous medium. The boundary value problem describing the process at the microscopic (pore) scale is given by the classical continuity and momentum balance equations

$$\begin{cases} \nabla \cdot \boldsymbol{v}_g = 0 & \\ \rho_g(\dfrac{\partial \boldsymbol{v}_g}{\partial t} + \boldsymbol{v}_g \cdot \nabla \boldsymbol{v}_g) = -\nabla p_g + \rho_g \boldsymbol{g} + \mu_g \nabla^2 \boldsymbol{v}_g & in\ V_g \\ BC1: \ \ \boldsymbol{v}_g = 0 & at\ A_{gs} \\ BC2: \ \ \boldsymbol{v}_g = \boldsymbol{v}_1(\boldsymbol{x}, t) & at\ \partial V_g \\ iC1: \ \ \boldsymbol{v}_g(t=0) = \boldsymbol{v}_0(\boldsymbol{x}) & in\ V_g \end{cases} \tag{1.1}$$

where $\boldsymbol{v_g}$ and p_g are, respectively, the velocity and pressure of the gas phase; A_{gs} represents the interface area between the gas phase and the solid phase contained within the REV.

The energy equation at the micro-scale is given as follows

$$\begin{cases} (\rho\, c_p)_g \dfrac{\partial T_g}{\partial t} + (\rho\, c_p)_g \boldsymbol{v}_g \cdot \nabla T_g = \nabla \cdot (k_g \nabla T_g) & in\ V_g \\ (\rho\, c_p)_s \dfrac{\partial T_s}{\partial t} = \nabla \cdot (k_s \nabla T_s) & in\ V_s \\ BC1: \quad T_g = T_s & at\ A_{gs} \\ BC2: \quad \boldsymbol{n_{gs}} \cdot k_g \nabla T_g = \boldsymbol{n_{gs}} \cdot k_s \nabla T_s & at\ A_{gs} \end{cases} \tag{1.2}$$

where $(\rho c_p)_i$, T_i, k_i, (i=g or s) are the i-phase specific heat, temperature and thermal conductivity respectively. The boundary conditions on A_{gs} are the continuity of temperature and heat flux across the interface, given as in $BC1$ and $BC2$.

1.2.2 Transport problem at the macro-scale

Several methodologies have been developed to upscale the micro-scale equations to obtain macro-scale models. In this section we will present the volume averaging method [67, 66, 70]. The superficial and intrinsic phase averages of any quantity φ_i associated with the i-phase are respectively given by

$$\langle \varphi_i \rangle = \frac{1}{V} \int_{V_i} \varphi_i dV \tag{1.3}$$

$$\langle \varphi_i \rangle^i = \varepsilon_i^{-1} \langle \varphi_i \rangle = \frac{1}{V_i} \int_{V_i} \varphi_i dV \tag{1.4}$$

In these relationships, V_i is the volume of the i-phase contained within the averaging volume V which is a REV of the porous medium. ε_i is the volume fraction of the i-phase. Using the upscaling method, one obtains the following averaged equations for the continuity

$$\nabla \cdot \langle \boldsymbol{v}_g \rangle = 0 \tag{1.5}$$

By volume averaging the single-phase flow momentum equation, the following macroscopic equation is obtained

$$\begin{aligned} \frac{\partial \rho_g \langle \mathbf{v}_g \rangle}{\partial t} + \rho_g \langle \mathbf{v}_g \rangle \cdot \nabla \langle \mathbf{v}_g \rangle^g + \nabla \cdot (\rho_g \langle \tilde{\mathbf{v}}_g \tilde{\mathbf{v}}_g \rangle) = \\ -\varepsilon_g \nabla \langle p_g \rangle^g + \varepsilon_g \rho_g \mathbf{g} + \underbrace{\mu_g \nabla^2 \langle \mathbf{v}_g \rangle - \mu_g \nabla \varepsilon_g \cdot \nabla \langle \mathbf{v}_g \rangle^g}_{\text{Brinkman terms}} + \frac{1}{V} \int_{A_{g\sigma}} \mathbf{n}_{g\sigma} \cdot \left(-\tilde{p}_g \mathbf{I} + \mu_g \nabla \tilde{\mathbf{v}}_g \right) dA \end{aligned} \tag{1.6}$$

where $\mathbf{v}_g$, $\langle \mathbf{v_g} \rangle^{\mathbf{g}}$, and $\tilde{\mathbf{v}}_g = \mathbf{v}_g - \langle \mathbf{v}_g \rangle^g$ are respectively the gas velocity within the pores, the intrinsic phase average velocity, and the deviation velocity. $\tilde{p}_g$ is the spatial deviation pressure in the gas phase. At low Reynolds numbers, the momentum equation described above can be represented by the Darcy equation, as shown below

$$\langle \boldsymbol{v_g} \rangle = -\frac{1}{\mu_g} \boldsymbol{K} \cdot (\nabla \langle p_g \rangle^g - \rho_g \boldsymbol{g}) \tag{1.7}$$

Increasing the Reynolds number, inertia terms start to play a dominant role. Staying in a laminar regime, one needs to add an extra, inertia term, in the macro-scale equation. Generally, it can be written as

$$\langle \boldsymbol{v_g} \rangle = -\frac{1}{\mu_g} \boldsymbol{K} \cdot (\nabla \langle p_g \rangle^g - \rho_g \boldsymbol{g}) - \mathbf{F} \cdot \langle \mathbf{v_g} \rangle \tag{1.8}$$

where $\mathbf{K}$ is the permeability tensor, $\mathbf{F}$ is the Forchheimer correction tensor, the last term $\mathbf{F} \cdot \langle \mathbf{v_g} \rangle$ is called the Forchheimer term [71]. While the above theoretical discussions suggest the potential existence of anisotropy effects for the Forchheimer terms, the engineering practice relies on simpler expressions, in particular, the use of Ergun's equation, which reads

$$\langle \boldsymbol{v_g} \rangle = -\frac{1}{\mu_g} \boldsymbol{K} \cdot (\nabla \langle p_g \rangle^g - \rho_g \boldsymbol{g} + \rho_g \beta |\mathbf{v}_g| \cdot \langle \mathbf{v}_g \rangle) \tag{1.9}$$

where β is the Forchheimer coefficient (also known as the non-Darcy coefficient or β factor). Based on collected experimental data, Ergun proposed correlations for K and β in the case of isotropic packed beds which are still very popular in the engineering practice

$$K = \frac{{d_{par}}^2 {\varepsilon_g}^3}{150 {\varepsilon_s}^2}, \qquad \beta = \frac{1.75 \varepsilon_s}{d_{par} {\varepsilon_g}^3} \tag{1.10}$$

where d_{par} is the equivalent particle diameter.

Averaging of the micro-scale energy equations leads to the following macroscopic equations

$$\begin{cases} \underbrace{\varepsilon_g \left(\rho c_p\right)_g \frac{\partial \langle T_g \rangle^g}{\partial t}}_{\text{accumulation}} + \underbrace{\varepsilon_g \left(\rho c_p\right)_g \langle \mathbf{v}_g \rangle^g \cdot \nabla \langle T_g \rangle^g}_{\text{convection}} = \\ \qquad \underbrace{\nabla \cdot \left[k_g \left(\varepsilon_g \nabla \langle T_g \rangle^g + \frac{1}{V} \int_{A_{g\sigma}} \mathbf{n}_{g\sigma} \tilde{T}_g dA \right) \right]}_{\text{conduction/tortuosity}} - \underbrace{\left(\rho c_p\right)_g \nabla \cdot \left\langle \tilde{\mathbf{v}}_g \tilde{T}_g \right\rangle}_{\text{dispersion}} + \underbrace{\frac{1}{V} \int_{A_{g\sigma}} \mathbf{n}_{g\sigma} \cdot k_g \nabla T_g dA}_{\text{interfacial flux}} \\ \varepsilon_s (\rho c_p)_s \frac{\partial \langle T_s \rangle^s}{\partial t} = \varepsilon_s k_s \nabla^2 \langle T_s \rangle^s + \nabla \cdot \left(\frac{1}{V} \int_{A_{\beta_s}} k_s \widetilde{T}_s \mathbf{n}_{sf} dA \right) + \frac{1}{V} \int_{A_{\beta_s}} k_s \nabla \widetilde{T}_s \cdot \mathbf{n}_{sf} dA. \end{cases} \tag{1.11}$$

where T_i, $\langle T_i \rangle^i$, and $\widetilde{T}_i = T_i - \langle T_i \rangle^i$ are respectively the point temperature in the i-phase, the intrinsic phase average temperature for the i-phase, and the spatial deviation temperature in the i-phase. The traditional terms arising when upscaling flows in porous media, i.e., dispersion, tortuosity effects, and exchange terms have been emphasized. Heat transfer in porous materials can either be studied under the assumption of LTE or LTNE. In LTE models, it is assumed that the average temperatures of the solid and gas phases are equal, $\langle T \rangle = \langle T_g \rangle^g = \langle T_s \rangle^s$ and the macroscopic energy conservation writes

$$\left(\varepsilon_g \rho_g c_{p,g} + \varepsilon_s \rho_s c_{p,s}\right) \frac{\partial \langle T \rangle}{\partial t} + \varepsilon_g \rho_g c_{p,g} \langle \mathbf{v_g} \rangle^{\mathbf{g}} \cdot \nabla \langle T \rangle = \nabla \cdot \left(\mathbf{k_{eff}} \cdot \nabla \langle T \rangle \right) \tag{1.12}$$

where the effective thermal conductivity tensor is given by

$$\mathbf{k_{eff}} = \left(\varepsilon_g k_g + \varepsilon_s k_s\right) \mathbf{I} + \frac{k_g - k_s}{V} \int_{A_{gs}} \mathbf{n}_{gs} \mathbf{b}_g dA - \left(\rho c_p\right)_g \langle \tilde{\mathbf{v}}_g \mathbf{b}_g \rangle \tag{1.13}$$

where the closure variable $\mathbf{b}_g$ is the vector field that maps $\nabla\langle T_g\rangle^g$ onto $\tilde{T}_g$ in the LTE model, $\tilde{T}_g = \mathbf{b_g}\cdot\nabla\langle T_g\rangle^g$. LTNE models are necessary when the transport properties of the various phases are highly contrasted.

$$\begin{cases} \frac{\partial}{\partial t}\left(\varepsilon_s\rho_s c_{p,s}\langle T_s\rangle^s\right) = \nabla\cdot\left(\mathbf{k_{s,eff}}\cdot\nabla\langle T_s\rangle^s\right) + h_v\left(\langle T_g\rangle^g - \langle T_s\rangle^s\right) \\ \frac{\partial}{\partial t}\left(\varepsilon_g\rho_g c_{p,g}\langle T_g\rangle^g\right) + \nabla\cdot\left(\rho_g c_{p,g}\langle\mathbf{v_g}\rangle^{\mathbf{g}}\langle T_g\rangle^g\right) = \nabla\cdot\left(\mathbf{k_{g,eff}}\cdot\nabla\langle T_g\rangle^g\right) + h_v\left(\langle T_s\rangle^s - \langle T_g\rangle^g\right) \end{cases} \tag{1.14}$$

A more detailed formulation of $\mathbf{k_{s,eff}}$, $\mathbf{k_{g,eff}}$ and h_v in the LTNE model obtained by the volume-averaging method are given as follows [72, 68, 73],

$$\begin{cases} \mathbf{k_{s,eff}} = \varepsilon_s k_s\mathbf{I} + \frac{k_s}{V}\int_{A_{gs}}\mathbf{n}_{sg}\mathbf{b_{ss}}dA \\ \mathbf{k_{g,eff}} = \varepsilon_g k_g\mathbf{I} + \frac{k_g}{V}\int_{A_{gs}}\mathbf{n}_{gs}\mathbf{b_{gg}}dA - \rho_g c_{p,g}\left\langle\tilde{\mathbf{v}}_g\mathbf{b_{gg}}\right\rangle \\ h_v = \frac{k_g}{V}\int_{A_{gs}}\mathbf{n}_{gs}\nabla s_g dA \end{cases} \tag{1.15}$$

where the closure variables $\mathbf{b_{ii}}$, and s_i are the vector and scalar fields that maps $\nabla\langle T_i\rangle^i$ onto $\tilde{T}_i$ in the LTNE model, $\tilde{T}_g = \mathbf{b_{gg}}\cdot\nabla\langle T_g\rangle^g - s_g(\langle T_g\rangle^g - \langle T_s\rangle^s) + ...$, and $\tilde{T}_s = \mathbf{b_{ss}}\cdot\nabla\langle T_s\rangle^s - s_s(\langle T_s\rangle^s - \langle T_g\rangle^g) + ...$ [68].

In this part, we have primarily introduced the mass, momentum, and energy equations for both micro-scale and macro-scale levels. Additionally, we have briefly introduced the upscaling process from the micro to the macro scale. By reviewing these classical transport problems within porous media from a multi-scale perspective, we have provided an overview of the interactions and relationships between different scales in porous media transport phenomena. Please note that this discussion provides a broad overview. More specific equations, like those for compressible fluid flow at the micro-scale, and those dealing with pyrolysis reactions at the macro-scale, will be delved into in forthcoming chapters.

1.3 Research Questions and Objectives

1.3.1 Research questions

The use of porous fibrous materials in TPS has led to questions about the validity of inherited hypotheses, such as the assumption of LTE often used in TPS design. While the LTE assumption has been demonstrated to be valid for dense charring materials, Scoggins et al. [28] found it to be invalid for PICA, a low-density carbon fiber material. They recommended performing experiments to measure the heat transfer coefficient in low-density carbon fiber materials, as such studies are currently lacking in the literature. The problem is further complicated because the flow of gas through porous media also modifies their effective thermal conductivity through a process known as dispersion. **The first research question, therefore, is: Given the use of low-density carbon fiber materials such as Calcarb in TPS, does the LTE hypothesis hold true? If not, what quantifiable value do the heat transfer coefficients take within the LTNE model?**

In high-temperature packed bed energy storage systems with fluid flow, traditional approaches assume laminar flow and constant fluid properties. Typically, solving the energy equation at the

macroscopic scale is sufficient. However, using air as the heat transfer medium in these systems results in non-uniform temperature, gas density, viscosity, and velocity distributions within the packed beds. Accurately describing temperature distribution solely using the energy equation becomes challenging in these cases. Coupling and solving mass, momentum, and energy equations simultaneously is necessary. Additionally, determining unknown variables like heat transfer coefficients and effective thermal conductivities for both fluid and solid phases is crucial due to the significant variations in thermophysical properties. **Therefore, the second research question is: How can we accurately model and describe the non-uniform temperature distribution in high-temperature packed bed TES systems with fluid flow, considering the varying thermophysical properties and the need for determining heat transfer coefficients and effective thermal conductivities for both fluid and solid phases?**

The development of two-equation models for describing heat transfer processes within biomass-packed beds, including a simplified model without considering drying processes and another accounting for pyrolysis, has raised questions about the validity of these approaches and the determination of effective parameters. While experimental techniques like the transient single-blow method have been employed to estimate parameters such as volumetric heat transfer coefficient h_v, effective solid thermal conductivity $\mathbf{k_{s,eff}}$, and effective gas thermal conductivity $\mathbf{k_{g,eff}}$, a comprehensive understanding of how moisture content affects these values remains elusive. Additionally, the extent of discrepancy between models considering water evaporation and those that do not still requires further investigation. **The third research question, therefore, is: How does the moisture content within biomass-packed beds influence the effective parameters such as the volumetric heat transfer coefficient, effective solid thermal conductivity, and effective gas thermal conductivity? Furthermore, how much do the predictions differ between models that take into account water evaporation and those that do not?**

In thermal protection systems (TPS), understanding the thermophysical properties and internal flow characteristics of porous materials like Calcarb is vital for accurately simulating spacecraft temperature distributions during atmospheric re-entry. While Darcy's Law can describe gas flow in porous media, Forchheimer's Law may be needed to adequately capture the complexity of the flow process in certain cases. A primary challenge in using Darcy's or Forchheimer's Law is determining the unknown permeability, $\mathbf{K}$, and Forchheimer coefficient, β, of Calcarb. In a previous work, [74] micro-scale simulations were performed to solve the Navier-Stokes equations under the Darcy flow assumption, and the permeability tensor was predicted based on the results. The permeability was then compared with values obtained by Borner et al. [75] using direct simulation Monte Carlo methods, revealing a difference of nearly 42%. **The fourth research question, therefore, is: What are the precise values of permeability and the Forchheimer coefficient for a material like Calcarb, and does the exponent in the equation match the commonly used value of 2 as suggested by Forchheimer's equation? Furthermore, how can we effectively amalgamate experimental findings with micro-scale simulation results to provide an explanation of Forchheimer flow from a micro-scale perspective?**

The investigation of pressure drop and heat transfer coefficients in randomly packed beds has led to questions about the accuracy of models and the need for a comprehensive multi-scale approach, which encompasses local microstructure and macro-structure. The discrete element method (DEM) has been used to generate randomly packed bed structures, based on the geometry of individual particles. Following the generation, both micro and macro-scale simulations have been executed on these structures. Despite this progress, there is a gap in studies addressing how high-temperature conditions affect the thermophysical properties of air and particles, which in turn influences effective parameters such as heat transfer coefficients. This complexity is further escalated within the multi-scale perspective, where the need for accurate numerical data for validation becomes crucial. **The fifth research question, therefore, is: How are fluid flow and heat transfer in packed beds affected by high temperatures in comparison to room temperature conditions? How influential are the thermophysical properties of fluids and solids in defining the pressure drop and heat transfer coefficients within the packed bed? Lastly, how can we combine micro and macro-scale simulation results to accurately determine the effective parameters under varying conditions?**

1.3.2 Objectives

The overall objective of this thesis is to contribute to the understanding and characterization of heat and mass transfer in high-temperature porous media. The adopted approach will consist in designing dedicated facilities adapted to the porous media and conditions of interest, carrying out fully instrumented experiments, and performing data analysis using state-of-the-art numerical modeling combined with advanced multi-objective optimization. To bring a comprehensive understanding, theoretical analysis - based on developments available in the volume-averaging community - and pore-scale numerical simulations will be undertaken to explain and justify the experimental results. More specifically, this approach is applied to address the following challenges and concerns in the field:

1. Investigate the validity of the LTE hypothesis experimentally and contribute to filling the knowledge gap by examining convective heat transfer in low-density carbon fiber materials like Calcarb.
2. Develop and validate a two-equation numerical model for high-temperature conditions, incorporating mass and momentum conservation, to accurately describe the temperature distribution in packed beds with non-uniform properties. Determine the effective conductivities and heat transfer coefficients required for the model.
3. Experimentally examine the validity of two-equation models describing heat transfer processes within biomass-packed beds with varying moisture content and investigate the effects of moisture on effective parameters and the discrepancy between models which consider water evaporation and those that do not.
4. Extend micro-scale simulations from Darcy flow to Forchheimer flow for porous materials like Calcarb, while experimentally determining permeability and Forchheimer coefficient values. Examine flows in both through-thickness (TT) and in-plane (IP) directions and investigate the consistency between experimental and numerical results.
5. Investigate the pressure drop and heat transfer coefficients inside randomly packed beds at high

temeperature through simulations at microscopic and macroscopic, ultimately contributing to a deeper understanding of these phenomena from a multi-scale perspective.

The numerical contributions of this Ph.D. project are made available Open Source in the Porous material Analysis toolbox based on OpenFoam (PATO).

1.4 Outline of the Thesis

This thesis is organized as shown in Fig.1.4. Chapter 1 provided an introduction to the context

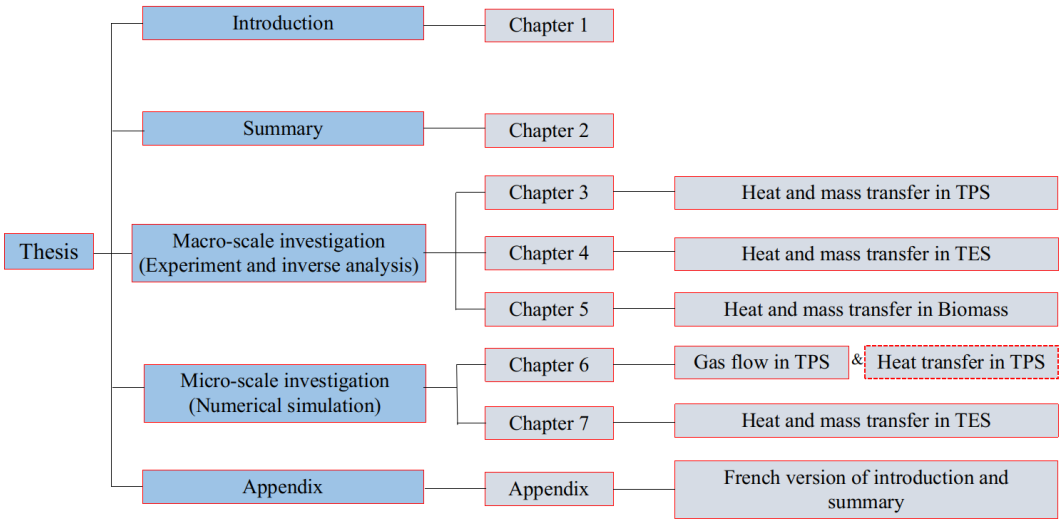

Figure 1.4 – Organization structure of the thesis

of the research, covering heat and mass transfer in TPS materials, packed bed TES, and pyrolysis of wood particles. This chapter also discussed the modeling of transport in porous media, addressing both micro-scale and macro-scale problems, and summarized the research questions and objectives that the thesis aims to address. Chapter 2 presents a summary of the thesis, including the research methodology, with a focus on governing equations, numerical simulation software, and experimental approaches. This chapter also provides the main results, which are divided into two parts, and concludes with a discussion of the research achievements and future perspectives.

The five independent articles that follow, each corresponding to a separate chapter, delve into the specific research questions and objectives mentioned in section 1.3. The article chapters are as follows:

Chapter 3: Experimental investigation on the validity of the local thermal equilibrium assumption in ablative-material response models;
Chapter 4: Development and validation of a local thermal non-equilibrium model for high-temperature thermal energy storage in packed beds;
Chapter 5: Detailed local thermal non-equilibrium model for biomass packed beds applied to wood chips and pellets of various moisture contents;

Chapter 6: Experimental measurement and 3D image-based numerical determination of the permeability and the Forchheimer correction tensor of Calcarb;
Chapter 7: Multi-scale investigation of flow and heat transfer coefficients in packed beds at high temperature.

These five chapters are divided into two main parts based on the scale of the research questions. The first part comprises chapters 3, 4, and 5, which focus on the macro-scale investigation of fluid flow and heat transfer characteristics in three different porous materials: anisotropic carbon fiber felts, regular granular porous materials, and irregular granular porous materials. The second part includes chapters 6 and 7, which concentrate on the micro-scale analysis of the numerical estimation of effective properties at the pore scale. Finally, the appendices of the thesis provide a French version of the Introduction (Appendix A) and Summary of the Thesis (Appendix B) sections, making the thesis more accessible and comprehensible for French-speaking readers.

Chapter 2

Summary of the Thesis

This summary presents an overview of the research methodology and synthesizes the most important results of the PhD.

2.1 Research Methodology

The research methodology adopted in this thesis involves a combination of numerical and experimental approaches to address the research questions and objectives presented in Chapter 1. The first subsection covers the description of the governing equations used at the macroscopic and microscopic scales. The numerical tool used during this study is presented in the second subsection. In the last subsection, the experimental approach and test conditions are described.

2.1.1 Governing equations

Two sets of equations are used to address the research questions at different scales. At the macro-scale, volume-averaged equations are employed to model mass, momentum, and energy conservation. Meanwhile, at the micro-scale, the conservation of mass, momentum, and energy is directly captured by the Navier-Stokes equations.

2.1.1.1 Macro scale equations

At the macro scale, mass, momentum and energy equations are introduced for both the local thermal equilibrium (LTE) and local thermal non-equilibrium (LTNE) models. Momentum equations are described using either creeping or inertial flow depending on the flow regime. For the first research question, which is the experimental investigation on the validity of the local thermal equilibrium assumption in ablative-material response models, Darcy's law with LTE and LTNE equations is used. For the second research question, which is the experimental investigation of convective heat transfer inside randomly packed beds at high temperatures, Forchheimer's model with LTNE equations is employed. For the third research question, which is the experimental validation of heat transfer

models in biomass-packed beds under different moisture content levels, Forchheimer's model with LTNE equations is utilized. In addition, we upgraded the model by incorporating a pyrolysis model. The different sets of governing equations mentioned are given below:

(1) Darcy's law with LTE equation

$$\begin{cases} \frac{\partial}{\partial t}\left(\varepsilon_g \frac{M\langle p\rangle^g}{R\langle T\rangle}\right) + \nabla \cdot \left(-\frac{M\langle p\rangle^g}{R\langle T\rangle}\frac{\mathbf{K}}{\mu_g} \cdot \nabla\langle p\rangle^g\right) = 0 \\ \left(\varepsilon_g \rho_g c_{p,g} + \varepsilon_s \rho_s c_{p,s}\right)\frac{\partial\langle T\rangle}{\partial t} + \varepsilon_g \rho_g c_{p,g}\langle \mathbf{v_g}\rangle^{\mathbf{g}} \cdot \nabla\langle T\rangle = \nabla \cdot \left(\mathbf{k_{eff}} \cdot \nabla\langle T\rangle\right) \end{cases} \tag{2.1}$$

where the first equation is the gas mass conservation written in terms of gas pressure (the gas velocity is substituted with Darcy's law) and the second equation is the energy conservation. The gas volume fraction ε_g is equal to the porosity of the porous medium. $\mathbf{K}$ and $\mathbf{k_{eff}}$ denote the permeability and effective thermal conductivity tensors respectively. $c_{p,i}$ denote the heat capacity of the i-phase. $\langle p\rangle^g$ and $\langle \mathbf{v_g}\rangle^g$ are the intrinsic average pressure and velocity of the gas. $\langle T\rangle$ denotes the superficial average temperature in the porous material (that is equal for both phases).

(2) Darcy's law with LTNE equations

$$\begin{cases} \frac{\partial}{\partial t}\left(\varepsilon_g \frac{M\langle p\rangle^g}{R\langle T_g\rangle^g}\right) + \nabla \cdot \left(-\frac{M\langle p\rangle^g}{R\langle T_g\rangle^g}\frac{\mathbf{K}}{\mu_g} \cdot \nabla\langle p\rangle^g\right) = 0 \\ \frac{\partial}{\partial t}\left(\varepsilon_s \rho_s c_{p,s}\langle T_s\rangle^s\right) = \nabla \cdot \left(\mathbf{k_{s,eff}} \cdot \nabla\langle T_s\rangle^s\right) + h_v\left(\langle T_g\rangle^g - \langle T_s\rangle^s\right) \\ \frac{\partial}{\partial t}\left(\varepsilon_g \rho_g c_{p,g}\langle T_g\rangle^g\right) + \nabla \cdot \left(\rho_g c_{p,g}\langle \mathbf{v_g}\rangle^{\mathbf{g}}\langle T_g\rangle^g\right) = \nabla \cdot \left(\mathbf{k_{g,eff}} \cdot \nabla\langle T_g\rangle^g\right) + h_v\left(\langle T_s\rangle^s - \langle T_g\rangle^g\right) \end{cases} \tag{2.2}$$

where the first equation in the set represents the gas mass conservation and is written in terms of gas pressure, with the gas velocity being replaced by Darcy's law. The second and third equations correspond to the energy conservation equations for solid and fluid phases, respectively. $\mathbf{k_{i,eff}}$ denote the effective thermal conductivity tensor of the i-phase. $\langle T_i\rangle^i$ and $\langle \mathbf{v_g}\rangle^{\mathbf{g}}$ denote the intrinsic phase average temperature for the i-phase and the intrinsic gas average velocity. h_v denotes the volumetric heat transfer coefficient between the gas stream and the sample.

(3) Forchheimer's model with LTNE equations

$$\begin{cases} \frac{\partial}{\partial t}\left(\varepsilon_g \frac{M\langle p\rangle^g}{R\langle T_g\rangle^g}\right) + \nabla \cdot \left(-\frac{M\langle p\rangle^g \mathbf{K}\mathbf{X}}{R\langle T_g\rangle^g} \cdot \nabla\langle p\rangle^g\right) = 0 \\ \frac{\partial}{\partial t}\left(\varepsilon_s \rho_s c_{p,s}\langle T_s\rangle^s\right) = \nabla \cdot \left(\mathbf{k_{s,eff}} \cdot \nabla\langle T_s\rangle^s\right) + h_v\left(\langle T_g\rangle^g - \langle T_s\rangle^s\right) \\ \frac{\partial}{\partial t}\left(\varepsilon_g \rho_g c_{p,g}\langle T_g\rangle^g\right) + \nabla \cdot \left(\rho_g c_{p,g}\langle \mathbf{v_g}\rangle^{\mathbf{g}}\langle T_g\rangle^g\right) = \nabla \cdot \left(\mathbf{k_{g,eff}} \cdot \nabla\langle T_g\rangle^g\right) + h_v\left(\langle T_s\rangle^s - \langle T_g\rangle^g\right) \end{cases} \tag{2.3}$$

where the first equation in the set expresses gas mass conservation in terms of gas pressure, with Forchheimer's law used to substitute gas velocity. The second and third equations describe energy conservation equations for solid and fluid phases, respectively. The Forchheimer tensor, represented as $\mathbf{X}$, is introduced to account for inertial effects [76].

$$X_{ij} = \frac{1}{\mu_g K_{ij} + \beta_{ij}\rho_g|\langle v_g\rangle|} \tag{2.4}$$

(4) Forchheimer's model with LTNE equations and a pyrolysis model

This model offers a numerical representation of the interactions between a multi-phase reactive material (N_s solid phases) and a multi-species reactive gas mixture (N_g gaseous elements/species) [77, 78]. The reactive material is assumed to be rigid, while the gas phase consists of a compressible and perfect mixture of gaseous elements/species. Water is modeled as a static solid phase. In the following discussion, the pyrolysis, mass conservation, momentum, and energy equations will be introduced separately.

In the pyrolysis model, we account for the fact that the material of interest may be composed of different phases and, even, sub-phases. For example, the main compounds of the wood pellets that are studied in this work are the wood-cell walls (composed of sub-phases of cellulose, hemicellulose, and lignin) and water (composed of bounded and free water). To address this aspect, we divide each phase i into $N_{p,i}$ sub-phases. A specific sub-phase, $P_{i,j}$, follows a predetermined kinetic mechanism, leading to the generation of species or element A_k based on the stoichiometric coefficients $v_{i,j,k}$.

$$P_{i,j} \rightarrow \sum_{k=1}^{N_g} v_{i,j,k} A_k \tag{2.5}$$

The Arrhenius model is employed to represent the pyrolysis reactions. The progression of the pyrolysis reaction $\chi_{i,j}$ for sub-phase j within phase i is defined as,

$$\partial_t \chi_{i,j} = (1 - \chi_{i,j})^{m_{i,j}} {T_s}^{n_{i,j}} \mathcal{A}_{i,j} exp(-\frac{\epsilon_{i,j}}{RT_s}) \tag{2.6}$$

where m_{ij} and n_{ij} denote the parameters of the Arrhenius law, $\mathcal{A}_{)|}$ is the Arrhenius law pre-exponential factor, ϵ_{ij} is the activation energy. By combining the contributions from the N_s solid phases, the total production rate π for species k can be calculated.

$$\pi_k = \sum_{i=1}^{N_s} \sum_{j=1}^{N_{p,i}} v_{i,j,k} \epsilon_{i,0} \rho_{i,0} F_{i,j} \partial_t \chi_{i,j} \tag{2.7}$$

where the initial volume fraction, intrinsic density, and mass fraction of sub-phase j within phase i are denoted by $\epsilon_{i,0}$, $\rho_{i,0}$, and $F_{i,j}$. By summing the contributions of all elements and species in the mixture, we can determine the total pyrolysis-gas production rate, Π.

$$\Pi = \sum_{k=1}^{N_g} \pi_k \tag{2.8}$$

Based on the chemical model employed in the gas phase, species for finite-rate chemistry may be considered. In cases involving finite-rate chemistry, the conservation equation for a generic species possessing a mass fraction of y_i can be expressed as:

$$\partial_t(\varepsilon_g \rho_g y_i) + \partial_t(\varepsilon_g \rho_g y_i \mathbf{v_g}) + \partial_{\mathbf{x}} \cdot \mathcal{F}_i = \pi_i \tag{2.9}$$

where $\mathcal{F}_i$ represents the effective multicomponent diffusion mass fluxes for the i-th species. The Mutation++ library is utilized to compute all thermodynamic and transport properties [77]. For the

gas mixture, the mass conservation accounts for the pyrolysis production rate as follows:

$$\partial_t \left(\varepsilon_g \rho_g\right) + \nabla \cdot \left(\varepsilon_g \rho_g \langle \mathbf{v_g} \rangle^{\mathbf{g}}\right) = -\sum_{i=1}^{N_s} \partial_t (\varepsilon_i \rho_i) = \Pi \tag{2.10}$$

Two energy conservation equations incorporating pyrolysis are required to represent the solid and gas phases. These equations are as follows:

$$\sum_{i=1}^{N_s} \varepsilon_i \rho_i c_{p,i} \partial_t \langle T_s \rangle^s + \sum_{i=1}^{N_s} h_i \partial_t \left(\varepsilon_i \rho_i\right) = \nabla \cdot \left(\mathbf{k_{s,eff}} \cdot \nabla \langle T_s \rangle^s\right) + h_v \left(\langle T_g \rangle^g - \langle T_s \rangle^s\right) \tag{2.11}$$

$$\begin{aligned} \varepsilon_g \rho_g c_{p,g} \partial_t \langle T_g \rangle^g - \partial_t \left(\varepsilon_g p\right) + \sum_{j=1}^{N_g} h_j \partial_t \left(\varepsilon_g \rho_g y_j\right) + \nabla \cdot \left(\varepsilon_g \rho_g h_g \mathbf{v_g}\right) + \nabla \cdot \sum_{j=1}^{N_g} \mathcal{Q}_j \\ = \nabla \cdot \left(\mathbf{k_{g,eff}} \cdot \nabla \langle T_g \rangle^g\right) + h_v \left(\langle T_s \rangle^s - \langle T_g \rangle^g\right) \end{aligned} \tag{2.12}$$

where h_i and h_j represent the absolute enthalpies of the i-th, and j-th components. $\mathcal{Q}_j$ is the heat transport by effective diffusion of the j-th species.

2.1.1.2 Micro scale equations

For the micro-scale numerical simulations, we use the transient laminar Navier-Stokes equations to model the fluid flow, without including energy conservation for the fluid. This is applied to the fourth research question, which involves deriving effective properties. For the fifth research question, the fluid flow is compressible, and heat transfer is described using conduction in both phases and convection in the fluid phase. We consider the coupling between density and temperature and model the system using the transient laminar Navier-Stokes equations, including conservation of mass, momentum, and energy equations. The different sets of governing equations for each case considered are given below:

(1) Isothermal incompressible flow

$$\begin{cases} \nabla \cdot \mathbf{v_g} = 0 \\ \rho_g (\frac{\partial \mathbf{v_g}}{\partial t} + \mathbf{v_g} \cdot \nabla \mathbf{v_g}) = -\nabla p + \mu_g \nabla^2 \mathbf{v_g} \\ \mathbf{v_g} = 0 \qquad \text{at} \quad A_{gs} \end{cases} \tag{2.13}$$

where $\mathbf{v_g}$ and p are, respectively, the velocity and pressure of the gas phase; A_{gs} represents the interface area between the gas phase and the solid phase contained within the considered region.

2) Non-isothermal compressible flow

$$\begin{cases} \partial_t \rho_g + \nabla \cdot (\rho_g \mathbf{v_g}) = 0 \\ \rho_g \left(\frac{\partial \mathbf{v_g}}{\partial t} + \mathbf{v_g} \cdot \nabla \mathbf{v_g}\right) = -\nabla p + \mu_g \nabla^2 \mathbf{v_g} \\ \rho_g c_{p,g} \frac{\partial T_g}{\partial t} + \rho_g c_{p,g} \mathbf{v_g} \cdot \nabla T_g = k_g \nabla^2 T_g \\ \rho_s c_{p,s} \frac{\partial T_s}{\partial t} = k_s \nabla^2 T_s \end{cases} \tag{2.14}$$

where heat transfer balance is derived in both fluid and solid phases. The gas density is calculated with the perfect gas law

$$\rho_g = \frac{Mp}{RT} \tag{2.15}$$

Here we consider the fluid to be non-isothermal and compressible. It remains interesting to compare pressure (compressibility) and temperature (dilatation) effects on the density variations for the problems of interest. To do this, we derive ρ_g with respect to T and p, which gives us a differential form of the gas density

$$\begin{aligned} d\rho_g &= \frac{\partial \rho_g}{\partial T} dT + \frac{\partial \rho_g}{\partial p} dp \\ &= -\frac{Mp}{RT^2} dT + \frac{M}{RT} dp \end{aligned} \tag{2.16}$$

By substituting Eq.2.15 and transforming we obtain

$$\frac{d\rho_g}{\rho_g} = -\frac{1}{T} dT + \frac{1}{p} dp = -\beta_g dT + \chi_T dp \tag{2.17}$$

where β_g is the volumetric coefficient of thermal expansion, χ_T is the coefficient of compressibility

$$\beta_g = \frac{1}{V} \left(\frac{\partial V}{\partial T} \right)_p \qquad \chi_T = \frac{1}{V} \left(\frac{\partial V}{\partial p} \right)_T \tag{2.18}$$

Let's consider a situation where T is 300 K. If the temperature goes up by 100 K, which is dT=100 K, then $\beta_g dT$ becomes around 0.333. With p at 101325 Pa and the Reynolds number at 300, a rise in pressure dp of about 40 Pa (typical of the tests with glass beads carried out in this work) leads to a $\chi_T dp$ value of around 0.000394. Looking at these numbers, it's clear that $\beta_g dT$ and $\chi_T dp$ are different by three orders of magnitude, which is a large difference. Therefore, compressibility effects are negligible compared to thermal expansion effects in the conditions of the experiments carried out in this work.

2.1.2 Numerical analysis

In this part, we introduce the software used for the numerical simulations. The numerical model used in this work is based on the Porous-Material Analysis Toolbox based on OpenFoam (PATO), which is implemented as a C++ top-level module of the open-source computational fluid dynamics software program OpenFOAM. OpenFOAM is a finite volume computational fluid dynamics software released by OpenCFD Limited and supported for Unix/Linux operating systems. PATO can be run as a simple Fourier heat transfer code or include more advanced features such as internal decomposition (pyrolysis, vaporization), gas-gas and gas-solid chemical interactions (combustion, cracking, cooking), gas species transport (convection, diffusion), and solid morphology evolutions (internal density changes, surface ablation). PATO uses the open-source thermodynamics, transport, and chemistry library Mutation++ produced by the von Karman Institute for Fluid Dynamics. Fig.2.1 shows an overview of the PATO software.

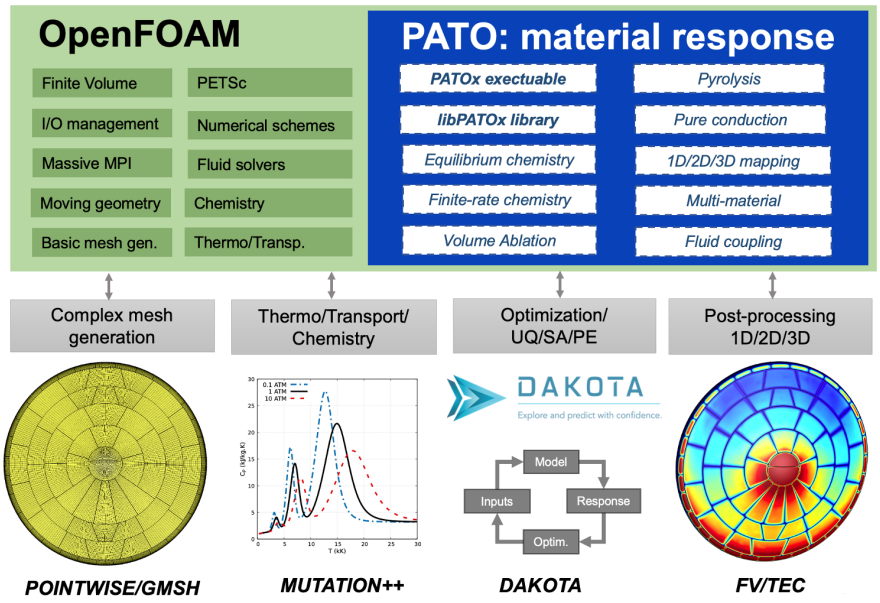

Figure 2.1 – Overview of the PATO software which was implemented as a top-level module of OpenFOAM enabling the coupling to mesh generation, thermochemistry, optimization, and post-processing libraries.

The optimization work in this thesis was conducted using the Design Analysis Kit for Optimization and Terascale Applications (DAKOTA), which includes modules for sensitivity analysis and multi-objective optimization. Specifically, Latin Hypercube Sampling (LHS) was employed for sensitivity analysis, while global optimization was performed using the DIviding RECTangles algorithm (NCSU DIRECT) and local optimization was carried out using the Adaptive NonLinear Least-Squares algorithm (NL2SOL) for multi-objective optimization. Figure 2.2 shows the schematic of the DAKOTA framework.

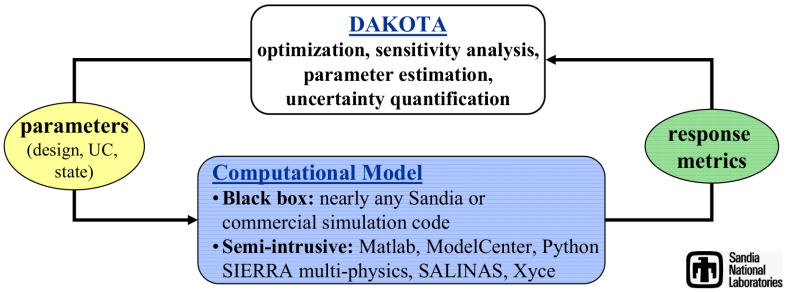

Figure 2.2 – Schematic of the DAkOTA framework.

2.1.3 Experimental approach

The experimental approach in this thesis focuses on macroscopic processes. The experiments conducted in this work include measurements of fundamental data, i.e., pressure drop, thermal conductivity, porosity, and moisture content, and determination of effective parameters such as volumetric heat transfer coefficients, effective thermal conductivities, and permeability.

To determine the volumetric heat transfer coefficients and effective thermal conductivities, either a steady-state [79, 80] or transient regime [81, 82, 83, 84] approach can be employed. In the steady-state approach, a porous medium (a sample of porous material or a packed-bed of granulate) is heated and maintained at a constant temperature, while cold gas is passed through the medium of interest. The gas temperature is measured at the inlet, outlet, and within the porous medium if possible. The heat transfer coefficient is determined from the spatial evolution of the gas temperature. Alternatively, in the transient approach, hot gas is used to heat a cold sample, and the time evolution of the gas temperature is recorded upwind and downwind of the sample. This method, known as the transient single blow technique (TSBT) [81, 85], allows for the measurement of the temperature increase of the solid, which provides robustness for inverse analysis. As both solid and gas temperatures vary in space, their effective thermal conductivities can be inferred simultaneously using this method. The experimental facility presented in this work is based on the TSBT method.

The pressure drop measurement is related to the permeability and Forchheimer coefficient of the sample. For a single Calcarb sample, due to its anisotropy, the pressure drop values need to be measured separately in the In-Plane (IP) and Through-Thickness (TT) directions. For the measurement of pressure drop in packed beds, an assumption of one-dimensional variation is made, neglecting anisotropy. When the fluid flow corresponds to the Darcy flow regime, the pressure drop versus velocity linear relationship is fitted, and the permeability value can be obtained. When the fluid flow corresponds to the Forchheimer flow regime, the pressure drop versus velocity nonlinear relationship is fitted, and the values of permeability and the Forchheimer coefficient can be obtained. The critical values separating the Darcy and Forchheimer flow regimes need to be determined in the experiment.

Other fundamental data, such as thermal conductivity of Calcarb, wood particles, porosity, and moisture content, can be obtained through various experimental techniques, including the Transient Plane Sources technique (Hot Disk, TPS 3500) [86], the steady-state measurement method (guarded hot plate) [87], gravimetric method, and thermogravimetric measurement method (moisture analyzer (METTLER TOLEDO, HC103)) [88].

Overall, the experimental approach employed in this thesis provides a comprehensive understanding of the macroscopic properties of the studied materials. This understanding is crucial for validating the numerical simulations and developing practical applications.

2.2 Main Results

This section provides an overview of the main results of the thesis, which can be divided into two parts as outlined in section 1.4. The specific conclusions and derivation process for each work can be

found in the corresponding chapters.

2.2.1 First Part

The first part of this work, presented in Chapters 3, 4, and 5, focuses on the study of the mass, momentum, and energy equations at the macroscopic scale.

Thermal Protection Systems (TPS) material response models rely on the assumption of local thermal equilibrium (LTE) between the solid phase and the gas phase. This assumption was challenged and investigated by several authors but a sufficiently precise knowledge of heat transfer coefficients in TPS materials was lacking to reach final conclusions. The objective of the work in Chapter 3 is to contribute to filling this gap by providing a literature review of available data in other communities (thermal energy storage, heat exchangers) and by performing an experimental characterization of Calcarb, a commercial carbon preform used for manufacturing thermal protection systems. Heat transfer within Calcarb was studied experimentally in the Through-Thickness (TT) and in the In-Plane (IP) directions for Reynolds numbers of 1 to 4 - representative of the TPS application - using the transient single-blow technique (TSBT). Numerical parameter estimation was performed using the Porous material Analysis Toolbox based on OpenFoam (PATO) and the Design Analysis Kit for Optimization and Terascale Applications (DAKOTA). To perform the parameter estimation, a two-dimensional axisymmetric numerical model as shown in Fig.2.3 was constructed that consisted of different regions identified as follows: flow1 (upwind flow field), sample (porous sample), flow2 (downwind flow field), tube (quartz tube), and thermocouple (downwind thermocouple). A typical

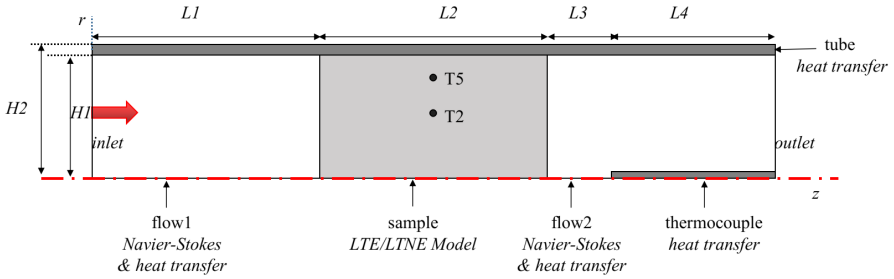

Figure 2.3 – Two-dimensional axisymmetric numerical model of the test section

comparison of the measured and predicted results is presented in Fig.2.4, where measured results are represented by dots, and predicted results obtained by solving the local thermal non-equilibrium (LTNE) model are represented by solid and dashed lines. The recorded inlet gas temperature, sample temperature at two locations (T2, T5), and outlet gas temperature are a function of time. The solid and dashed lines represent the predicted solid and gas temperatures, respectively. The heat transfer coefficient h_v was estimated to be greater than or equal to 10^8 W/(m^3 · K), the gas and solid temperatures overlapped, and the LTE assumption was shown to be valid under the conditions of the experiment. The results obtained in this chapter provide crucial information for the validation of TPS material response models.

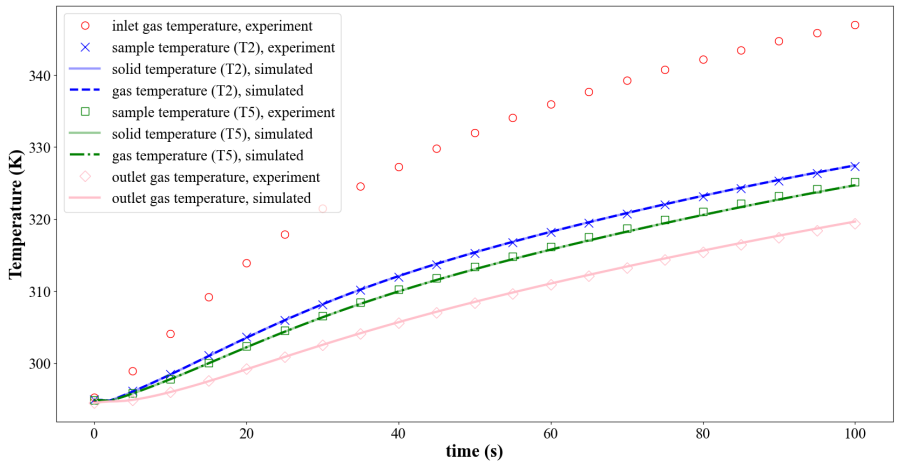

Figure 2.4 – The comparison of predicted and measured temperature in TT direction ($qm = 7.68 \times 10^{-5}$ kg/s).

Chapter 4 explores coupled heat and mass transfer inside packed beds used for thermal energy storage at high temperatures. Traditional heat transfer correlations are not sufficient to describe the temperature fields accurately due to non-uniform temperature, gas density, viscosity, and velocity distributions within the packed beds. An experimental-numerical inverse analysis method was employed to determine the effective conductivities and heat transfer coefficients required to inform the local thermal non-equilibrium (LTNE) model under high-temperature conditions. Experiments were conducted using hot air at different mass flow rates, and a two-equation model incorporating mass and momentum conservation was implemented and validated. A schematic drawing of the experimental setup that we have developed and an enlarged view of the test section, where thermocouple positions are shown, are displayed in Fig.2.5. Fig.2.6 presents a comparison of the measured and predicted

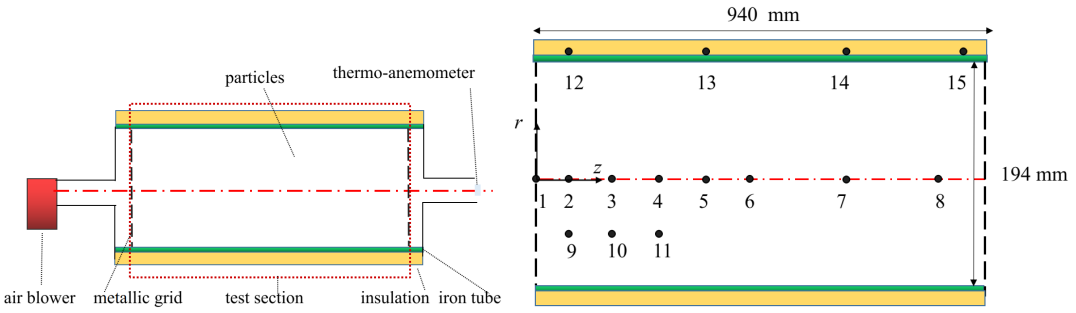

(a) experimental setup (b) test section part

Figure 2.5 – Schematic diagram of the experimental system and enlarged view of the test section showing the thermocouple identification numbers

results for four different values of mass-flow rate, where measured results are represented by dots, and predicted results obtained by solving the two-equation model are represented by solid and dashed lines. The results indicate that the value of the heat transfer coefficient h_v in the LTNE model falls

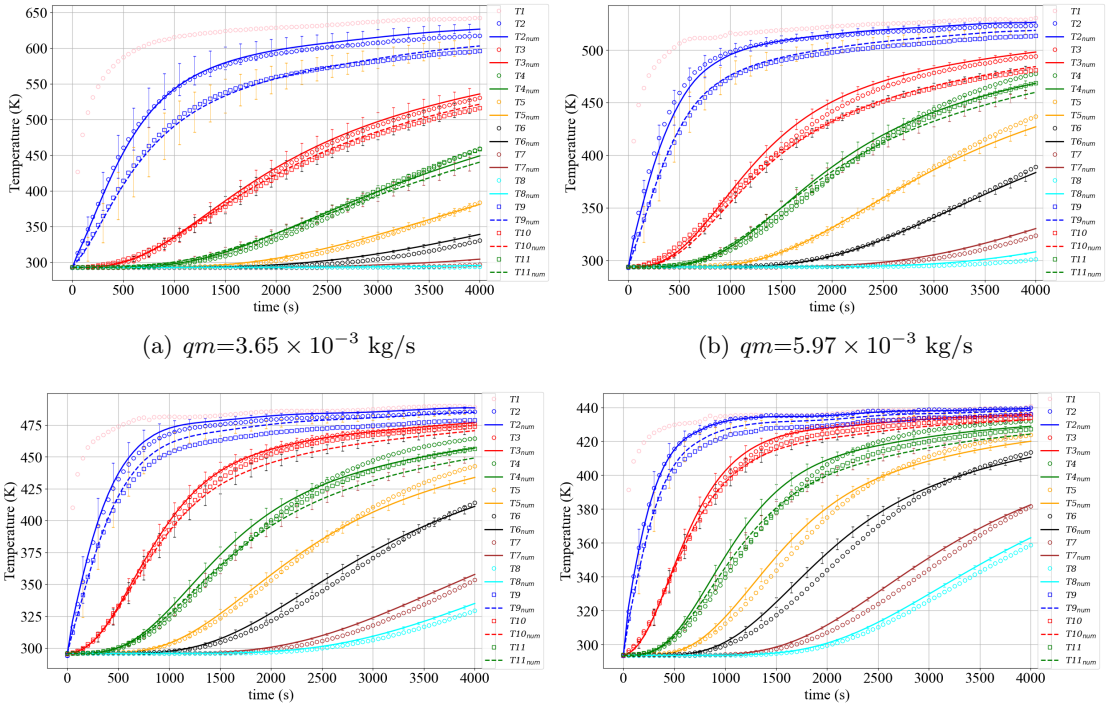

(a) qm=3.65 × 10^{-3} kg/s

(b) qm=5.97 × 10^{-3} kg/s

(c) qm=7.34 × 10^{-3} kg/s

(d) qm=1.02 × 10^{-2} kg/s

Figure 2.6 – The comparison of predicted and measured temperatures for different mass-flow rates

in the range of 1.0× 10^4 to 2.0× 10^4 W/(m^3 · K) under the given conditions. The axial dispersion gas thermal conductivity was found to be around 4 and 55 times higher than the gas thermal conductivity at Peclet numbers of around 55 and 165, respectively. Furthermore, two improved correlations of Nusselt number ($Nu = 2 + 1.54Re^{0.6}Pr^{1/3}$) and of axial dispersion gas thermal conductivity ($k_{dis,||}$=$0.00011Re^{2.49}Pr \cdot k_g$) are proposed which are valid for a range of Reynolds number from 58 to 252.

Chapter 5 of this work aimed to establish a two-equation model for describing heat transfer processes within biomass-packed beds. Effective parameters such as the volumetric heat transfer coefficient h_v, effective solid thermal conductivity $\mathbf{k_{s,eff}}$, and effective gas thermal conductivity $\mathbf{k_{g,eff}}$ need to be determined. These parameters are difficult to obtain due to the complex characteristics of biomass particles, such as geometric configurations, anisotropy, moisture content, and pore structure. To determine these parameters, a novel experimental facility based on the transient single-blow technique was designed, and experiments were conducted using air to heat four types of materials: moist wood pellets, dry wood pellets, moist wood chips, and dry wood chips. To maintain a single variable of moisture content, velocities were maintained at specific values for each material. To prevent pyrolysis, which can pose safety risks in laboratory-scale experimental setups, the maximum inlet temperature was set to 349 K, focusing solely on the drying process of the biomass packed-beds. Parameter estimations were carried out using numerical inverse analysis. The numerical model was implemented using finite volumes in the Porous Material Analysis Toolbox based on OpenFOAM (PATO). A local optimization method, NL2SOL, was employed to minimize the error between measured and predicted temperatures. To perform the parameter estimation, a two-dimensional axisymmetric numerical model as shown in Fig.2.7 was constructed that consisted of two regions: packed bed and tube. Fig.2.8 presents the com-

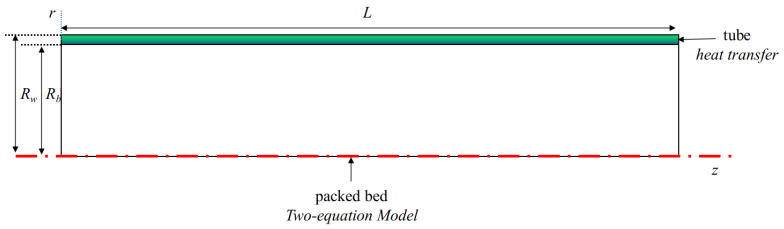

Figure 2.7 – Two-dimensional axisymmetric numerical model of the test section

parison of predicted and measured temperatures in wood pellets and wood chips. The results revealed that moisture content significantly affects the volumetric heat transfer coefficient and effective thermal conductivity in the test range. The volumetric heat transfer coefficient increased from 13429-13850 W/(m^3 K) to 16333-16450 W/(m^3 K) under the same flow conditions when the moisture content decreased from 6.2% to 0 for wood pellets. It increased from 12340-12570 W/(m^3 K) to 13924-13950 W/(m^3 K) when the moisture content decreased from 9.1% to 0 for wood chips. As one may expect, water evaporation is responsible for a blockage effect at the particle scale. These findings contribute to a deeper understanding of heat and mass transfer phenomena in biomass-packed beds and can inform the development of more accurate models for various applications. They also show the importance of accounting for degassing for pyrolysis applications in general, calling for a continuation of this work

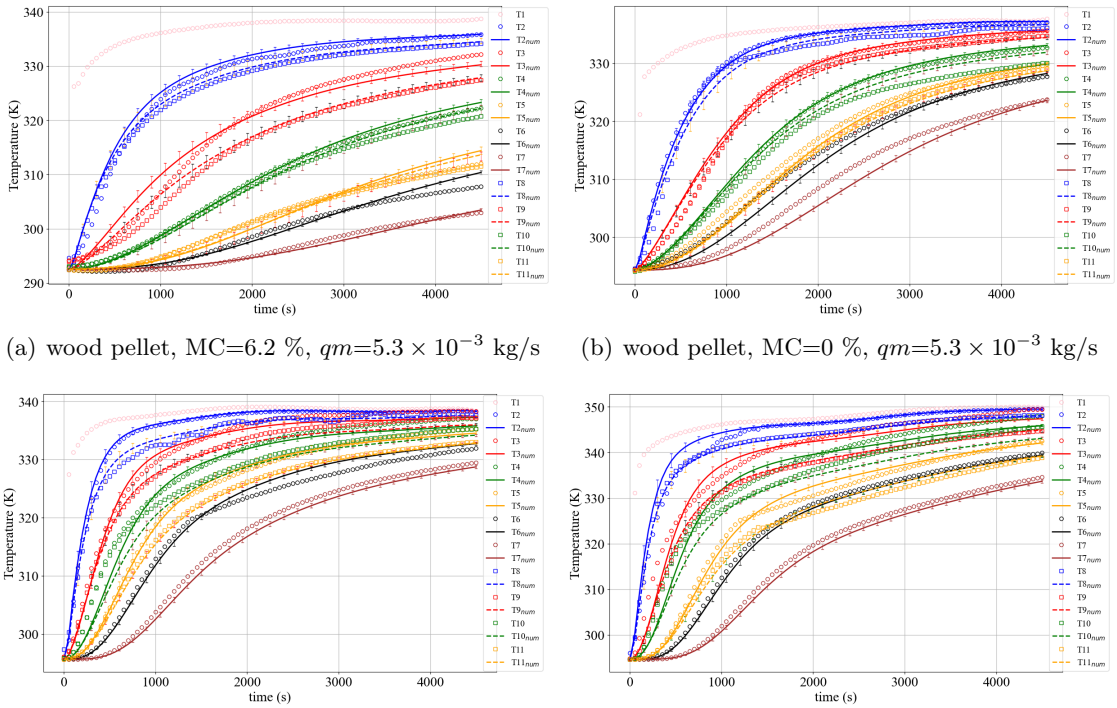

(a) wood pellet, MC=6.2 %, qm=5.3 $\times$ 10^{-3} kg/s

(b) wood pellet, MC=0 %, qm=5.3 $\times$ 10^{-3} kg/s

(c) wood chips, MC=9.1 %, qm=5.1 $\times$ 10^{-3} kg/s

(d) wood chips, MC=0 %, qm=5.1 $\times$ 10^{-3} kg/s

Figure 2.8 – The comparison of predicted and measured temperature in wood pellets and wood chips.

past the drying temperature.

2.2.2 Second part

In Chapters 6 and 7, we investigate the mass, momentum, and energy equations at the microscopic scale to estimate effective properties for non-periodic anisotropic porous media. Chapter 6 focuses on determining the permeability and Forchheimer coefficient, while Chapter 7 determines the volumetric heat transfer coefficient h_v.

Chapter 6 of this work focuses on micro-scale simulations and experimental analysis of creeping to inertial flows within Calcarb, a carbon fiber preform used as an insulator in TPS applications. Experimental measurements of the pressure gradient across Calcarb samples were conducted for Reynolds numbers ranging from 0.05 to 10 in both in-plane (IP) and through-thickness (TT) orientations, and nitrogen was used as the working fluid. Permeability and Forchheimer coefficients were inferred both from experimental data and from micro-scale numerical solutions based on a 3D digital images of a Calcarb sample. The numerical model used for micro-scale simulations is presented in Fig.2.9. Fig.2.10

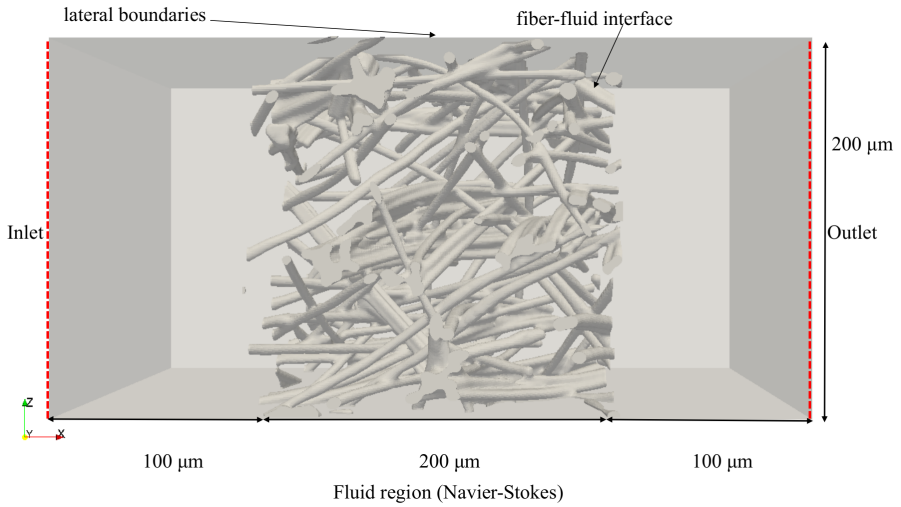

Figure 2.9 – Three-dimensional numerical structure used in micro-scale simulations

presents the variation of pressure gradient with respect to Reynolds number in both the IP and TT directions in the experiments, along with the curves obtained through data fitting. The values of the Forchheimer coefficient β and exponent n are calculated using the least-squares approximation method and presented in Tab.2.1. First, we use the classic Forchheimer equation with a fixed exponent of 2 to get the Forchheimer coefficient, as shown in Table 2.1's second column, where R^2 denotes the level of fit of the model to the data. Next, we improve the fit by adjusting both the Forchheimer coefficient and the exponent n, with results shown in the third column of the same table. Rather than typically being set as 2, the exponent exhibits minor differences, like Aguilar et al.[71] found in their work with porous rocks. Moreover, the values of β and n differ between the IP and TT directions due to the inherent anisotropy of the sample.

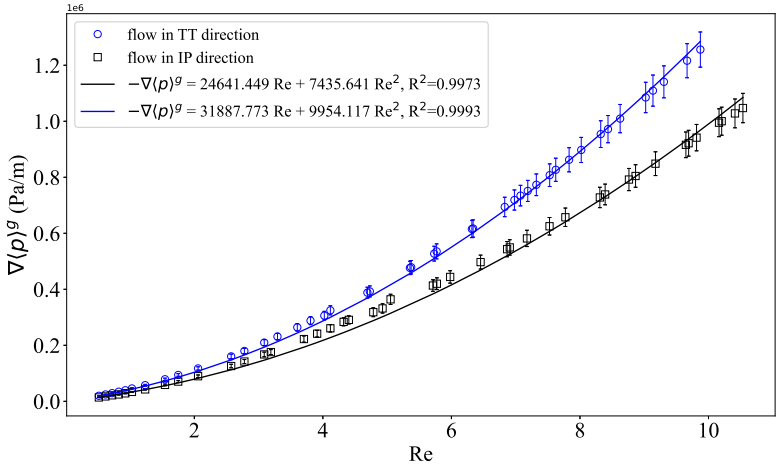

Figure 2.10 – Relationship between pressure gradient and Reynolds number in both the IP and TT directions in the experimental

.

Table 2.1 – Forchheimer coefficient β (1/m) and exponent n in the IP and TT direction

Flow direction	β and n $(n = 2)$	β and n $(n \neq 2)$
IP	1.4948×10^5, 2 $(R^2 = 0.9973)$	2.7015×10^5, 1.73 $(R^2 = 0.9999)$
TT	2.0010×10^5, 2 $(R^2 = 0.9993)$	2.7782×10^5, 1.84 $(R^2 = 0.9999)$

Fig.2.11 presents the comparison of experimental and simulation results within the Forchheimer flow regime, where the Reynolds number in the experiments ranges from 0.50 to 10.46. The data representing the experimental correlations are sourced from Table 2.1. When comparing values within the Forchheimer flow regime, one can notice that the largest differences in pressure gradient between simulation and experiment reach up to 64.5% and 68.2% in the IP and TT directions respectively. Given the assumption of one-dimensional flow in the experiments, only the pressure drop in the direction of flow was taken into account. However, in the three-dimensional simulation, the dispersion of flow due to pressure drop in other directions was also considered. This dispersion, occurring in directions other than the main flow, leads to a decrease in pressure drop along the main flow direction, which could result in simulation values being lower than experimental values. Furthermore, as displayed in Fig.2.11, when the Reynolds number is less than 2.4, the difference between the simulation and experimental values is 4.5% and 5.2% in the IP and TT directions, respectively. As the Reynolds number increases, the pressure gradient components in non-main flow directions become more significant, causing the simulated pressure drop along the main flow direction to diverge increasingly from the experimental value.

Chapter 7 focuses on using a multi-scale approach to investigate the pressure drop and heat transfer coefficient within randomly packed beds at high temperatures. For the reproduction of the local microstructure, a 3D model of randomly packed beds filled with sphere particles was developed using the LIGGGHTS DEM code. Two microscopic models are solved in this packed bed for different

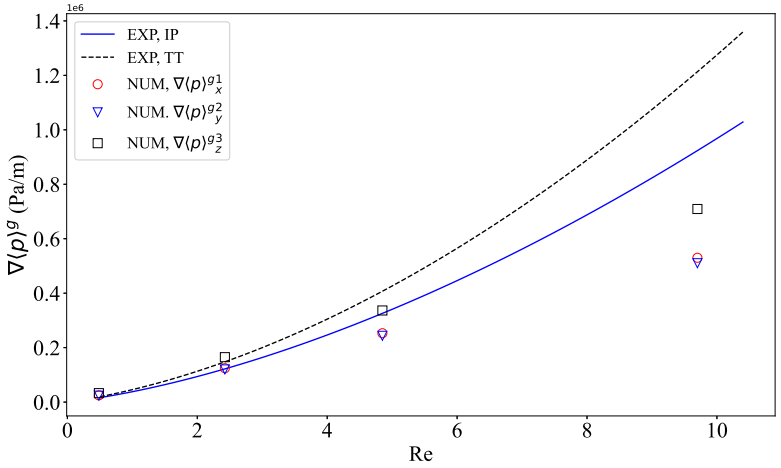

Figure 2.11 – The comparison of numerical and experiment results in the Forchheimer flow regime.

situations: the first one is an incompressible flow under constant temperature, characterized by the incompressible Navier-Stokes equations, the solutions are then used to obtain permeability and the Forchheimer coefficient. The second is a transient compressible flow, with high-temperature gas (800K) entering from the inlet, by a model coupling mass and momentum equations for the fluid phase, and energy equations for fluid and solid phases, respectively. Once the temperature field is obtained, h_v can be evaluated by using an integration method (as shown in Eq.7.2).

For the simulations at the macro-scale, based on the volume-averaged equations, a 2D axisymmetric structure was used to represent the 3D randomly packed beds. Numerical tools based on porous material analysis toolbox software PATO are used to solve Forchheimer's flow and the LTNE model within macroscopic domain. The effective parameters, that is, the thermal conductivities and heat transfer coefficients, are obtained by carrying out an inverse analysis.

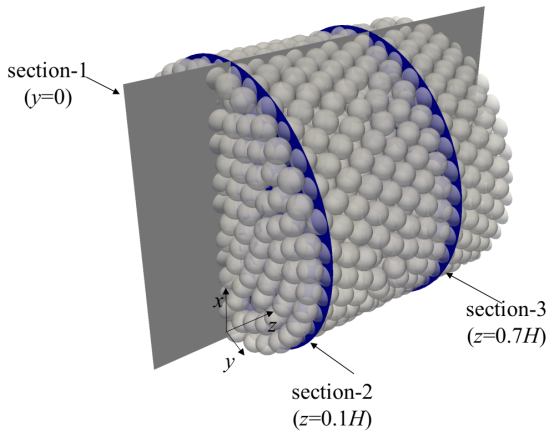

Figure 2.12 – Selected sections in a randomly packed bed of spheres.

At the micro-scale, three typical cross-sections were selected to illustrate the velocity and temper-

ature distributions inside the packed beds, as shown in Fig.2.12. Fig.2.13 displays the temperature distribution in section-1 of the randomly packed bed with uniform spheres at t=1000s. The method adopted allows automatic optimization of parameters by coupling the Open Source optimization software Dakota with PATO. The permeability and Forchheimer coefficient are determined, and the critical transition from Darcy flow to Forchheimer flow is observed at a specific Reynolds number. The volumetric heat transfer coefficient exhibited transient behavior, with significant increases observed at higher inlet velocities. The discrepancy between the value of h_v obtained by integration of micro-scale fields and the one obtained at macro-scale by inverse analysis is found to be less than 3.8%.

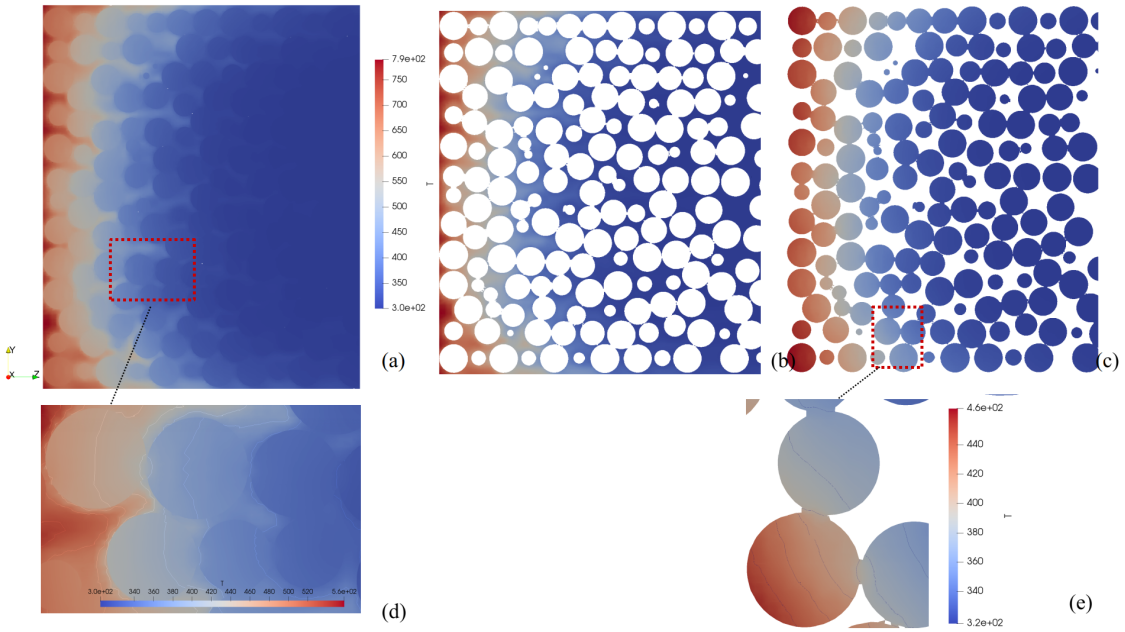

Figure 2.13 – Gas and solid temperature fields in section-1 of the randomly packed bed (u=0.1m/s, t=1000s). a) Total temperature (gas and solid), b) gas temperature, c) solid temperature, d) Gas and solid temperature with contour Line in the red box, e) solid temperature with contour line in the red box.

2.3 Conclusions and Perspectives

2.3.1 Achievements

Numerous technologies in development rely on porous materials, and fundamental developments in heat and mass transfer are crucial for application-specific phenomenological models. In this Ph.D. project, the focus was on three applications: heat and mass transfer in TPS, packed bed TES, and pyrolysis of wood particles. The objective was to develop a generic numerical framework to assess and model heat exchanges between the solid structure of a porous material and fluid flowing through the network of pores. The first objective was to extend the fluid flow and heat transfer database in

different porous materials through experimental research. The second objective was to establish and validate numerical strategies by comparing experimental results and multi-scale simulations.

The first part of the work, presented in chapters 3, 4, and 5, investigated fluid flow and heat transfer in three different porous materials: anisotropic carbon fiber felts, uniform-shaped granular porous materials, and non-uniform shaped porous materials. In the first application, we experimentally examined convective heat transfer in low-density carbon fiber materials like Calcarb and validated the LTE hypothesis. The results showed that the LTE assumption was valid, since the estimated heat transfer coefficient h_v was at least 10^8 W/(m^3 · K). In the second application, we developed and validated a two-equation model for high-temperature conditions to describe the temperature distribution in packed beds where thermophysical properties are temperature-dependent. The results showed that the value of heat transfer coefficient h_v in the LTNE model ranged from 1.0×10^4 to 2.0×10^4 W/(m^3 · K) under the given conditions. We also proposed two improved correlations for Nusselt number and axial dispersion gas thermal conductivity for a range of Reynolds numbers from 58 to 252. In the third application, we implemented two-equation models to describe heat transfer processes within biomass-packed beds, with and without considering the drying processes. The results showed that moisture content significantly affects the volumetric heat transfer coefficient and the effective thermal conductivity in the test range. The volumetric heat transfer coefficient increased when the moisture content decreased for both wood pellets and wood chips. We found that the model that neglects water evaporation yields about a ten-percent error on the heat transfer coefficients.

The second part of the work, presented in chapters 6 and 7, investigated effective properties for non-periodic anisotropic porous media at the microscopic scale. We extended micro-scale simulations from Darcy flow to Forchheimer flow and experimentally determined permeability and the Forchheimer coefficient for Calcarb. The experimental results reveal the limit of Re (based on the cluster diameter) of the Darcy flow regime in Calcarb to be around 0.43. Experimental permeability values were 1.615×10^{-10} m^2 (IP) and 1.248×10^{-10} m^2 (TT), exhibiting 12.3% relative difference compared to the simulations. In the Forchheimer flow regime, the experimental Forchheimer coefficient β for the Forchheimer equation is determined as 1.4948×10^5 m^{-1} (IP) and 2.0010×10^5 m^{-1} (TT). While the simulation did not provide a specific value for β or the Forchheimer correction tensor $\mathbf{F}$ due to the non-linear dependence of $\mathbf{F}$ on gas velocity. In the second application, a multi-scale approach was used to investigate the flow and heat transfer coefficients in a randomly packed bed at high temperatures. The results at the micro-scale revealed that at room temperature, the permeability was 2.451×10^{-7} m^2, and the Forchheimer coefficient was 1.188×10^3 m^{-1}. The critical Reynolds number (based on particle diameter) for the transition from Darcy flow to Forchheimer flow was observed at $Re = 10.1$, where the ratio of the packed bed diameter to particle diameter was 12.5. The volumetric heat transfer coefficient h_v exhibited transient behavior, but at low inlet velocities (e.g., 0.01 m/s and 0.1 m/s) corresponding to $Re = 10.1$ and 101 at room temperature, respectively, h_v could be considered around constant. For higher inlet velocities (e.g., 1 m/s) corresponding to $Re = 1001$, h_v increased significantly over time during the heat transfer process. It experienced an increase of approximately 71% from 13529.99 to 23218.36 W/(m^3·K). Additionally, h_v increased as the Biot number (Bi) decreased at the same gas velocity. This further demonstrated that when Bi exceeded 0.1, the temperature distribution within individual particles could not be considered uniform. The comparison between the h_v value obtained

by integration of micro-scale results and the one calculated from the inverse analysis is found to be less than 3.8%, with the maximum difference occurring at the highest inlet velocity.

2.3.2 Perspectives

This work contributes to the ongoing efforts aimed at improving the understanding of heat transfer characteristics between porous media and fluids. In the following paragraphs, the main perspectives covered in the five articles are presented in the order of their topics.

In chapter 3, an inverse analysis method was used to validate the local thermal equilibrium (LTE) hypothesis in ablative-material response models. The work allowed to obtain a precise minimum value for h_v, but it was not possible to determine a specific value for the effective thermal conductivity of gas in the transverse and flow directions due to experimental uncertainty. One potential approach for further investigation is using the flying laser-spot technique to study the dispersion mechanism and determine specific values for the effective thermal conductivity of gas in Calcarb.

In chapter 4, a two-equation model for high-temperature conditions, incorporating mass and momentum conservation, to accurately describe the temperature distribution in packed beds was implemented and validated. However, it is important to note that our current work focuses on sensible thermal energy storage. In future works, our goal is to improve the model by incorporating phase change terms, thereby expanding its applicability to latent heat thermal energy storage systems.

In chapter 5, a two-equation model describing heat transfer processes within biomass-packed beds with varying moisture content was proposed. For safety reasons, the effect of biomass particle pyrolysis on the heat transfer coefficient was not investigated, as the maximum temperature was limited to 349 K. In future works, a new experimental setup will be constructed with a smaller tube diameter of 60 mm, where nitrogen will be used, and the inlet nitrogen temperature will be raised to 500°C. By collecting and analyzing the composition of the pyrolysis gases, the two-equation model will be coupled with the chemical reactions taking place during pyrolysis.

In chapter 6, micro-scale simulations from Darcy flow to Forchheimer flow for porous materials like Calcarb were performed, and the permeability and Forchheimer coefficient values were experimentally determined. However, it should be noted that the procedure used for the computation of the permeability tensor, which involved imposing a velocity (or pressure gradient) successively along the three directions of the unit cell to obtain the full permeability tensor, is no longer valid here due to the non-linear dependence of $\mathbf{F}$ on $\langle \mathbf{v_g} \rangle$. In future work, a possible approach is to compute $\mathbf{F}$ on a periodic unit cell by solving a tensorial closure problem with a Navier-Stokes structure.

In chapter 7, a multi-scale approach was used to investigate the flow and heat transfer coefficients in a randomly packed bed at high temperatures. The study involved a transient compressible flow, where high-temperature gas (800K) was entered from the inlet. The model incorporated mass and

momentum equations for the fluid phase, as well as energy equations for both the fluid and solid phases. By solving the temperature field, the heat transfer coefficient, h_v, could be evaluated using integration methods. However, the determination of the effective thermal conductivity was not addressed in this study. Future work could involve computing the effective thermal conductivity by analyzing the velocity and temperature distributions obtained from microscale simulations of the packed bed. This may be done by solving a closure problem on the same geometry.

Part I

Macro-scale investigation

Chapter 3

Experimental investigation on the validity of the local thermal equilibrium assumption in ablative-material response models

Preamble

Authors: S.Liu; A.Ahmadi-Senichault; C.Levet; J. Lachaud;
Affiliations: Arts et Métiers Institute of Technology, Univ. Bordeaux, CNRS, Bordeaux INP, I2M, UMR 5295, F-33400 Talence, France;
Published: 14 July 2023;
DOI: https://doi.org/10.1016/j.ast.2023.108516;
Journal: Aerospace Science and Technology;
Conference: This work has been presented at the 2nd International Conference on Flight Vehicles, Aerothermodynamics and Re-entry Missions & Engineering (FAR), 2 June 2022 - Heilbronn (Germany);

Abstract

Thermal Protection Systems (TPS) material response models rely on the assumption of local thermal equilibrium (LTE) between the solid phase and the gas phase. This assumption was challenged and investigated by several authors but a sufficiently precise knowledge of heat transfer coefficients in TPS materials was lacking to reach final conclusions. The objective of this work is to contribute to filling this gap by providing a literature review of available data in other communities (thermal energy storage, heat exchangers) and by performing an experimental characterization of Calcarb, a commercial carbon preform used for manufacturing thermal protection systems. Heat transfer within Calcarb was studied experimentally in the Through-Thickness (TT) and in the In-Plane (IP) directions for Reynolds numbers of 1 to 4 - representative of the TPS application - using the transient single-blow technique (TSBT). Numerical parameter estimation was performed using the Porous material Analysis

Toolbox based on OpenFoam (PATO) and the Design Analysis Kit for Optimization and Terascale Applications (DAKOTA). The heat transfer coefficient h_v is found to be greater than or equal to 10^8 W/(m^3 · K) and the LTE assumption is shown to be valid in the conditions of the experiment. To assess the validity of the LTE assumption for other conditions, the above bound of h_v may now be used in combination with a local thermal non-equilibrium model.

Keywords: Local thermal non-equilibrium; Anisotropic porous materials; Macroscopic numerical simulations; Heat exchange coefficient; Experimental study ; Inverse method

3.1 Introduction

Carbon fiber felts are widely used in the industry as insulators in high-temperature furnaces. At the end of the 1990s, NASA used a rigid carbon felt called FiberForm, produced by Fiber Materials Inc., to develop a new generation of low-density heat shields to protect space vehicles during hypersonic atmospheric entry [89]. This new class of materials called Phenolic Impregnated Carbon Ablators (PICA) has flawlessly been used since then: Stardust (NASA, 2006) [10, 11], Mars Science Laboratory (NASA, 2012) [12, 13], Mars 2020 (NASA, 2021) [14], Dragon vehicles (SpaceX, since 2012) [15]. The European Space Agency and ArianeGroup have developed ASTERM [16] based on Calcarb, produced by Mersen. FiberForm and Calcarb are both made of chopped carbon fibers of millimeter length and of about 10 micrometers in diameter [89, 90] as shown in Fig.3.1. During the manufacturing process, the carbon fibers tend to align according to the compression plane resulting in anisotropic properties. The direction perpendicular to this plane is referred to as "Through-Thickness" (TT) and that parallel as "In-Plane" (IP); they are shown in Fig.3.2. The thermal conductivity ratio between IP and TT directions is of about two [91]. When possible, the anisotropy is used to optimize the design of thermal protection systems (TPS) by placing the TT direction perpendicular to the vehicle's surface. This obviously helps reducing heat transfer towards the internal structure but it is also helpful in diffusing heat away from hot spots (stagnation point, shoulders) thanks to the higher IP-direction conductivity. Additionally, carbon preforms are impregnated with a low-density phenolic polymer to improve thermal protection by reducing internal radiation, by acting as a heat sink through endothermic pyrolysis processes, and by blowing pyrolysis gases in the boundary layer that partially block the incoming heat flux [92]. The velocity of the pyrolysis gases is of the order of 1 m/s at peak heating [13]. Detailed TPS material response models, taking into account this complex physics, have been developed since the 1950s, with strong progress in the 1960s during the design of the Apollo heat shield [17, 18]. They are currently being improved and adapted to new generations of materials by an active community [93] with the goal of reducing design uncertainties [19, 20]. The generalization of the use of porous fibrous materials raises new questions regarding the validity of the inherited hypotheses, such as the assumption of local thermal equilibrium ubiquitously used in TPS design. Heat transfer in porous materials can either be studied under the assumption of local thermal equilibrium (LTE) [4] or local thermal non-equilibrium (LTNE) [21, 22, 23, 24]. In LTE models, it is assumed that the average temperatures of the solid and gas phases are equal. Florio [25] and Puiroux [26, 27]

demonstrated the validity of the local thermal equilibrium assumption for dense charring materials. However, Scoggins et al. [28] showed that the local thermal equilibrium assumption was invalid for PICA using available literature correlations to estimate the heat transfer coefficient between the solid phase and the gas flowing through the pores [28]. Unfortunately, correlations for materials similar to PICA were not available in the literature and the major recommendation of Scoggins et al. [28] was to perform experiments to measure the heat transfer coefficient in low-density carbon fiber materials. As such studies are still unavailable, the objective of this work is to contribute to filling this gap by investigating experimentally convective heat transfer in Calcarb. The problem is however more complex than it appears because the flow of gas through porous media also modifies their effective thermal conductivity through a process known as dispersion [72].

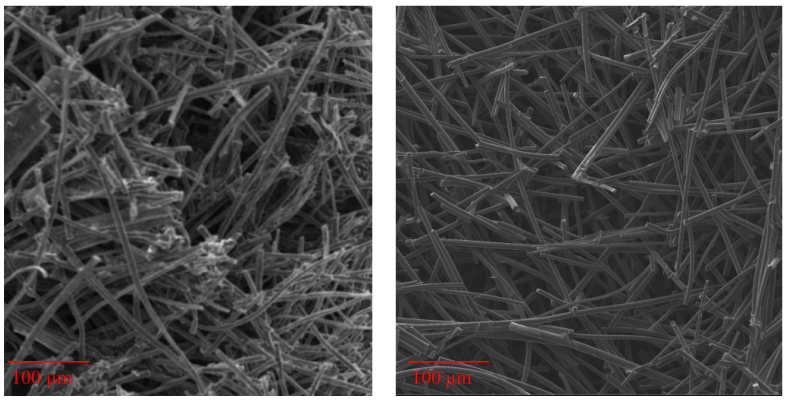

Figure 3.1 – Scanning electron micrography (SEM) images of FiberForm (left) and Calcarb (right)

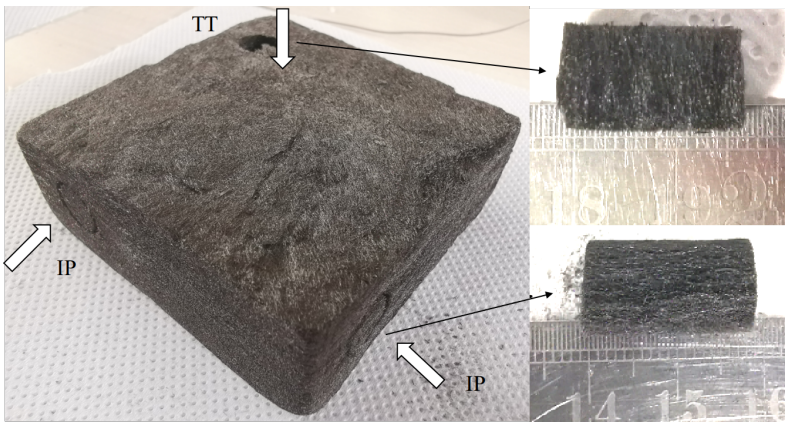

Figure 3.2 – "Through-Thickness" (TT) and "In-Plane" (IP) directions in Calcarb

To introduce the studied problem, let us start by presenting a generic model that was proposed for porous reactive materials submitted to high temperatures under the assumption of local thermal equilibrium. This model implements the physics encountered in materials submitted to very high temperatures in different applications such as thermal protection systems of space vehicles, porous materials submitted to fire, or biomass in thermochemical processes of biofuel production [4]. For

the purpose of this work we may ignore pyrolysis and chemistry terms and the mass and energy conservation equations write

$$\begin{cases} \frac{\partial}{\partial t}\left(\varepsilon_g \frac{M\langle p\rangle^g}{R\langle T\rangle}\right) + \nabla\cdot\left(-\frac{M\langle p\rangle^g}{R\langle T\rangle}\frac{\mathbf{K}}{\mu_g}\cdot\nabla\langle p\rangle^g\right) = 0 \\ \left(\varepsilon_g\rho_g c_{p,g} + \varepsilon_s\rho_s c_{p,s}\right)\frac{\partial\langle T\rangle}{\partial t} + \varepsilon_g\rho_g c_{p,g}\langle\mathbf{v_g}\rangle^{\mathbf{g}}\cdot\nabla\langle T\rangle = \nabla\cdot\left(\mathbf{k_{eff}}\cdot\nabla\langle T\rangle\right) \end{cases} \tag{3.1}$$

where the first equation is the gas mass conservation written in terms of gas pressure (the gas velocity is substituted with Darcy's law) and the second equation is the energy conservation. The gas volume fraction ε_g is equal to the porosity of the porous medium. $\mathbf{K}$ and $\mathbf{k_{eff}}$ denote the permeability and effective thermal conductivity tensors respectively. $\langle p\rangle^g$ and $\langle\mathbf{v_g}\rangle^g$ are the intrinsic average pressure and velocity of the gas. $\langle T\rangle$ denotes the superficial average temperature of the porous material (that is equal for both phases). The superficial and intrinsic phase averages of any quantity φ_i associated to the i-phase are respectively given by $\langle\varphi_i\rangle = \frac{1}{V}\int_{V_i}\varphi_i dV$, $\langle\varphi_i\rangle^i = \varepsilon_i^{-1}\langle\varphi_i\rangle = \frac{1}{V_i}\int_{V_i}\varphi_i dV$. In these relationships, V_i is the volume of the i-phase contained within the averaging volume V which is a representative elementary volume of the porous medium.

In Eq.3.1, the permeability $\mathbf{K}$ can be determined by experimental measurements or numerical simulations [74]. The effective conductivity, $\mathbf{k_{eff}}$, is known to be bounded by the arithmetic ($\mathbf{k_{eff}} = (\varepsilon_g k_g + \varepsilon_s k_s)\mathbf{I}$) and the harmonic ($\mathbf{k_{eff}} = (\varepsilon_s/k_s + \varepsilon_g/k_g)^{-1}\mathbf{I}$) averages of the solid and gas conductivities. Correlations for granular porous materials have been proposed in the literature [3, 94, 95], amongst which the most simple and often used one that reads $\mathbf{k_{eff}} = {k_g}^{\varepsilon_g}{k_s}^{\varepsilon_s}\mathbf{I}$ corresponds to the geometric average. In these equations, $\mathbf{k_{eff}}$ is treated as a spherical tensor and the effect of the gas flow on the effective thermal conductivity is not captured.

A theoretical expression of $\mathbf{k_{eff}}$ was later derived using upscaling techniques such as the volume-averaging method [72, 68, 67, 96]. As shown in Eq.3.2, besides the arithmetic average, two additional terms are involved: the tortuosity term that accounts for the microstructure of the material and the dispersion term that accounts for gas flow effects. These two terms may be numerically estimated by solving a closure problem on a periodic unit cell representative of the structure [68, 67, 66, 97].

$$\mathbf{k_{eff}} = \left(\varepsilon_g k_g + \varepsilon_s k_s\right)\mathbf{I} + \frac{k_g - k_s}{V}\int_{A_{gs}}\mathbf{n}_{gs}\mathbf{b}_g dA - \left(\rho c_p\right)_g\langle\tilde{\mathbf{v}}_g\mathbf{b}_g\rangle \tag{3.2}$$

where $\mathbf{v}_g$, $\langle\mathbf{v_g}\rangle^{\mathbf{g}}$, and $\tilde{\mathbf{v}}_g = \mathbf{v}_g - \langle\mathbf{v}_g\rangle^g$ are respectively the gas velocity within the pores, the intrinsic phase average velocity, and the deviation velocity. The closure variable $\mathbf{b}_g$ is the vector field that maps $\nabla\langle T_g\rangle^g$ onto $\tilde{T}_g$ in the LTE model, $\tilde{T}_g = \mathbf{b_g}\cdot\nabla\langle T_g\rangle^g$ and the LTE condition is represented by $\langle T\rangle = \langle T_g\rangle^g = \langle T_s\rangle^s$.

The generic LTE model needs to be upgraded when local thermal equilibrium is no longer valid, as explained in the previous paragraph. The mass and energy conservation equations for the LTNE model in their simplest form [68] in the case of compressible and non reacting flows write

$$\begin{cases} \frac{\partial}{\partial t}\left(\varepsilon_g \frac{M\langle p\rangle^g}{R\langle T_g\rangle^g}\right) + \nabla\cdot\left(-\frac{M\langle p\rangle^g}{R\langle T_g\rangle^g}\frac{\mathbf{K}}{\mu_g}\cdot\nabla\langle p\rangle^g\right) = 0 \\ \frac{\partial}{\partial t}\left(\varepsilon_s\rho_s c_{p,s}\langle T_s\rangle^s\right) = \nabla\cdot\left(\mathbf{k_{s,eff}}\cdot\nabla\langle T_s\rangle^s\right) + h_v\left(\langle T_g\rangle^g - \langle T_s\rangle^s\right) \\ \frac{\partial}{\partial t}\left(\varepsilon_g\rho_g c_{p,g}\langle T_g\rangle^g\right) + \nabla\cdot\left(\rho_g c_{p,g}\langle\mathbf{v_g}\rangle^{\mathbf{g}}\langle T_g\rangle^g\right) = \nabla\cdot\left(\mathbf{k_{g,eff}}\cdot\nabla\langle T_g\rangle^g\right) + h_v\left(\langle T_s\rangle^s - \langle T_g\rangle^g\right) \end{cases} \tag{3.3}$$

where $c_{p,i}$ and $\mathbf{k_{i,eff}}$ respectively denote the heat capacity and effective thermal conductivity tensor of the i phase. $\langle T_i \rangle^i$ and $\langle \mathbf{v_g} \rangle^{\mathbf{g}}$ denote the intrinsic phase average temperature for the i-phase and the intrinsic gas average velocity. h_v denotes the volumetric heat transfer coefficient between the gas stream and the sample. There are three effective properties, h_v, $\mathbf{k_{s,eff}}$ and $\mathbf{k_{g,eff}}$ to be determined. In many research works, regardless of the experimental conditions, simple expressions of $\mathbf{k_{s,eff}}$ and $\mathbf{k_{g,eff}}$ as a function of gas and solid phase conductivities and the porosity of the homogeneous and isotropic porous medium (metal foams, ceramic foams) have been considered [3, 95, 81, 85, 82]. $\mathbf{k_{i,eff}}$ are treated as scalars and are given by

$$\mathbf{k_{s,eff}} = \varepsilon_s k_s \mathbf{I} \qquad \mathbf{k_{g,eff}} = \varepsilon_g k_g \mathbf{I} \tag{3.4}$$

A more detailed formulation of $\mathbf{k_{s,eff}}$, $\mathbf{k_{g,eff}}$ and h_v in the LTNE model obtained by the volume-averaging method are given as follows [72, 68, 73],

$$\begin{cases} \mathbf{k_{s,eff}} = \varepsilon_s k_s \mathbf{I} + \frac{k_s}{V} \int_{A_{gs}} \mathbf{n}_{sg} \mathbf{b_{ss}} dA \\ \mathbf{k_{g,eff}} = \varepsilon_g k_g \mathbf{I} + \frac{k_g}{V} \int_{A_{gs}} \mathbf{n}_{gs} \mathbf{b_{gg}} dA - \rho_g c_{p,g} \langle \tilde{\mathbf{v}}_g \mathbf{b_{gg}} \rangle \\ h_v = \frac{k_g}{V} \int_{A_{gs}} \mathbf{n}_{gs} \nabla s_g dA \end{cases} \tag{3.5}$$

where the closure variables $\mathbf{b_{ii}}$, and s_i are the vector and scalar fields that maps $\nabla \langle T_i \rangle^i$ onto $\tilde{T}_i$ in the LTNE model, $\tilde{T}_g = \mathbf{b_{gg}} \cdot \nabla \langle T_g \rangle^g - s_g(\langle T_g \rangle^g - \langle T_s \rangle^s) + ...$, and $\tilde{T}_s = \mathbf{b_{ss}} \cdot \nabla \langle T_s \rangle^s - s_s(\langle T_s \rangle^s - \langle T_g \rangle^g) + ...$ [68]. Compared to Eq.3.2, Eq.3.5 splits the effective conductivity of the material into a gas and a solid contribution and includes a heat exchange term. Quintard et al. [68, 67] constructed pore-scale closure problems and solved them on a model porous medium composed of arrays of cylinders to study the variations of the effective properties as a function of the parameters of the problem. The results show that the effective thermal conductivities $\mathbf{k_{i,eff}}$ and the volumetric heat transfer coefficient h_v in the LTNE model vary as a function of the Peclet number Pe ($\rho_g c_{p,g} \mathbf{u} l_g / k_g$), the ratio of the solid thermal conductivity to the gas thermal conductivity and the gas-phase volume fraction ε_g. The determination of these tensors is not independent of h_v, therefore all these properties should be sought simultaneously.

The heat transfer coefficient may be determined either by pore-scale numerical simulation in representative geometries [98, 99, 100] or experimentally [81, 85, 82]. In the first method, the volume averaging theory is often applied to periodic structures, such are arrays of cylinders, to obtain h_v [98, 101]. With the progress of the resolution of computed microtomography and computer resources, pore-level numerical simulations are becoming a realistic approach to determine h_v [102, 103, 104]. Concerning the experimental method, the progress in optimisation algorithms and computer resources has allowed the general usage of inverse methods to infer the parameters with more accuracy [81, 82, 83, 84]. Using these two approaches, numerous correlations were obtained for the heat transfer coefficient h_v for a large variety of porous materials, like metal foams [81, 82], ceramic foams [102, 84] and graphite foams [85] under diverse experimental conditions. A summary of the most widely used correlations and of their validity ranges is proposed in Table 3.1. However, none of the available correlations are suitable for carbon fiber felt due to its complex anisotropic microstructure.

In this context, the purpose of this article is to determine the effective conductivities and the heat transfer coefficients needed to inform the LTE and the LTNE models for Calcarb. In Section

Table 3.1 – Empirical correlations for the heat transfer coefficient

Investigators	Media	Correlation	Remarks	Predicted h_v in (W/(m^3·K)) for Re =1
[105]	packed beds	$Nu_s = 2 + 1.1 Pr^{1/3} Re^{0.6}$	$Nu_s = h_s \cdot d_{par}/k_g$, $Re = \rho_g d_{par} u/\mu_g$ $1 \leq Re \leq 10^4$	1.83 $\times 10^7$
[81]	metal foam	$Nu_v = 0.34 \varepsilon_g^{-2} Pr^{1/3} Re^{0.61}$	$Nu_v = h_v \cdot d_p^2/k_g$, $Re = \rho_g d_p u/\mu_g$ $20 \leq Re \leq 10^3$, $0.87 \leq \varepsilon_g \leq 0.97$	4.47 $\times 10^6$ (extrapolated for $Re = 1$)
[82]	metal foam	$Nu_v = 0.3248 Re^{0.601}$	$Nu_v = h_v \cdot d_p^2/k_g$, $Re = \rho_g L u/\mu_g$ $1900 \leq Re \leq 7800$, $\varepsilon_g = 0.95$	3.89 $\times 10^6$ (extrapolated for $Re = 1$)
[106]	ceramic foam	$Nu_v = 0.638 Re^{0.42}$	$Nu_v = h_v \cdot d_p^2/k_g$, $Re = \rho_g d_p u/\mu_g$ $24 \leq Re \leq 91$, $d_p = 0.29mm$	7.49 $\times 10^6$ (extrapolated for $Re = 1$)
[79]	open cellular foam	$Nu_v = 0.124 (RePr)^{0.791}$	$Nu_v = h_v \cdot d_p^2/k_g$, $Re = \rho_g d_p u/\mu_g$ $1 \leq Re \leq 1000$	1.14 $\times 10^6$
Current work	carbon fiber felt	not applicable (asymptotic behavior)	$Re = \rho_g d_{cl} u/\mu_g$ $1 \leq Re \leq 4$	$> 1 \times 10^8$ (local thermal equilibrium)

3.2, the experimental facility and the test procedure are presented. In Section 3.3, the numerical inverse analysis method developed to infer the intrinsic parameters is described. It is based on a multi-objective optimization method to minimize errors between measured and predicted data. In Section 3.4, the experimental results and the estimated values of the LTE and LTNE parameters are presented and discussed. In section 3.5, a conclusion provides recommendations regarding the choice of a convective heat transfer model for Calcarb.

3.2 Experimental method

The experiments may be conducted using either a steady state [79, 80] or a transient regime [81, 82, 83, 84] approach. With the steady state approach, the sample is heated up and maintained at a given temperature. Cold gas is flown through the sample. The gas temperature is measured at the inlet and at the outlet of the sample. It is also measured within the sample when possible, that is, when the pores are large enough to allow measuring the gas temperature. The heat transfer coefficient is obtained by the analysis of the spatial evolution of the gas temperature. In the transient method instead, hot gas is used to heat a cold sample. The time evolution of the gas temperature is recorded upwind and downwind of the sample. This method is called the transient single blow technique (TSBT) [81, 85]. This method provides more information as one may measure the increase of temperature of the solid, which brings robustness for the inverse analysis. Last, but not least, as the solid and gas temperatures now both vary in space, one may infer simultaneously their effective thermal conductivities. The experimental facility presented in the following section is based on this method.

3.2.1 Experimental system and test procedure

A schematic drawing of the experimental setup that we have developed and an enlarged view of the test section, where thermocouple positions are shown, are displayed in Fig.3.3. The setup consists of a nitrogen gas inlet, a mass flow controller, a heat exchanger to heat the gas, and an insulated test section that contains the sample.

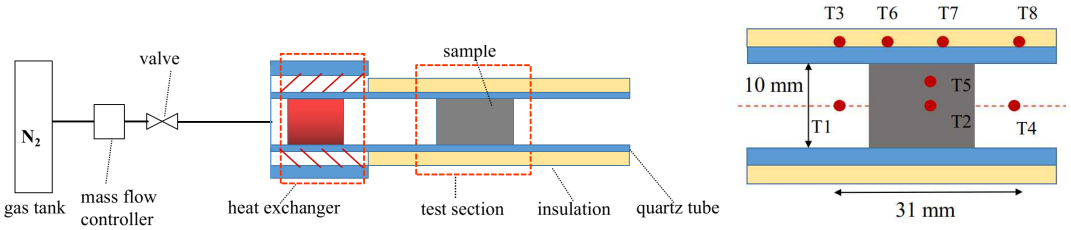

(a) experimental setup (b) test section part

Figure 3.3 – Schematic diagram of the experimental system and enlarged view of the test section showing the thermocouple identification numbers

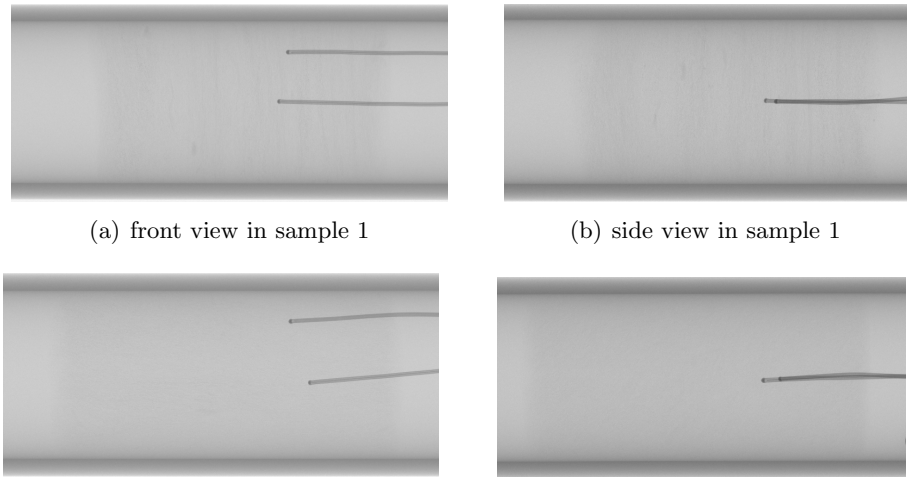

(a) front view in sample 1 (b) side view in sample 1

(c) front view in sample 2 (d) side view in sample 2

Figure 3.4 – X-ray images of the thermocouple positions inside sample 1 (TT direction) and sample 2 (IP direction)

In the experiment, the first step is to set the flow rate of inlet gas. This value is controlled and measured by the mass flow controller (Bronkhorst F-201CV-020-AAD-11-Z) with a range of 1 to 4 liters/min, that is, a mass flow rate of Nitrogen ranging from 1.92×10^{-5} kg/s to 7.68×10^{-5} kg/s. The magnitude of the Darcy velocity u varies from 0.21 m/s to 0.84 m/s at room temperature ($T0 = 20°C$). The intrinsic gas velocity $\langle v_g \rangle^g$ inside the sample varies from 0.233 m/s to 0.932 m/s. When the gas temperature T_g rises to 80°C, v_g varies from 0.27 m/s to 1.08 m/s as the gas density ρ_g decreases from 1.15 kg/m^3 to 0.99 kg/m^3. This velocity range is consistent with the order of magnitude of 1

m/s of the pyrolysis gas velocity encountered in the TPS application, previously mentioned in the introduction.

The gas flows through a heat exchanger made of a Calcarb plug heated by a Ni-Cr wire wrapped around a quartz tube, as shown in Fig.3.3. The Ni-Cr wire is heated by Joule effect with a continuous power supply (Velleman LABPS3020). The red points in Fig.3.3 indicate the positions of the thermocouples (type K, 0.25 mm sheath diameter). The inlet and outlet gas temperatures, the tube surface temperature, and the temperature inside the sample are measured. The thermocouples are connected to a display data logger (Pico Technology TC-08) that records the temperature with a time step of 1.0 s. To measure the anisotropic properties of the materials, different experiments were performed by changing the orientation of the sampling (sample 1: Through-Thickness (TT) and sample 2: In-Plane (IP)). We performed X-ray scans for both samples to determine the exact location of the thermocouples (Fig. 3.4) in view of the inverse analysis. The sample dimension and the architectural properties of Calcarb are listed in Table 3.2. Due to the manufacturing process, there are clusters of fibers made of five to ten fibers. The mean diameter of the fiber clusters has been shown to be the most relevant characteristic length to compute the Reynolds number as it triggers the formations of eddies in the pores [74]. It will be used in the modeling section.

Table 3.2 – Dimension and structural properties of the Calcarb samples

Sample dimensions diameter × length (mm)	Porosity ε_g	fiber diameter d_f (μm)	cluster diameter d_{cl} (μm)	pore diameter d_p (μm)	permeability K (m^2)	fiber density ρ_s (kg/m^3)
10×17.4	0.9	10	80	50	1.741^{-10}	1600

3.2.2 Experimental uncertainty analysis

There are two types of experimental uncertainties: the first one is the direct measurement error (caused by the experimental device), and the second one is the error arising from the measurement process. In this work, the ranges and uncertainties of the different sensors are reported in Table

Table 3.3 – The uncertainty analysis in the experimental measurements

	Range	Uncertainty
Temperature sensor (Pico Technology)	-270°C to +1820°C	± 0.2% of the reading
K-type thermocouple	-100°C to + 800°C	± 0.5 %
Volume mass flow controller	0 to 4 L/min	± 0.5 % of the reading
Temperature measurement in the flow region (due to the position of the thermocouple)	310 K to 360 K	0.1%

3.3. Errors from the temperature measurement process are chiefly due to the positioning of the thermocouples in the flow region, upwind and downwind of the sample. In the sample, there is no uncertainty on the position as it is precisely measured with X-ray scans before testing. In the flow, the maximum temperature difference is 0.4 K within 2 mm of the front and rear of the measurement

point. So the maximum resulting uncertainty on the temperature measurement in the flow regions is found to be 0.1%.

3.3 Parameter estimation method

Due to the complexity of the problem, we used numerical inverse analysis to estimate the quantities of interest. In the first subsection, we present the numerical model, and in the second subsection we detail the optimization algorithm used to infer the parameters.

3.3.1 Numerical model

For the purpose of parameter estimation, it is necessary to model the whole test section represented in Fig. 3.3. The numerical model is sketched in Fig. 3.5. It consists of a two-dimensional axisymmetric geometry where the different regions are identified as follows: flow1 (upwind flow field), sample (porous sample), flow2 (downwind flow field), tube (quartz tube), and thermocouple (downwind thermocouple).

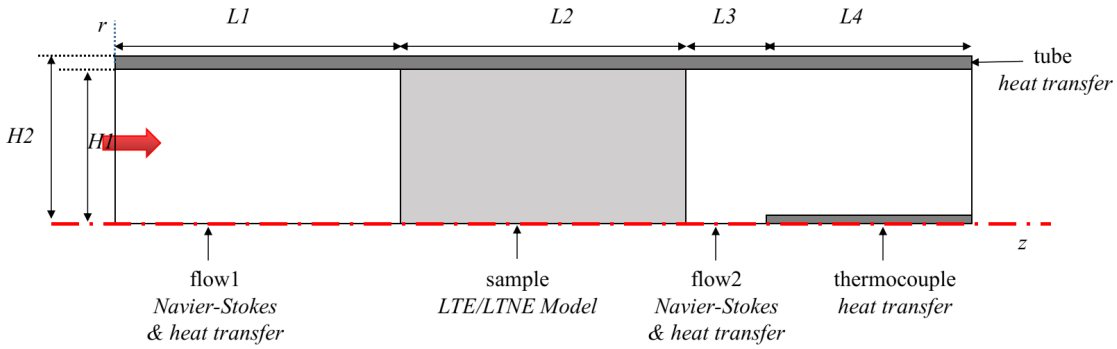

Figure 3.5 – Two-dimensional axisymmetric numerical model of the test section

3.3.1.1 Mathematical model and numerical implementation

The flow regions (flow1 and flow2) are modeled with the transient compressible laminar Navier-Stokes equations (conservation of mass, momentum, and energy). For the dense solid regions (tube, thermocouple), transient heat conduction is considered (energy conservation in a solid). In the porous sample region (sample), we consider either the LTE model (Eq.3.1) or the LTNE model (Eq.3.3). The Reynolds number based on the cluster diameter (d_{cl}) is defined as, $Re = \rho_g u d_{cl}/\mu_g$. Considering the gas velocity and density ranges provided in the previous section, Re is found to vary from 0.95 to 4.2. In a previous study, it was proved that Darcy's law remains valid with an error under 1% for $Re < 5$ [74]; hence, in this work, we will use Darcy's law. The coupling between the different regions is done by considering the conservation of mass and the continuity of temperatures and heat fluxes at the interfaces. The detailed expressions of the boundary conditions and of the initial conditions for the system of Eq.3.1 (LTE model) and the system of Eq.3.3 (LTNE model) are provided in Table

3.4 and Table 3.5 respectively. To simplify the notations, $\langle T_g \rangle^g$, $\langle T_s \rangle^s$, and $\langle T \rangle$, will be denoted by T_g, T_s and T respectively. In what follows, T is the temperature in the open flow regions (flow1 and flow2), T_g and T_s are the gas and solid temperatures in the sample and T_t is the temperature in the tube and thermocouple regions. The solid thermal conductivity in the tube and thermocouple regions are denoted by k_t. The imposed external boundary conditions are given by a second-order polynomial fitting of the experimental data.

The numerical model was implemented in finite volumes in the Porous material Analysis Toolbox based on OpenFOAM (PATO) [4] - where it is made available in open access. A multi-block approach is used, that is, in each region a different set of equations is solved at each time step with appropriate boundary conditions, computed from the mass and energy balances at the interfaces. The dense solid and flow region fields are computed using the conjugate heat transfer solver (chtMultiRegionFoam) of OpenFOAM 7 [107]. For the sample region, the pressure equation is solved semi-implicitly using first order schemes in time (Euler) and space (Gauss linear). The pressure gradient term is implicit and the other terms are explicit. The same approach is used for the energy equations, where the temperature terms are implicit and other quantities explicit. The equations are solved in series, with appropriate mesh refinement and time steps to guaranty that the order of convergence is reached, as described in Appendix.3.6.

Table 3.4 – Initial and boundary conditions of the LTE model

Region	Initial conditions		Boundary conditions		
flow1	$T = T0$	inlet $T = T1$ $p = \frac{u \cdot \mu_g \cdot L2}{\mathbf{K}} + p_{atm}$	flow1-tube interface $k_g \frac{\partial T}{\partial r} = k_t \frac{\partial T_t}{\partial r}$ $\frac{\partial p}{\partial r} = 0$, $u = 0$	flow1-sample interface $k_g \frac{\partial T}{\partial z} = k_{eff} \frac{\partial T}{\partial z}$ $p = p$, $u = \varepsilon_g \langle v_g \rangle^g$	
sample	$T = T0$	sample-flow1 interface $k_{eff} \frac{\partial T}{\partial z} = k_g \frac{\partial T}{\partial z}$ $p = p$, $\varepsilon_g \langle v_g \rangle^g = u$	sample-tube interface $k_{eff} \frac{\partial T}{\partial r} = k_t \frac{\partial T_t}{\partial r}$ $\frac{\partial p}{\partial r} = 0$, $\frac{\partial \langle v_g \rangle^g}{\partial r} = 0$	sample-flow2 interface $k_{eff} \frac{\partial T}{\partial z} = k_g \frac{\partial T}{\partial z}$ $p = p$, $\varepsilon_g \langle v_g \rangle^g = u$	
flow2	$T = T0$	flow2-sample interface $k_g \frac{\partial T}{\partial z} = k_{eff} \frac{\partial T}{\partial z}$ $\frac{\partial p}{\partial z} = 0$, $u = \varepsilon_g \langle v_g \rangle^g$	flow2-tube interface $k_g \frac{\partial T}{\partial r} = k_t \frac{\partial T_t}{\partial r}$ $\frac{\partial p}{\partial r} = 0$, u=0	flow2-therm interface $k_g \frac{\partial T}{\partial z} = k_t \frac{\partial T_t}{\partial z}$ $k_g \frac{\partial T}{\partial r} = k_t \frac{\partial T_t}{\partial r}$ $\frac{\partial p}{\partial r} = 0$, $\frac{\partial p}{\partial z} = 0$	outlet $p = p_{atm}$ u=0
therm-couple	$T_t = T0$	therm-flow2 interface $k_t \frac{\partial T_t}{\partial z} = k_g \frac{\partial T}{\partial z}$ $k_t \frac{\partial T_t}{\partial r} = k_g \frac{\partial T}{\partial r}$	outlet $\frac{\partial T_t}{\partial z} = 0$		
tube	$T_t = T0$	top T_t is a function of $T3$, $T6$, $T7$, $T8$	tube-flow1 interface $k_t \frac{\partial T_t}{\partial r} = k_g \frac{\partial T}{\partial r}$	tube-sample interface $k_t \frac{\partial T_t}{\partial r} = k_{eff} \frac{\partial T}{\partial r}$	tube-flow2 interface $k_t \frac{\partial T_t}{\partial r} = k_g \frac{\partial T}{\partial r}$

3.3.1.2 Thermal properties of Calcarb and of Nitrogen

The effective conductivity of Calcarb in static conditions was measured in IP and TT directions using the Transient Plane Sources technique (Hot Disk, TPS 3500) [86]. At room temperature, these values are ($k_{eff,IP,static}$=0.399) and ($k_{eff,TT,static}$=0.212) W/(m·K) with an uncertainty of 5 % . The effective conductivity tensor $\mathbf{k_{eff,static}}$ at room temperature may be defined in cylindrical coordi-

Table 3.5 – Initial and boundary conditions of the LTNE model

Region	Initial conditions		Boundary conditions		
flow1	$T = T0$	inlet $T = T1$ $p = \frac{u \cdot \mu_g \cdot L2}{\mathbf{K}} + p_{atm}$	flow1-tube interface $k_g \frac{\partial T}{\partial r} = k_t \frac{\partial T_t}{\partial r}$ $\frac{\partial p}{\partial r} = 0$, $u = 0$	flow1-sample interface $k_g \frac{\partial T}{\partial z} = k_{g,eff} \frac{\partial T_g}{\partial z}$ $p = p$, $u = \varepsilon_g \langle v_g \rangle^g$	
sample	$T_g = T0$ $T_s = T0$	sample-flow1 interface $k_{g,eff} \frac{\partial T_g}{\partial z} = k_g \frac{\partial T}{\partial z}$, $\frac{\partial T_s}{\partial z} = 0$ $p = p$, $\varepsilon_g \langle v_g \rangle^g = u$	sample-tube interface $\frac{\partial T_g}{\partial r} = 0$, $k_{s,eff} \frac{\partial T_s}{\partial r} = k_t \frac{\partial T_t}{\partial r}$ $\frac{\partial p}{\partial r} = 0$, $\frac{\partial \langle v_g \rangle^g}{\partial r} = 0$	sample-flow2 interface $k_{g,eff} \frac{\partial T_g}{\partial z} = k_g \frac{\partial T}{\partial z}$, $\frac{\partial T_s}{\partial z} = 0$ $p = p$, $\varepsilon_g \langle v_g \rangle^g = u$	
flow2	$T = T0$	flow2-sample interface $k_g \frac{\partial T}{\partial z} = k_{g,eff} \frac{\partial T_g}{\partial z}$ $\frac{\partial p}{\partial z} = 0$, $u = \varepsilon_g \langle v_g \rangle^g$	flow2-tube interface $k_g \frac{\partial T}{\partial r} = k_t \frac{\partial T_t}{\partial r}$ $\frac{\partial T}{\partial z} = 0$, u=0 $\frac{\partial p}{\partial r} = 0$	flow2-therm interface $k_g \frac{\partial T}{\partial z} = k_t \frac{\partial T_t}{\partial z}$ $k_g \frac{\partial T}{\partial r} = k_t \frac{\partial T_t}{\partial r}$ $\frac{\partial p}{\partial r} = 0$, $\frac{\partial p}{\partial z} = 0$	outlet $p = p_{atm}$ u=0
therm-couple	$T_t = T0$	therm-flow2 interface $k_t \frac{\partial T_t}{\partial z} = k_g \frac{\partial T}{\partial z}$ $k_t \frac{\partial T_t}{\partial r} = k_g \frac{\partial T}{\partial r}$	outlet $\frac{\partial T_t}{\partial z} = 0$		
tube	$T_t = T0$	top T_t is a function of $T3$, $T6$, $T7$, $T8$	tube-flow1 interface $k_t \frac{\partial T_t}{\partial r} = k_g \frac{\partial T}{\partial r}$	tube-sample interface $k_t \frac{\partial T_t}{\partial r} = k_{s,eff} \frac{\partial T_s}{\partial r}$	tube-flow2 interface $k_t \frac{\partial T_t}{\partial r} = k_g \frac{\partial T}{\partial r}$

nates as shown in Eq.3.6, where z represents the TT direction. For the same type of fiber materials (FiberForm), the mean thermal conductivity values obtained in the literature [6] are 0.392 and 0.167 W/(m·K) in the IP and TT directions. In these materials, as well as in our measurement, the thermal conductivity value in the IP direction is nearly twice the value obtained in the TT direction.

$$\mathbf{k_{eff,static}}_{\text{, room temperature}} = \begin{bmatrix} k_{eff,IP,static} & 0 & 0 \\ 0 & k_{eff,IP,static} & 0 \\ 0 & 0 & k_{eff,TT,static} \end{bmatrix}_{(r,\theta,z)} = \begin{bmatrix} 0.399 \pm 5\% & 0 & 0 \\ 0 & 0.399 \pm 5\% & 0 \\ 0 & 0 & 0.212 \pm 5\% \end{bmatrix}_{(r,\theta,z)} \tag{3.6}$$

Fig. 3.6 shows the variations as a function of temperature of the nitrogen gas thermal conductivity k_g and heat capacity $c_{p,g}$, and of the effective thermal conductivity $k_{eff,IP,static}$, $k_{eff,TT,static}$ and heat capacity $c_{p,s}$ of the Calcarb sample. Presented data for the gas thermal conductivity k_g and heat capacity $c_{p,g}$ were obtained from the literature [108]. The effective thermal conductivities $k_{eff,IP,static}$ and $k_{eff,TT,static}$ were measured at 291 K (room temperature), 301 K, 311 K, and extended linearly to 370 K. The solid heat capacity $c_{p,s}$ of the Calcarb sample were obtained from a recently published work [109].

When considering the dispersion effect due to the flow of gas [30, 68], the effective conductivity $\mathbf{k_{eff}}$ used in the LTE model (Eq.3.1) and presented in Eq.3.2 may be defined in cylindrical coordinates as shown in Eq.3.7, where $k_{dis,1}$ and $k_{dis,2}$ represent the two components of dispersion term $\mathbf{k_{dis}}$ in the horizontal and transverse flow directions. For the purpose of carrying out the inverse analysis, we use coefficients $c1$ and $c2$ multiplied by the effective conductivity of Calcarb under static conditions to represent the components of effective conductivity. The solid effective thermal conductivity $\mathbf{k_{s,eff}}$, and gas effective thermal conductivity $\mathbf{k_{g,eff}}$ used in the LTNE model (Eq.3.3) and presented in Eq.3.5 may be sought as shown in Eq.3.8 and Eq.3.9, where $c3 \cdot k_g$ and $c4 \cdot k_g$ represent the two components of tortuosity term $\mathbf{k_{tor}}$, $c5$ and $c6$ indicate the two components of dispersion term $\mathbf{k_{dis}}$. The parameters

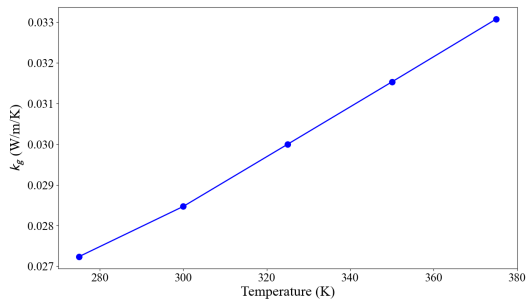

(a) gas thermal conductivity

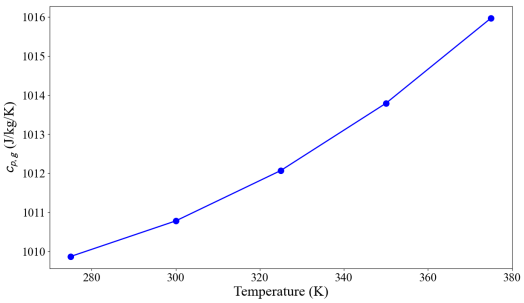

(b) gas heat capacity

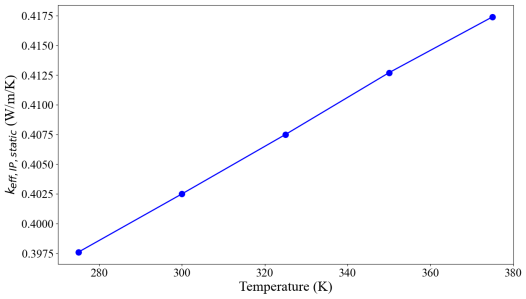

(c) effective thermal conductivity in IP direction

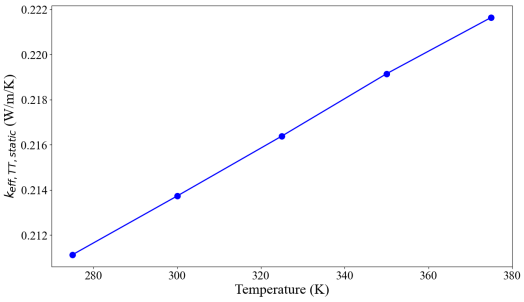

(d) effective thermal conductivity in TT direction

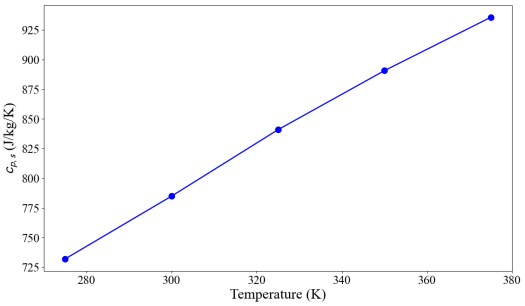

(e) solid heat capacity

Figure 3.6 – Thermal conductivity and heat capacity as a function of temperature for Nitrogen and for the solid phase of Calcarb

$c1$ to $c6$ will be optimized as described in section 3.3.2.

$$\begin{aligned}\mathbf{k_{eff}} &= \begin{bmatrix} k_{eff,IP,static} + k_{dis,1} & 0 & 0 \\ 0 & k_{eff,IP,static} + k_{dis,1} & 0 \\ 0 & 0 & k_{eff,TT,static} + k_{dis,2} \end{bmatrix}_{(r,\theta,z)} \\ &= \begin{bmatrix} c1 \cdot k_{eff,IP,static} & 0 & 0 \\ 0 & c1 \cdot k_{eff,IP,static} & 0 \\ 0 & 0 & c2 \cdot k_{eff,TT,static} \end{bmatrix}_{(r,\theta,z)}\end{aligned} \tag{3.7}$$

$$\mathbf{k_{s,eff}} = \begin{bmatrix} k_{eff,IP,static} - \varepsilon_g k_g - c3 \cdot k_g & 0 & 0 \\ 0 & k_{eff,IP,static} - \varepsilon_g k_g - c3 \cdot k_g & 0 \\ 0 & 0 & k_{eff,TT,static} - \varepsilon_g k_g - c4 \cdot k_g \end{bmatrix}_{(r,\theta,z)} \tag{3.8}$$

$$\mathbf{k_{g,eff}} = \begin{bmatrix} \varepsilon_g k_g + c3 \cdot k_g + c5 & 0 & 0 \\ 0 & \varepsilon_g k_g + c3 \cdot k_g + c5 & 0 \\ 0 & 0 & \varepsilon_g k_g + c4 \cdot k_g + c6 \end{bmatrix}_{(r,\theta,z)} \tag{3.9}$$

3.3.2 Optimization process

An inverse analysis method was used to infer the intrinsic parameters from experimental measurements to minimize errors between measured and predicted data. We possess four data sequences $\{T1^i\}_{i=0}^n$, $\{T4^i\}_{i=0}^n$, $\{T2^i\}_{i=0}^n$, $\{T5^i\}_{i=0}^n$ that correspond to the measured temperatures collected at every time step indicated by the index i, respectively at the inlet, at the outlet and inside the sample (see Fig.3.3). The transient inlet gas temperature data $T1$ is fitted into a second-order polynomial using least squares, and it is used as a boundary condition. The objective function S for the optimization processes is defined as the average of the root mean squared relative error between measured and predicted temperatures on the three positions already mentioned ($T4$, $T2$, $T5$):

$$S = \frac{1}{3}\left(\sqrt{\frac{1}{n}\sum_{i=1}^{n}\left(\frac{T4^i_{num} - T4^i}{T4^i}\right)^2} + \sqrt{\frac{1}{n}\sum_{i=1}^{n}\left(\frac{T2^i_{num} - T2^i}{T2^i}\right)^2} + \sqrt{\frac{1}{n}\sum_{i=1}^{n}\left(\frac{T5^i_{num} - T5^i}{T5^i}\right)^2}\right) \tag{3.10}$$

The minimization of S was performed with the Open Source optimization software Dakota [110]. A combination of the global optimization method DIviding RECTangles algorithm (NCSU DIRECT) [111] and of the local optimization method Adaptive nonlinear least-squares algorithm (NL2SOL) [112] were used. NCSU DIRECT, as a global optimization algorithm, always find the global optimum of a function within a given domain given enough function evaluations and highly sensitive stopping criteria. However, this exhaustive search can be computationally expensive to reach the minimum [111]. Therefore, if final convergence becomes slow, NL2SOL is used to speed-up convergence within the sub-region identified by NCSU DIRECT. An overview of this optimization strategy is presented in Fig.3.7. It will be further explained taking examples of applications to LTE and LTNE model optimisations in the next section.

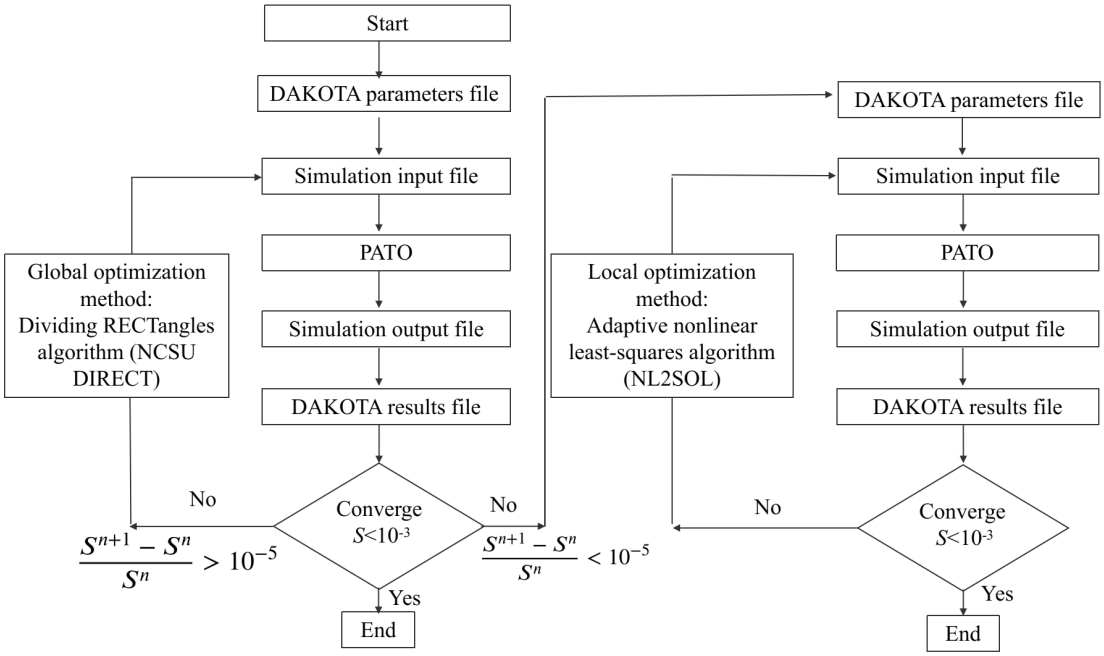

Figure 3.7 – The steps of optimization process

3.4 Results and discussions

Results of measured and predicted temperatures are reported in this section. In the first subsection, the volumetric heat transfer coefficient h_v used in the LTNE model is determined and the pressure, velocity, and temperature fields predicted with the LTNE model are presented. The second subsection focuses on assessing the validity of the LTE model in the conditions of the experiment.

3.4.1 Determination of the volumetric heat transfer coefficient used in the LTNE model

Fig.3.8 presents a typical comparison of the measured and predicted results, where measured results are represented by dots, and predicted results obtained by solving the LTNE model are represented by solid and dashed lines. The recorded inlet gas temperature, sample temperature at two locations (T2, T5), and outlet gas temperature are a function of time. The temperature data presented is the subset used in the optimization process. For the predicted results, solid temperatures are represented with solid lines and gas temperatures with dashed lines. The procedure for solving h_v is then presented.

According to the model presented in the previous section, there are five parameters to optimize : h_v, $c3$, $c4$, $c5$ and $c6$. Studies have indicated that the tortuosity terms represented by $c3 \cdot k_g$ and $c4 \cdot k_g$ in $\mathbf{k_{g,eff}}$ are significantly smaller than the dispersion terms represented by $c5$ and $c6$ [73, 68]. One can also notice that when summing the effective conductivity of the solid (Eq.3.8) and the effective conductivity of the gas (Eq.3.9), the tortuosity terms cancel each other. Due to the combination of these two properties, the sensitivity on $c3$ and $c4$ becomes very small when approaching local thermal

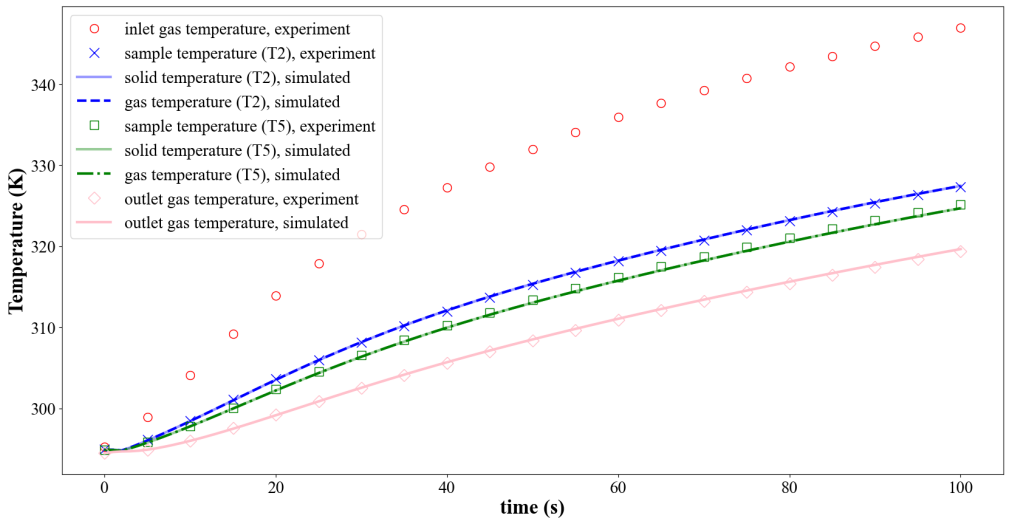

Figure 3.8 – The comparison of predicted and measured temperature in TT direction ($qm = 7.68 \times 10^{-5}$ kg/s).

equilibrium (that - we will see - is reached in our case). Therefore, in what follows, we set the values of $c3$ and $c4$ to zero and run the optimization on three parameters: h_v, $c5$, and $c6$.

As a large number of simulations were carried out, a representative case (1m/s in the TT-direction) was selected to demonstrate the optimisation procedure and to present the two-dimensional simulation results. In order to choose minimum and maximum values of the parameters to be optimized, orders of magnitude are sought from the literature. We used the correlations provided by Essence et al. [30] for packed beds and obtained estimates of the dispersion terms of about 0.1 W/(m · K) and of the volumetric heat transfer coefficient h_v of the order of 10^7 W/(m^3·K) for a Reynolds number of 4. Taking advantage of the global optimization ability of the NCSU DIRECT algorithm, we respectively set $c5$, $c6$, and h_v from 0 to 0.5 W/(m · K), 0 to 0.5 W/(m · K), and 10^6 to 10^{11} W/(m^3·K). Convergence ($S < 0.001$) was reached after 115 iterations of the global optimization algorithm (in this case local optimisation was not necessary). Fig.3.9 shows the influence of the three variables (h_v, $c5$ and $c6$) on the error S. The grey scale indicates the value of $c6$, and the size of points indicates the value of S. As shown in Fig.3.9, when S is below 0.0025, the values of $c6$ are distributed between 0.05 to 0.17 W/(m · K), the values of $c5$ are concentrated around on 0.115 W/(m · K), and the values of h_v span four orders of magnitude ranging from 10^7 to 10^{11} W/(m^3·K). To analyse further the behavior of the error when varying h_v, we set $c5$ to 0.115 W/(m · K) and $c6$ to the average of the range obtained above, that is, 0.11 W/(m · K). As shown in Fig.3.10, S displays an asymptotic behavior. Beyond a critical value of h_v of 10^8 W/(m^3·K), a change in h_v does not affect the error. This is due to the fact that local thermal equilibrium is reached. The temperature predictions for $h_v = 10^8$ W/(m^3·K) are plotted in Fig.3.8; the predicted solid and gas temperatures overlap at the thermocouple positions. To present further the overall behavior of the sample, the color maps of the simulation results are now presented.

Figs. 3.11, 3.12 and 3.13 show the pressure, velocity, and temperature fields in the test section at

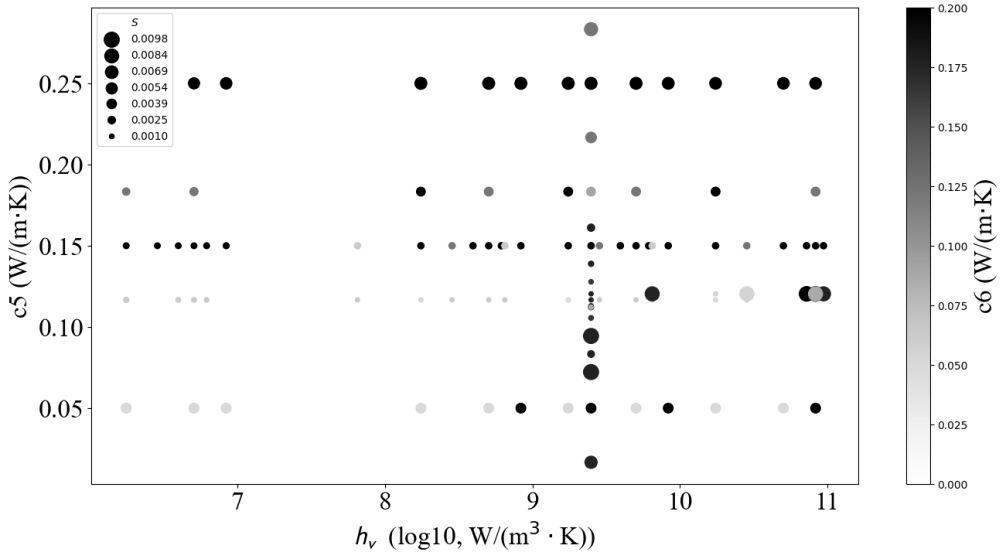

Figure 3.9 – The influence of three variables on the error S, qm=7.68×10^{-5} kg/s

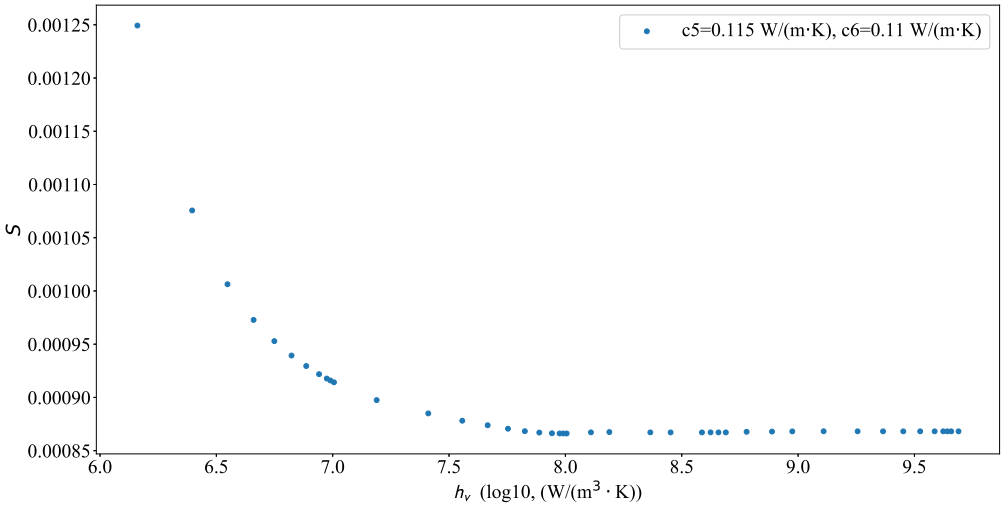

Figure 3.10 – The influence of h_v on the error S

100 s. Fig.3.14 shows the temperature fields inside the sample region at 100 s. The pressure gradient in the flow1 and flow2 regions is very small, whereas in the sample region the pressure gradient is driven by the permeability of the sample.

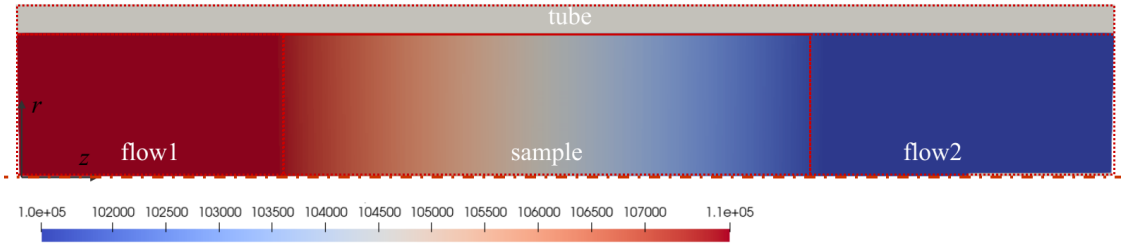

Figure 3.11 – Pressure p (Pa) distribution predicted with the LTNE model

In the flow1 and flow2 regions the gas flow is laminar ($Re = \rho_g u D/\mu_g = 1.17{\times}0.84{\times}0.01/0.000019 = 517$) and the velocity distribution is in agreement with Poiseuille's law where it is fully developed (entrance of flow1, exit of flow2). The gas velocity inside the sample $\langle \mathbf{v_g} \rangle^{\mathbf{g}}$ is equal to the Darcy velocity $\mathbf{u}$ divided by the porosity ε_g. The gas velocity profile can be considered unidirectional in the sample.

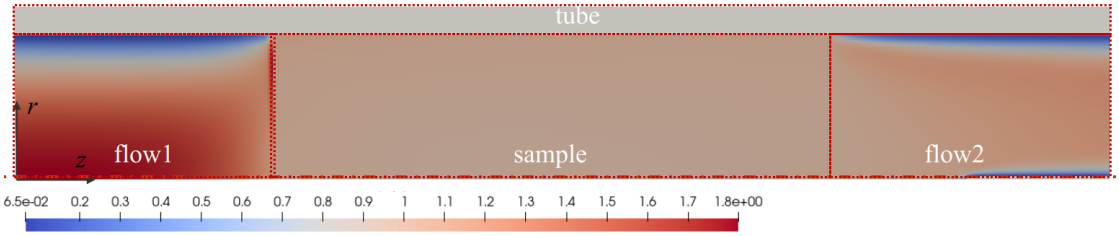

Figure 3.12 – Velocity magnitude u (m/s) predicted with the LTNE model

In the sample region, the difference between the local average gas and solid temperatures T_g and T_s is negligible. This indicates that in this case, for which the value of h_v is large ($h_v = 10^8 \mathrm{W/m^3\,K}$), heat transfer between the gas and the solid phases is important and local thermal equilibrium is reached.

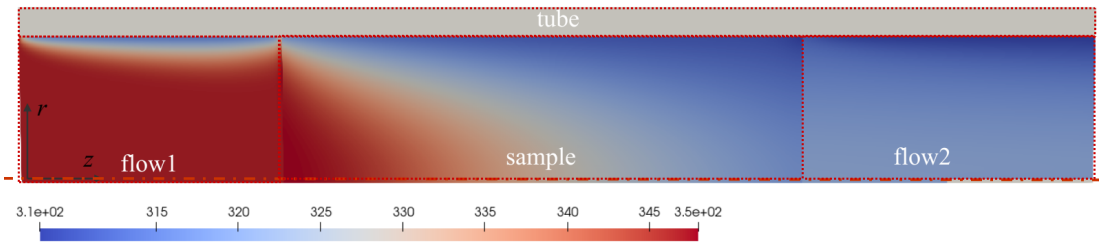

Figure 3.13 – Gas temperature T (K) predicted with the LTNE model

The same methodology was applied for the other studied cases (flow rates from qm=1.9×10^{-5} kg/s to qm=7.68×10^{-5} kg/s for both TT and IP directions) and the same conclusions were reached, that

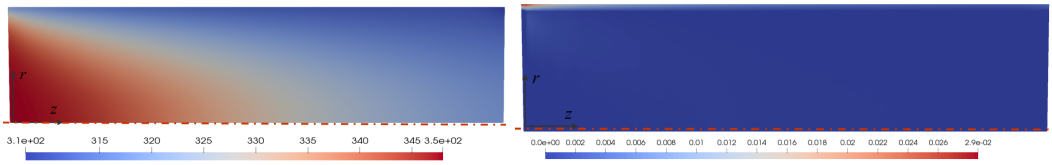

(a) solid temperature T_s

(b) temperature difference between gas and solid $T_g - T_s$

Figure 3.14 – Solid temperature and the difference $T_g - T_s$ (in K) in the sample region predicted with the LTNE model

is, h_v is greater than or equal to 10^8, in the conditions of the experiment (no chemical reactions, unity Reynolds number) and the local thermal equilibrium assumption holds.

3.4.2 Validation of the LTE model

The objective of this section is to infer the effective thermal conductivity $\mathbf{k_{eff}}$ and to validate the LTE model. Experimental data are presented using dots in Fig.3.15 and Fig.3.16. As shown in Eq.3.7, there are two dimensionless coefficients $c1$ and $c2$ to optimize to infer the effective thermal conductivity $\mathbf{k_{eff}}$. They are respectively linked to $k_{eff,IP}$ and $k_{eff,TT}$. As mentioned in Subsection 3.3.2, the global optimization algorithm (NCSU DIRECT) and the local optimization algorithm (NL2SOL) are used. To guide the choice of the minimum and maximum for the parameters to optimize, we used the correlations provided by Quintard et al. [67] for packed beds and obtained estimates of the maximum dispersion terms of about 0.1 W/(m K) for a Reynolds number of 4, that is, $0.25 \cdot k_{eff,IP,static}$ or $0.47 \cdot k_{eff,TT,static}$. The effective conductivity equals the effective conductivity in static conditions plus the dispersion terms. As a first step, we perform global optimization with the NCSU DIRECT algorithm with ranges for $c1$ and $c2$ between 0.1 and 3. During the optimization process, if the NCSU DIRECT algorithm reaches the convergence criterion ($S < 10^{-3}$), the optimisation ends. If the global optimisation fails to converge ($(S^{n+1} - S^n)/S^n < 10^{-5}$), the NL2SOL algorithm should be manually defined within a sub-region which is obtained from the NCSU DIRECT, such that we can eventually achieve the final convergence.

Fig.3.17 shows the optimization results of $(c1, c2)$ in the IP and TT directions for the different mass-flow rates of the study. The errors S obtained from the NCSU DIRECT and NL2SOL algorithms are respectively represented with squares and dots. Their sizes indicate the value of error S. Figs.3.17(a) and (b) respectively correspond to the mass-flow rate of qm=1.9×10^{-5} kg/s in the IP and TT directions; NCSU DIRECT converges after approximately 90 iterations. For the other six cases in Figs.3.17(c)-(h), the final convergence was reached after around 60 iterations of NCSU DIRECT and then around 30 iterations of NL2SOL.

For the optimization in the IP direction as shown in Fig.3.17 (left), $c1$ and $c2$ are respectively associated with the component of the effective thermal conductivity in the horizontal and transverse flow directions. When the error $S < 0.001$, the values of $c2$ are distributed between 1.45 and 2.03. More specifically, for the four mass-flow rates, they are respectively 1.50 ± 0.05, 1.59 ± 0.05, 1.85

$\pm$ 0.05, and 1.98 $\pm$ 0.05. However, the sensitivity is smaller for $c1$ because there is less temperature gradient in the flow direction. For the optimization in the TT direction as shown in Fig.3.17 (right), oppositely, $c1$ and $c2$ are respectively associated with the transverse and horizontal flow directions. When the error $S < 0.001$, the values of $c1$ span from 1.05 to 1.34. Precisely, they are respectively 1.08 $\pm$ 0.03, 1.12 $\pm$ 0.03, 1.19 $\pm$ 0.03, and 1.31 $\pm$ 0.03. Similarly with the previous case, the sensitivity of $c2$ is small. To sum-up, when the error S converges to the level of 10^{-4}, the ranges of the effective thermal conductivity from the optimization solution are given in Table 3.6. The effective thermal conductivity is found to increase with the Peclet number Pe as expected from the theory presented in the introduction.

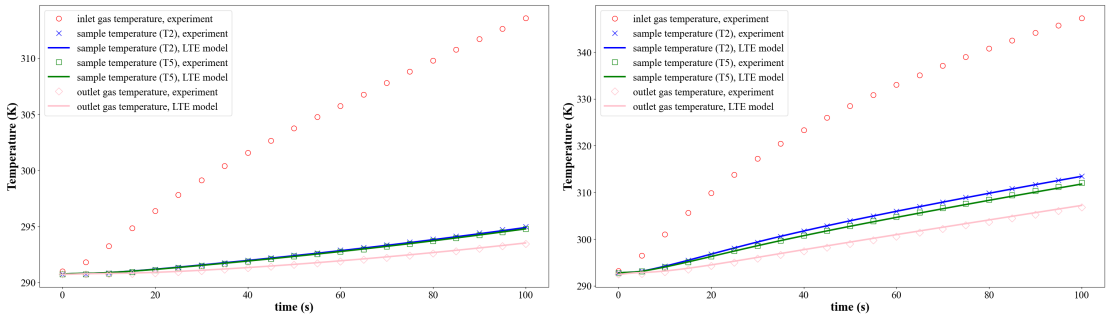

(a) qm=1.9×10^{-5} kg/s (b) qm=3.82×10^{-5} kg/s

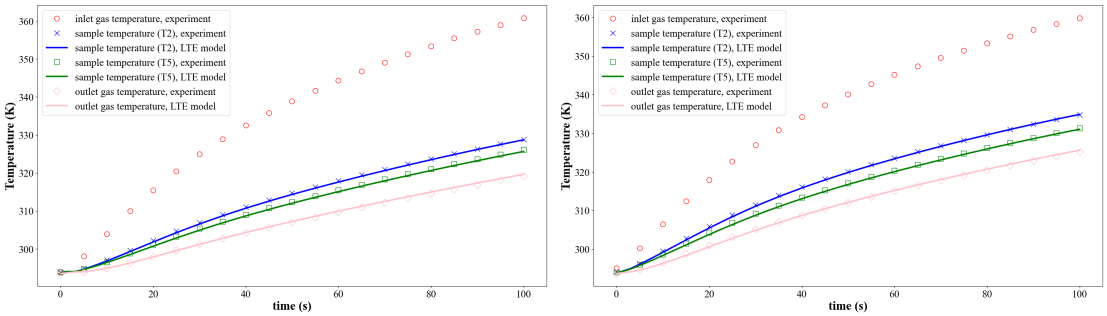

(c) qm=5.73×10^{-5} kg/s (d) qm=7.68×10^{-5} kg/s

Figure 3.15 – Comparison of predicted and measured temperatures in IP direction with the LTE model.

Fig.3.15 and Fig.3.16 show the comparisons between the measured and predicted temperatures in the IP and TT directions with different mass-flow rates. The solid line represents the predicted temperature curve, obtained by minimizing the error S. Taking Fig.3.15 (d) as an example, the values of the error S equals 8.01 $\times$ 10^{-4}, which is the average of 8.20 $\times$ 10^{-4}, 7.53 $\times$ 10^{-4}, and 8.30 $\times$ 10^{-4} corresponding to the three positions: T2, T5, and the outlet point. For reference, the temperature difference between the predicted and measured values is around 0.25 K at the outlet point. This implies that the LTE model may be used with a good level of accuracy to model materials such as Calcarb in the conditions of our experiments, that is, for non reactive flows and Reynolds numbers up to 4.

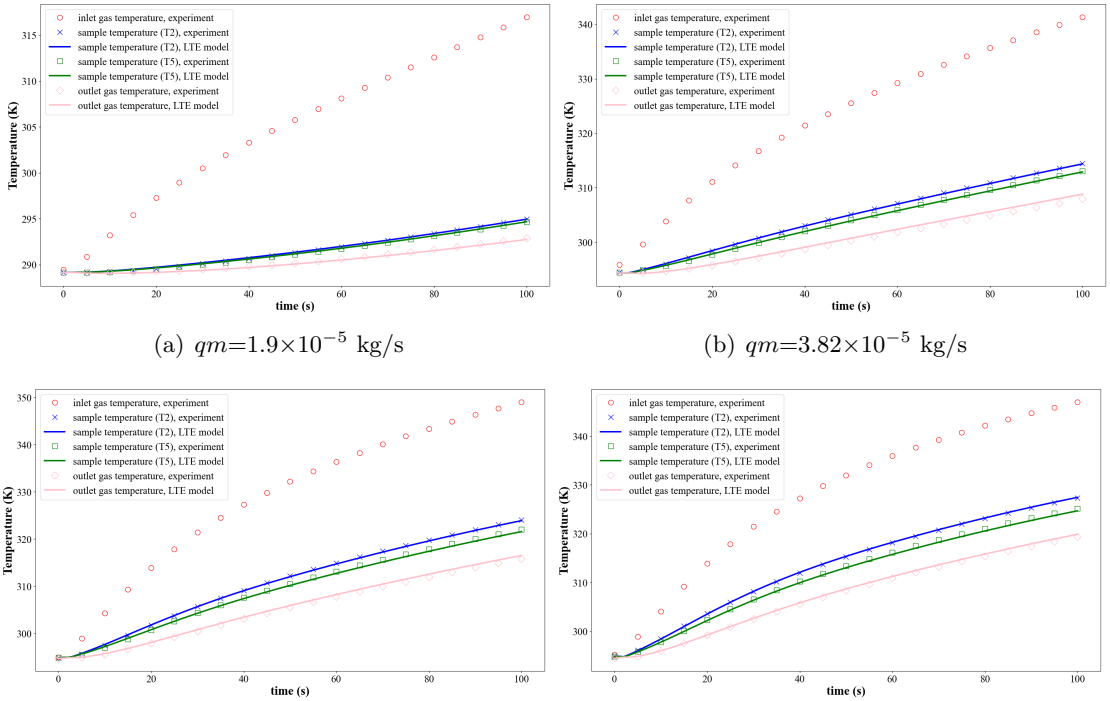

(a) qm=1.9×10^{-5} kg/s

(b) qm=3.82×10^{-5} kg/s

(c) qm=5.73×10^{-5} kg/s

(d) qm=7.68×10^{-5} kg/s

Figure 3.16 – Comparison of predicted and measured temperatures in TT direction with the LTE model.

Flow direction	qm (kg/s)	Pe	$k_{eff,IP}$ (W/(m · K))	LTE $k_{eff,TT}$(W/(m · K))	S
IP	1.9×10^{-5}	0.7	0.399±0.11	0.319±0.01	1.57×10^{-4}
	3.82×10^{-5}	1.4	0.399±0.12	0.339±0.01	5.17×10^{-4}
	5.73×10^{-5}	2.1	0.399±0.13	0.396±0.01	8.51×10^{-4}
	7.68×10^{-5}	2.8	0.399±0.19	0.422±0.01	8.01×10^{-4}
TT	1.9×10^{-5}	0.7	0.432±0.01	0.318±0.11	4.50×10^{-4}
	3.82×10^{-5}	1.4	0.448±0.01	0.318±0.11	7.85×10^{-4}
	5.73×10^{-5}	2.1	0.475±0.01	0.360±0.11	8.80×10^{-4}
	7.68×10^{-5}	2.8	0.523±0.01	0.360±0.11	6.93×10^{-4}

Table 3.6 – The value of $\mathbf{k_{eff}}$, and error S between LTE model and measured values for different mass-flow rates

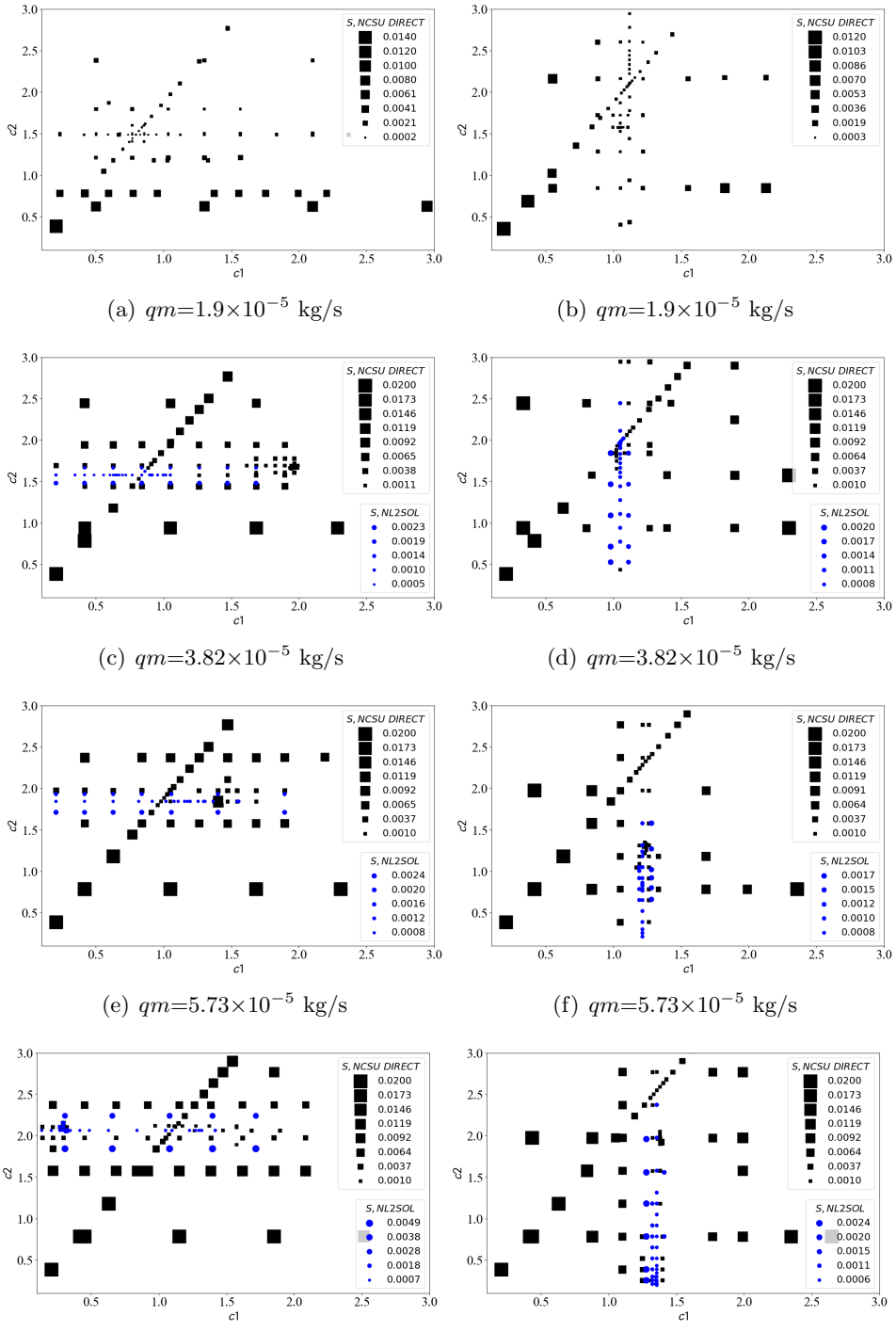

(a) qm=1.9×10^{-5} kg/s (b) qm=1.9×10^{-5} kg/s

(c) qm=3.82×10^{-5} kg/s (d) qm=3.82×10^{-5} kg/s

(e) qm=5.73×10^{-5} kg/s (f) qm=5.73×10^{-5} kg/s

(g) qm=7.68×10^{-5} kg/s (h) qm=7.68×10^{-5} kg/s

Figure 3.17 – The optimization results in IP direction (left) and TT direction (right) in the LTE model

3.5 Conclusions

The objective of this work was to study coupled heat and mass transfer in Calcarb, a carbon fiber preform used as insulator in many applications, and, in particular, in TPS materials. The TPS community has recently been questioning the validity of the local thermal equilibrium hypothesis and was lacking experimental data to conclude. In this work we designed a new experimental facility, based on the transient single blow technique, to determine the heat transfer coefficient h_v of low density porous materials. Experiments were conducted with nitrogen for Reynolds numbers representative of the TPS application (1 to 4) for both in-plane (IP) and through-thickness (TT) orientations. Parameter estimations were carried out using numerical inverse analysis. Local thermal equilibrium (LTE) and local thermal non-equilibrium (LTNE) models have been employed to investigate heat and mass transfer phenomena. The numerical model was implemented in finite volumes in the Porous material Analysis Toolbox based on Open-FOAM (PATO). Two optimization algorithms were employed in this work: a global optimization method, NCSU DIRECT, and a local optimization method, NL2SOL to minimize the error between measured and predicted temperatures. The optimization process was performed with the Open Source optimization software Dakota. The results revealed that the value of the heat transfer coefficient h_v was greater than or equal to 10^8 W/(m^3·K), demonstrating that for non-reactive flows and for Reynolds numbers up to 4 the local thermal equilibrium assumption holds. The maximum error S between measured and predicted (LTE) results is 8.8×10^{-4}. This implies that the LTE model may be used with a good level of accuracy to model materials such as Calcarb in the conditions of our experiments. One should note that although the LTNE model is not necessary in this case, the value of h_v determined in this work is useful for porous media applications such as ablative heat-shield design, where chemical non-equilibrium may challenge local thermal equilibrium. Pioneering works, such as the study of Scoggins et al. [28], may now be revisited in the light of this newly available data.

3.6 Appendix. Mesh and time convergence

A structured mesh was generated using the blockMesh application of OpenFoam. The mesh was refined at the near-wall and near-thermocouple regions. The final mesh is shown in Fig.3.18.

Mesh dependency was tested in flow and radial directions for the conditions presented in subsection 3.4.1. The mesh sensitivity analysis is plotted in Fig.3.19. While time-step independence is shown in Fig 3.20. As can be seen from Fig.3.19, when the number of cells increases in the gas flow direction from 5.29 $\times 10^4$ to 6.97 $\times 10^4$ and in the radial direction from 4.32×10^4 to 5.02 $\times 10^4$, there is no noticeable variation in the value of the volume averaged solid temperature T_s in the porous sample. Therefore, 5.29 $\times 10^4$ cells in the gas flow direction and 4.32 $\times 10^4$ cells in the radial direction are acceptable for the numerical simulations. Adjustable time steps with a user-set maximum value are used in the simulations. When the maximum time step decreases from 1×10^{-4} s to 8×10^{-5} s, there is no noticeable evolution in the value of volume averaged solid temperature T_s. Therefore, the maximum

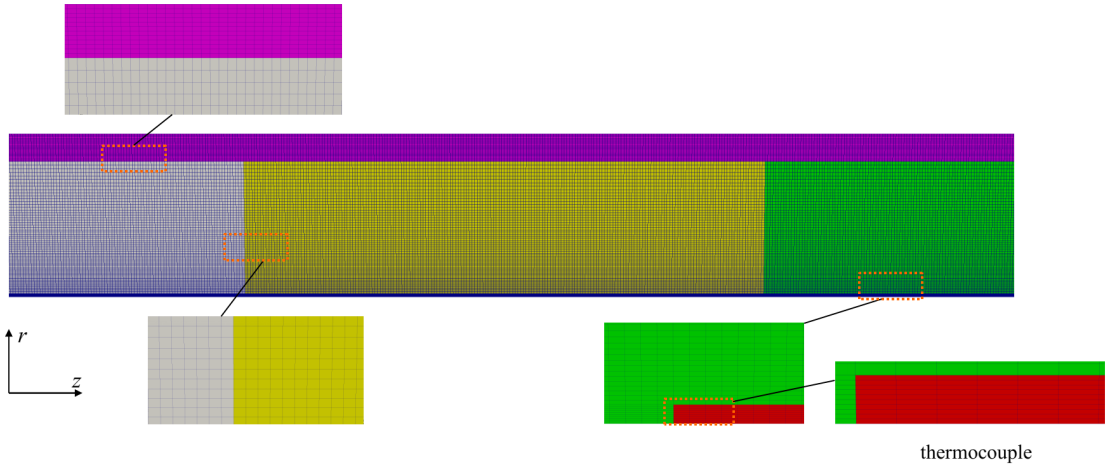

Figure 3.18 – Mesh of the test section

time step is set to 1×10^{-4} s. The error in Fig.3.19 and Fig.3.20 are defined as:

$$\text{Error} = \left| \frac{T_{s,n+1} - T_{s,n}}{T_{s,n+1}} \right| \tag{3.11}$$

where the index n+1 indicates the numerical simulation with more mesh refinement and a smaller max time step respectively.

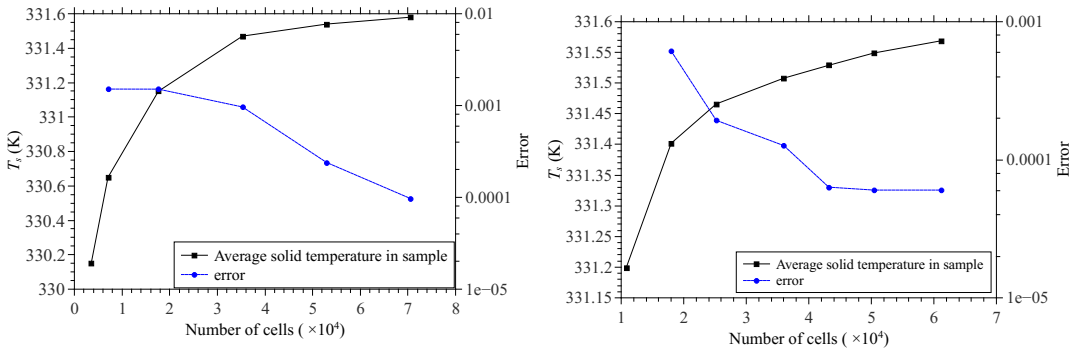

(a) flow direction

(b) radial direction

Figure 3.19 – Mesh dependency test in gas flow direction and radial direction

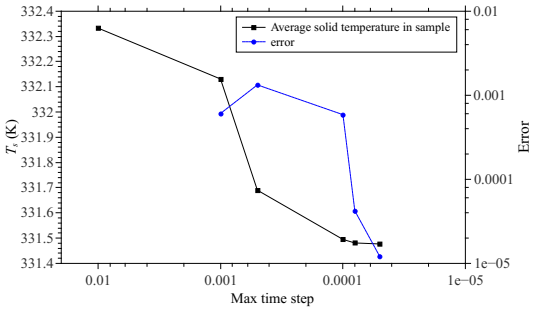

Figure 3.20 – Time step dependency test

Chapter 4

Development and validation of a local thermal non-equilibrium model for high-temperature thermal energy storage in packed beds

Preamble

Authors: S.Liu; A.Ahmadi-Senichault; C.Levet; J. Lachaud;
Affiliations: Arts et Métiers Institute of Technology, Univ. Bordeaux, CNRS, Bordeaux INP, I2M, UMR 5295, F-33400 Talence, France;
Published: No, the current version is to be submitted to *Applied energy*;
Conference: This work has been presented at the 14th Annual International Conference on Porous Media (InterPore2022), 30th May 2022 - Online ;

Abstract

High-temperature packed-beds thermal energy storage (TES) are gaining interest for industrial energy recovery. The wide range of temperature distributions causes significant variations in thermophysical properties of the fluid and solid phases, leading to inaccuracies of classical TES models and heat transfer correlations. The objective of this work is to develop and validate a detailed but pragmatic model accounting for high-temperature effects. Based on a literature survey spanning over several communities interested in high-temperature porous media, we propose a generic local thermal non-equilibrium model for granulate porous media accounting for conservation of mass, momentum and energy (two-equation temperature model). The effective parameters needed to inform the model are the effective thermal conductivities of the different phases and the heat transfer coefficient. An experimental-numerical inverse analysis method is employed to determine these parameters. A dedicated experimental facility has been designed and built to study a model granulate made of glass bead

of 16 mm diameter. Experiments are conducted using the Transient Single-Blow Technique (TSBT) by passing hot air (ranging from 293 K to 630 K) through cold particles at various mass flow rates, covering a Reynolds number range of 58 to 252. The new model was implemented in the Porous material Analysis Toolbox based on OpenFoam (PATO) used to compute the transient temperature fields. Two optimization algorithms were employed to determine the parameters by minimizing the error between experimental and simulated temperatures: a Latin Hypercube Sampling (LHS) method, and a local optimization method Adaptive nonlinear least-squares algorithm (NL2SOL). The results indicate that the value of heat transfer coefficient h_v in the two-equation model falls in the range of $1.0\times\ 10^4\ \sim\ 2.0\times\ 10^4$ W/(m^3 $\cdot$ K) under the given conditions. The axial dispersion gas thermal conductivity was found to be around 4 and 55 times higher than the gas thermal conductivity at Peclet numbers of around 55 and 165, respectively. Furthermore, two improved correlations of Nusselt number ($Nu = 2 + 1.54Re(T)^{0.6}Pr(T)^{1/3}$) and of axial dispersion gas thermal conductivity ($k_{dis,||}$=$0.00011Re(T)^{2.49}Pr(T) \cdot k_g$) are proposed and validated for a range of Reynolds number from 58 to 252. The overall approach is therefore validated for the model granulate of the study, opening new perspectives towards more precise design and and monitoring of high-temperature TES systems.

Keywords: Local thermal non-equilibrium; Macroscopic numerical simulations; Packed bed storage; Numerical inverse analysis ; Variable thermophysical properties

4.1 Introduction

Thermal energy storage (TES) is receiving increased attention for the development of energy recovery technologies such as concentrated solar power (CSP) [30, 113, 33], advanced adiabatic compressed air energy storage (AACAES) [113, 114, 115], and industrial waste heat recovery [32]. There are mainly three ways of storing heat: sensible and latent heat storage[116, 117], and chemical energy storage [118]. Sensible heat storage is the most developed and used in the industry [30, 119, 31]. Most industrial sensible heat storage systems rely on packed beds that offer advantages such as a large heat transfer area, low cost, and a wide temperature range (293 K to 1000 K) [113, 120].

To optimize the design of these systems, the coupled heat and mass transfer between the carrier fluid and the packed-bed material needs to be well understood and modeled. Many authors have contributed to this topic [30, 113, 33, 31, 120, 121, 122, 123, 105, 38, 36, 34]. Heat transfer in a packed bed can either be studied under the assumption of local thermal equilibrium (LTE) or local thermal non-equilibrium (LTNE) [30]. These models are also referred to as one-equation and two-equation models, respectively. Pati et al. [124] reviewed the applicability of one- and two-equation models. The choice of model is influenced by parameters such as the gas-to-solid thermal diffusivity ratio (α_g/α_s), Reynolds number ($Re = \rho_g u d_{par}/\mu_g$), and Darcy number ($Da = K/d_{par}^2$). Specifically, when the Reynolds number is greater than 50 and the thermal diffusivity ratio between the gas and solid phases (α_g/α_s) is higher than 30 [66], the two-equation model is required. Schumann [121] was the first to propose a two-equation energy model - one for carrier fluid and one for the packed-bed material;

however, the heat capacity of the fluid and the thermal conductivities of both phases were neglected, and the model was one-dimensional. Saez et al. [123] improved Schumann's one-dimensional model by including heat capacity for the fluid and thermal conductivities and adding thermal dispersion in the flow direction (increase in conductivity due to the gas flow). The thermophysical properties were assumed to be constant because the inlet gas temperature was at most 70°C. Hanchen et al. [31] applied the model proposed by Saez et al. to high-temperature conditions (527°C) but neglected the dispersion term and assumed constant gas properties. Zanganeh et al. [38, 36] proposed a more comprehensive model that considered the radiative term in the effective gas thermal conductivity and variable thermophysical properties for a packed bed of rocks in the temperature range of 20-650°C. Anderson et al. [33, 34] further validated the two-equation one-dimensional model with varying thermophysical properties for a packed bed of alumina particles at both low (120°C) and high (700°C) temperatures. Ma et al. [125] developed a transient two-equation two-dimensional model that fully considers thermal dispersion and changes in thermophysical properties, expanding on the existing literature. In these works, the carrier fluid density and velocity are considered constant, which is a correct approximation for incompressible fluids (water, molten nitrate salts, ...). Using air as the carrier fluid, non-uniform temperature distributions inside packed beds leads to non-uniform gas density and viscosity, affecting the velocity and pressure distributions. We aim to fill this gap by accounting for mass and momentum conservation, namely by including the volume-averaged conservation of mass and momentum (Darcy-Forchheimer's law) into the model. Such models have been employed since the 1960's for very high-temperature applications such as space-vehicle heat shields [4]. Also, in previous TES studies, the dimensionless numbers (Reynolds, Prandtl) used in the correlations were assumed to be constant. We would like to discuss this assumption when variations of velocity and thermophysical properties are not negligible. The two-equation energy model writes as follows [68]:

$$\frac{\partial}{\partial t}\left(\varepsilon_s \rho_s c_{p,s} \langle T_s \rangle^s\right) = \nabla \cdot \left(\mathbf{k_{s,eff}} \cdot \nabla \langle T_s \rangle^s\right) + h_v \left(\langle T_g \rangle^g - \langle T_s \rangle^s\right) \tag{4.1}$$

$$\frac{\partial}{\partial t}\left(\varepsilon_g \rho_g c_{p,g} \langle T_g \rangle^g\right) + \nabla \cdot \left(\rho_g c_{p,g} \langle \mathbf{v_g} \rangle^{\mathbf{g}} \langle T_g \rangle^g\right) = \nabla \cdot \left(\mathbf{k_{g,eff}} \cdot \nabla \langle T_g \rangle^g\right) + h_v \left(\langle T_s \rangle^s - \langle T_g \rangle^g\right) \tag{4.2}$$

where the gas volume fraction ε_g is equal to the porosity of the packed bed, h_v is the volumetric heat transfer coefficient, $c_{p,i}$ and $\mathbf{k_{i,eff}}$ respectively denote the heat capacity and effective thermal conductivity tensor of the i phase, $\langle T_i \rangle^i$ and $\langle \mathbf{v_g} \rangle^{\mathbf{g}}$ denote the intrinsic phase average temperature for the i-phase and the intrinsic gas average velocity. For the development of TES models, three effective properties need to be evaluated: h_v, $\mathbf{k_{s,eff}}$ and $\mathbf{k_{g,eff}}$.

The heat transfer coefficient and corresponding correlation can be determined either experimentally [120, 105, 126, 127, 128, 129, 130, 131] or through pore-scale simulation in representative geometries [68, 132, 133]. The experimental methods include both steady state [127, 128, 130, 131] and transient regime [120, 129] approaches. With the steady state approach, particles within the packed beds are heated with a resistive heater. Compressed air, serving as the working fluid, extracts heat from these heated particles. After reaching steady-state, the temperatures of the gas flow at the inlet, outlet, within the packed bed, as well as the surface temperature of the particles are monitored. These measurements are used to estimate the heat exchange and infer the heat transfer coefficient. In the transient method, cold particles are heated using hot gas. The time evolution of average inlet, outlet,

and inside gas flow temperatures, and particle temperatures, are recorded. The local heat transfer coefficient is derived from analyzing the spatial and time evolution of air and particle temperatures. The progress in optimization algorithms and computer resources has allowed the general usage of inverse methods to infer the parameters with more accuracy. Concerning the pore-scale simulation method, the volume averaging theory [68] have been applied to periodic structures, such are arrays of cylinders, to obtain h_v. With the progress of the resolution of computed micro- tomography and computer resources, pore-scale simulations are becoming a realistic approach to determine h_v [29, 134]. Using these two methods, numerous correlations were obtained for the heat transfer coefficient h_v in packed-bed under diverse conditions. A summary of the most widely used correlations and of their validity ranges is proposed in Table 4.1. However, the influence of temperature variations

Table 4.1 – Empirical correlations for the heat transfer coefficient in packed beds.

Year	Investigators	Correlation	Range	Remarks
1952	W. Ranz [127]	$Nu = 2 + 1.8Re^{0.5}Pr^{1/3}$	$10 < Re/\varepsilon_g < 1000$ not mentioned for T	experimental method, steady state constant properties
1970	Galloway et al. [128]	$Nu = 2 + 1.354Re^{1/2}Pr^{1/3} + 0.0326RePr^{1/2}$	$Re/\varepsilon_g < 5000$ T=310 K	experimental method, steady state constant properties
1979	Wakao et al. [105]	$Nu = 2 + 1.1Re^{0.6}Pr^{1/3}$	$3 < Re < 10000$ not mentioned for T	analysis of experimental data from the literature
2012	Yang et al. [129]	$Nu = 2.1 + 0.465Re^{0.63}Pr^{1/3}$	$100 < Re/\varepsilon_g < 5000$ 298 K $< T <$ 358 K	experimental method, transient constant properties
2016	Naghash et al. [130]	$Nu = (0.0012 \pm 0.00273)Re_{d_h}{}^{(1.647\pm0.501)}Pr^{1/3}$ $Re_{dh} = Re/1000(2\varepsilon_g/3\varepsilon_s)d_{par}$	$40 < Re < 120$ 299 K $< T <$ 338 K	experimental method, steady state variable properties
2022	Qu et al. [120]	$Nu = 0.345/\varepsilon_g \cdot (2 + 1.033(Re/\varepsilon_g)^{0.6}Pr^{1/3}$	$200 < Re/\varepsilon_g < 1000$ 283 K $< T <$ 345 K	experimental method, transient constant properties
2023	this work	$Nu = 2 + 1.54Re(T)^{0.6}Pr(T)^{1/3}$	$58 < Re < 252$ 293 K $< T <$ 630 K	experimental method, transient variable properties

on these correlations is not specified. Taking the Wakao correlation as an example, it is based on published experimental data in the range of $3 < Re < 10000$, mostly based on intermediate temperature conditions and without providing the temperature range of validity. Most simulation models for high-temperature storage systems used this correlation for temperatures up to 1173 K [113, 125, 135, 136]. At high temperatures, a wide temperature distribution can cause non-uniform gas density and viscosity inside the packed bed. These varying thermal physical properties affect Re, which in turn affects Nu in the Wakao correlation. Temperature-dependent parameters should replace constant parameters in such correlations; also the linear coefficients (1.1 in Wakao's correlation) should be validated or re-evaluated.

Concerning the effective gas and solid thermal conductivities, a large amount of theoretical work has been done by theoreticians and there is now a good agreement that they respectively write [68, 73, 137]

$$\mathbf{k_{g,eff}} = \varepsilon_g k_g \mathbf{I} + \frac{k_g}{V}\int_{A_{gs}} \mathbf{n}_{gs}\mathbf{b_{gg}} dA - \rho_g c_{p,g} \left\langle \tilde{\mathbf{v}}_g \mathbf{b_{gg}} \right\rangle = \mathbf{k_{g,con}} + \mathbf{k_{g,tor}} + \mathbf{k_{dis}} \tag{4.3}$$

$$\mathbf{k_{s,eff}} = \varepsilon_s k_s \mathbf{I} + \frac{k_s}{V}\int_{A_{gs}} \mathbf{n}_{sg}\mathbf{b_{ss}} dA = \mathbf{k_{s,con}} + \mathbf{k_{s,tor}} \tag{4.4}$$

where k_i denotes the thermal conductivity of the i phase, V is a representative elementary volume of the porous medium, A_{gs} is the area of the g-s interface contained in the averaging volume, $\mathbf{n_{gs}}$ is the outwardly directed unit normal vector pointing from the gas phase toward the solid phase, $\mathbf{n_{gs}} = -\mathbf{n_{sg}}$. $\mathbf{v}_g$, $\langle \mathbf{v_g} \rangle^{\mathbf{g}}$, and $\tilde{\mathbf{v}}_g = \mathbf{v}_g - \langle \mathbf{v}_g \rangle^g$ are respectively the gas velocity within the pores, the intrinsic phase average velocity, and the deviation velocity. The closure variables $\mathbf{b_{ii}}$ $(i = g, s)$ are the vector fields that map $\nabla \langle T_i \rangle^i$ onto $\tilde{T}_i$, where $\tilde{T}_i$ is the spatial deviation temperature in the i-phase, more precisely [68], $\tilde{T}_g = \mathbf{b_{gg}} \cdot \nabla \langle T_g \rangle^g - s_g(\langle T_g \rangle^g - \langle T_s \rangle^s) + ...$, $\tilde{T}_s = \mathbf{b_{ss}} \cdot \nabla \langle T_s \rangle^s + s_s(\langle T_s \rangle^s - \langle T_g \rangle^g) + ...$ Note that in these derivations the effective radiative conductivity may be added as a contribution the effective solid conductivity for optically thick media [138]; this hypothesis is verified for packed beds as the grain size is small compared to the system.

In many research works, regardless of the experimental conditions, simple expressions of $\mathbf{k_{g,eff}}$ and $\mathbf{k_{s,eff}}$ as a function of gas and solid phase conductivities and the porosity of the homogeneous and isotropic packed beds have been considered [31, 34, 95, 81]. In Eq.4.3, $\mathbf{k_{g,eff}}$ is composed of three parts: the conductivity term $\mathbf{k_{g,con}}$ accounts for a simple average of the thermal conductivity, the tortuosity term $\mathbf{k_{g,tor}}$ represent the tortuosity of the phase repartition and the dispersion term $\mathbf{k_{dis}}$ accounts for gas flow effects. $\mathbf{k_{g,tor}}$ and $\mathbf{k_{dis}}$ could be numerically estimated by solving a closure problem on a periodic unit cell representative of the structure [68, 73]. $\mathbf{k_{g,tor}}$ is often neglected since $\mathbf{k_{dis}}$dominates [73]. Wakao et al. [126] and DeGroot et al. [73] described $\mathbf{k_{dis}}$ in the axial and radial directions (respectively horizontal and transverse flow directions) as different coefficients multiplied with Reynolds Re and Prandtl Pr numbers. In Eq.4.4, $\mathbf{k_{s,eff}}$ consists of the conductivity of the solid $\mathbf{k_{s,con}}$ corrected to account for its tortuosity $\mathbf{k_{s,tor}}$ [139], whereas the closure variable $\mathbf{b_{ss}}$ which is a function of the gas velocity $\mathbf{v_g}$ [68] integrates dispersion effects. Therefore, for high temperatures, the best approach is to use the models of Eq.4.3 and 4.4 with temperature-dependent thermal conductivities k_g and k_s.

In this context, the purpose of this article is to propose a generic two-equation model coupled with mass and momentum conservation for high-temperature conditions and to determine the effective parameters needed to inform the model, namely, the thermal conductivities and the heat transfer coefficient. For this purpose, we have designed and built a laboratory-scale heat storage facility where the gas temperatures at the inlet, at the outlet and within the packed bed are monitored. Glass beads with a diameter of 16 mm were selected as the heat storage medium. In Section 4.2, the experimental setup and test procedure are presented. In section 4.3, we present a numerical inverse analysis method that we have developed to infer the intrinsic parameters and that consists of a detailed numerical model of the packed bed and an advanced multi-objective optimization algorithm. In section 4.4, the experimental results and the estimated values of the two-equation parameters are presented and new correlations accounting for high-temperature effects are proposed and compared with the literature. Conclusions and outlook are discussed in section 4.5.

4.2 Experimental facility

The main characteristics of gas/solid packed-bed TES described in the literature have been reviewed by Esence et al [30]. These encompass a mix of large-scale industrial systems [38, 36] and a majority of reduced-scale laboratory set-ups [120, 125, 129, 140, 141]. In studies conducted at the laboratory scale, the diameter ratios (tube diameter to particle size) range from 3 to 32, with gas flow rates varying between 0.035 to 3.23 m/s [30]. To minimize the effect of diameter ratios on the distribution of fluid velocity, it is recommended that diameter ratio remains greater than 10 [142]. In most cases, the velocity of the gases is of the order 0.3 m/s [120, 140, 141]. The experimental facility presented in the following section was designed in alignment with these characteristics. It is based on a method called the transient single-blow technique (TSBT) [30]. With this approach, hot gas is used to heat particles inside packed beds and the time evolution of the gas temperature is recorded at the inlet, at the outlet and also at different locations within the packed bed to bring robustness to the inverse analysis.

4.2.1 Experimental system and test procedure

A schematic drawing and photograph of the experimental setup that we have developed and an enlarged view of the test section, where thermocouple positions are shown, are displayed in Fig.4.1. The setup consists of a hot air blower (BAK Thermoplastic) to supply and heat air, an insulated test section made of an iron tube and two metallic grids to maintain the particles a differential pressure transmitter (EMERSON FISHER ROSEMOUNT) to measure pressure drop, and a thermo-anemometer (VT 110-2014 THERMO-ANEMOMETER) to measure the gas velocity. The iron tube has dimensions of 940 mm in length, 194 mm in inner diameter, and a thickness of 3 mm. These dimensions are suitable to study glass beads with a diameter of 16 mm, while respecting the diameter aspect ratio of at least 10, recalled in the introduction.

In the experiment, the first step is to set the flow rate of the inlet gas. This parameter is controlled by the air blower and measured using the thermo-anemometer. The maximum flow rate is 800 liters/min, equivalent to a mass flow rate of 1.6×10^{-2} kg/s. The maximum Darcy velocity u (also known as superficial gas velocity, $u = qm/(\rho_g \pi R_b^2)$) reaches 0.451 m/s at room temperature (293 K), where ρ_g is the gas density of 1.2 kg/s and R_b is the radius of the tube at 0.097 m. Once the inlet air mass flow rate is determined at room temperature, the next step involves setting the heating power, which is also controlled by the air blower. To ensure data reproducibility, we repeated each experiment following a consistent procedure. After an initial experiment, with a two-day cooldown period to return particles to room temperature, subsequent runs exhibited only minor temperature differences (1-2 °C) initially due to the room temperature. After 15 minutes of heating, the temperature differences remained minimal, within 0.3 °C, confirming data reliability across trials.

The black points in Fig.4.1 indicate the positions of the thermocouples (type K, 2 mm sheath diameter). Temperature measurements are taken at various locations: the inlet gas temperature (1) at z=0 mm, r=0 mm; the gas temperature inside the test section at seven central axis locations (from 2 to 8) at z=50, 150, 250, 350, 450, 650, and 850 mm, r=0 mm; and three radial locations (from 9

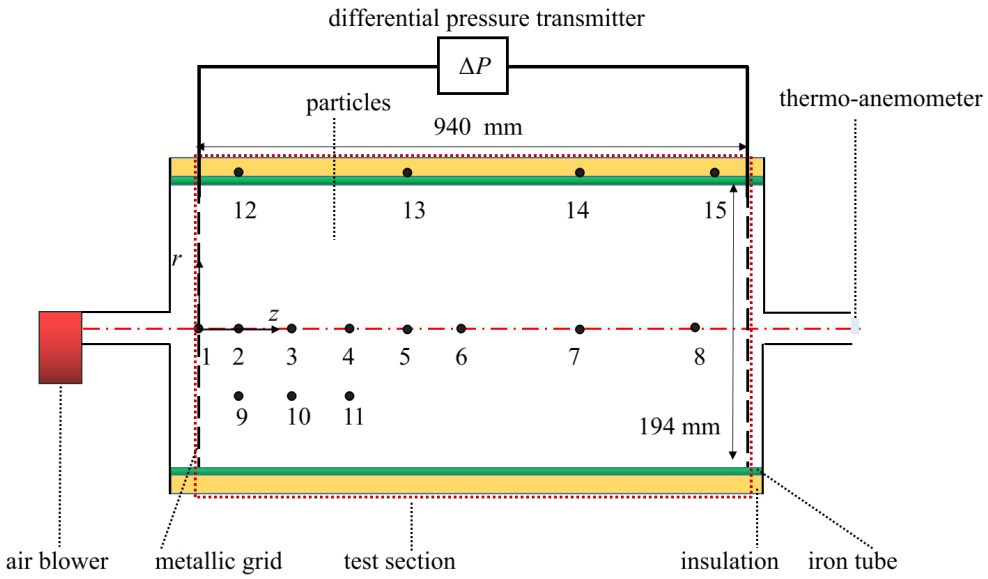

(a) experimental setup

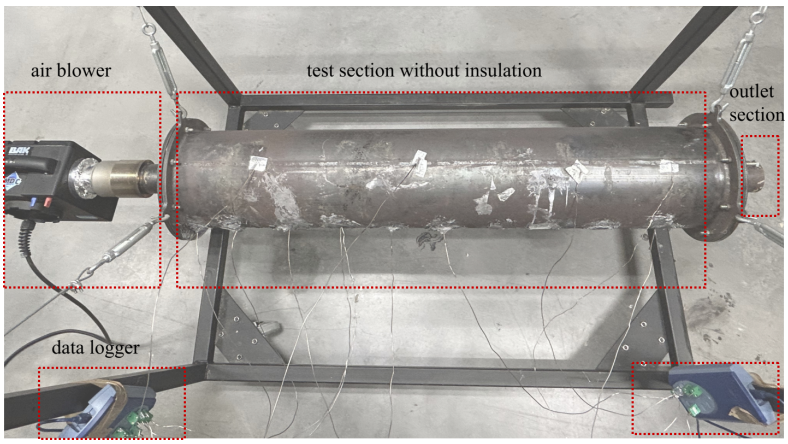

(b) photograph of the experimental setup

Figure 4.1 – Schematic diagram and photograph of the experimental system and enlarged view of the test section showing the thermocouple identification numbers.

to 11) at z=50, 150, and 250 mm, r=-45 mm. The tube surface temperature is also measured at four axis locations (from 12 to 15) at x=50, 350, 650, and 900 mm, z=100 mm. To ensure accurate gas temperature measurement, the thermocouple is securely fixed in the gap between the glass beads using ST-1000 thermal glue, as shown in Fig. 4.2. The thermal glue is capable of withstanding temperatures up to 950°C.

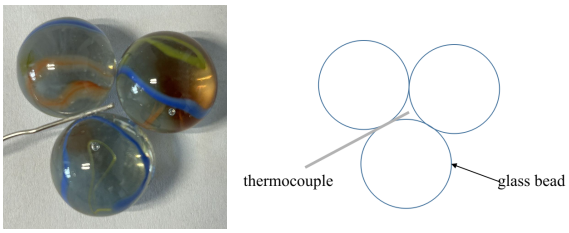

Figure 4.2 – A schematic of the thermocouple position.

The thermocouples are connected to two display data loggers (Pico Technology TC-08) that record the temperature with a time step of 1.0 s. Experimental variations in the inlet air mass-flow rate and heating power were performed to verify the model's suitability for different Reynolds numbers (Re). The test section dimensions and the architectural properties of particles are listed in Table 4.2. The gas volume fraction (porosity, ε_g) in Table 4.2 is calculated using the Muller correlation [142, 143] as shown in Eq.4.5. The permeability and Forchheimer coefficient are calculated using the Ergun equation, as shown in Eq.4.6 [30], where these two parameters are treated as scalars. These defined parameters will be used in the subsequent modeling section. Ergun equation is validated for modeling pressure variations in the experiments, as explained in Appendix 4.6.

Table 4.2 – Dimension and structural properties of the packed bed and glass beds.

Test section dimensions diameter D_b × length L (mm)	Porosity ε_g	Particle diameter d_{par} (mm)	Particle density ρ_s (kg m^{-3})	Permeability K (m^2)	Forchheimer coefficient β (m^{-1})
194 × 940	0.383	16	2500	2.52×10^{-7}	1201.18

$$\varepsilon_g = 0.365 + 0.22/(D_b/d_{par}) \tag{4.5}$$

$$K = \frac{{d_{par}}^2 {\varepsilon_g}^3}{150{\varepsilon_s}^2}, \qquad \beta = \frac{1.75\varepsilon_s}{d_{par}{\varepsilon_g}^3} \tag{4.6}$$

4.2.2 Experimental uncertainty analysis

Experimental uncertainties can be categorized into two types: direct measurement errors resulting from the experimental device, and errors arising from the measurement process itself. In this work, the ranges and uncertainties associated with the experimental devices are presented in Table 4.3. Errors from the temperature measurement process are chiefly due to the positioning of the thermocouples in the tube. The thermocouples are fixed in the gap between the glass beads, which are positioned with

a tolerance of ± 10 mm. The uncertainty in temperature measurement within the tube, attributed to the thermocouple positioning, is determined through repeated experiments, resulting in an uncertainty value of 1.19%.

Table 4.3 – The uncertainty analysis in the experimental measurements.

	Range	Uncertainty
Temperature sensor (Pico Technology)	-270°C to +1820°C	± 0.2% of the reading
K-type thermocouple	-100°C to + 800°C	± 0.5 %
Thermo-anemometer	0.15 to 30 m/s	± 3 % of the reading
Temperature measurement in the tube (due to the position of the thermocouple)	293 K to 1000 k	1.19 % of the reading

4.3 Numerical inverse analysis method

To tackle the complexity of the problem, numerical inverse analysis was employed to estimate the desired quantities. Firstly, we present the model describing fluid flow and heat transfer within the test section. Secondly, we detail the multi-objective optimization algorithm used to infer the effective parameters.

4.3.1 Numerical model

To facilitate parameter estimation, we model the entire test section as shown in Fig.4.1 (b). The corresponding numerical model, presented in Fig.4.3, represents a two-dimensional axisymmetric geometry. The model consists of two regions, namely the packed bed (porous sample) and the tube (iron tube).

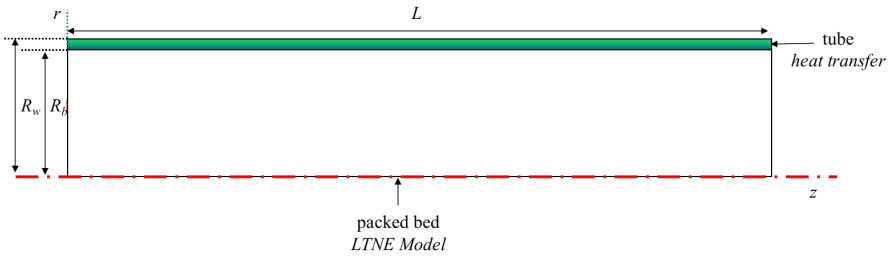

Figure 4.3 – Two-dimensional axisymmetric numerical model of the test section.

4.3.1.1 Mathematical model and numerical implementation

In the packed bed region, we consider the two-equation model (Eq.4.1 and 4.2) for energy conservation. For the tube region, transient heat conduction is considered (energy conservation in a solid).

The Reynolds number based on the particle diameter (d_{par}) is defined as $Re = \rho_g u d_{par}/\mu_g$. Throughout the entire experimental process, the minimum value of Re is 18.34 (corresponding to T_g=630 K, ρ_g=0.563 kg/m^3, u=0.067 m/s, μ_g=3.29e-05 kg/(m $\cdot$ s)), and the maximum value of Re is 453.36 (corresponding to T_g=293 K, ρ_g=1.2 kg/m^3, u=0.451 m/s, μ_g=1.91e-05 kg/(m $\cdot$ s)). Considering the range of applicability of the Forchheimer law inside a packed bed, which typically lies between 5 [144] and 500 to 600 [145], the average gas velocity is determined by solving the Forchheimer law. The two regions are coupled by ensuring the conservation of heat fluxes at their interfaces. The mass and energy conservation equations for the two-equation model in the packed bed region and the energy equation in the tube region write,

$$\begin{cases} \dfrac{\partial}{\partial t}\left(\varepsilon_g \dfrac{M\langle p\rangle^g}{R\langle T_g\rangle^g}\right) + \nabla\cdot\left(-\dfrac{M\langle p\rangle^g \mathbf{KX}}{R\langle T_g\rangle^g}\cdot\nabla\langle p\rangle^g\right) = 0 \quad \text{(Mass equation)} \\ \dfrac{\partial}{\partial t}\left(\varepsilon_s\rho_s c_{p,s}\langle T_s\rangle^s\right) = \nabla\cdot\left(\mathbf{k_{s,eff}}\cdot\nabla\langle T_s\rangle^s\right) + h_v\left(\langle T_g\rangle^g - \langle T_s\rangle^s\right) \quad \text{(Energy equation)} \\ \dfrac{\partial}{\partial t}\left(\varepsilon_g\rho_g c_{p,g}\langle T_g\rangle^g\right) + \nabla\cdot\left(\rho_g c_{p,g}\langle \mathbf{v_g}\rangle^{\mathbf{g}}\langle T_g\rangle^g\right) = \nabla\cdot\left(\mathbf{k_{g,eff}}\cdot\nabla\langle T_g\rangle^g\right) + h_v\left(\langle T_s\rangle^s - \langle T_g\rangle^g\right) \quad \text{(Energy equation)} \\ \rho_t c_{p,t}\dfrac{\partial T_t}{\partial t} = \nabla\cdot\left(k_t\cdot\nabla T_t\right) \quad \text{(Energy equation)} \end{cases} \tag{4.7}$$

where $\langle p\rangle^g$ is the intrinsic average pressure, the mass equation is derived from the perfect gas law (Eq. 4.8), gas mass conservation (Eq. 4.9) [4], and the Forchheimer equation (Eq. 4.10). The Forchheimer tensor, represented as $\mathbf{X}$, is introduced to simplify the computation process [76].

$$\rho_g = \frac{M\langle p\rangle^g}{R\langle T_g\rangle^g} \tag{4.8}$$

$$\partial_t\left(\varepsilon_g\rho_g\right) + \nabla\cdot\left(-\varepsilon_g\rho_g\langle\mathbf{v_g}\rangle^{\mathbf{g}}\right) = 0 \tag{4.9}$$

$$\langle\mathbf{v_g}\rangle^{\mathbf{g}} = -\frac{1}{\varepsilon_g}(\mathbf{KX})\cdot\nabla\langle p\rangle^g, \quad X_{ij} = \frac{1}{\mu_g K_{ij} + \beta_{ij}\rho_g|\langle v_g\rangle|} \tag{4.10}$$

It should be noted that glass beds exhibit significant opacity at a wavelength of 4.9 μm, which coincides with the peak intensity wavelength at 700 K. For 5 mm glass beds, radiation contributes to nearly 0% of the total heat transfer at temperatures below 700 K, while it increases to 50% at 1000 K [146]. Therefore, it is reasonable to neglect radiation heat transfer effects when the temperature is below 700 K. The initial and boundary conditions for the systems of Eq.4.7 are described in detail in Table 4.4. In the packed bed region, T_g and T_s represent the gas and solid temperatures, respectively, while T_t represents the temperature in the tube region. The thermal conductivity of the tube is denoted as k_t. For simplicity, we use T_g, T_s, and p to represent the average gas temperature $\langle T_g\rangle^g$, average solid temperature $\langle T_s\rangle^s$, and average pressure $\langle p\rangle^g$, respectively. The gas temperature T_g at the inlet side is determined from the experimental study. Numerically, we imposed the inlet mass flux using a pressure gradient inlet boundary condition based on Darcy-Forchheimer's law projected on the inlet patch normal $\boldsymbol{n}$. The expression of the inlet pressure gradient imposed is provided in Table 4.4. In the tube region, the wall surface temperature T_t is measured throughout the experimental period. At the interface between the packed bed and the tube, the condition of $T_s = T_t$, $k_{s,eff}\frac{\partial T_s}{\partial r} = k_t\frac{\partial T_t}{\partial r}$ were applied for the solid phase. By implementing this boundary condition, which implies that the solid

temperature T_s and the tube temperature T_t are equal at this interface, it also guarantees that the heat flux entering one region on one side of the interphase matches the heat flux leaving the other region on the opposite side of the domain. At the packed bed-tube interface, the condition of $\partial T_g/\partial r = 0$ was used for the gas phase. The rationale for this choice was explained in Appendix 4.7. A linear part variation of T_t within each interval is assumed in line with the findings reported by Cascetta et al. [136] in a similar experimental setup. The temperatures at the four measuring points (from 12 to 15) shown in Fig. 4.1 (b) are expressed as follows

$$\begin{cases} T_t = T12 + (T12 - T13)/(z13 - z12) \cdot (z12 - z) & 0 < z < z13 \\ T_t = T13 + (T13 - T14)/(z14 - z13) \cdot (z13 - z) & z13 \leq z < z14 \\ T_t = T14 + (T14 - T15)/(z15 - z14) \cdot (z14 - z) & z14 \leq z < L \end{cases} \tag{4.11}$$

Fig.4.4 shows the temperature distribution of T_t on the wall surface, which is calculated using Eq.4.11. In this case, the inlet gas temperature T_g gradually increases from 292 K to 530K, and the inlet mass-flow rate qm is chosen as 5.97 $\times$ 10^{-3} kg/s. As shown in Fig.4.4, T_t exhibits a linear variation along the z-axis within each of the three zones as a function of time and space.

Table 4.4 – Initial and boundary conditions of the LTNE model.

Region	Initial conditions		Boundary conditions		
		inlet	packed bed-tube interface	outlet	
packed bed	$T_g = T0$ $T_s = T0$	$T_g = T1$, $\frac{\partial T_s}{\partial z} = 0$ $\partial_w p = -\left(\frac{\mu_g}{\mathbf{K}\cdot\boldsymbol{n}\cdot\boldsymbol{n}} + \rho_g \beta \cdot \boldsymbol{n} \cdot \boldsymbol{n}\ |\epsilon \boldsymbol{v_g}|\right)(\epsilon \boldsymbol{v_g} \cdot \boldsymbol{n}) + \rho_g\ g$	$\frac{\partial T_g}{\partial r} = 0$, $T_s = T_t$,$k_{s,eff}\frac{\partial T_s}{\partial r} = k_t \frac{\partial T_t}{\partial r}$ $p = p_{atm}$	$\frac{\partial T_g}{\partial z} = 0$, $\frac{\partial T_s}{\partial z} = 0$	
tube	$T_t = T0$	inlet $\frac{\partial T_t}{\partial z} = 0$	tube-packed bed interface $k_t \frac{\partial T_t}{\partial r} = k_{s,eff}\frac{\partial T_s}{\partial r}$	top T_t is a function of wall surface temperature	outlet $\frac{\partial T_t}{\partial z} = 0$

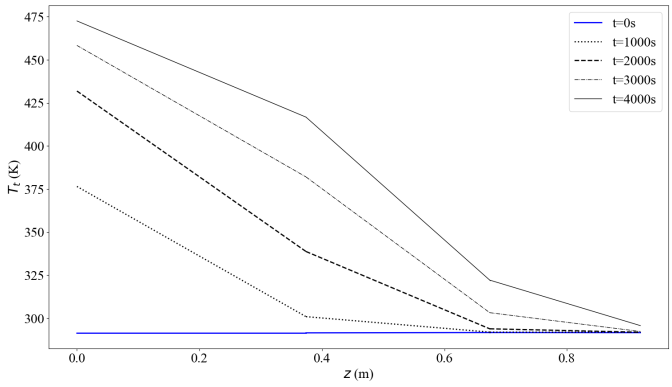

Figure 4.4 – Wall surface temperatures input in the simulation (qm=5.97$\times$$10^{-3}$ kg/s.)

The numerical model was implemented in the Porous material Analysis Toolbox based on OpenFOAM (PATO) [92], using a finite volume method. A multi-block approach was employed, where different sets of equations were solved in each region at each time step, incorporating appropriate

boundary conditions derived from the energy balances at the interfaces. A wedge-mesh for axisymmetrical simulations was generated using the *blockMesh* application of OpenFOAM. The mesh is refined at the near-tube region as shown in Fig.4.5. In the packed bed region, the pressure equation was solved semi-implicitly using first-order schemes in time (Euler) and space (Gauss linear). Similarly, the energy equations were solved with an implicit treatment of the temperature terms and an explicit treatment of other quantities. In the tube region, only the energy equation needed to be solved, with the temperature terms treated implicitly and other quantities treated explicitly. The equations are solved in series, with appropriate mesh refinement and time steps to guarantee that the order of convergence is reached.

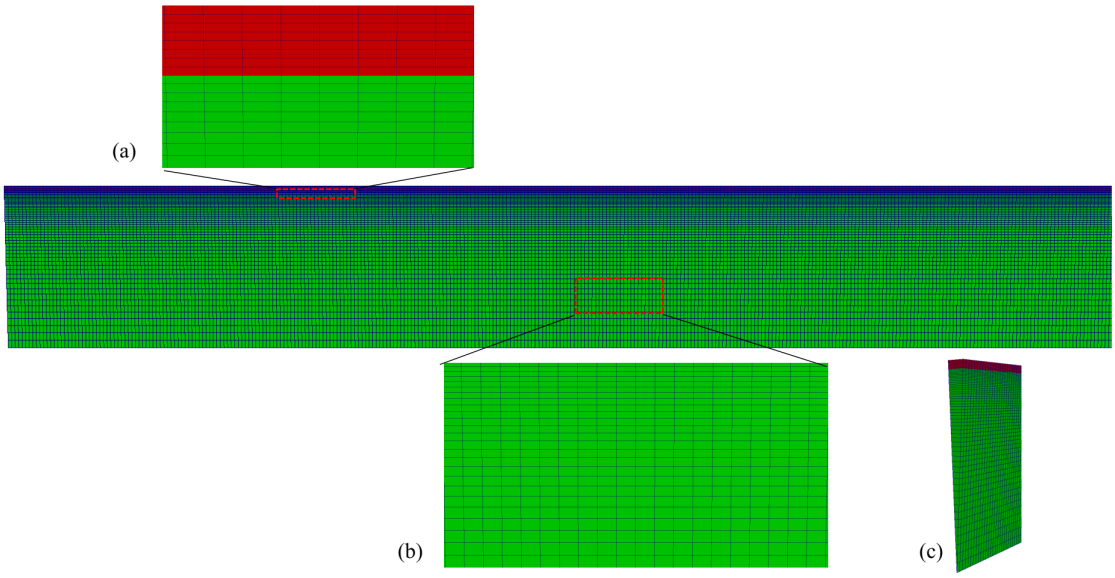

Figure 4.5 – PATO multi-block mesh. (a) Zoom at the interface. (b) Zoom at the packed bed region (c) Side view of wedge-mesh.

4.3.1.2 Physical properties of air and glass

This model takes into account the temperature-dependent properties of both the gas and solid phases. The density of air, ρ_g, is calculated using the perfect gas law, while the values for the heat capacity, $c_{p,g}$, dynamic viscosity, μ_g, and thermal conductivity, k_g, are obtained from the NASA-9 database [147]. The density of glass, ρ_s, is assumed to be constant at 2500 kg/m^3, while the heat capacity, $c_{p,s}$, and thermal conductivity, k_s, are determined by fitting experimental data from Pertermann et al. [148] as described in Eq.4.12.

$$\begin{cases} k_s = 0.59206 + 0.00062T_s + 1.0013 \times 10^{-6}T_s^2 - 2.778 \times 10^{-10}T_s^3 \\ c_{p,s} = 316.506 + 2.0745T_s - 0.00199T_s^2 + 7.4369 \times 10^{-7}T_s^3 \end{cases} \tag{4.12}$$

Table 4.5 provides the temperature-dependent properties for both the gas and solid phases used in the numerical model. The values for each property are given at specific temperatures, and linear interpo-

lation is employed between two adjacent values to estimate the property at intermediate temperatures.

Table 4.5 – Thermal properties of gas and solid as a function of temperature.

	gas			solid	
T(K)	$c_{p,g}$ ($\mathrm{J\,kg^{-1}\,K^{-1}}$)	μ_g ($\mathrm{kg\,m^{-1}\,s^{-1}}$)	k_g ($\mathrm{W\,m^{-1}\,K^{-1}}$)	$c_{p,s}$ ($\mathrm{J\,kg^{-1}\,K^{-1}}$)	k_s ($\mathrm{W\,m^{-1}\,K^{-1}}$)
273	1009.8	1.853e-05	0.02713	749.54	0.831
290	1010.4	1.909e-05	0.02798	768.75	0.850
340	1013	2.105e-05	0.03091	820.82	0.909
390	1017.5	2.306e-05	0.03401	866.73	0.971
440	1023.9	2.507e-05	0.03719	907.02	1.035
490	1032	2.710e-05	0.04049	942.27	1.105
540	1041.5	2.9135e-05	0.044	973.03	1.177
590	1055.7	3.1198e-05	0.0476	1000.48	1.249
640	1067.6	3.2993e-05.	0.0508	1024.03	1.326
690	1079.8	3.4712e-05	0.0541	1044.78	1.405
740	1092.06	3.6432e-05	0.0574	1063.27	1.486

As discussed in Section 4.1, the determination of three unknown effective parameters, namely the effective solid thermal conductivity $\mathbf{k_{s,eff}}$, effective gas thermal conductivity $\mathbf{k_{g,eff}}$, and volumetric heat transfer coefficient h_v, is required in the two-equation model (Eq.4.1 and 4.2). To facilitate the optimization algorithm, several dimensionless coefficients, including c_1, c_2, c_3, and f, are defined as presented in Eq.4.13.

$$\begin{cases} \mathbf{k_{s,eff}} = \mathbf{k_{s,con}} + \mathbf{k_{s,tor}} = c_1 \cdot k_s I \\ k_{g,eff,||} = k_{g,con} + k_{g,tor,||} + k_{dis,||} = \varepsilon_g k_g + 0 + c_2 \cdot Re \cdot Pr \cdot k_g = \varepsilon_g k_g + c_2 \cdot d_{par} \cdot \varepsilon_g \cdot |\langle v_g \rangle^g| \cdot \rho_g \cdot c_{p,g} \\ k_{g,eff,\perp} = k_{g,con} + k_{g,tor,\perp} + k_{dis,\perp} = \varepsilon_g k_g + 0 + c_3 \cdot Re \cdot Pr \cdot k_g = \varepsilon_g k_g + c_3 \cdot d_{par} \cdot \varepsilon_g \cdot |\langle v_g \rangle^g| \cdot \rho_g \cdot c_{p,g} \\ h_v = (6\varepsilon_s / d_{par}) \cdot (2 + f Re^{0.6} Pr^{1/3}) k_g / d_{par} \end{cases} \tag{4.13}$$

The effective gas thermal conductivity, $\mathbf{k_{g,eff}}$, is influenced by the tortuosity and dispersion terms, which have different values in the horizontal ($||$) and transverse ($\perp$) flow directions [30, 126]. Typically, the tortuosity term is neglected compared to the dispersion term [73]. The relationship between $\mathbf{k_{dis}}$ and the thermal properties of the gas is modeled similarly to the formulation proposed by Wakao et al. [126]. The volumetric heat transfer coefficient, h_v, is modeled using the functional form proposed by Wakao et al. [105]. The parameters c_1, c_2, c_3, and f will be optimized as described in section 4.3.2.

4.3.2 Optimization process and methods

A numerical inverse analysis method was employed to infer the intrinsic parameters from experimental measurements to minimize errors between measured and predicted data. We possess eleven data sequences $\{T1^i\}_{i=0}^n$, $\{T2^i\}_{i=0}^n$, $\{T3^i\}_{i=0}^n$, $\{T4^i\}_{i=0}^n$, $\{T5^i\}_{i=0}^n$, $\{T6^i\}_{i=0}^n$, $\{T7^i\}_{i=0}^n$, $\{T8^i\}_{i=0}^n$, $\{T9^i\}_{i=0}^n$, $\{T10^i\}_{i=0}^n$, $\{T11^i\}_{i=0}^n$ that correspond to the measured gas temperatures collected at every time step indicated by the index i (see Fig.4.1). The transient inlet gas temperature data $T1$ is fitted into a second-order polynomial using least squares, and it is used as a boundary condition. The objective function S for the optimization processes is defined as the average of the root mean squared relative error between measured and predicted temperatures on the ten positions already mentioned ($T2$, $T3$, $T4$, $T5$, $T6$, $T7$, $T8$, $T9$, $T10$, $T11$):

$$S = \frac{1}{10}\left(\sqrt{\frac{1}{n}\sum_{i=1}^{n}\left(\frac{T2^i_{num}-T2^i}{T2^i}\right)^2}+\sqrt{\frac{1}{n}\sum_{i=1}^{n}\left(\frac{T3^i_{num}-T3^i}{T3^i}\right)^2}+.....+\sqrt{\frac{1}{n}\sum_{i=1}^{n}\left(\frac{T11^i_{num}-T11^i}{T11^i}\right)^2}\right) \tag{4.14}$$

The minimization of S was performed using the Design Analysis Kit for Optimization and Terascale Applications (Dakota) [149]. The optimization process involved a combination of the Latin hypercube sampling (LHS) method [150] for sensitivity analysis and the Adaptive nonlinear least-squares algorithm (NL2SOL) [112] for local optimization. LHS was employed initially for sensitivity analysis to identify the most important input variables and their interactions. This stratified sampling technique divides the range of each uncertain variable into N_s segments of equal probability, resulting in a more accurate estimate of the mean value compared to random sampling. The next step involved local optimization using NL2SOL. This algorithm utilizes a quasi-Newton update to quickly converge to an optimal solution. By employing a simplification scheme to approximate the Hessian, NL2SOL achieves faster convergence compared to global optimization methods when performing least square calculations. An overview of this optimization strategy is presented in Fig.4.6, which will be further explained in the subsequent section through examples of applications to two-equation model optimizations.

4.4 Results and discussions

In this section, we present the results of both measured and predicted temperatures. In the first subsection, we determine the volumetric heat transfer coefficient h_v, the effective solid thermal conductivity $\mathbf{k_{s,eff}}$, and the effective gas thermal conductivity $\mathbf{k_{g,eff}}$ used in the two-equation model. Additionally, we provide the predicted fields of gas properties, pressure, velocity, temperature, and volumetric heat transfer coefficient using the two-equation model. In the second subsection, we focus on evaluating the validity of the obtained effective parameters.

Fig.4.7 presents a comparison of the measured and predicted results for four mass-flow rates. The relative errors, represented by the objective function S, are below 10^{-2} for all cases. Detailed data can be found in Table 4.7. A discussion of these results can be found in the following subsections. The measured results are represented by dots, while the predicted results obtained by solving the

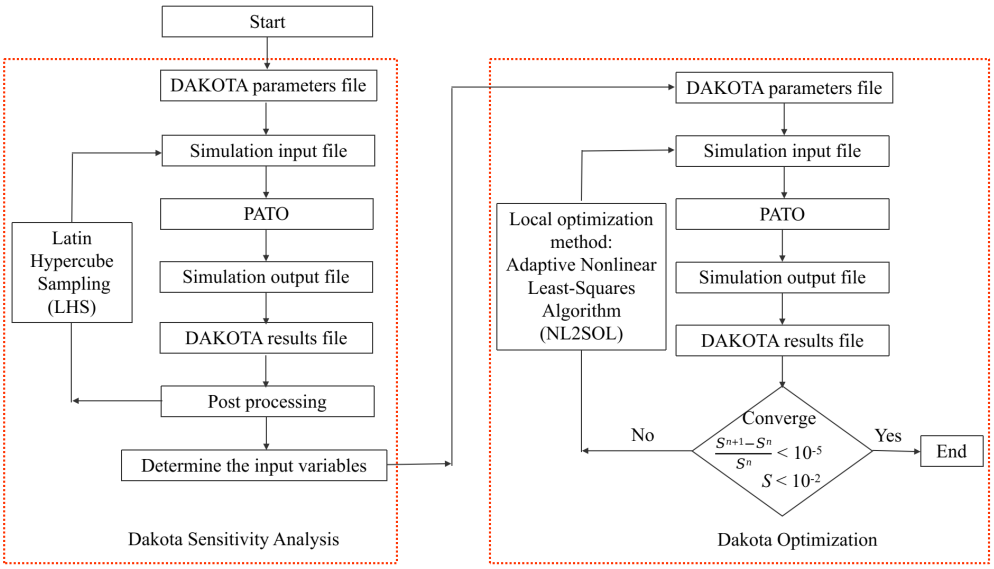

Figure 4.6 – The steps of sensitivity analysis and optimization process

Table 4.6 – Experimental parameters at room temperature.

case	inlet gas temperature $T1(K)$	mass-flow rate qm (kg/s)	magnitude Darcy velocity u	Reynolds number Re
case1	630	3.65×10^{-3}	0.10	101
case2	530	5.97×10^{-3}	0.16	165
case3	490	7.34×10^{-3}	0.20	203
case4	440	1.02×10^{-2}	0.28	282

two-equation model are shown as solid and dashed lines. The recorded inlet gas temperature ($T1$), and gas temperature at ten locations ($T2$ to $T11$) are plotted as a function of time. The presented temperature data represents the subset that was used in the optimization process. In the predicted results, gas temperatures at seven points along the central axis ($T2_{num}$ to $T8_{num}$) are shown as solid lines, and the other three points ($T9_{num}$ to $T11_{num}$)) with dashed lines.

The experimental parameters at room temperature are shown in Table 4.6. In the first case, the inlet gas temperature gradually increases from room temperature to 630 K, the inlet gas mass-flow rate is 3.65×10^{-3} kg/s, and the superficial gas velocity at room temperature is 0.10 m/s. The Reynolds number at room temperature is 101. The fluctuation in the inlet gas temperature might be caused by the tolerance of the thermocouple. Error bars indicate the uncertainty in the measured temperatures, as described in Section 4.2, where it was noted that the error due to the uncertain position of the thermocouples was estimated to be 1.19%. The major parameters that can affect the predicted temperatures are $\mathbf{k_{s,eff}}$, $\mathbf{k_{g,eff}}$, and h_v. In the following, we present the procedure for determining these parameters.

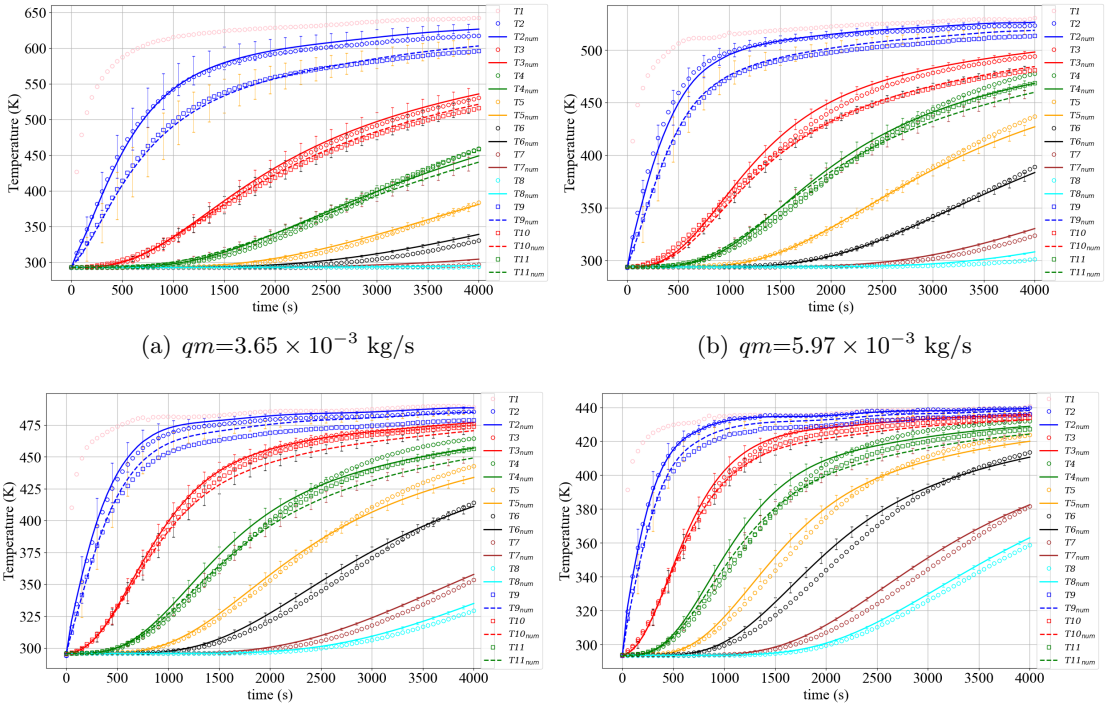

(a) qm=3.65 × 10^{-3} kg/s

(b) qm=5.97 × 10^{-3} kg/s

(c) qm=7.34 × 10^{-3} kg/s

(d) qm=1.02 × 10^{-2} kg/s

Figure 4.7 – Comparison of predicted and measured temperatures with different mass-flow rates.

4.4.1 Optimization and numerical results

In this subsection, we focus on determining the three effective parameters used in the two-equation model. Next, we present the numerical results, including the pressure, velocity, and temperature fields

throughout the whole test section.

4.4.1.1 Determination of three effective parameters used in the two-equation model

As discussed in Subsection 4.3.2, the estimation of these effective parameters involves two modules: sensitivity analysis and the optimization process. To begin, a sensitivity analysis is performed to understand the relationship between the output result (S) and the input variables (f, c_1, c_2, c_3). In this analysis, we use a high mass-flow rate case ($qm = 1.02 \times 10^{-2}$ kg/s) as an example to demonstrate the sensitivity analysis and optimization method. Additional case results are presented in Appendix 4.8.

During the sensitivity analysis, it is important to select appropriate minimum and maximum values for the parameters to be optimized. To determine these values, we refer to the correlations provided by Esence et al. [30] for packed beds. Based on their work, the coefficients f, c_1, c_2, and c_3 are estimated to be 1.1, 0.617, 0.1, and 0.001, respectively, for Reynolds numbers less than 8000. In order to assess the sensitivity of the model to these parameters, we employ the Latin hypercube sampling (LHS) method. The ranges for f, c_1, c_2, and c_3 are defined as follows: f ranges from 0.7 to 2.5, c_1 ranges from 0.4 to 1.8, c_2 ranges from 0.01 to 0.5, and c_3 ranges from 0 to 0.01. The LHS method ensures that the input variables are evenly distributed within these minimum and maximum boundaries.

Fig.4.8 presents a typical result of the sensitivity analysis. The red line represents the strength and direction of the relationship between the independent variables (f, c_1, c_2, and c_3) and the dependent variable (S). The slope of the red line corresponds to the partial correlation coefficient (PCC), which quantifies the linear relationship between two variables (x: f or c_1 or c_2) and y (S) while accounting for the influence of one or more additional variables [149, 151]. The PCC is calculated using the following formula:

$$\mathrm{Corr}(x,y) = \frac{\sum_i (x_i - \bar{x})(y_i - \bar{y})}{\sqrt{\sum_i (x_i - \bar{x})^2 \sum_i (y_i - \bar{y})^2}} \quad \hat{x}_i = c_0 + \sum_{p=1, p\neq i}^{n} c_p x_p, \quad \hat{y} = b_0 + \sum_{p=1, p\neq i}^{n} b_p x_p \tag{4.15}$$

where $\bar{x}$ and $\bar{y}$ are the mean values of x and y, x_i and y_i denote individual values (samples) of the two variables. $\hat{x}_i$ and $\hat{y}$ are the regression equations, where b and c represent real number coefficients, and x_p represents the other variables except for x_i. PCC can help to identify which variables have the strongest impact on the output results and should be prioritized in the optimization process. In this case, the PCC between the input variables (f, c_1, c_2, and c_3) and the output variable (S) are -0.14, -0.85, -0.22, and -0.05, respectively. A coefficient closer to ± 1 indicates a strong correlation between the input and output variables. The results show a very low correlation between c_3 and S. Therefore, we shifted our focus to the effects of the other three variables, f, c_1, and c_2, on the output result S.

During the optimization process, the boundary values for the three variables (f, c_1, c_2) were set the same as in the sensitivity analysis: f ranging from 0.7 to 2.5, c_1 ranging from 0.4 to 1.8, and c_2 ranging from 0.01 to 0.5. Convergence ($S < 0.01$) was reached after 50 iterations of the local optimization algorithm NL2SOL. Fig.4.9 shows the influence of the three variables (f, c_1, c_2) on the error S. The size of the points in Fig.4.9 (a) represents the value of S, while the grey scale indicates the value of f.

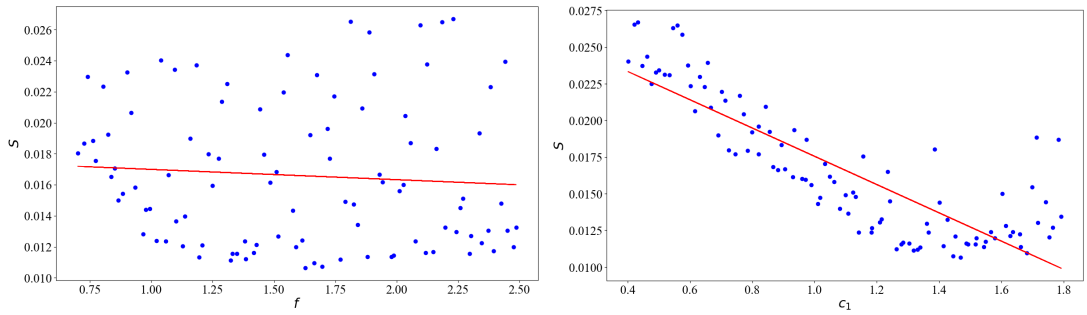

(a) S vs. f

(b) S vs.c_1

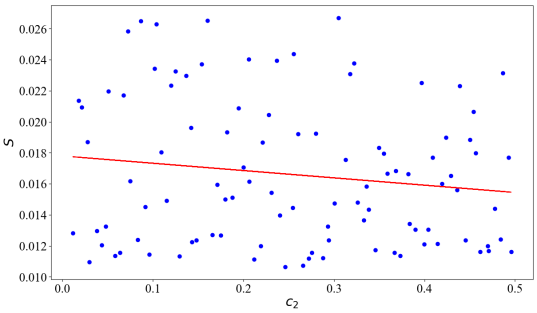

(c) S vs.c_2

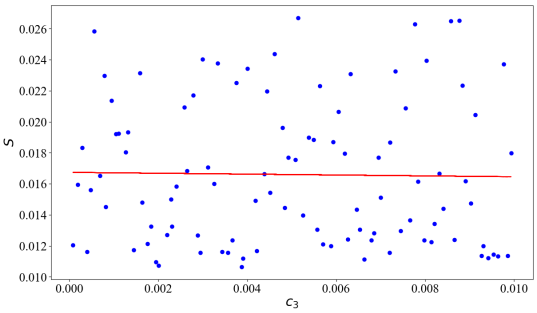

(d) S vs.c_3

Figure 4.8 – Sensitivity analysis of the error S to input parameters (f, c_1, c_2, c_3), qm= 1.02×10^{-2} kg/s.

As shown in Fig.4.9 (a), when S is below 0.01, the values of c_1 are concentrated around 1.29 and c_2 are concentrated around 0.35, while the values of f range from 1.0 to 2.0. To further analyze the behavior of the error when varying f, we set c_1 to 1.29 and c_2 to 0.35 and only varied f as the input parameter. As shown in Fig. 4.9 (b), S displays a decreasing and then increasing behavior. The minimum error S is reached when the value of f is 1.34 with an uncertainty of 5%. With the convergence of the error S to the level of 10^{-2}, we have determined the values of c_1, c_2, and f to be 1.29, 0.35, and 1.34, respectively. Consequently, the corresponding values of h_v, $k_{s,eff}$, and $k_{g,eff,||}$ are established as well and summarized in Table 4.7.

As shown in Table 4.7, when considering the two-equation model coupled with the mass and momentum equations (Eq.4.7) and accounting for the temperature dependency of the gas and solid thermal properties, some coefficients exhibit different values compared to their original correlations. The coefficient c_1, which is related to the solid phase volume fraction ε_s, is found to increase from 0.617 to 1.22. This value remains relatively constant across different inlet velocities. On the other hand, the coefficient c_2, associated with gas dispersion, shows an increasing trend with higher inlet velocities and is not a constant value. This is in line with the fact that the dispersion effect increases with the gas velocity. Lastly, the coefficient f increases from 1.1 to around 1.5 compared to the original Wakao correlation.

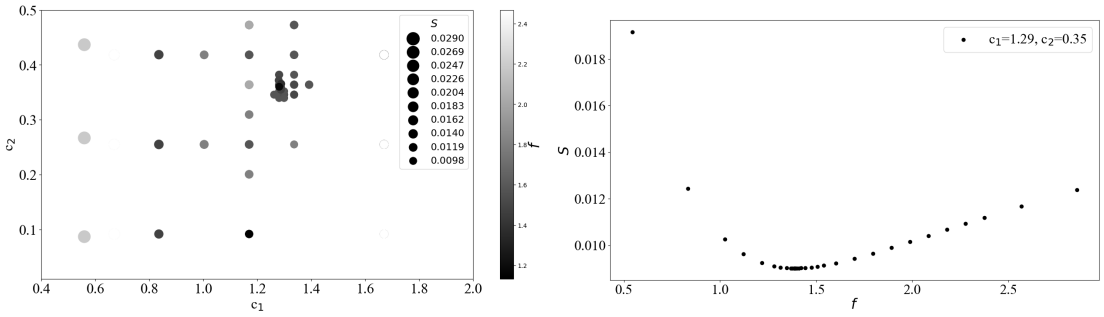

(a) Three variables (c_1, c_2, f) (b) One variable (f)

Figure 4.9 – The influence of three variables (c_1, c_2, f)on the error S.

Now let's revisit the comparison between the best-predicted temperature values and the measured values in Fig.4.7. The solid and dashed lines represent the predicted temperature curves obtained by minimizing the error S. Taking Fig. 4.7 (d) as an example, the value of the error S is 9.82×10^{-3}, which is the average error across ten different locations ($T2$ to $T11$). The maximum error among these locations is 1.48×10^{-2}. For reference, the maximum temperature difference between the predicted and measured values is approximately 6.5 K. This indicates that the numerical model can accurately capture the transient temperature profiles in a packed bed with a high level of accuracy. To illustrate further the overall behavior of the packed bed, the upcoming subsection will present color maps of the simulation results.

Table 4.7 – The value of f, c_1 and c_2 obtained in the optimization process for different mass-flow rates.

qm (kg/s)	3.65×10^{-3}	5.97×10^{-3}	7.34×10^{-3}	1.02×10^{-2}
Re	58∼100	100∼151	150∼190	223∼252
c_1	1.22 ± 0.03	1.23 ± 0.03	1.25 ± 0.03	1.29 ± 0.03
c_2	0.069 ± 0.004	0.15 ± 0.008	0.24 ± 0.02	0.35 ± 0.03
f	1.61 ± 0.09	1.59 ± 0.07	1.65 ± 0.07	1.34 ± 0.09
$k_{s,eff}$ (W/(m · K))	1.1∼1.6	1.1∼1.5	1.1∼1.4	1.2∼1.4
$k_{g,eff,\|\|}$ (W/(m · K))	0.083∼0.094	0.29∼0.31	0.98∼1.08	2.14∼2.22
h_v (W/(m^3·K))	1.0×10^4∼1.3×10^4	1.15×10^4∼1.45×10^4	1.54×10^4∼1.83×10^4	1.72×10^4∼1.97×10^4
S	9.71×10^{-3}	9.99×10^{-3}	9.88×10^{-3}	9.82×10^{-3}

4.4.1.2 Color maps of the simulation results in the full domain

In this subsection, we present a simulation result using the experimental conditions from case 1 at 4000 s. The inlet gas temperature T_g gradually increases from 292 K to 630 K within 4000 s. The inlet mass-flow rate qm is 3.56×10^{-3} kg/s, resulting in a Darcy velocity u of 0.1 m/s at room temperature. The values of c_1, c_2, c_3, and f are set to 1.22, 0.069, 0, and 1.61, respectively. These values were obtained from the optimization process in the previous subsubsection.

Fig.4.10 shows the distribution of dynamic viscosity μ_g and air density ρ_g within the packed bed region at 4000 s. The thermodynamic properties of air are updated based on the pressure and gas temperature using a linear interpolation method, utilizing the data provided in Table 4.5. The coupling between air density and temperature is accounted for in the mass equation in Eq.4.7. At the inlet of the packed bed, the air temperature is 630 K, accompanied by a dynamic viscosity of 3.3e-5 Pa·s and a density of 0.56 kg/m^3. At the outlet, the air temperature remains at room temperature, resulting in a dynamic viscosity of 1.9e-5 Pa·s and a density of 1.20 kg/m^3. The dynamic viscosity of air increases by 74% over the modeled temperature range of 290 K to 630 K, while the air density experiences a decrease of 53%.

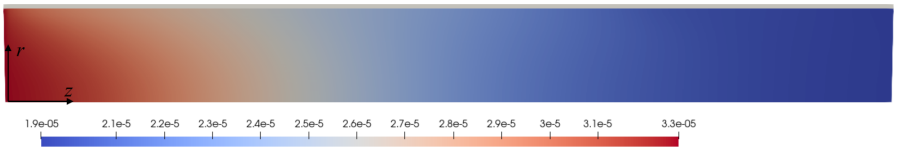

(a) dynamic viscosity μ_g (Pa·s)

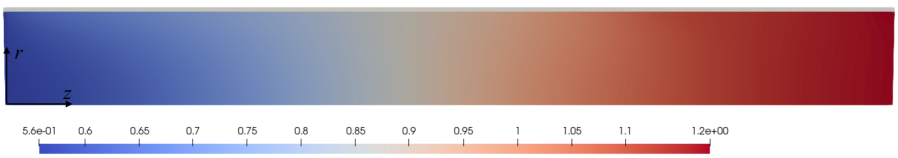

(b) air density ρ_g (kg/m^3)

Figure 4.10 – Dynamic viscosity and air density distribution predicted with the two-equation model.

Fig.4.11 presents the pressure p and Darcy velocity magnitude u fields within the packed bed region at 4000 s.The pressure at the inlet is 101358 Pa, while at the outlet, it is 101325 Pa. The significant pressure gradient observed in the packed bed region can be attributed to the inclusion of the Forchheimer equation in the model. The Darcy velocity magnitude u is 0.22 m/s at the inlet and 0.1 m/s at the outlet. The velocity is updated based on the pressure and gas temperature. Inside the packed bed, the gas velocity $\langle \mathbf{v_g} \rangle^{\mathbf{g}}$ is determined by dividing the Darcy velocity $\mathbf{u}$ by the porosity ε_g.

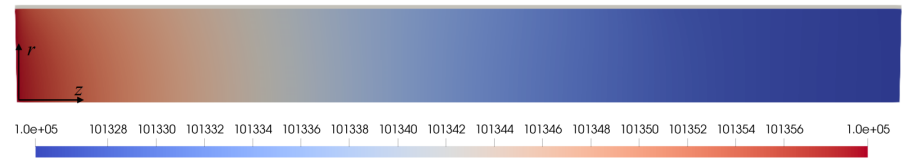

(a) pressure p (Pa)

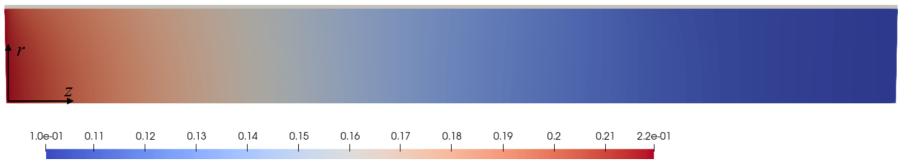

(b) velocity magnitude u (m/s)

Figure 4.11 – Pressure and velocity magnitude predicted with the two-equation model.

Fig.4.12 shows the temperature fields in the packed bed region at 4000 s. The gas temperature T_g at the inlet is 630 K, while at the outlet, it is 300 K. The temperature of the gas and solid phases is updated by solving the energy equations in Eq.4.7. In the packed bed region, the difference between the local average gas and solid temperatures ($dT = T_g - T_s$) is around 5 K. The distribution of dT is influenced by the heat transfer coefficients h_v. It is worth noting that in Fig. 4.12 (b) there is a significant temperature difference in the upper left region. This is primarily due to the strong coupling between the solid temperature inside the packed bed and the solid temperature at the wall surface, which is much lower than the gas temperature inside the packed bed.

Fig.4.13 shows the distribution of the volumetric heat transfer coefficients, h_v, within the packed bed region at 4000 s. It is worth noting that h_v is a function of space and time within the packed bed, as described by Eq. 4.13. The value of h_v at the inlet is 13400 (W/m^3· K) and at the outlet is 11400 (W/m^3· K). Throughout the modeled temperature range of 290–630 K, h_v experiences a decrease of 15 %, and its calculation incorporates the Wakao correlation with the factor f. The distribution of h_v aligns with the distribution of gas velocity, meaning that higher gas velocities correspond to higher h_v values. To further investigate the transient distribution of h_v within the packed bed, we plotted the values of h_v along the central axis at different times for four mass-flow rates. h_v is a function of the air density, viscosity, velocity, heat capacity, and thermal conductivity. Fig.4.14 demonstrates that as the transient temperature increases, the heat transfer coefficient gradually increases as well.

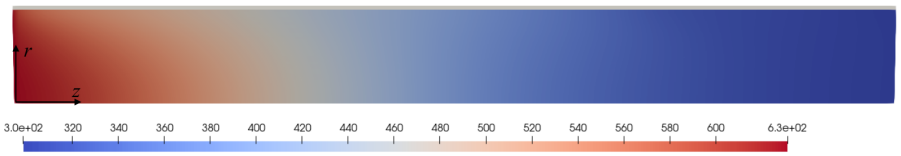

(a) gas temperature T_g (K)

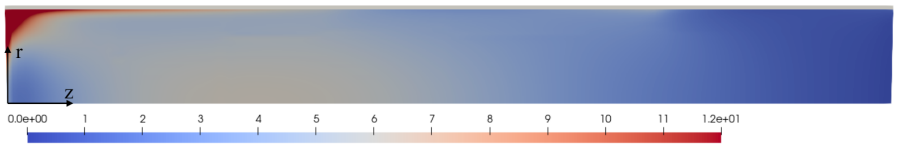

(b) temperature difference between gas and solid $T_g - T_s$ (K)

Figure 4.12 – Gas temperature and temperature difference in the porous materials region predicted with the two-equation model.

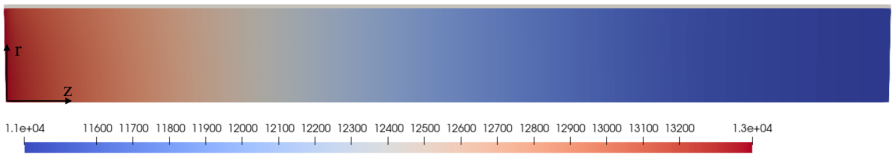

Figure 4.13 – Volumetric heat transfer coefficient h_v (W/m^3· K) distribution predicted with the two-equation model.

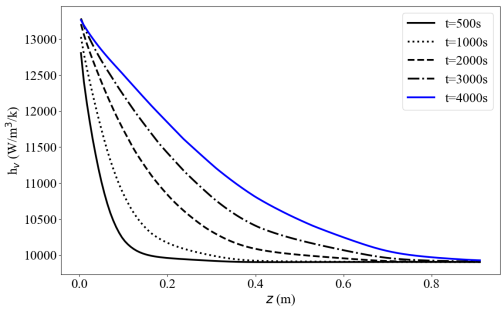

(a) qm=3.65 × 10^{-3} kg/s

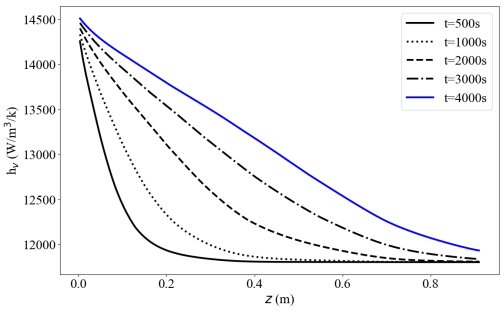

(b) qm=5.97 × 10^{-3} kg/s

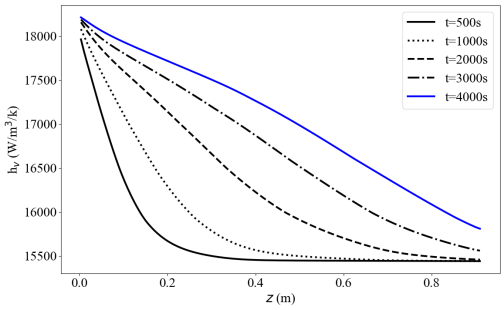

(c) qm=7.34 × 10^{-3} kg/s

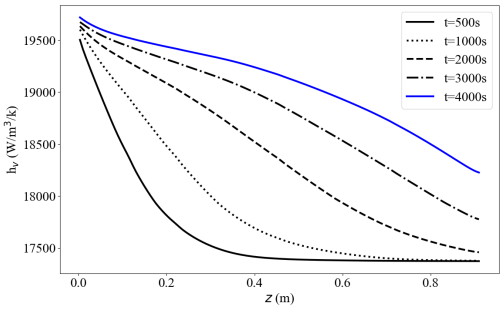

(d) qm=1.02 × 10^{-2} kg/s

Figure 4.14 – The distribution of h_v along the central axis with different mass flow rates.

4.4.2 Comparing the heat transfer coefficient and the effective gas thermal conductivity

Heat and mass transfer in packed beds with randomized packing of particles at high temperatures is a complex phenomenon. In this study, a new correlation is developed based on the numerical inverse analysis method, taking the glass bead diameter d_{par} as the characteristic length. The dimensionless heat transfer correlation is given by:

$$Nu = 2 + 1.54 Re(T)^{0.6} Pr(T)^{1/3} \tag{4.16}$$

where the value of f (1.54) is obtained as the average of the four f values listed in Table 4.7. $Re(T)$ and $Pr(T)$ indicate that the Reynolds number (Re) and Prandtl number (Pr) are functions of temperature.

Fig.4.15 (a) presents a comparison between heat transfer correlations reported in the work of Wakao [105] and the results obtained from the inverse analysis in this study. The correlation proposed by Wakao et al is based on a large amount of experimental data. It is obvious that the Nusselt numbers increase with increasing Reynolds numbers. As presented in Fig.4.15 (a), for lower Reynolds number values ($Re = 58 \sim 252$), the data from Wilke and Hougen [152], Malling and Thodos [153], and De Acetis and Thodos [154] are slightly above the solid blue line (Nu = 2+1.1 $Re^{0.6}Pr^{1/3}$). The reason for the Galloway [155] data being lower than predicted for all correlations is due to unique aspects of his study. Galloway investigated water evaporation into air from 17 mm porous spheres, arranged differently, and with solid particles maintaining constant surface temperatures. The newly proposed correlation (Nu = 2+1.54 $Re(T)^{0.6}Pr(T)^{1/3}$) demonstrates better suitability for the low Reynolds number range ($Re = 58 \sim 252$). It should be noted that the Reynolds number (Re) varies within the packed bed during each test, and thus the red dots in Fig. 4.15 (a) represent the average values of Re.

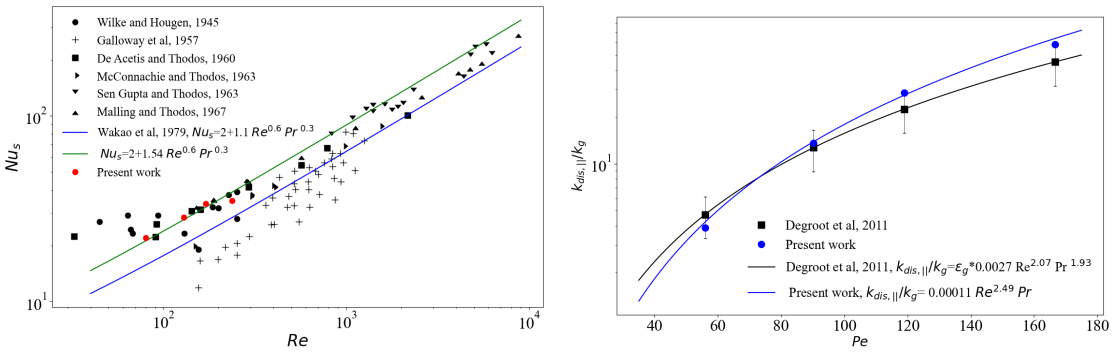

(a) Nusselt number vs. Reynolds number

(b) dispersion gas thermal conductivity vs. Peclet number

Figure 4.15 – Comparison between the experimental data and data obtained using the numerical inverse analysis.

The axial gas effective thermal conductivity, $k_{g,eff,||}$, is expressed by Eq.4.13, which is a function of both Reynolds number (Re) and Prandtl number (Pr). Table 4.7 demonstrates that the value of the factor c_2 is not constant but increases with increasing Re. To account for the dispersion effect resulting

from the gas flow, a new correlation is developed based on the inverse analysis results obtained in this study. A previous work by DeGroot et al. [73] suggests that the commonly used characterization of dispersion based solely on the Peclet number ($Pe = Re \cdot Pr$) is not entirely accurate. In this study, we adopted a proposed function of the form $n_1 Re^{n_2} Pr$ to account for the dispersion effect caused by the gas flow. A least-squares analysis reveals that a suitable function for the dimensionless axial dispersion conductivity can be expressed as:

$$k_{dis,||}/k_g = 0.00011 Re(T)^{2.49} Pr(T) \tag{4.17}$$

Fig. 4.15 (b) presents a comparison between the dimensionless axial dispersion conductivity $k_{dis,||}/k_g$ obtained in this study and the results of DeGroot et al. [73]. The error bars indicate that the maximum difference between the two is within 30%. It is observed that the dispersion gas thermal conductivity increases with the Peclet number, as expected from the theory presented in the introduction. In this study, the axial dispersion gas thermal conductivity is about 4 times and 58 times higher than the gas thermal conductivity when the Peclet numbers are around 55 and 165, respectively.

4.5 Conclusions

The objective of this work was to develop and validate a generic two-equation model coupled with mass and momentum conservation for high-temperature TES and determine the effective conductivities and the heat transfer coefficients needed to inform the two-equation model. Packed beds undergoes a transient heat storage process, resulting in a broad range of temperatures for high-temperature systems. As a consequence, the thermophysical properties of both the fluid and solid exhibit significant variations. In this work, we developed a novel packed bed TES device, based on the transient single blow technique, to investigate the effective thermal conductivity of the gas and solid phases, and the heat transfer coefficient under high-temperature operating conditions. Experiments were conducted by passing hot air through cold particles at four different mass flow rates, within a Reynolds number range of 58 to 252. Gas temperature was measured at ten points, including seven axial positions and three radial positions. Unknown parameters are simultaneously determined using numerical inverse analysis, consisting in detailed simulations and state-of-the-art multi-objective optimization. Flow inside packed beds is considered compressible and laminar; its thermal expansion is directly implemented in the mass equation by using the perfect gas law. The velocity field is modeled by the Forchheimer equation based on the Reynolds number. Heat transfer equations are described using the two-equation model in both phases inside packed beds. The variable gas and solid thermophysical properties are used over a wider range of temperatures (293K to 630K). The numerical model was implemented in finite volumes in the Porous Material Analysis Toolbox based on Open-FOAM (PATO). The optimization part, which included sensitivity analysis using the Latin Hypercube Sampling (LHS) method and the optimization process using a local optimization method (NL2SOL), was performed using the open-source optimization software Dakota. The results indicate that the value of heat transfer coefficient h_v in the two-equation model falls in the range of $1.0\times 10^4 \sim 2.0\times 10^4$ W/(m$^3 \cdot$ K) under the given conditions. It was observed that the gas and solid temperatures exhibit local thermal non-equilibrium within the packed bed. A new correlation has been proposed based on the Wakao correlation [105]

as follows: $Nu = 2 + 1.54Re(T)^{0.6}Pr(T)^{1/3}$. This correlation that accounts for the first time for the temperature variations of the dimensionless numbers was validated in the Reynolds number range of $Re = 58$ to 252. It was observed in this study that the dispersion gas thermal conductivity increased with increasing Peclet number. Specifically, the axial dispersion gas thermal conductivity was found to be around 4 and 58 times higher than the gas thermal conductivity at Peclet numbers of around 55 and 165, respectively. Results for the axial dispersion gas thermal conductivity have been fitted to a new correlation: $k_{dis,||}/k_g = 0.00011Re(T)^{2.49}Pr(T)$. The detailed high-temperature heat and mass transfer model proposed in this work was therefore validated for a large range of conditions, and new correlations were obtained to account for high-temperature effects for glass beads and air. This open perspectives towards more accurate sizing and monitoring models for high-temperature TES systems.

4.6 Appendix. Validation of Ergun equation

To capture the pressure drop across the packed bed, a differential pressure transmitter from EMERSON FISHER ROSEMOUNT was used, which has an uncertainty of ±0.055% F.S. (Full Span is 0-620 mbar). The transmitter's electrical signals were relayed to a data acquisition system for real-time observation and subsequent analysis.

The pressure drop and superficial velocity were measured for the ten mass-flow rates (qm) considered in this work. Fig. 4.16 compares measured results (represented by dots) with calculated results using Ergun's equation (shown as solid lines). Ergun's equation is found to accurately predict the pressure drops across the packed beds, with an R^2 value of 0.998.

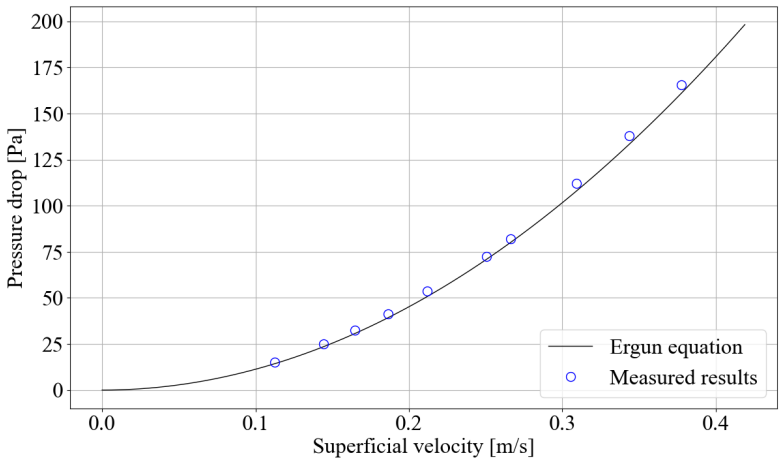

Figure 4.16 – The comparison of measured and calculated pressure drop as a function of superficial velocity for the packed bed.

4.7 Appendix. Temperature boundary condition at the interface

As shown in Fig .4.17, the thermal exchange between the gas and the tube surface can be expressed as:

$$\Phi_t = h_t(T_g - T_t) \cdot S_t \tag{4.18}$$

where h_t represents the heat transfer coefficient between the gas and the tube, and S_t is the surface area of contact between the gas and the tube.

Thermal exchange between the gas and the glass bead can be expressed as:

$$\Phi_\mathrm{s} = h_s(T_g - T_s) \cdot S_\mathrm{s} \tag{4.19}$$

where h_s represents the heat transfer coefficient between the gas and the glass bead and S_s is the surface area of contact between the gas and the glass bead.

Given that the glass beads are in contact with the tube surface, our boundary condition is set as $T_s = T_t$. Therefore, the ratio between the two can be calculated as:

$$\frac{\Phi_t}{\Phi_s} = \frac{h_t(T_g - T_t) \cdot S_t}{h_s(T_g - T_s) \cdot S_s} = \frac{h_t \cdot S_t}{h_s \cdot S_s} = 0.035 \tag{4.20}$$

where:

$$\frac{h_t}{h_s} = \frac{Nu_t}{Nu_s} = \frac{0.12Re^{0.75}Pr^{1/3}}{2 + 1.54Re^{0.6}Pr^{1/3}} = 0.14 \qquad \frac{S_t}{S_s} = \frac{\pi r_{par}^2}{4\pi r_{par}^2} = 0.25 \tag{4.21}$$

where the expressions for Nu_t are obtained from the work of Esence et al. [30], the formula for Nu_s is based on our own work. For quantitative analysis, we set $Pr = 0.69$ and $Re = 100$.

Hence, the thermal exchange between the gas and the tube (Φ_t) is significantly smaller than the thermal exchange with the glass bead (Φ_s), and can thus be neglected. This is why we established this boundary condition $\partial T_g/\partial r = 0$.

4.8 Appendix.Optimization results at different mass flow rates

In section 4.4.1.1, the determination of the effective thermal conductivity of gas and solid, as well as the heat transfer coefficient, was described using a case with a high mass-flow rate (qm=1.02×10^{-2} kg/s). A sensitivity analysis was conducted, revealing that the coefficient c_3, which is related to $k_{g,eff,\perp}$, had minimal impact on the output results, even at high flow rates. Next, an optimization process was performed to obtain the values of c_1, c_2, and f. In this appendix, we present the optimization results for three additional cases. The results are shown in Fig. 4.18, and the optimization process was conducted using the adaptive nonlinear least-squares algorithm (NL2SOL) in the Dakota software.

In the left side of Fig. 4.18, we can observe the effects of three variables, c_1, c_2, and f, on the error S. On the right side, the impact of a single variable, f, on the error S is presented. The optimization process initially involves determining the values of c_1 and c_2 by including all three

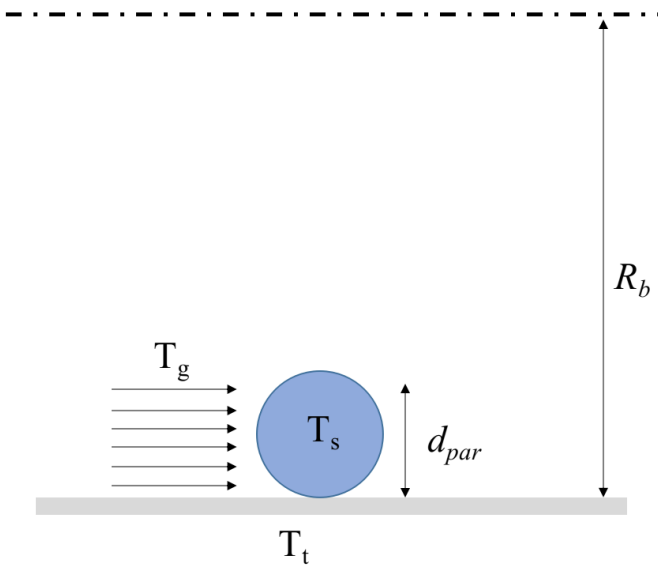

Figure 4.17 – Schematic diagram of thermal exchange at the tube surface.

variables. Then, the values of c_1 and c_2 are fixed, and the value of f is determined by introducing a single variable. Convergence ($S < 0.01$) usually takes 50 iterations with three variables, but only 25 with a single variable (f). Fig.4.18 (a) shows that the values of c_1 are concentrated around 1.22 and c_2 are concentrated around 0.069 when S is below 0.01, and the values of f range from 1.0 to 2.0. To further analyze the effect of f on the error, we fixed c_1 to 1.22 and c_2 to 0.069 and only varied f as the input parameter in the software. As shown in Fig.4.18 (b), the minimum value of the error S is achieved when the value of f is 1.61 with an uncertainty of 5%. Similarly, in the second case, the values of c_1, c_2, and f are 1.23, 0.15, and 1.59, respectively. In the third case, the values of c_1, c_2, and f are 1.25, 0.24, and 1.65, respectively. All the optimization results are summarized in Table 4.7.

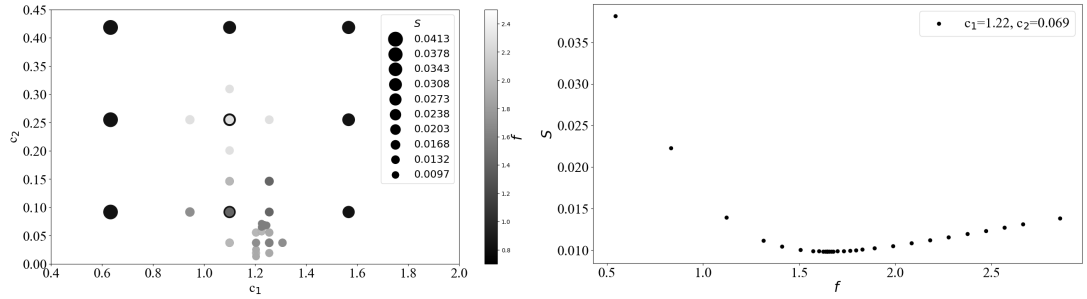

(a) qm=3.65 × 10^{-3} kg/s (b) qm=3.65 × 10^{-3} kg/s

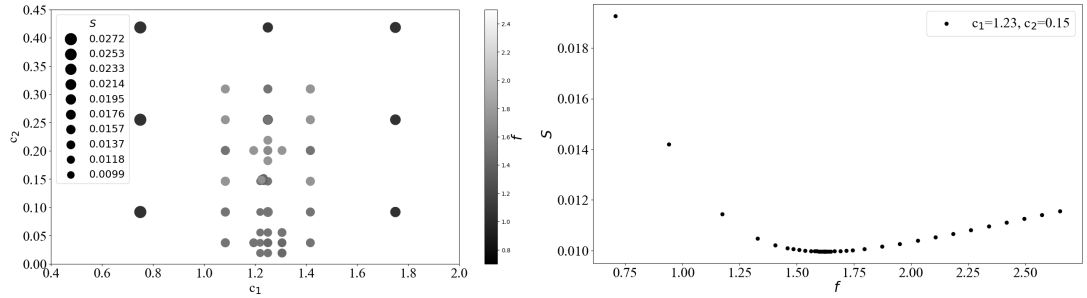

(c) qm=5.97 × 10^{-3} kg/s (d) qm=5.97 × 10^{-3} kg/s

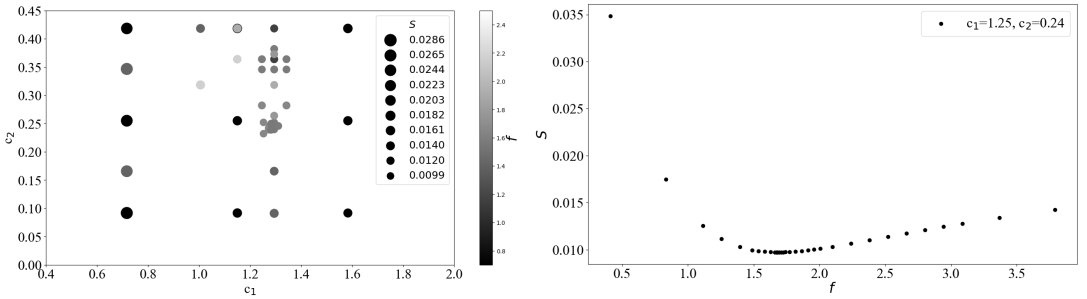

(e) qm=7.34 × 10^{-3} kg/s (f) qm=7.34 × 10^{-3} kg/s

Figure 4.18 – The influence of three variables (f,c_1,c_2) on the error S.

Chapter 5

Detailed local thermal non-equilibrium model for biomass packed beds applied to wood chips and pellets of various moisture contents

Preamble

Authors: S.Liu; A.Ahmadi-Senichault; C.Levet; J. Lachaud;
Affiliations: Arts et Métiers Institute of Technology, Univ. Bordeaux, CNRS, Bordeaux INP, I2M, UMR 5295, F-33400 Talence, France;
Published: No;
Conference: No;

Abstract

The aim of this study was to develop a detailed local thermal non-equilibrium (LTNE) model to describe heat and mass transfer within biomass packed beds when considering the drying process. To determine the effective parameters, namely, the volumetric heat transfer coefficient and the effective (solid and gas) thermal conductivities, a novel experimental facility was designed based on the transient single-blow technique. The study was carried out on wood pellets and wood chips. The numerical model was implemented using finite volumes in the Porous Material Analysis Toolbox based on OpenFOAM (PATO). Parameter identification was performed with the open-source optimization software Dakota, and a local optimization method, NL2SOL, was employed. Results revealed that the volumetric heat transfer coefficient increased significantly as moisture content decreased from 6.2% to 0 for wood pellets (13429-13850 to 16333-16450 W/(m^{3}K)) and from 9.1% to 0 for wood chips (12340-12570 to $13924 - 13950$W/(m^{3}K)). The consistency of the results for different moisture contents and both materials brings confidence in the model. This study contributes to a better understanding of heat

and mass transfer phenomena in biomass packed beds and will be useful to inform the development of more accurate models for industrial applications.

Keywords: Biomass packed beds; Inverse analysis; Pressure drop; Wood drying; Variable thermophysical properties

5.1 Introduction

Wood by-products constitute a renewable and clean energy source [156, 51]. Processed into chips or compressed pellets [45] they are used as combustible for residential heating, industrial boilers, and power plants, providing sustainable heat sources [157], or converted in biochar and biofuels by pyrolysis and gasification [55, 49, 48]. For these applications, the most common reactors are packed bed and fluidized bed [158], the latter being typically used in large scale system and the former being rather used for small scale systems [55, 159].

In a packed bed reactor, the bed may be seen as a porous medium composed of a solid wood matrix and pores filled with gas [160]. Heat transfer in a wood bed can either be studied under the assumption of local thermal equilibrium (LTE) or local thermal non-equilibrium (LTNE) [51, 55, 77]. In LTE models, it is assumed that the average temperatures of the solid and gas phases are equal [57]. In LTNE models, the temperature difference between the two phases is evaluated by considering two energy conservation equations - one for the solid phase and one for the gas phase - that are coupled through a heat exchange term [58, 161]. Guo et al. [45] used the LTE model to study the effective thermal conductivity and specific heat capacity of wood pellets in a packed bed. They found the ratio of evaporation heat loss to total energy change to be 0.0073 at a maximum temperature of 55°C, so they neglect the evaporation heat loss in the energy equation. Bennamoun et al. [162] included the latent heat of vaporization into the solid phase energy equation in the LTNE model, along with drying kinetic to complete calculations. Souza et al. [159] applied an LTNE model for their research on simultaneous heat and mass transfer in a packed bed dryer, incorporating additional constitutive equations for drying kinetics, and equilibrium sorption. In these works, the impact of the drying process on the thermodynamic properties of the gas phase, i.e., gas thermal conductivity, gas density, and gas dynamic viscosity, has not been addressed. For high-temperature applications at the particle scale, detailed LTE model that account for the temperature dependency of the thermodynamic properties have been developed [77]. They consists of models of drying and pyrolysis, and of conservation of gas mass, solid mass, species, momentum and energy. The aim of this study is to expand such models to LTNE conditions. To feed this detailed model, several effective parameters, namely, the permeability, K, the Forchheimer coefficient, β, the volumetric heat transfer coefficient, h_v, the effective (solid and gas) thermal conductivities, $\mathbf{k_{s,eff}}$ and $\mathbf{k_{g,eff}}$, need to be determined. [30]. However, in complex geometries, like packed beds of wood chips or pellets, obtaining accurate values for these parameters becomes challenging due to factors including geometric configurations [163], anisotropic fuel shapes [164], moisture content [51], and fuel pore structure.

To introduce the studied effective parameters, let us start by discussing the permeability, K, and the Forchheimer coefficient, β, which are used in momentum conservation to describe the pressure drop for single-phase fluid flow in a biomass-packed bed. The primary factors influencing the pressure drop include the physical properties of gas, such as density and dynamic viscosity, the physical properties of biomass particles, such as particle shape and size, the orientation of particles within the packed bed, and the porosity of the packed bed. The relationship between pressure drop and these factors using a single formula is not easy to describe. The Ergun equation [165] serves as a reference for calculating the pressure drop through packed beds. In this equation, parameters such as permeability and the Forchheimer coefficient are expressed in forms related to packed bed porosity and the equivalent diameter of bed particles. Some available values from the literature are summarized in Table 5.1. As shown in the table, for common types of biomass like wood pellets and wood chips, the data are not constant. The pressure drop is affected by numerous factors. Consequently, it is essential to measure the pressure drop experimentally.

Table 5.1 – Some available values for the permeability $\mathbf{K}$ and the Forchheimer coefficient β

Investigators	Gas velocity u ($\mathrm{m \cdot s^{-1}}$)	permeability K ($\mathrm{m^2}$)	Forchheimer coefficient β ($\mathrm{m^{-1}}$)	Porosity ε_g	Remarks
Yazdanpanah et al. [164]	0.014 to 0.8	5.36×10^{-8}	2.77×10^{3}	0.29	wood pellet, mixed sizes Forchheimer's law
	0.014 to 0.8	6.37×10^{-8}	2.25×10^{3}	0.33	wood pellet, mixed sizes Forchheimer's law
Pozzobon [166]	0.005 to 0.05	1.83×10^{-8} to 1.19×10^{-8}		0.44	wood chips, Darcy's law and Forchheimer's law
Mayerhofer [160]	0.05 to 0.8	7.80×10^{-8} to 1.30×10^{-7}	5.7×10^{2} to 6.44×10^{3}	0.5	wood chips, mixed sizes Forchheimer's law

Numerous heat transfer correlations for packed beds have been documented in the literature, as reviewed by Esence et al. [30]. Researchers frequently employ correlations that associate Nusselt, Reynolds, and Prandtl numbers with diverse wood particle geometries to model biomass drying [167]. Among these correlations, Wakao's correlation [105], expressed as $Nu = 2 + 1.1Re^{0.6}Pr^{0.3}$, is the most renowned. However, this correlation neglects the influence of particle shape on the heat transfer process. Additionally, the experimental results from Tremblay et al. [168] implied that the heat transfer coefficient is a function of both velocity and moisture content during biomass drying. Pedrazzi et al. [46] estimated a heat transfer coefficient of 110 $\mathrm{W/(m^2\,K)}$ for an inert packed bed of wood pellets during the pyrolysis process. Sassanis et al. [163] conducted pore-scale numerical simulations to study the heat transfer coefficient within a packed bed of torrefied wood chips, obtaining heat transfer coefficient values of 5 $\mathrm{W/(m^2\,K)}$ for $Re < 5$, and 7.7 for $Re = 10$. Taken together, these studies suggested that the volumetric heat transfer coefficient h_v constitutes a complex function, contingent upon the internal heat transfer mechanisms within the biomass packed bed.

Numerous studies often simplify $\mathbf{k_{s,eff}}$ and $\mathbf{k_{g,eff}}$ into functions of the conductivities of the solid and gas phases and the porosity of homogeneous and isotropic porous media like metal and ceramic foams [81, 85, 82]. The effective conductivities, $\mathbf{k_{i,eff}}$, were treated as scalars and are given by $\mathbf{k_{i,eff}} = \varepsilon_i k_i \mathbf{I}$, where ε_i is the volume fraction of the $i-$ phase, $i = s$ or g. The volume fraction of the

gas phase (porosity) inside a biomass-packed bed can be divided into two parts, as described by Igathinathane et al. [169]: a major volume of voids in the packed bed (outside the wood particles) and a minor volume of voids inside the wood particles. The moisture content of the wood particle also affects the porosity of the packed bed. Guo et al. [45] developed an empirical relationship between effective thermal conductivity, moisture content, and porosity under static conditions that reads $k_{eff} = (0.0219 + 0.01MC)\varepsilon_s + 0.027\varepsilon_g$, where MC is the moisture content. When considering the dispersion effect due to gas flow, a more detailed formulation of $\mathbf{k_{g,eff}}$ and $\mathbf{k_{s,eff}}$ in the LTNE model obtained by the volume-averaging method are given as follows [68, 170],

$$\begin{cases} \mathbf{k_{g,eff}} = \varepsilon_g k_g \mathbf{I} + \frac{k_g}{V}\int_{A_{gs}} \mathbf{n}_{gs}\mathbf{b_{gg}} dA - \rho_g c_{p,g} \langle \tilde{\mathbf{v}}_g \mathbf{b_{gg}} \rangle = \mathbf{k_{g,con}} + \mathbf{k_{g,tor}} + \mathbf{k_{dis}} \\ \mathbf{k_{s,eff}} = \varepsilon_s k_s \mathbf{I} + \frac{k_s}{V}\int_{A_{gs}} \mathbf{n}_{sg}\mathbf{b_{ss}} dA = \mathbf{k_{s,con}} + \mathbf{k_{s,tor}} \end{cases} \tag{5.1}$$

where V is a representative elementary volume of the porous medium, A_{gs} is the area of the g-s interface contained in the averaging volume, $\mathbf{n_{gs}}$ is the outwardly directed unit normal vector pointing from the gas phase toward the solid phase, $\mathbf{n_{gs}} = -\mathbf{n_{sg}}$. $\mathbf{v}_g$, $\langle \mathbf{v_g} \rangle^{\mathbf{g}}$, and $\tilde{\mathbf{v}}_g = \mathbf{v}_g - \langle \mathbf{v}_g \rangle^g$ are the gas velocity within the pores, the intrinsic phase average velocity, and the deviation velocity respectively. The closure variables $\mathbf{b_{ii}}$ $(i = g, s)$ are the vector fields that map $\nabla\langle T_i \rangle^i$ onto $\tilde{T}_i$, where $\langle T_i \rangle^i$ is the intrinsic phase averaged temperature for the i-phase, $\tilde{T}_i$ is the spatial deviation temperature in the i-phase, more precisely [68], $\tilde{T_g} = \mathbf{b_{gg}} \cdot \nabla\langle T_g \rangle^g - s_g(\langle T_g \rangle^g - \langle T_s \rangle^s) + ...$, $\tilde{T_s} = \mathbf{b_{ss}} \cdot \nabla\langle T_s \rangle^s + s_s(\langle T_s \rangle^s - \langle T_g \rangle^g) + ...$ As illustrated in Eq.5.1, $\mathbf{k_{g,eff}}$ is composed of three components: the conductivity term $\mathbf{k_{g,con}}$, the tortuosity term $\mathbf{k_{g,tor}}$, and the dispersion term $\mathbf{k_{dis}}$. $\mathbf{k_{g,tor}}$ is often neglected since $\mathbf{k_{dis}}$ dominates [73]. Although various correlations for $\mathbf{k_{dis}}$ had been proposed by researchers such as Wakao et al. [105], Degroot et al. [73], and Afshari et al.[170], studies specifically focusing on the dispersion effect in biomass-packed beds remain limited. $\mathbf{k_{s,eff}}$ is influenced by $\mathbf{k_{s,tor}}$, while the closure variable $\boldsymbol{b_{ss}}$, a function of the gas velocity $\mathbf{v_g}$ [68], encompasses dispersion effects. Therefore, for biomass-packed beds, the best approach is to use Eq.5.1 with moisture content thermal conductivities k_s.

In this context, the purpose of this article is to develop a detailed LTNE model coupled with mass and momentum conservation to describe heat transfer within biomass-packed beds when considering the drying process and to determine the effective parameters needed to inform these models, namely, the heat transfer coefficient and the thermal conductivities. For this purpose, we have constructed a laboratory-scale packed bed facility, wherein we monitor the gas temperature at the inlet, the outlet, and the temperature of wood particles within the packed bed. Four types of materials: moist and dry wood pellets and wood chips were selected for the experiments. In Section 5.2, the wood particles, experimental facilities and test procedures are presented. In Section 5.3, we outline the developed numerical inverse analysis method. This method employs a multi-objective optimization approach to minimize errors between experimental and simulated data. In Section 5.4, we present the experimental results, and the determined effective values of this detailed LTNE model, and analyze the effects of moisture content. Conclusions and outlook are discussed in Section 5.5.

5.2 Materials and experiment

The experimental facility discussed in this section employs a method known as the transient single-blow technique (TSBT) [30]. This approach involves using hot gas to heat biomass particles within packed beds. At the same time, the evolution of the gas temperature at the inlet, the outlet, and the temperature of the wood particles within the packed bed are monitored. This approach offers additional information, as it enables the measurement of the solid temperature increase at different locations, thereby enhancing the robustness of the inverse analysis.

5.2.1 Materials

Four types of wood fuels were utilized in this work: moist and dry wood pellets and wood chips. We discuss the material properties from two perspectives: one focusing on the intrinsic characteristics of the material, such as length, shape, density, and moisture content; and the other on the main features of the packed bed, such as the bulk density of the sample and packing porosity. The thermal properties of the material, such as thermal conductivity and specific heat capacity, will be discussed in Section 5.3.

Commercially produced wood pellets have a diameter of around 6.1 mm, with lengths ranging from 6 to 24 mm according to the supplier data. Fig.5.1 displays an image of the pellets and the size distribution of pellet samples used in the experiments. The size distribution of the pellets was determined by measuring the lengths of 400 pellets from each lot using a micrometer. A single wood pellet can be approximated as a cylindrical shape. Fig.5.1 indicates that the most widespread length distribution of pellets lies between 10.1 and 11.3 mm. Here, we adopt an average length of 10.7 mm to calculate the equivalent diameters of wood pellets. The equivalent diameters of wood pellets, d_{ep}, are calculated as $d_{ep} = \frac{6V_p}{S} = \frac{6d_p l_p}{4l_p+2d_p}$, where d_p is the pellet diameter and l_p is the pellet average length. The calculated equivalent diameter is 7.1 mm. The density of a single wood pellet, obtained through multiple measurements, is 1197 kg/m^3 with an uncertainty of $\pm$1.9%. The moisture content of the pellet was measured using a moisture analyzer (METTLER TOLEDO, HC103) and is equal to 6.2%. The packing porosity is calculated based on gravimetric analysis and is found to be 0.43. The bulk density of pellets is 682.3 kg/m^3.

Now, let us discuss the characteristics of wood chips. Although wood chips exhibit a wide range of shapes and sizes, they can be considered rough parallelepipeds. According to the supplier data, their granulometry should range between 2.0 and 30 mm. The equivalent diameters of wood chips, d_{ec}, are calculated as $d_{ec} = \frac{6V_p}{S} = \frac{6l_c h_c w_c}{2(l_c w_c + w_c h_c + w_c l_c)}$, where l_c, w_c, and h_c represent the chip's length, width, and height, respectively. Fig.5.2 displays an image of the chips and the size distribution of chip samples used in the experiments. Fig.5.2 indicates that the most widespread equivalent diameters are between 6.8 and 7.4 mm. Here, we adopt an average value of 7.1 mm as the equivalent diameters of wood chips. The density of a single wood chip, obtained through multiple measurements, is 552 kg/m^3 with an uncertainty of $\pm$2.0%. The moisture content was measured and found to be 9.1% (weight dry basis). The packing porosity is 0.47. Table 5.2 lists the physical properties of these two materials.

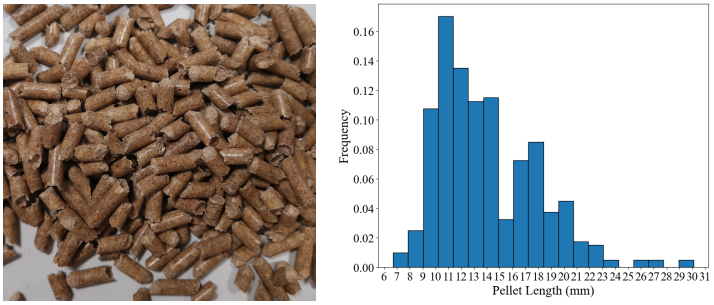

(a) wood pellets (b) pellets length distribution

Figure 5.1 – Picture of wood pellets and size distribution of pellet samples used in experiments.

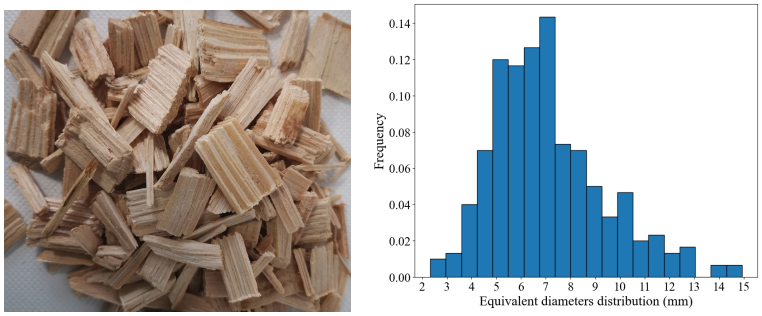

(a) wood chips (b) chips equivalent diameters distribution

Figure 5.2 – Picture of wood chips and size distribution of chip samples used in experiments.

Table 5.2 – Main characteristics of the wood pellets and wood chips

	Wood pellet	Wood chip
Average length, $\bar{l_p}$ (mm)	10.7	
Equivalent diameter, d_{ep} or d_{ec} (mm)	7.1	7.1
Moisture content, MC (%)	6.2	9.1
Single sample density, ρ_p or ρ_c (kg/m^3)	1197 ($\pm$1.9%)	552 ($\pm$2.0%)
Packing porosity, ε_g	0.43	0.47

5.2.2 Experimental system and test procedure

All experiments were conducted in a laboratory-scale packed bed specifically designed for this study. A schematic diagram of the experimental setup and a more detailed view of the test section, including thermocouple positions are shown in Fig.5.3. The experimental setup consists of several parts, systematically arranged from left to right. On the left side, an hot air blower (BAK Thermoplastic) functions to supply and heat the air. Moving toward the middle section, a test section comes into view, which is made of an iron tube surrounded by insulation. This tube, purposed for housing wood particles, measures 940 mm in length, with an inner diameter of 194 mm, and a thickness of 3 mm. These dimensions are suitable to study wood pellets and chips with an equivalent diameter of 7.1 mm, while respecting the diameter aspect ratio of at least 10. Inside the iron tube, two metallic grids are strategically placed to keep the position of the wood particles. On the right side, a thermo-anemometer (VT 110-2014 THERMO-ANEMOMETER) is placed to record the airflow velocity. A photograph of the experimental setup can be seen in Fig.5.4.

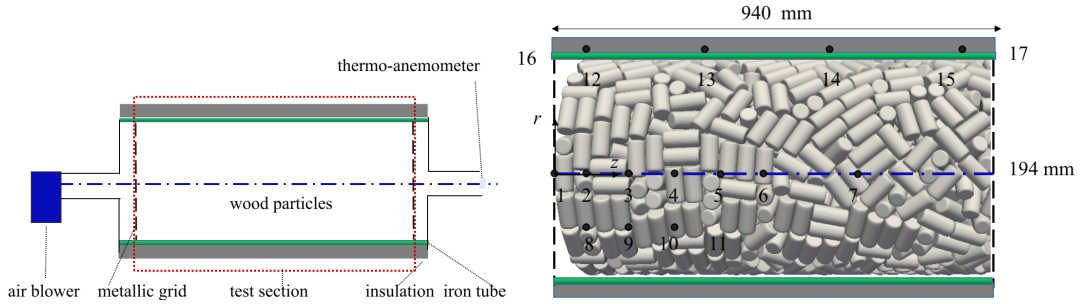

(a) experimental setup (b) test section domain

Figure 5.3 – Diagram of the experiment system and thermocouple positions in the test section.

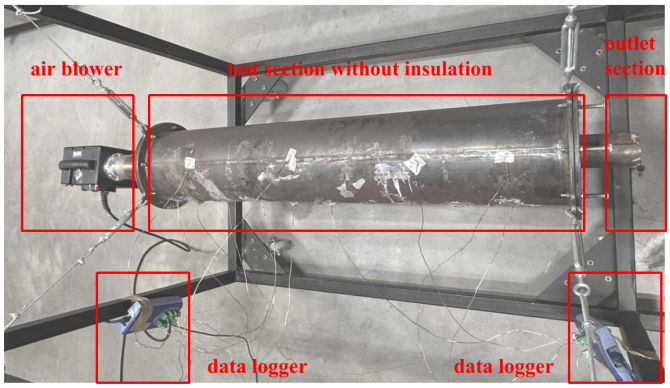

Figure 5.4 – Photograph of the experimental apparatus.

To investigate the effect of moisture content on the heat transfer characteristics of wood pellets and wood chips, both materials were dried using a convection oven at 90 °C for 24 hours. As a result,

we now have four kinds of materials: moist wood pellets (MC=6.2 %), dry wood pellets, moist wood chips (MC=9.1 %), and dry wood chips. In the experiment, the first step is to set the flow rate of the inlet gas. To control a single variable in the experiment, the inlet gas velocity is kept constant. For both moist wood pellets and dry wood pellets, the mass flow rate of air is set at 5.30 $\times$ 10^{-3} kg/s, corresponding to a magnitude of the Darcy velocity u (or superficial gas velocity) of 0.150 m/s at room temperature (293 K). For moist wood chips (MC=9.1 %) and dry wood chips, the mass-flow rate is set at 5.10 $\times$ 10^{-3} kg/s, corresponding to a magnitude of the Darcy velocity u of 0.144 m/s. After obtaining the inlet air mass-flow rate at room temperature, the next step is to set the heating power, which is also controlled by the air blower. To prevent pyrolysis of wood samples due to high temperatures during the experiment, the maximum inlet temperature was set to 349 K, focusing solely on the drying process of the wood material.

The black points in Fig.5.3 indicate the positions of the thermocouples (type K, 2 mm sheath diameter). The inlet gas temperature (point 1, z=0 mm, r=0 mm), the solid temperature inside the test section at six central axis locations (points 2 to 7, z=50, 150, 250, 350, 450, 650 mm, r=0 mm), and four radial locations (points 8 to 11, z=50, 150, 250, 350 mm, r=-45 mm), as well as the tube surface temperature at four axis locations (points 12 to 15, z=50, 300, 600, 900 mm, r=100 mm) are measured. The thermocouples were carefully placed inside the wood pellets and wood chips, as shown in Fig. 5.5, to ensure accurate measurement of the solid temperature. The pressure difference is measured between point 16 and point 17.

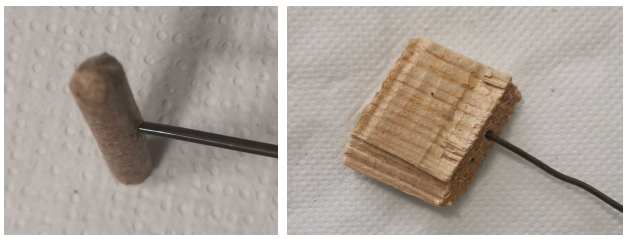

(a) thermocouple inside wood pellet

(b) thermocouple inside wood chip

Figure 5.5 – A schematic of the thermocouple position.

5.3 Numerical approach

The numerical approach is presented in this section. With the progress in optimization algorithms and computing resources, inverse methods have become a popular tool for precise parameter estimation. In the first subsection, we introduce the macroscopic numerical model, and in the second subsection, we detail the optimization algorithm used in the inverse analysis to determine the parameters.

5.3.1 Numerical model

In order to estimate the parameters, the entire test section is modeled as shown in Fig.5.3 (b), with the insulation excluded. The model represents an axisymmetric problem and thus, is specified as a narrow wedge ($< 5°$) as presented in Fig.5.6. The model's length is the same as the test section, measuring 940 mm, and the height of the wedge corresponds to the tube radius, that is, 100 mm. The model includes a two-dimensional axisymmetric geometry and differentiates between the packed bed (wood particles) and the tube (iron tube).

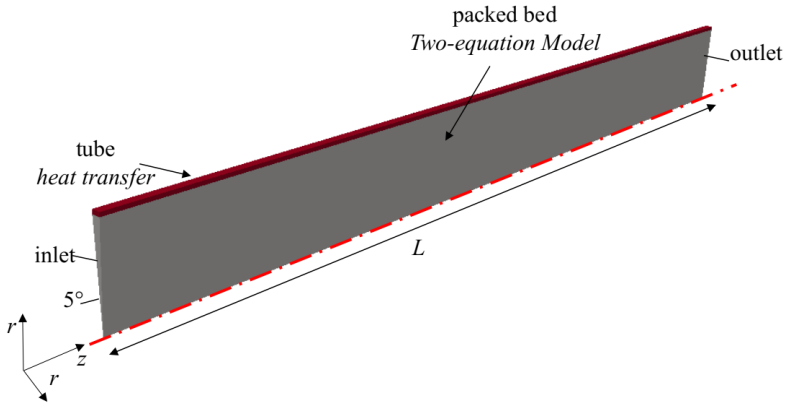

Figure 5.6 – The configuration of a two-dimensional axisymmetric numerical model.

5.3.1.1 Mathematical model and numerical implementation

The dense solid region (tube) is modeled using the transient heat conduction equation (energy conservation in a solid). For the packed bed region (wood particles), the situation becomes more complex. The detailed LTNE model takes into account the effect of moisture content on the heat transfer process, with the gas phase being considered a mixture of air and water vapor. The model offers a numerical representation of the interactions between a multiphase reactive material (N_s solid phases) and a multi-species reactive gas mixture (N_g gaseous elements/species) [77, 78]. The reactive material is assumed to be rigid, while the gas phase consists of a compressible and perfect mixture of gaseous elements/species. Water is modeled as a static solid phase. In what follows, the governing equations in the packed bed region are presented.

In the pyrolysis model, we account for the fact that the material of interest may be composed of different phases and, even, sub-phases. For example, the main compounds of the wood pellets that are studied in this work are the wood-cell walls (composed of sub-phases of cellulose, hemicellulose, and lignin) and water (composed of bounded and free water). To address this aspect, we divide each phase i into $N_{p,i}$ sub-phases. A specific sub-phase, $P_{i,j}$, follows a predetermined kinetic mechanism, leading to the generation of species or element A_k based on the stoichiometric coefficients $v_{i,j,k}$.

$$P_{i,j} \rightarrow \sum_{k=1}^{N_g} v_{i,j,k} A_k \tag{5.2}$$

The Arrhenius model [78] is employed to represent the pyrolysis reactions. It considers the reaction and thermal time scales, which are valid for various temperatures. The progression of the pyrolysis reaction $\chi_{i,j}$ for sub-phase j within phase i is defined as,

$$\partial_t \chi_{i,j} = (1-\chi_{i,j})^{m_{i,j}} {T_s}^{n_{i,j}} \mathcal{A}_{i,j} exp(-\frac{\epsilon_{i,j}}{RT_s}) \tag{5.3}$$

Given that we are only considering the drying process, Eq.5.3 can be simplified as follows

$$\partial_t \chi_{H_2O} = (1-\chi_{H_2O})^{m_{H_2O}} {T_s}^{n_{H_2O}} \mathcal{A}_{H_2O} exp(-\frac{\epsilon_{H_2O}}{RT_s}) \tag{5.4}$$

where m and n denote the parameters of the Arrhenius law, $\mathcal{A}$ is the Arrhenius law pre-exponential factor, ϵ is the activation energy. By combining the contributions from the N_s solid phases, the total production rate π for species H_2O can be calculated.

$$\pi_{H_2O} = \varepsilon_{H_2O,0} \rho_{H_2O,0} \partial_t \chi_{H_2O} \tag{5.5}$$

where the initial volume fraction and intrinsic density of H_2O within solid phase are denoted by $\varepsilon_{H_2O,0}$, $\rho_{H_2O,0}$. By summing the contributions of all elements and species in the mixture, we can determine the total pyrolysis-gas production rate, Π.

$$\Pi = \pi_{H_2O} \tag{5.6}$$

Based on the chemical model employed in the gas phase, species for finite-rate chemistry may be considered. In cases involving finite-rate chemistry, the conservation equation for a generic species possessing a mass fraction of y_i reads:

$$\partial_t(\varepsilon_g \rho_g y_i) + \partial_t(\varepsilon_g \rho_g y_i \mathbf{v_g}) + \partial_{\mathbf{x}} \cdot \mathcal{F}_i = \pi_i \tag{5.7}$$

Where $\mathcal{F}_i$ represents the effective multicomponent diffusion mass fluxes for the i-th species. In this case, we assume $\mathcal{F}_i = 0$, thus allowing Eq.5.7 to be simplified to:

$$\begin{cases} \partial_t(\varepsilon_g \rho_g y_{O_2}) + \partial_t(\varepsilon_g \rho_g y_{O_2} \mathbf{v_g}) = 0 \\ \partial_t(\varepsilon_g \rho_g y_{N_2}) + \partial_t(\varepsilon_g \rho_g y_{N_2} \mathbf{v_g}) = 0 \\ \partial_t(\varepsilon_g \rho_g y_{H_2O}) + \partial_t(\varepsilon_g \rho_g y_{H_2O} \mathbf{v_g}) = \pi_{H_2O} \end{cases} \tag{5.8}$$

The Mutation++ library is utilized to compute all thermodynamic and transport properties [77]. For the gas mixture, the mass conservation accounts for the pyrolysis production rate as follows:

$$\partial_t(\varepsilon_g \rho_g) + \nabla \cdot (\varepsilon_g \rho_g \langle \mathbf{v_g} \rangle^{\mathbf{g}}) = \pi_{H_2O} \tag{5.9}$$

In the momentum conservation, the average gas velocity $\langle \mathbf{v_g} \rangle^{\mathbf{g}}$ is obtained from the resolution of Forchheimer's law

$$\langle \mathbf{v_g} \rangle^{\mathbf{g}} = -\frac{1}{\varepsilon_g} (\mathbf{KX}) \cdot \nabla \langle p \rangle^g, \quad X_{ij} = \frac{1}{\mu K_{ij} + \beta_{ij} \rho_g |u|} \tag{5.10}$$

where the Forchheimer tensor, represented as $\mathbf{X}$, is introduced to simplify the computation process [76]. The permeability K and Forchheimer coefficient β are treated as scalars, and their values are

provided in Appendix 5.6. This expression for the gas velocity vector can be substituted back into the gas mass conservation (Eq.5.9) to read

$$\frac{\partial}{\partial t}\left(\varepsilon_g \rho_g\right) + \nabla \cdot \left(-\rho_g \mathbf{KX} \cdot \nabla \langle p \rangle^g\right) = \pi_{H_2O} \tag{5.11}$$

which, under the assumption that the perfect gas law holds, rewrites

$$\frac{\partial}{\partial t}\left(\varepsilon_g \frac{M\langle p \rangle^g}{R\langle T_g \rangle^g}\right) + \nabla \cdot \left(-\frac{M\langle p \rangle^g \mathbf{KX}}{R\langle T_g \rangle^g} \cdot \nabla \langle p \rangle^g\right) = \pi_{H_2O} \tag{5.12}$$

In the LTNE model, two energy conservation equations incorporating the drying process are required to represent the solid and gas phases. These equations are:

$$\sum_{i=1}^{N_s} \varepsilon_i \rho_i c_{p,i} \partial_t \langle T_s \rangle^s + \sum_{i=1}^{N_s} h_i \partial_t \left(\varepsilon_i \rho_i\right) = \nabla \cdot \left(\mathbf{k_{s,eff}} \cdot \nabla \langle T_s \rangle^s\right) + h_v \left(\langle T_g \rangle^g - \langle T_s \rangle^s\right) \tag{5.13}$$

$$\begin{aligned} \varepsilon_g \rho_g c_{p,g} \partial_t \langle T_g \rangle^g - \partial_t \left(\varepsilon_g p\right) + \sum_{j=1}^{N_g} h_j \partial_t \left(\varepsilon_g \rho_g y_j\right) + \nabla \cdot \left(\varepsilon_g \rho_g h_g \mathbf{v_g}\right) + \nabla \cdot \sum_{j=1}^{N_g} \mathcal{Q}_j \\ = \nabla \cdot \left(\mathbf{k_{g,eff}} \cdot \nabla \langle T_g \rangle^g\right) + h_v \left(\langle T_s \rangle^s - \langle T_g \rangle^g\right) \end{aligned} \tag{5.14}$$

where $c_{p,i}$ and $\mathbf{k_{i,eff}}$ respectively denote the heat capacity and effective thermal conductivity tensor of the i phase. $\langle T_i \rangle^i$ and $\langle \mathbf{v_g} \rangle^{\mathbf{g}}$ denote the intrinsic phase average temperature for the i-phase and the intrinsic gas average velocity. h_v denotes the volumetric heat transfer coefficient between the gas stream and the sample. h is the absolute enthalpy, and $\mathcal{Q}_j$ is the heat transport by effective diffusion of the j-th species.

The detailed expressions of the initial and boundary conditions for the system of Eq.5.13 and 5.14 (LTNE model) are provided in Tables 5.3. To simplify the notation, we introduce a few notational substitutions: average temperature $\langle T_g \rangle^g$ and $\langle T_s \rangle^s$ in packed bed region are denoted as T_g and T_s, while average pressure $\langle p \rangle^g$ is represented as p. The solid temperatures and thermal conductivity in the tube region are denoted by T_t and k_t, respectively. The initial, and boundary conditions for T_g, T_s, p, y_{N_2} and y_{O_2} are set within the packed bed region and T_t within the tube region. The gas temperature T_g at the inlet is derived from experimental observations. The inlet boundary condition for the pressure p is calculated based on the outlet velocity, under the assumption of constant mass-flow rate in the packed bed. The velocity field is modeled by the Forchheimer law, based on the Reynolds number. The wall surface temperature T_t in the tube region is measured throughout the experiments.

The Porous Material Analysis Toolbox based on Open-FOAM (PATO) [92] was employed for computations, using a multi-block approach. In this method, a different set of equations is solved for each region at every time step, along with respective boundary conditions derived from energy balances at the interfaces. Within the packed bed region, a semi-implicit solution to the pressure equation is achieved using first-order schemes in time (Euler) and space (Gauss linear). The same methodology applies to energy equations, where temperature terms are implicitly solved, while other quantities are explicitly addressed. For the tube region, only the energy equation requires a solution, with temperature terms handled implicitly and all other variables explicitly. All equations are solved

Table 5.3 – Initial and boundary conditions of the second strategy

Region	Initial conditions	Boundary conditions			
		inlet	packed bed-tube interface	outlet	
packed bed	$T_g = T0$ $T_s = T0$ $y_{N_2} = 0.79$ $y_{O_2} = 0.21$	$T_g = T1$, $\frac{\partial T_s}{\partial z} = 0$ $p = \frac{u \cdot \mu_g \cdot L}{\mathbf{K}} + \beta \cdot (\rho_g \cdot u^2) \cdot L + p_{atm}$ $\frac{\partial y_{N_2}}{\partial z} = 0$ $\frac{\partial y_{O_2}}{\partial z} = 0$	$\frac{\partial T_g}{\partial r} = 0$, $k_{s,eff} \frac{\partial T_s}{\partial r} = k_t \frac{\partial T_t}{\partial r}$ $\frac{\partial p}{\partial r} = 0$ $\frac{\partial y_{N_2}}{\partial z} = 0$ $\frac{\partial y_{O_2}}{\partial z} = 0$	$\frac{\partial T_g}{\partial z} = 0$, $\frac{\partial T_s}{\partial z} = 0$ $p = p_{atm}$ $\frac{\partial y_{N_2}}{\partial z} = 0$ $\frac{\partial y_{O_2}}{\partial z} = 0$	
		inlet	tube-packed bed interface	top	outlet
tube	$T_t = T0$	$\frac{\partial T_t}{\partial z} = 0$	$k_t \frac{\partial T_t}{\partial r} = k_{s,eff} \frac{\partial T_s}{\partial r}$	T_t	$\frac{\partial T_t}{\partial z} = 0$

sequentially, using optimal mesh refinement and time steps to ensure the attainment of convergence order.

5.3.1.2 Physical properties of air and wood sample

This study made two assumptions: 1) the thermal conductivity of individual wood particles is considered isotropic and represented by a scalar value, and 2) the thermal conductivity remains constant throughout the experiment, not changing with temperature. Using the transient plane source technique (Hot Disk, TPS 3500), thermal conductivities of four materials were measured: moist wood pellets (MC=6.2%, 0.283 W/m·K), dry wood pellets (0.259 W/m·K), moist wood chips (MC=9.1%, 0.286 W/m·K), and dry wood chips (0.221 W/m·K). Specific heat capacities were obtained from the literature: moist wood pellets (1185 J/(kg·K)), dry wood pellets (1088 J/(kg·K)), moist wood chips (1163 J/(kg·K)), and dry wood chips (1088 J/(kg·K)) [45]. The density of air (ρ_g) was calculated using the perfect gas law, and the values for heat capacity ($c_{p,g}$), dynamic viscosity (μ_g), and thermal conductivity (k_g) were obtained from the NASA-9 database [171].

As outlined in Section 5.1, the resolution of the LTNE models (Eq.5.13 and 5.14) demands the evaluation of three indeterminate effective parameters: the effective solid thermal conductivity ($\mathbf{k_{s,eff}}$), effective gas thermal conductivity ($\mathbf{k_{g,eff}}$), and the volumetric heat transfer coefficient (h_v). To perform an optimization algorithm, various dimensionless coefficients - c_1, c_2, c_3, and f - are defined as shown in Eq.5.15. Notably, $\mathbf{k_{g,eff}}$ is subject to the effects of tortuosity and dispersion, exhibiting differing values in horizontal ($||$) and transverse ($\perp$) flow directions [30]. The tortuosity term is often overlooked in relation to the dispersion term [73]. The interrelationship between $\mathbf{k_{dis}}$ and the gas's thermal properties are modeled similarly to the form proposed by Wakao et al. [105]. The volumetric heat transfer coefficient, h_v, is modeled according to the format established by Wakao et al.[105]. Adopting this approach, relationships are established between the unknown effective parameters and the dimensionless numbers (Re, Pr), thermal properties of the gas and solid (k_g, ρ_g, $c_{p,g}$, k_s), volume

fractions of gas and solid (ε_g, ε_s), and the characteristic length of the solid, d_{ep}.

$$\begin{cases} \mathbf{k_{s,eff}} = \mathbf{k_{s,con}} + \mathbf{k_{s,tor}} = c_1 \cdot k_s I \\ k_{g,eff,||} = k_{g,con} + k_{g,tor,||} + k_{dis,||} = \varepsilon_g k_g + 0 + c_2 \cdot Re \cdot Pr \cdot k_g = \varepsilon_g k_g + c_2 \cdot d_{ep} \cdot \varepsilon_g \cdot |\langle v_g \rangle^g| \cdot \rho_g \cdot c_{p,g} \\ k_{g,eff,\perp} = k_{g,con} + k_{g,tor,\perp} + k_{dis,\perp} = \varepsilon_g k_g + 0 + c_3 \cdot Re \cdot Pr \cdot k_g = \varepsilon_g k_g + c_3 \cdot d_{ep} \cdot \varepsilon_g \cdot |\langle v_g \rangle^g| \cdot \rho_g \cdot c_{p,g} \\ h_v = (6\varepsilon_s / d_{ep}) \cdot (2 + f Re^{0.6} Pr^{1/3}) k_g / d_{ep} \end{cases} \tag{5.15}$$

5.3.2 Optimization process and methods

A numerical inverse analysis method was implemented here to determine effective parameters, minimizing errors between experimental measurements and predicted results. Eleven temperature data sequences are available, designated as $\{T1^i\}_{i=0}^n$ through $\{T11^i\}_{i=0}^n$. Each sequence corresponds to temperatures measured at each time step, as indicated by the index i. The positions of the measurement points from $T1$ to $T11$ are shown in Fig.5.3. The time-varying inlet gas temperature data $T1$ is smoothed into a second-order polynomial through least squares fitting, which is then used as a boundary condition. The optimization process employs an objective function S, defined as the average of the root mean squared relative error. This error is computed between the measured and predicted temperatures at ten specified positions ($T2$ through $T11$).

$$S = \frac{1}{10} \sum_{j=2}^{11} \sqrt{\frac{1}{n} \sum_{i=1}^{n} \left(\frac{Tj_{num}^i - T_j^i}{Tj^i} \right)^2} \tag{5.16}$$

where j represents the temperature sequence ($T2$ through $T11$), n is the total number of indices. Tj_{num}^i and Tj^i represent the predicted and measured temperatures, respectively.

To minimize S, we employed the Design Analysis Kit for Optimization and Terascale Applications (Dakota) [149]. Within this, the Adaptive Nonlinear Least-Squares algorithm (NL2SOL) [112], a local optimization method, was used. NL2SOL is noted for its rapid delivery of optimal value estimates, thanks to the quasi-Newton update it employs. The efficiency of NL2SOL is further increased through a simplification scheme used to approximate the Hessian, allowing it to outpace global methods in performing least square calculations. An overview of this optimization strategy is shown in Fig.5.7, and its application to two-equation model optimizations will be discussed in the subsequent section.

5.4 Results and discussions

Results of measured and predicted temperatures are reported in this section. The gaseous transport and thermodynamic properties are updated as a function of pressure, temperature, and species mass composition using the Mutation++ library [172]. The gas mixture is composed of nitrogen, oxygen, and water vapor. The species mass fraction is updated by solving the species mass conservation equation. In the first subsection, the detailed LTNE model (Eq.5.13, 5.14) is considered. The volumetric heat transfer coefficient h_v, the effective solid thermal conductivity $\mathbf{k_{s,eff}}$, and the effective gas thermal conductivity $\mathbf{k_{g,eff}}$ used in that model are determined. In the second subsection, the

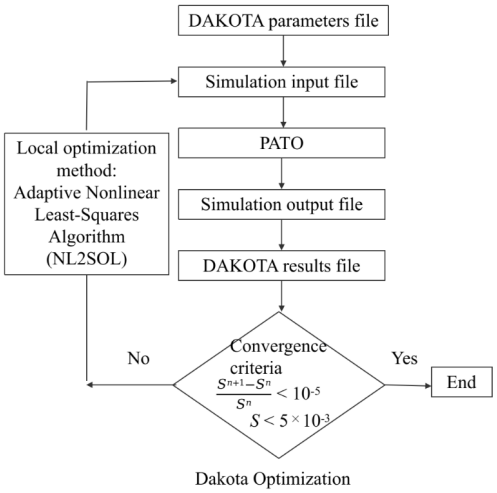

Figure 5.7 – The steps of the optimization process.

pressure, velocity, temperature, volumetric heat transfer coefficient, and gas mixture properties fields predicted with the LTNE model are presented.

Fig.5.8 showcases a comparison between the experimental data and the predictions of the LTNE model, across four different conditions: moist wood pellets (MC=6.2 %), dry wood pellets, moist wood chips (MC=9.1 %) and dry wood chips. The experimentally obtained data is denoted by points, while the model predictions are indicated by solid and dashed lines. The plotted data includes the inlet gas temperature ($T1$) and the solid temperature at ten locations ($T2$ to $T11$), varying over time. It's worth noting that this subset of temperature data is the same used in our optimization process. Solid lines represent the predicted solid temperatures at six points along the central axis ($T2_{num}$ to $T7_{num}$), while dashed lines depict the four remaining points ($T8_{num}$ to $T11_{num}$). The slight variation in the measured temperatures could be attributed to the accuracy limit of the thermocouple. The primary parameters influencing the predicted temperatures are the effective solid thermal conductivity $\mathbf{k_{s,eff}}$, the effective gas thermal conductivity $\mathbf{k_{g,eff}}$, and the volumetric heat transfer coefficient h_v. The subsequent sections detail the process for determining these parameters.

5.4.1 Determination of three effective parameters used in the LTNE model

According to the model presented in the previous section (Eq.5.15), there are four parameters to optimize: f, c_1, c_2, and c_3. Studies have indicated that the dispersion terms represented by $c3{\cdot}Re{\cdot}Pr{\cdot}k_g$ in $k_{g,eff,\perp}$ are significantly smaller [173]. Therefore, in what follows, we set the values of c_3 to zero and run the optimization on three parameters: f, c_1, and c_2.

Among the simulations executed, we've chosen a representative instance - the case of wood pellets with a moisture content of 6.2% and a mass flow rate of 5.3×10^{-3} kg/s, to detail the optimization process and present the two-dimensional simulation results. Before initiating the optimization process, setting appropriate bounds for the parameters to be optimized is crucial. The upper and lower

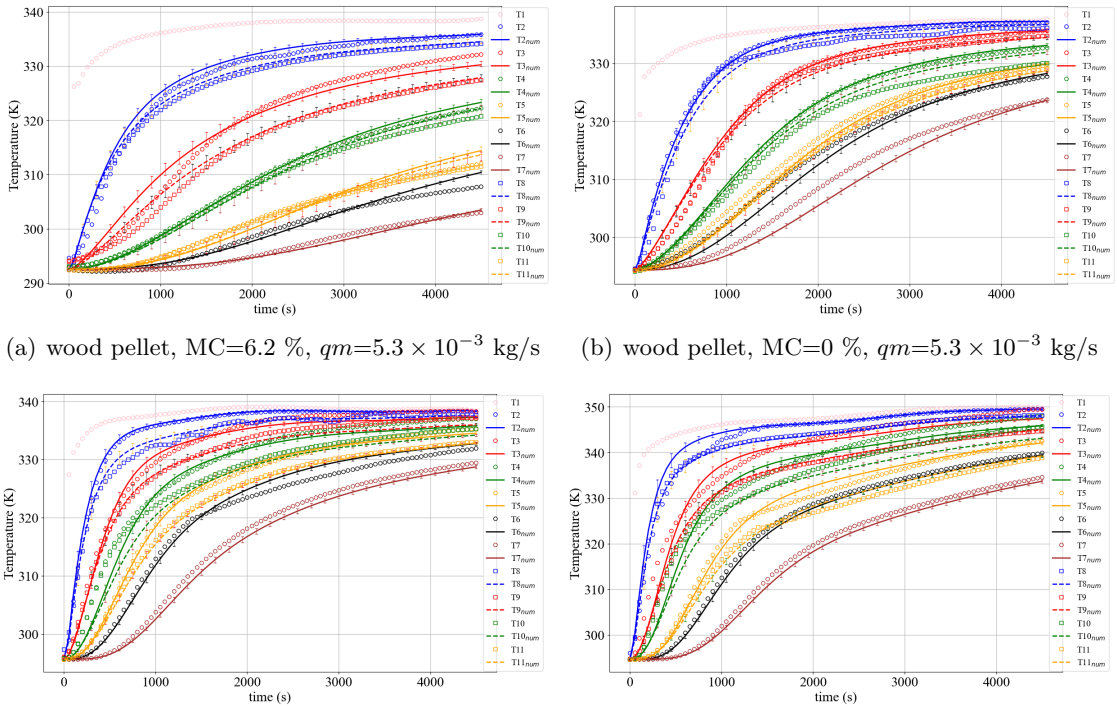

(a) wood pellet, MC=6.2 %, qm=5.3 $\times$ 10^{-3} kg/s

(b) wood pellet, MC=0 %, qm=5.3 $\times$ 10^{-3} kg/s

(c) wood chips, MC=9.1 %, qm=5.1 $\times$ 10^{-3} kg/s

(d) wood chips, MC=0 %, qm=5.1 $\times$ 10^{-3} kg/s

Figure 5.8 – The comparison of predicted and measured temperature in wood pellets and wood chips.

limits may affect the viability of an optimal solution. We established these bounds based on existing literature. In particular, using the correlations provided by Essence et al.[30] for packed beds, we determined the coefficients f, c_1, and c_2 to be 1.1, 0.57, and 0.1 respectively, when the Reynolds number is less than 8000. Guided by the order of magnitudes from literature and computational efficiency, we defined the parameter boundaries for f, c_1, and c_2 as 0 to 2, 0 to 2, and 0 to 0.5, respectively. The initial guess values and lower and upper bounds of the three variables are shown in Table 5.4.

Table 5.4 – Initial guess values and lower and upper bounds of the three variables.

Parameters	f	c_1	c_2
Initial guess	1.1	0.57	0.1
Chosen lower bounds	0	0	0
Chosen upper bounds	2	2	0.5

After 80 iterations of the local optimization algorithm, the model converged ($S < 0.005$). In Fig.5.9, we can see the impact of the three variables (f, c_1, and c_2) on the error term S. In this figure, the point sizes on the left side (a) correspond to the values of S, while the color scale reflects f values. As displayed in Fig.5.9 (a), when S falls below 0.005, the c_1 values are mainly around 0.79,

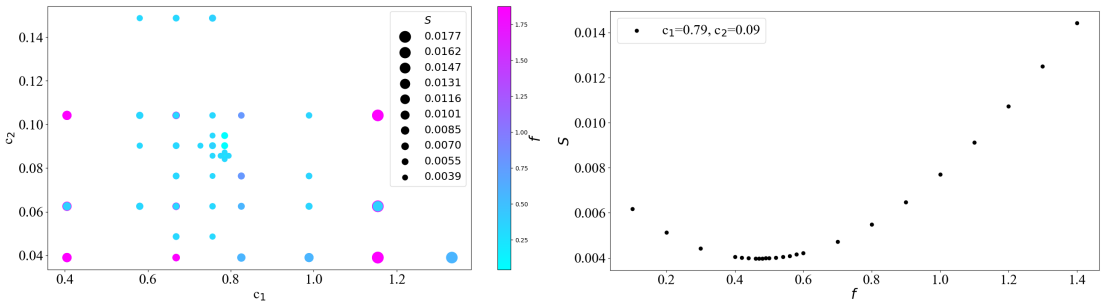

(a) three variables (c_1, c_2, f) (b) one variable (f)

Figure 5.9 – Impact of parameter variations (c_1, c_2, f) on error S.

and the c_2 values are mainly around 0.09, with f ranging from 0.3 to 1.4. For a deeper analysis of the error in relation to f, we set c_1 to 0.79 and c_2 to 0.09, adjusting only the f input. As presented in Fig.5.9 (b), the error S initially decreases and then increases, with the minimum error at $f = 0.47$, accompanied by a 5% uncertainty. This concludes the optimization process, defining the final values of our variables. Specifically, for this case, c_1, c_2, and f have been determined to be 0.79, 0.09, and 0.47, respectively. In summary, when the error S converges to the level of 5×10^{-3}, the optimal values for f, c_1, and c_2, along with their corresponding h_v, $k_{s,eff}$, and $k_{g,eff,||}$, are outlined in Table 5.5.

Values of f, c_1 and c_2 for the four different materials are given in Table 5.5. Starting with f, Wakao's suggested value is 1.1, which does not take into account the shape and moisture of wood particles. In our study, the values of f for wet and dry wood pellets are 0.47±0.03 and 0.54±0.03 respectively, corresponding to h_v values of 13429 and 16333 W/(m^3 K). For wet and dry wood chips,

Table 5.5 – The value of f, c_1 and c_2 got in the optimization process

	Wood pellets		Wood chips	
MC (% w.b.)	6.2	0	9.1	0
qm (kg/s)	5.30×10^{-3}	5.30×10^{-3}	5.10×10^{-3}	5.10×10^{-3}
T_{inlet} (K)	294∼338	294∼ 338	294∼ 338	294∼ 349
Re	61∼65	61∼65	59∼62	59∼62
f	0.47 ± 0.03	0.54 ± 0.03	0.44 ± 0.03	0.52 ± 0.03
c_1	0.79 ± 0.02	0.70± 0.02	0.74 ±0.02	0.67 ± 0.02
c_2	0.09 ± 0.01	0.09 ±0.01	0.08± 0.01	0.08 ±0.01
h_v (W/(m^3·K))	13429-13850	16333-16450	12340-12570	13924-13950
$\mathbf{k_{s,eff}}$ (W/(m · K))	0.224	0.174	0.212	0.142
$\mathbf{k_{g,eff}}$ (W/(m · K))	0.128	0.128	0.111	0.111
S	3.99×10^{-3}	3.70×10^{-3}	3.53×10^{-3}	3.97×10^{-3}

the values of f are 0.44±0.03 and 0.52±0.03, respectively, with corresponding h_v values of 12340 and 13924 W/(m^3 K). The heat transfer coefficient of air flowing through wood pellets or chips increases with decreasing moisture, with the increase rates being 21.6% and 12.8%. As one may expect, water evaporation is responsible for a blockage effect at the particle scale. Next, we examine c_1, which is suggested to be the solid phase volume fraction ε_s, i.e., 0.57 for wood pellets (dry or wet) and 0.53 for wood chips (dry or wet). Our values are 0.79±0.02 and 0.70±0.02 for wet and dry wood pellets, with corresponding $\mathbf{k_{s,eff}}$ values of 0.224 and 0.174 W/(mK). For wet and dry wood chips, the values are 0.74±0.02 and 0.67±0.02, with corresponding $\mathbf{k_{s,eff}}$ values of 0.212 and 0.142 W/(m K). As the moisture decreases, $\mathbf{k_{s,eff}}$ decreases by 22.3% and 33.0%. Lastly, we look at c_2, which affects the dispersion term. Within our experimental range, roughly around a Reynolds number of 60, we get values of 0.09±0.01 for wet and dry wood pellets, with corresponding $\mathbf{k_{g,eff}}$ values of 0.128 W/(m K). The value of the dispersion term of gas thermal conductivity $k_{dis,||}$ is 9.1 times that of the conductivity term $k_{g,con}$. For wet and dry wood chips, the corresponding $\mathbf{k_{g,eff}}$ values are 0.111 W/(m K), where $k_{dis,||}$ is 7.1 times the value of $k_{g,con}$.

Now let's revisit Fig.5.8, we'll compare the temperatures obtained from both experimental and simulation methods as referenced in Table 5.5. For the case of wet wood pellets, displayed in Fig.5.8 (a), the calculated value of S from Eq.5.16 is 3.99×10^{-3}. This value is an average of the errors across all positions from $T2$ to $T11$. The maximum error, seen at position $T3$, is 6.57×10^{-3}, which equates to a maximum temperature difference of 2.18 K between the measured and predicted values. This close correspondence further confirms the consistency between experimental and simulated results.

5.4.2 Color maps of the simulation results in the full domain

The simulation results for the case of wood pellets with a moisture content of 6.2%, displayed as color maps, are now outlined. Figs. 5.10, 5.11, and 5.12 present the pressure and velocity fields in the test section and the temperature difference fields within the packed bed at 4500s. The pressure changes follow the Forchheimer equation (Eq.5.10). When the inlet gas mass flow rate remains constant and the temperature rises, the gas density decreases. This reduction in density increases the inlet gas velocity and, in turn, the inlet pressure. Within the packed bed, the distribution of pressure and velocity is uneven. Near the gas inlet (left side), the flow velocity and pressure are higher than near the gas outlet (right side).

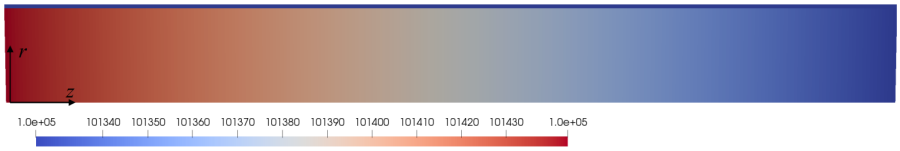

Figure 5.10 – Pressure p (Pa) distribution predicted with the LTNE model (t=4500 s).

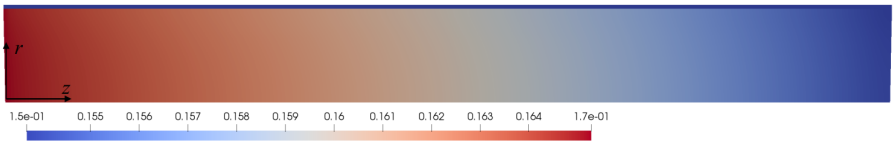

Figure 5.11 – Velocity magnitude u (m/s) predicted with the LTNE model (t=4500 s).

In the packed bed region, the maximum difference between the local average gas temperature (T_g) and solid temperature (T_s) is less than 1.5 K. In most areas, this difference sits around 0.7 K. The difference is notably larger in the top-left corner of the graph. This is due to the strong coupling between the solid temperature inside the packed bed and the surface temperature of the wall, which is considerably lower than the gas temperature inside the packed bed. Thermal equilibrium is reached.

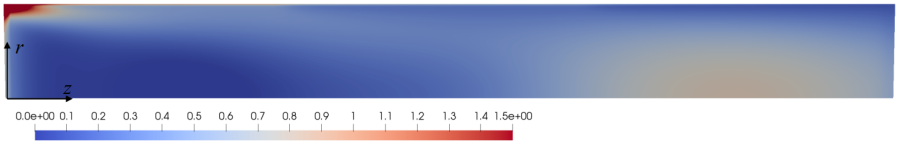

Figure 5.12 – Temperature difference $T_g - T_s$ (K) in the sample region predicted with the LTNE model (t=4500 s).

Fig. 5.13 (a-d) displays the fields of thermophysical gas mixture properties in the full domain (wood pellets, MC=6.2%, t=4500s). When the inlet gas temperature rises to 338 K, the values of viscosity, specific heat capacity, thermal conductivity, and gas density at the left inlet are 2.06 kg/(m·s), 1052 J/(kg·K), 0.0314 W/(m·K), and 1.01 kg/m^3, respectively. In comparison, the values for the pure air gas phase (wood pellets, MC=0, t=4500s) are 2.10 kg/(m·s), 1028 J/(kg·K), 0.03 W/(m·K), and 1.05

kg/m^3. It can be observed that, compared to the case of dry wood pellets, the most significant impact on gas properties is on the gas thermal conductivity, which only increased by 4.7%.

Fig. 5.13 (e) presents the fields of the gaseous mass fraction of water vapor in the packed bed region. In comparison to pure air, the gaseous mass fraction of water vapor increases from 0 at the initial moment to 0.04. Concurrently, the gaseous mass fractions of nitrogen and oxygen decrease from 0.79 and 0.21 at the initial moment to 0.76 and 0.20, respectively.

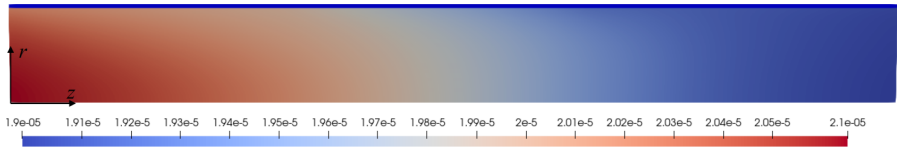

(a) viscosity μ_g (kg/(m · s))

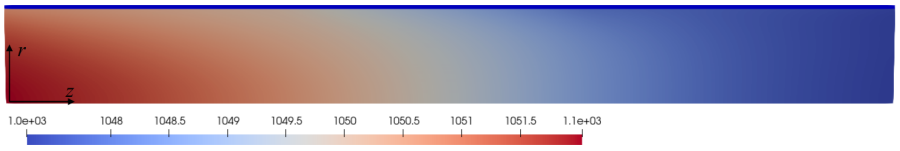

(b) specific heat capacity cp_g (J/(kg · K))

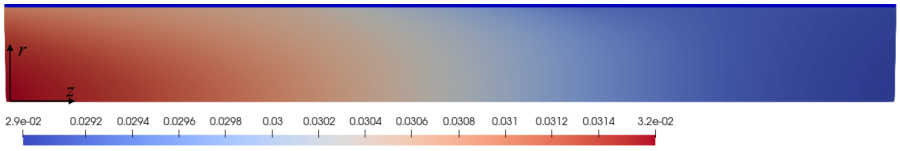

(c) gas thermal conductivity k_g (W/(m · K))

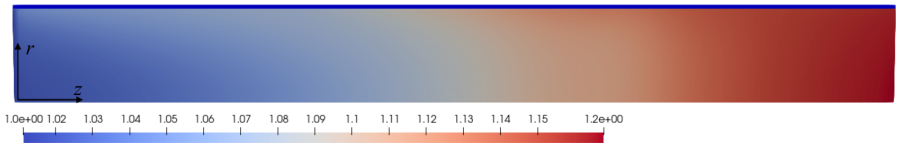

(d) gas density ρ_g (Kg/(m^3))

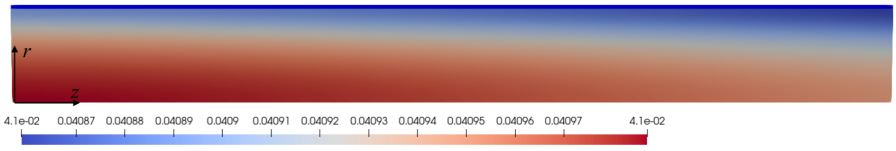

(e) water vapor mass fraction, H_2O

Figure 5.13 – The fields of thermophysical mixture gas properties (wood pellets, MC=6.2%, t=4500s)

5.5 Conclusion

The objective of this work was to develop a detailed local thermal non-equilibrium model to describe heat and mass transfer within biomass packed beds when considering the drying process. To

feed this detailed model, several effective parameters, namely, the volumetric heat transfer coefficient h_v, effective solid thermal conductivity $\mathbf{k_{s,eff}}$, and effective gas thermal conductivity $\mathbf{k_{g,eff}}$ need to be determined. Due to the complex characteristics of biomass particles, such as geometric configurations, anisotropic fuel shapes, moisture content, and fuel pore structure, these parameters cannot be readily obtained through appropriate correlations. In this work, we designed a novel experimental facility based on the transient single-blow technique to determine these parameters for biomass particles. Experiments were conducted using hot air to heat four types of materials: moist wood pellets (MC=6.2%), dry wood pellets, moist wood chips (MC=9.1%), and dry wood chips. To maintain a single variable of wood moisture, velocities were maintained at 0.150 m/s and 0.144 m/s for wood pellets and wood chips, respectively. To prevent pyrolysis of wood samples due to high temperatures during the experiment, the maximum inlet temperature was set to 349 K, focusing solely on the drying process of the wood material. Parameter estimations were carried out using numerical inverse analysis. The numerical model was implemented using finite volumes in the Porous Material Analysis Toolbox based on OpenFOAM (PATO). A local optimization method, NL2SOL, was employed to minimize the error between measured and predicted temperatures. The optimization process was performed with the Open Source optimization software Dakota. The results revealed that moisture content significantly affects the volumetric heat transfer coefficient and effective thermal conductivity in the test range. Results revealed that the volumetric heat transfer coefficient increased significantly as moisture content decreased from 6.2% to 0 for wood pellets (13429-13850 to 16333-16450 W/(m^{3}K)) and from 9.1% to 0 for wood chips (12340-12570 to 13924 − 13950W/(m^{3}K)). As one may expect, water evaporation is responsible for a blockage effect at the particle scale. These findings contribute to a deeper understanding of heat and mass transfer phenomena in biomass-packed beds and can inform the development of more accurate models for various applications. They also show the importance of accounting for degassing for pyrolysis applications in general, calling for a continuation of this work past the drying temperature.

5.6 Appendix. Determination of the permeability and Forchheimer coefficient

During the experiment, four measurements were conducted between two points (16 and 17, as shown in Fig. 5.3) for each of the eight different mass flow rate values (qm). The distance between the two measurement points is 0.94 m. A relationship between the pressure gradient (∇p) and gas velocity (u) is plotted in Fig. 5.14. The average values of the pressure gradient are obtained from several experiments. In the case of incompressible gas flow, a modified 1D version of Forchheimer's law can be expressed as follows:

$$-\frac{dp}{dx} = \mu \mathbf{K}^{-1} \cdot (\mathbf{v}_g \cdot \varepsilon) + \beta \rho_g (\mathbf{v}_g \cdot \varepsilon)^2 = a_1 \cdot u + a_2 \cdot u^2 \tag{5.17}$$

where a_1 and a_2 are factors. The values of a_1 and a_2 are determined using the least-squares approximation method. Fig.5.14 displays the experimental data and the fitted curve for wood pellets and wood chips. The parameters obtained from the experimental data are summarized in Tab.5.6.

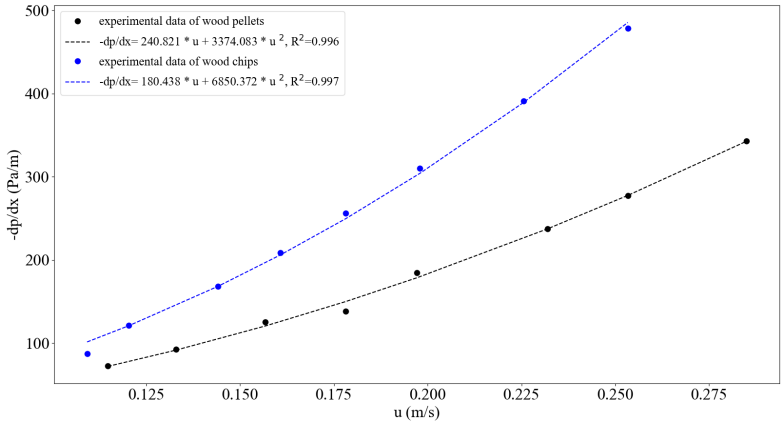

Figure 5.14 – Pressure drop per unit length vs. airflow

Table 5.6 – Parameters computed based on the experimental data

	Re	a_1 (kg/(m^3· s)	a_2 (kg/m^4)	**K** (m^2)	β (m^{-1})
Wood pellets	50.19 $\sim$ 124.41	240.821	3374.083	7.50×10^{-8}	2.79×10^{3}
Wood chips	48.02 $\sim$ 110.44	180.438	6850.372	1×10^{-7}	5.67×10^{3}

Part II

Micro-scale investigation

Chapter 6

Experimental measurement and 3D image-based numerical determination of the permeability and the Forchheimer correction tensor of Calcarb

Preamble

Authors: S.Liu; A.Ahmadi-Senichault; H.Scandelli; J. Lachaud;
Affiliations: Arts et Métiers Institute of Technology, Univ. Bordeaux, CNRS, Bordeaux INP, I2M, UMR 5295, F-33400 Talence, France;
Published: No, the current version is to be submitted to *Aerospace Science and Technology*;
Conference: No;

Abstract

The aim of this work is to extend micro-scale simulations from the Darcy flow regime to the Forchheimer flow regime, and experimentally determine permeability and Forchheimer coefficient of Calcarb, a carbon fiber preform used in thermal protection systems (TPS) applications. For that purpose, the pressure gradient across Calcarb samples is experimentally investigated in both In-Plane (IP) and Through-Thickness (TT) directions, covering Reynolds numbers Re ranging from 0.05 to 10.46, which represent gas flow in both Darcy and Forchheimer flow regimes. Micro-scale simulations, based on the direct resolution of the Navier-Stokes equations under both flow regimes, are performed using the Porous Material Analysis Toolbox based on OpenFOAM (PATO). The experimental results reveal the limit of Re of the Darcy flow regime in Calcarb to be around 0.43. Experimental permeability values were 1.615×10^{-10} m^2 (IP) and 1.248×10^{-10} m^2 (TT), exhibiting an 12.3% relative difference compared to the simulations. In the Forchheimer flow regime, the experimental Forchheimer coefficient β for the Forchheimer equation is determined as 1.4948×10^5 m^{-1} (IP) and 2.0010×10^5 m^{-1} (TT).

However, the simulation did not provide a specific value for β or the Forchheimer correction tensor $\mathbf{F}$ due to the non-linear dependence of $\mathbf{F}$ on gas velocity. Instead, the pressure gradient was presented as a function of Re in the three primary directions: x, y, and z. The maximum difference between the simulated and experimental pressure gradients reached up to 64.5% and 68.2% in the IP and TT directions, respectively.

Keywords: Calcarb; Permeability; micro-scale simulations; Anisotropy; Forchheimer correction tensor; Micro-CT image

6.1 Introduction

Thermal protection systems (TPS) are essential for maintaining acceptable temperatures on a spacecraft's outer surface during all mission phases, especially during atmospheric re-entry [6, 7, 8]. TPS materials can be classified into two main categories: ablative materials [9], used in the Apollo missions [174], Stardust (NASA, 2006) [7, 175], Mars Science Laboratory (NASA, 2012) [176, 177], and Mars 2020 (NASA, 2021) [178]; and non-ablative materials, such as the ceramic tiles used on the space shuttle [179]. Ablative materials can be further subdivided into charring (pyrolyzing) and non-charring ablators. Pyrolyzing ablators primarily consist of a resin that fills the pores of a carbon matrix [9, 180, 181], such as FiberForm produced by Fiber Materials Inc. [91] and Calcarb produced by Mersen. During the pyrolysis process, the polymer matrix undergoes carbonization, generating pyrolysis gases that are transported out of the material through the pore network via diffusion and convection. Simulating pyrolysis gas flow within the TPS is crucial, as these gases can significantly impact re-entry modeling.

A steady-state momentum equation for calculating the gas velocity within an ablator has been proposed [180]:

$$\langle \mathbf{v_g} \rangle = -\frac{1}{\mu} \frac{1 + \beta_0/p}{1 + Fo} \mathbf{K} \cdot \nabla \langle p \rangle^g \tag{6.1}$$

where $\langle \mathbf{v_g} \rangle$ is the superficial average velocity or Darcy velocity and $\langle p \rangle^g$ is the intrinsic average pressure. The permeability, $\mathbf{K}$, is a second-order tensor since most materials are anisotropic. The Klinkenberg coefficient, β_0, accounts for a slip at the gas-solid interface at the pore scale and is significant when the Knudsen number is not small [91, 92]. The Forchheimer number, Fo ($\beta K \rho |\langle v_g \rangle| / \mu$), accounts for the convective flux and should be taken into account when gas velocities exceed 50 m/s (that is, in high-density ablative materials submitted to very high heat fluxes) [9, 92]. Simplifying the momentum equation by neglecting β_0 and Fo leads to Darcy's law [182], where gas velocity varies linearly with the pressure gradient. Neglecting only β_0 results in Forchheimer's law [70, 183], where gas velocity varies nonlinearly. Numerous studies have employed Darcy's law to examine pyrolysis gas behavior [7, 177, 181, 78], as gas velocity remains below 50 m/s during the pyrolysis process [177]. However, Martin et al. [9] found that using Forchheimer's law, while not significantly affecting temperature distribution, could impact inner pressure variations, potentially causing spallation. The main challenge in utilizing Darcy's or Forchheimer's law is the unknown permeability, $\mathbf{K}$, and the

Forchheimer coefficient, β, of Calcarb. In a previous work, [74], micro-scale simulations were performed to solve the Navier-Stokes equations under the Darcy flow assumption, and the permeability tensor was predicted based on the results. The permeability was then compared with values obtained by Borner et al. [75] using direct simulation Monte Carlo methods, revealing an error of nearly 42%. The objective of this work is to extend micro-scale simulations from Darcy flow to Forchheimer flow and deduce $\mathbf{K}$ and $\mathbf{F}$, β from the simulations, while experimentally determining $\mathbf{K}$ and β values for Calcarb.

To provide a detailed overview of the state-of-the-art, we begin by presenting Darcy's law and Forchheimer's law for anisotropic porous media. The tensorial form of both laws for the case of negligible gravity is given in Eq.6.2 [184, 185],

$$\begin{cases} \langle \mathbf{v_g} \rangle = -\frac{\mathbf{K}}{\mu} \cdot \nabla \langle p \rangle^g \\ \langle \mathbf{v_g} \rangle = -\frac{\mathbf{K}}{\mu} \cdot \nabla \langle p \rangle^g - \mathbf{F} \cdot \langle \mathbf{v_g} \rangle \end{cases} \tag{6.2}$$

where superficial and intrinsic phase averages of any quantity φ_i associated with the i-phase are given by $\langle \varphi_i \rangle = \frac{1}{V} \int_{V_i} \varphi_i dV$ and $\langle \varphi_i \rangle^i = \varepsilon_i^{-1} \langle \varphi_i \rangle = \frac{1}{V_i} \int_{V_i} \varphi_i dV$, respectively. In these relationships, V_i denotes the volume of the i-phase contained within the averaging volume V, which represents a representative elementary volume of the porous medium. For the pressure term, $\langle p \rangle^g = \frac{1}{V_g} \int_{V_g} p dV$, while for the velocity term, $\langle \mathbf{v_g} \rangle = \frac{1}{V} \int_{V_g} \mathbf{v_g} dV$. $\mathbf{F}$ is the Forchheimer correction tensor and the last term $\mathbf{F} \cdot \langle \mathbf{v_g} \rangle$ is called the Forchheimer term [71]. There is no assumption on the dependence of $\mathbf{F}$ on $\langle \mathbf{v_g} \rangle$ in this general formulation. In the work of Wang et al. [185], $\mathbf{F}$ has been expressed as follows: $\mathbf{F} = (\mathbf{K} \cdot \boldsymbol{\beta}) |\langle \mathbf{v_g} \rangle| \rho / \mu$, where $\mathbf{K}$ is the permeability tensor, $\boldsymbol{\beta}$ is the Forchheimer coefficient tensor. It should be noted that $\boldsymbol{\beta}$ in this expression is considered as an independent property dependent only on the geometry of the microstructure. Therefore the expression presents a linear dependence of $\mathbf{F}$ on the velocity magnitude, i.e. quadratic Forchheimer term. Other parameters are the gas viscosity μ and density ρ. Two main approaches can be utilized to estimate the permeability and Forchheimer correction tensors numerically: one based on direct micro-scale simulations using classical Navier-Stokes equations, and the other on upscaling theories and solving of the associated closure problems [70, 183, 74, 71, 186]. In cases involving periodic media or when dealing with representative elementary volumes, both methods provide the same results. However, defining a numerical approach for non-periodic anisotropic porous media still remains necessary. In the first method, the permeability tensor, as derived from Darcy's law, is determined by solving the Navier-Stokes equations to obtain pressure and velocity terms which are then suitably averaged [74, 186]. In the second method, the permeability tensor and Forchheimer correction tensor can be numerically estimated by solving a closure problem on a periodic unit cell representative of the structure, such as arrays of spheres [70, 183] or a digital structure based on tomographic images of porous media, such as porous rocks [71]. The permeability tensor $\mathbf{K}$ should be symmetric (and positive definite) and depends solely on the structure of the porous medium. The Forchheimer correction tensor $\mathbf{F}$ relies on various parameters, such as structure, Reynolds number, and pressure gradient direction [183].

In terms of experiments, measurements of the Forchheimer coefficient β for TPS materials have not been reported in the literature. However, data is available for various other materials, such as porous carbon foams [187], porous ceramic foams [188], porous rocky materials [189], and carbon

fiber electrode backing layers [190]. During the experimental process, the volumetric flow rate and pressure drop across the porous sample are typically measured. Subsequently, the permeability and Forchheimer coefficient can be obtained by fitting either Darcy's law or Forchheimer's law in one dimension to the experimental data. The concept of effective permeability K_{eff}, proposed by Sobieski et al. [144], is utilized to analyze the variation between different flow regimes. In Darcy's flow, effective permeability is equivalent to permeability, while in Forchheimer's flow, it represents the combined effect of permeability and the Forchheimer coefficient. Marschall et al. [191, 192] proposed a method for measuring the permeability of porous refractory insulators at room temperature, with measurements performed for both in-plane and transverse sample orientations. This method has been applied to various materials, such as silica-based tiles, PICA, and ceramics. Panerai et al. [91] further extended the experimental conditions to measure the permeability of carbon fibers at high temperatures, up to 1503 K. These experiments [91, 191, 192] are focused on investigating the permeability in the slip regime, that is, considering the Klinkenberg effect.

Both experimental and numerical methods have been employed to derive numerous correlations for the Forchheimer coefficient β or tensor $\boldsymbol{\beta}$ in various porous materials. A summary of the most widely used correlations and their validity ranges can be found in Table 6.1. One of the simplest forms of the Forchheimer coefficient β is presented by Martin et al. [9], who used Ergun's equation [165]. It should be noted that Ergun's equation is commonly employed to describe gas flow through packed beds. Aguilar et al. [71] utilized digital images of porous rocks as microstructures, while Lasseux et al. [183] employed simple unit 2D cells with ordered and disordered arrangement of solid squares. Both approaches applied the volume averaging method and closure problems for solving the permeability and the Forchheimer coefficient or tensor. Although the correlations in Table 6.1 can provide some straightforward reference values, further research through experiments and micro-scale simulations is necessary to accurately determine the permeability tensor and Forchheimer coefficient tensor.

Table 6.1 – Empirical numerical correlations for the Forchheimer coefficient β

Investigators	Media	Method	Correlation	Remarks
Martin et al. [9]	carbon phenolic	experimental	$K = \frac{{d_p}^2 \varepsilon_g^3}{150(1-\varepsilon_g)^2}$, $\beta = \frac{\beta_k}{\sqrt{K}} = \frac{1}{7}\frac{1}{\varepsilon_g^{3/2}}\frac{1}{\sqrt{K}}$, $Fo = \beta_k \frac{\sqrt{K}\rho\lvert\langle v_g\rangle\rvert}{\mu}$	Ergun's equation for a packed bed
Wang et al. [185]	arrays of spheres	experimental	$\boldsymbol{\beta} = 10^{-3.25}\mathbf{K}^{-1.023}\boldsymbol{\tau}^{1.943}$ $logC_{ii} = -3.25 + 2.006 \cdot log\tau_{ii}$ $\mathbf{C} = \mathbf{K} \cdot \boldsymbol{\beta}$	$\boldsymbol{\tau}$ is tortuosity tensor, $\mathbf{C}$ is product tensor
Petrasch et al.[103]	porous ceramic	pore-scale numerical simulation	$K = \frac{d_p^2}{64\varepsilon_s^{3/2}(1+56\varepsilon_s^3)}$, $\beta = \frac{0.550}{\sqrt{K}}$	K used the classical correction for fibrous media
Ahn et al. [193, 191, 194]	Ceramic ablators	experimental	$K = 9.78 \times 10^{-11}\varepsilon_g^{0.381}$ $\beta = 1.222(1/\sqrt{K})$	K= $10^{-10} - 10^{-15}$ m^{-2}
Aguilar et al. [71]	porous rocks	pore-scale numerical simulation	Forchheimer term $\propto \langle v_g\rangle^n$ exponent n are around 1.74 -4.18	

In this context, the objective of this article is to extend micro-scale simulations from Darcy flow regime to Forchheimer flow regime and compute the permeability and Forchheimer coefficient for Calcarb, while experimentally determining these values. We will investigate flows in both through-thickness (TT) and in-plane (IP) directions to assess the relationship between pressure gradient and gas velocity. The remainder of the article is organized into four sections. In Section 6.2, we introduce

the experimental setup and the porous sample. In Section 6.3, we present the numerical method employed for micro-scale simulation. In Section 6.4, we provide the experimental and numerical results of permeability and Forchheimer coefficients for TT and IP directions, followed by a comparison of the two sets of results. Finally, Section 6.5 offers concluding remarks.

6.2 Experimental method

This section presents the experimental setup, sample characteristics, and data analysis method. In the first subsection, we provide a detailed description of the experimental procedures and discuss the uncertainties associated with the experimental setup. The second subsection focuses on the structural properties of the Calcarb samples. Lastly, the third subsection outlines the process of analyzing the experimental data.

6.2.1 Experimental setup and test procedure

Our experimental setup for the measurement of pressure drop in Calcarb is shown in Fig.6.1. The setup consists of a nitrogen gas inlet, a mass flow controller, a pressure transmitter, and a quartz cylindrical tube that contains the sample. Nitrogen is steadily supplied through a piping system.

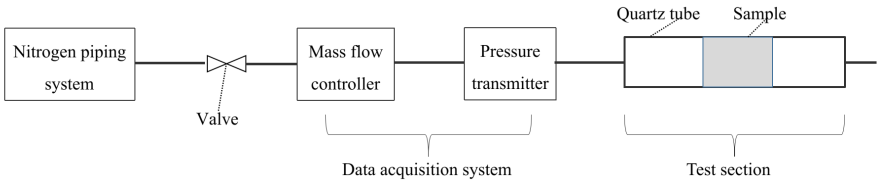

Figure 6.1 – Schematic diagram of the experimental setup

The mass-flow rate is controlled and measured by the mass-flow controller (Bronkhorst) with a range of 0.05 to 10 L/min (q_v), that is, a mass flow rate of Nitrogen, q_m ranging from 9.6×10^{-7} kg/s to 1.92×10^{-4} kg/s at room temperature. The Darcy velocity $\langle v_g \rangle$ varies from 0.0105 m/s to 2.1 m/s. The mass-flow controller's accuracy is $\pm0.5\%$ of the reading. The pressure drop is measured using a differential pressure transmitter (EMERSON FISHER ROSEMOUNT) with an uncertainty of $\pm0.055\%$ F.S. (Full Span is 0-620 mbar). The electrical signal detected by the transmitter is then relayed to a data acquisition system for display. The sample of a length of 20 mm and a diameter of 10 mm is positioned within the test section. To assess the anisotropic properties of the materials, experiments were conducted with samples with different orientations vs the microstructure of the fibrous porous media. (sample 1: Through-Thickness (TT) and sample 2: In-Plane (IP).

In this study, all experiments were carried out in triplicate. For the lower nitrogen flow range (0.05 to 3 L/min), pressure differences were measured at 20 distinct flow rate levels, while for the higher nitrogen flow range (3 L/min to 10 L/min), pressure differences were measured at 30 distinct flow rate levels. The ambient temperature was recorded for each test, with a value of 20 $\pm$ 1 ^{o}C.

6.2.2 Description of Calcarb

Calcarb is composed of chopped carbon fibers with 1 millimeter length and approximately 15 micrometers in diameter [89, 90]. During the manufacturing process, carbon fibers tend to align along the compression plane, resulting in anisotropic properties. The direction perpendicular to this plane is referred to as "Through-Thickness" (TT), while the parallel direction is called "In-Plane" (IP). Fig.6.2 displays the macro and micro-scale structures of the Calcarb sample examined in this study. Fig.6.2 (a) presents a macroscopic image of the sample in the IP and TT plane, demonstrating its anisotropy. Fig.6.2 (b) is a microscopic image captured using a scanning electron microscope (SEM), which reveals that the diameter of individual carbon fibers is around 15 μm. The porosity of Calcarb, denoted as ε_g, is 0.9, and the average fiber diameter is 15 μm. The samples utilized in the experiments were

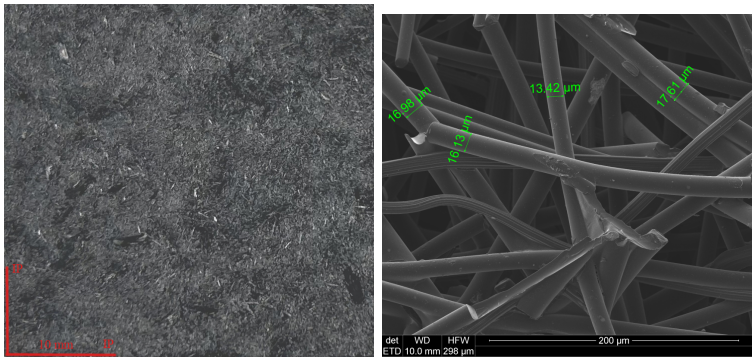

(a) photography (b) SEM image

Figure 6.2 – Macro and micro-scale structures of Calcarb.

extracted from larger billets of material in the IP and TT directions. Each sample was cut into a cylindrical shape with a length and diameter of 20 mm and 10 mm, respectively.

6.2.3 Data analysis

The one-dimensional flow of compressible fluid through a sample based on Darcy's law is given by the following equation:

$$-\frac{\Delta\langle p\rangle^g}{L} = \frac{\mu}{K}\cdot\frac{q_v}{A} = \frac{\mu^2}{K\rho d_{cl}}Re \tag{6.3}$$

where $\Delta\langle p\rangle^g$ is the pressure drop measured by the differential pressure transmitter, L is the length of the sample, μ is the gas viscosity at room temperature, q_v is the volumetric flow rate set by the mass flow controller, and A is the cross-section of the sample. Eq.6.3 is applicable when the Reynolds number ($Re = \rho(q_v/A)d_{cl}/\mu$) is smaller than 0.5, where d_{cl} is fiber cluster diameter. Due to the manufacturing process, there are clusters of fibers made of five to ten fibers. The mean diameter of the fiber clusters has been shown to be the most relevant characteristic length to compute the Reynolds number [74]. The components of $\mathbf{K}$ in the IP and TT directions were determined using Eq.6.3. For higher Reynolds number, the one-dimensional flow based on the Forchheimer equation is expressed as

follows:

$$-\frac{\Delta\langle p\rangle^g}{L} = \frac{\mu}{K}\cdot\frac{q_v}{A} + \rho\beta(\frac{q_v}{A})^n = \frac{\mu^2}{K\rho d_{cl}}Re + \frac{\beta\mu^2}{\rho {d_{cl}}^2}Re^n \tag{6.4}$$

where β is the Forchheimer coefficient. The value of the exponent n is typically 2. At a low Reynolds number, the last term disappears, and the Forchheimer equation reduces to Darcy's law. The data analysis method involves initially defining an effective permeability K_{eff}, as specified in Eq.6.5. It is crucial to note that within the range of Darcy's Law, the effective permeability remains constant, representing the permeability K we aim to find. Conversely, within the Forchheimer regime, the effective permeability encompasses both the permeability K and a term involving the Forchheimer coefficient β. This allows us to achieve two objectives: first, determine the critical Reynolds number separating the two flow regimes, and second, obtain the permeability K within the Darcy regime by fitting the data to Eq.6.3, while acquiring the Forchheimer coefficient β within the Forchheimer regime by fitting the data to Eq.6.4.

$$K_{eff} = -\frac{q_v}{A}\cdot\mu\cdot\frac{L}{\Delta\langle p\rangle^g} = -\frac{\mu^2}{\rho d_{cl}}\frac{L}{\Delta\langle p\rangle^g}Re \tag{6.5}$$

The values of β and the exponent n can be computed using the least-squares approximation method.

6.3 Numerical method

In this section, micro-scale simulations are employed to investigate the incompressible flow of gas within the anisotropic Calcarb sample. The isothermal condition and the under variation in pressure in the domain justify the assumption of incompressible flow. The structure of the Calcarb under investigation is obtained through tomography scanning. Classical Navier-Stokes equations are solved at the pore scale, and the pressure drop is investigated under steady-state conditions across the sample. Ultimately, the permeability tensor and the Forchheimer correction tensor are analyzed.

6.3.1 Numerical model

To determine the permeability and Forchheimer correction tensor, micro-scale simulations must be conducted through a three-dimensional digitized microstructure (Fig.6.3). Detailed information regarding the sample can be found in Subsection 6.3.1.2.

6.3.1.1 Mathematical model and numerical implementation

The fluid region is modeled using the transient laminar Navier-Stokes equations (conservation of mass and momentum) at the pore scale, as presented in Eq.6.6.

$$\begin{cases} \nabla\cdot\mathbf{v_g} = 0 \\ \rho(\frac{\partial\mathbf{v_g}}{\partial t} + \mathbf{v_g}\cdot\nabla\mathbf{v_g}) = -\nabla p + \mu\nabla^2\mathbf{v_g} \\ \mathbf{v_g} = 0 \qquad \text{at} \quad A_{gs} \end{cases} \tag{6.6}$$

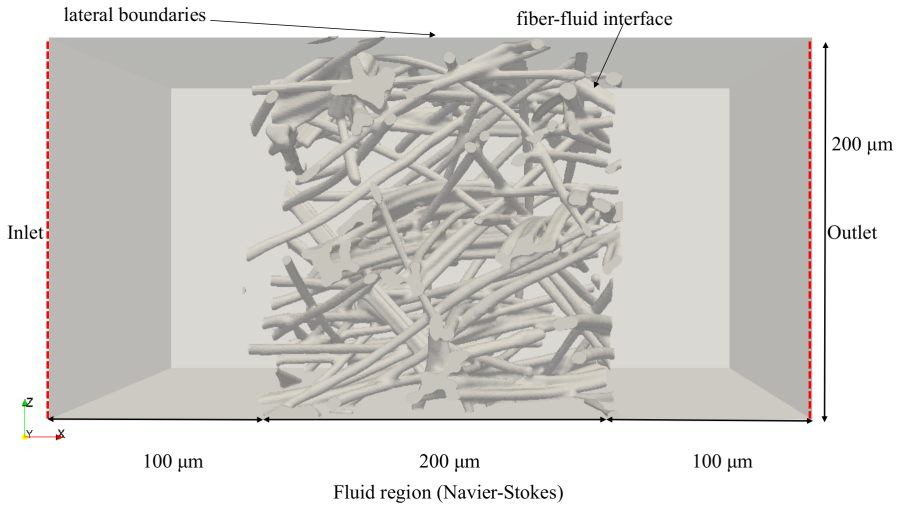

Figure 6.3 – Three-dimensional numerical model used in micro-scale simulation

where $\mathbf{v_g}$ and p are, respectively, the velocity and pressure of the gas phase; A_{gs} represents the interface area between the gas phase and the solid phase contained within the considered region.

Detailed descriptions of the boundary conditions for the system in Eq.6.6 are provided in Table 6.2. These boundary conditions have been demonstrated to be the most suitable for non-periodic porous materials and have been employed in previous studies for permeability calculations [74]. In this work we assume that these boundary conditions are also suitable for the determination of the Forchheimer correction tensor. Regarding velocity, the *slip* condition maintains the tangential velocity at the lateral boundaries while setting the normal component to zero. For pressure, the *zero gradient* condition ensures that the pressure gradient normal to the lateral boundaries is zero.

Table 6.2 – Boundary conditions for the micro-scale simulation

fluid	inlet	outlet	lateral boundaries	fiber-fluid interface
$\mathbf{v_g}$	*fixed value*	*zero gradient*	*slip*	*noslip*
p	*zero gradient*	*fixed value*	*zero gradient*	*zero gradient*

The numerical model was implemented using the OpenFOAM C++ open-source library [195]. Fluid flow was solved with the pimpleFoam solver, which combines the pressure-implicit split-operator (PISO) and semi-implicit method for pressure-linked equations (SIMPLE) algorithms [196]. Second-order schemes, with flux limiters, were used for spatial discretization.

6.3.1.2 Sample geometry and mesh Convergence Analysis

The microstructure of Calcarb was digitally represented using data acquired at the Advanced Light Source at Lawrence Berkeley National Laboratory. Each scan involved capturing 1024 radiographs over a 180° rotation, utilizing X-ray energy of 14 keV. Further details can be found in Borner et al.

[75]. The sample was derived from large billets of material in the TT direction. The volume rendering of the computed micro-tomography for Calcarb is displayed in Fig.6.5. The Calcarb fibers are observed to be aligned at an angle of approximately $\pm 15°$ with respect to the YZ plane (IP). The volume has a resolution of $200 \times 200 \times 200$ voxels, with a voxel size of 2.6 μm. This cubic volume (520 μm length) was selected as the computational domain for micro-scale simulations.

The OpenFOAM automatic mesher, *snappyHexMesh*, [195] was utilized to mesh the fluid domain between the fibers. This tool is a mesh manipulation software that allows users to refine a given background mesh into a desired configuration. The meshing algorithm functions through three primary steps. First, a background mesh is created. Then, the carbon fibers' surface is overlaid onto the background mesh. The algorithm identifies cells that are intersected by the carbon fibers' surface and subsequently subdivides them into four parts, generating mesh refinement near the body surface. Following this, the mesh points in close proximity to the body surface are moved to align with the surface, ensuring that the boundary surfaces of the mesh adhere closely to the prescribed geometry. The quality of the final mesh is highly dependent on the settings of various parameters. Once the parameter configuration process is determined, the next step is to perform a mesh independence verification to ensure that the final mesh does not influence the simulation results. We conduct micro-scale simulations with varying mesh refinement levels, monitoring changes in specific physical quantities. In this case, we choose the pressure difference between the inlet and outlet as an appropriate criterion for evaluating mesh convergence. Two distinct inlet velocities, corresponding to two different Reynolds numbers ($Re = \rho|\langle v_g \rangle| d_{cl}/\mu$), were selected to incorporate the Forchheimer flow regime into the mesh analysis. A mesh convergence study was carried out, ensuring that the pressure residuals remained below 1×10^{-6} and the velocity residuals below 10^{-8}. Fig.6.4 shows the mesh convergence analysis results. Fig.6.4(a) presents the convergence of the pressure drop as the mesh is refined.

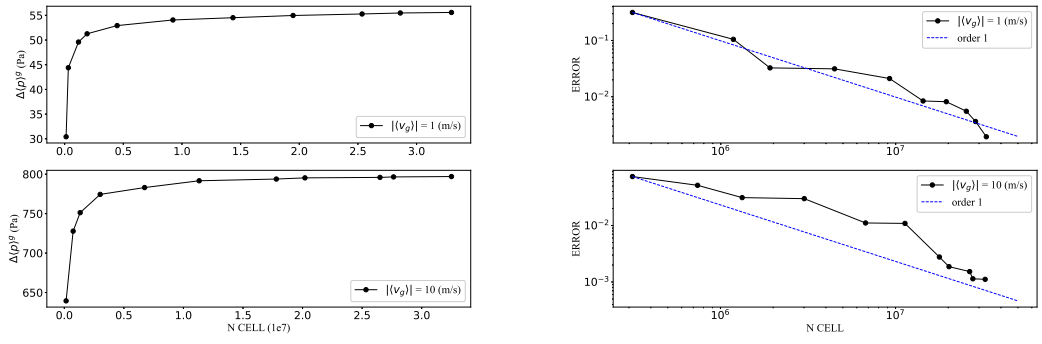

(a) pressure difference

(b) relative error

Figure 6.4 – Mesh convergence analysis results

Starting from a small value (e.g., 30 Pa when the inlet velocity is 1 m/s) for a coarse mesh, the pressure drop rapidly converges towards a stabilized value (e.g., 55 Pa). Fig.6.4(b) plots the numerical

error between two consecutive simulations, which is defined as:

$$ERROR = \frac{\Delta\langle p\rangle^g_{n+1} - \Delta\langle p\rangle^g_n}{\Delta\langle p\rangle^g_{n+1}} \tag{6.7}$$

where the index n represents the simulation with the mesh before refinement. The blue dotted line corresponds to the first-order slopes. The numerical method is then first order with respect to the discretization. The results suggest that when the number of cells surpasses 20 million, the error gradually decreases until it reach a steady state around 1×10^{-2} for $|\langle v_g\rangle| = 1$ m/s and 1×10^{-3} for $|\langle v_g\rangle| = 10$ m/s. Fig.6.5 provides some details of the meshed geometry.

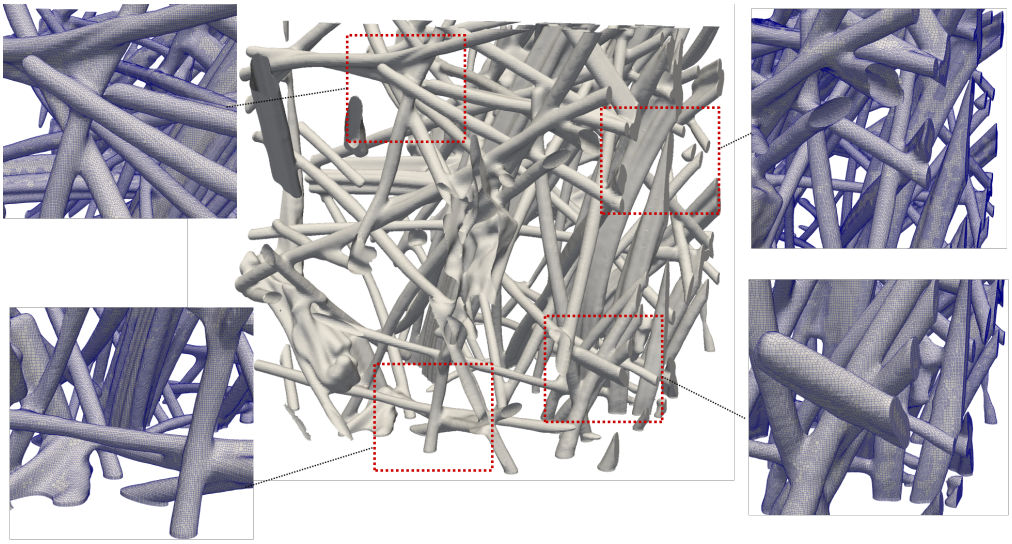

Figure 6.5 – Details of the meshed geometry

6.3.2 Mathematical Description of the Forchheimer term

6.3.2.1 Description of the Forchheimer correction tensor

For the scales of flow in porous media, upscaling of micro-scale problems has been proposed using either homogenization theory [197] or the volume-averaging technique [198]. The macroscopic model is given by Eq.6.8 [70, 183, 74]. When the Reynolds number is small, the second term $\mathbf{F}\cdot\langle\mathbf{v_g}\rangle$ in Eq.6.8 is negligible, validating Darcy's law. In a previous work [74], the case with this term neglected was discussed, and the permeability tensor $\mathbf{K}$ was obtained. In this study, we specifically examine the case where this term is present.

$$\begin{cases} \nabla\cdot\langle\mathbf{v_g}\rangle = 0 \\ \langle\mathbf{v_g}\rangle = -\frac{\mathbf{K}}{\mu}\cdot\nabla\langle p\rangle^g - \mathbf{F}\cdot\langle\mathbf{v_g}\rangle \end{cases} \tag{6.8}$$

The velocity $\mathbf{v_g}$ and pressure p fields at the pore scale are obtained from the resolution of Eq.6.6. Then pressure gradients and velocity components are averaged at the macroscopic scale and substituted

into Forchheimer's law as shown in Eq.6.8. The latter is conveniently expressed as the following system:

$$\begin{cases} \langle v_g\rangle_x = -\frac{1}{\mu}\left(K_{xx}\nabla\langle p\rangle_x^g + K_{xy}\nabla\langle p\rangle_y^g + K_{xz}\nabla\langle p\rangle_z^g\right) - (F_{xx}\langle v_g\rangle_x + F_{xy}\langle v_g\rangle_y + F_{xz}\langle v_g\rangle_z) \\ \langle v_g\rangle_y = -\frac{1}{\mu}\left(K_{yx}\nabla\langle p\rangle_x^g + K_{yy}\nabla\langle p\rangle_y^g + K_{yz}\nabla\langle p\rangle_z^g\right) - (F_{yx}\langle v_g\rangle_x + F_{yy}\langle v_g\rangle_y + F_{yz}\langle v_g\rangle_z) \\ \langle v_g\rangle_z = -\frac{1}{\mu}\left(K_{zx}\nabla\langle p\rangle_x^g + K_{zy}\nabla\langle p\rangle_y^g + K_{zz}\nabla\langle p\rangle_z^g\right) - (F_{zx}\langle v_g\rangle_x + F_{zy}\langle v_g\rangle_y + F_{zz}\langle v_g\rangle_z) \end{cases} \tag{6.9}$$

Upon completing the micro-scale simulations, the macroscopic velocity components $\langle v_g\rangle_x$, $\langle v_g\rangle_y$, and $\langle v_g\rangle_z$ are determined as average values in the domain. The pressure gradient components throughout the sample, $\nabla\langle p\rangle_x^g$, $\nabla\langle p\rangle_y^g$, and $\nabla\langle p\rangle_z^g$ are determined from the mean pressure values at the boundaries and the dimensions of the domain in the x, y, and z directions. Since $\mathbf{K}$ is already determined from a simulation at low Re, the remaining unknowns in the system comprise the nine correction tensor components: F_{xx}, F_{xy}, ..., F_{zz}.

Although the tensorial form of the macroscopic inertial resistance has been pointed out clearly [183], the computation of the Forchheimer correction tensor $\mathbf{F}$ (Eq. 6.8) is very costly in terms of computation time and resources. Indeed, $\mathbf{F}$ can be computed on a periodic unit cell by solving a tensorial closure problem with a Navier-Stokes structure. The procedure used for the computation of the permeability tensor [74], i.e. imposing a velocity (or pressure gradient) successively along the three directions of the unit cell to obtain the full permeability tensor, is no longer valid here due to the non-linear dependence of $\mathbf{F}$ on $\langle\mathbf{v_g}\rangle$. In this work, first of all, for a given direction of the flow, we can only compute three components of the $\mathbf{F}$ tensor. For example, when the inlet velocity is set as (1, 0, 0), indicating the flow direction is along the x-axis, the resulting velocity fields are $\langle v_g\rangle_x$=1.094 m/s, $\langle v_g\rangle_y$=0.022 m/s, and $\langle v_g\rangle_z$=0.011 m/s. Similarly, the corresponding pressure values are $\langle p\rangle_x^g$=-50.873 Pa, $\langle p\rangle_y^g$=-4.001 Pa, and $\langle p\rangle_z^g$=-3.122 Pa. Given that the magnitude of $\langle v_g\rangle_x$ is 49.7 and 99.5 times greater than $\langle v_g\rangle_y$ and $\langle v_g\rangle_z$ respectively, we simplify the problem by neglecting terms related to $\langle v_g\rangle_y$ and $\langle v_g\rangle_z$ in Eq. 6.8. therefore $F_{xy}\langle v_g\rangle_y$, $F_{xz}\langle v_g\rangle_z$, $F_{yy}\langle v_g\rangle_y$, $F_{yz}\langle v_g\rangle_z$, $F_{zy}\langle v_g\rangle_y$, and $F_{zz}\langle v_g\rangle_z$ are 0. By substituting the known quantities into the simplified Eq. 6.9, we can calculate the values of F_{xx}, F_{yx}, and F_{zx}. In a similar way, when the flow direction is along the y-axis, we can only derive the values of F_{xy}, F_{yy}, and F_{zy}. Lastly, for flow along the z-axis, we can ascertain the values of F_{xz}, F_{yz}, and F_{zz}. Detailed information about $\mathbf{F}$ will be explained in the following subsection 6.4.2.1.

6.3.2.2 Description of the Forchheimer coefficient tensor

As outlined in section 6.1, Wang et al. [185] represented $\mathbf{F}$ as $\mathbf{F} = \rho/\mu|\langle v_g\rangle|(\mathbf{K}\cdot\boldsymbol{\beta})$, assuming $\boldsymbol{\beta}$ to be independent of the gas velocity direction. Thus, we calculate $\boldsymbol{\beta}$ following the same procedure used for the computation of the permeability tensor: applying a velocity successively along the three image directions to derive the full $\boldsymbol{\beta}$ tensor. Firstly, we transform tensor $\mathbf{F}$ in Eq. 6.9 into a form involving

$\boldsymbol{\beta}$.

$$\begin{cases} \langle v_g\rangle_x = -\frac{1}{\mu}\left(K_{xx}\nabla\langle p\rangle_x^g + K_{xy}\nabla\langle p\rangle_y^g + K_{xz}\nabla\langle p\rangle_z^g\right) - \rho/\mu|\langle v_g\rangle|((K_{xx}\beta_{xx} + K_{xy}\beta_{yx} + K_{xz}\beta_{zx})\langle v_g\rangle_x \\ \quad +(K_{xx}\beta_{xy} + K_{xy}\beta_{yy} + K_{xz}\beta_{zy})\langle v_g\rangle_y + (K_{xx}\beta_{xz} + K_{xy}\beta_{yz} + K_{xz}\beta_{zz})\langle v_g\rangle_z) \\ \langle v_g\rangle_y = -\frac{1}{\mu}\left(K_{yx}\nabla\langle p\rangle_x^g + K_{yy}\nabla\langle p\rangle_y^g + K_{yz}\nabla\langle p\rangle_z^g\right) - \rho/\mu|\langle v_g\rangle|((K_{yx}\beta_{xx} + K_{yy}\beta_{yx} + K_{yz}\beta_{zx})\langle v_g\rangle_x \\ \quad +(K_{yx}\beta_{xy} + K_{yy}\beta_{yy} + K_{yz}\beta_{zy})\langle v_g\rangle_y + (K_{yx}\beta_{xz} + K_{yy}\beta_{yz} + K_{yz}\beta_{zz})\langle v_g\rangle_z) \\ \langle v_g\rangle_z = -\frac{1}{\mu}\left(K_{zx}\nabla\langle p\rangle_x^g + K_{zy}\nabla\langle p\rangle_y^g + K_{zz}\nabla\langle p\rangle_z^g\right) - \rho/\mu|\langle v_g\rangle|((K_{zx}\beta_{xx} + K_{zy}\beta_{yx} + K_{zz}\beta_{zx})\langle v_g\rangle_x \\ \quad +(K_{zx}\beta_{xy} + K_{zy}\beta_{yy} + K_{zz}\beta_{zy})\langle v_g\rangle_y + (K_{zx}\beta_{xz} + K_{zy}\beta_{yz} + K_{zz}\beta_{zz})\langle v_g\rangle_z) \end{cases} \tag{6.10}$$

To establish a closed system, it is essential to perform three simulations, taking into account three distinct flow directions. This method allows for the creation of a global system of nine equations, as depicted in Eq.6.11.

$$\begin{bmatrix} \langle v_g\rangle_x^1 \\ \langle v_g\rangle_y^1 \\ \langle v_g\rangle_z^1 \\ \langle v_g\rangle_x^2 \\ \langle v_g\rangle_y^2 \\ \langle v_g\rangle_z^2 \\ \langle v_g\rangle_x^3 \\ \langle v_g\rangle_y^3 \\ \langle v_g\rangle_z^3 \end{bmatrix} = -\frac{\mathbf{K}\nabla\langle p\rangle^g}{\mu} - \rho/\mu|\langle v_g\rangle| \begin{bmatrix} \langle v_g\rangle_x^1 & \langle v_g\rangle_y^1 & \langle v_g\rangle_z^1 & 0 & 0 & 0 & 0 & 0 & 0 \\ 0 & 0 & 0 & \langle v_g\rangle_x^1 & \langle v_g\rangle_y^1 & \langle v_g\rangle_z^1 & 0 & 0 & 0 \\ 0 & 0 & 0 & 0 & 0 & 0 & \langle v_g\rangle_x^1 & \langle v_g\rangle_y^1 & \langle v_g\rangle_z^1 \\ \langle v_g\rangle_x^2 & \langle v_g\rangle_y^2 & \langle v_g\rangle_z^2 & 0 & 0 & 0 & 0 & 0 & 0 \\ 0 & 0 & 0 & \langle v_g\rangle_x^2 & \langle v_g\rangle_y^2 & \langle v_g\rangle_z^2 & 0 & 0 & 0 \\ 0 & 0 & 0 & 0 & 0 & 0 & \langle v_g\rangle_x^2 & \langle v_g\rangle_y^2 & \langle v_g\rangle_z^2 \\ \langle v_g\rangle_x^3 & \langle v_g\rangle_y^3 & \langle v_g\rangle_z^3 & 0 & 0 & 0 & 0 & 0 & 0 \\ 0 & 0 & 0 & \langle v_g\rangle_x^3 & \langle v_g\rangle_y^3 & \langle v_g\rangle_z^3 & 0 & 0 & 0 \\ 0 & 0 & 0 & 0 & 0 & 0 & \langle v_g\rangle_x^3 & \langle v_g\rangle_y^3 & \langle v_g\rangle_z^3 \end{bmatrix} \begin{bmatrix} K_{xx}\beta_{xx} + K_{xy}\beta_{yx} + K_{xz}\beta_{zx} \\ K_{xx}\beta_{xy} + K_{xy}\beta_{yy} + K_{xz}\beta_{zy} \\ K_{xx}\beta_{xz} + K_{xy}\beta_{yz} + K_{xz}\beta_{zz} \\ K_{yx}\beta_{xx} + K_{yy}\beta_{yx} + K_{yz}\beta_{zx} \\ K_{yx}\beta_{xy} + K_{yy}\beta_{yy} + K_{yz}\beta_{zy} \\ K_{yx}\beta_{xz} + K_{yy}\beta_{yz} + K_{yz}\beta_{zz} \\ K_{zx}\beta_{xx} + K_{zy}\beta_{yx} + K_{zz}\beta_{zx} \\ K_{zx}\beta_{xy} + K_{zy}\beta_{yy} + K_{zz}\beta_{zy} \\ K_{zx}\beta_{xz} + K_{zy}\beta_{yz} + K_{zz}\beta_{zz} \end{bmatrix} \tag{6.11}$$

By solving Eq.6.11, we obtain the product tensor $(\mathbf{K}\cdot\boldsymbol{\beta})$. We can then compute the values of $\boldsymbol{\beta}$ by applying an inverse operation, i.e., $(\mathbf{K}^{-1}\cdot(\mathbf{K}\cdot\boldsymbol{\beta}))$. Detailed information about $\boldsymbol{\beta}$ will be explained in the following subsection 6.4.2.1.

6.4 Results and discussions

This section presents a comprehensive analysis of both experimental and simulation results. The experimental results show the pressure drop as a function of gas velocity and utilizing the aforementioned data analysis method, the permeability K and Forchheimer coefficient β are calculated for both IP and TT directions. The simulation results illustrate the relationship between the simulated pressure drop and gas velocity. Based on the simulation methodology, the values of permeability and Forchheimer term are obtained. Furthermore, the gas flow distribution within the sample is discussed in this section. Finally, a comparison between the experimental and simulation results is conducted.

6.4.1 Experimental results

The experimental results are summarized in the Appendix 6.5, where q_v represents the gas volume-flow rate, $\langle v_g\rangle$ is the magnitude of the Darcy velocity, and $\Delta\langle p\rangle^g$ denotes the pressure drop between the inlet and outlet. The experimental parameters are as follows: room temperature at 293 K, gas density ρ of 1.17 kg/m^3, gas dynamic viscosity μ of 1.93×10^{-5} kg/(m $\cdot$ s), sample cross-sectional area A of 7.854×10^{-5} m^2, and fiber cluster diameter d_{cl} of 80 μm. Based on the data in Table.6.6, the

experimental results are illustrated in Fig.6.6. Fig.6.6 (a) and (b) display the variations of pressure gradient and effective permeability as a function of the Reynolds number, respectively. The error bars shown in Fig.6.6(a) were calculated based on the uncertainties in the experimental process. The effective permeability is calculated using Eq.6.5. As demonstrated in Fig.6.6 (a), the pressure gradient exhibits a non-linear relationship, and the experimental region covers both Darcy and Forchheimer flow regimes. This observation is further supported by Fig.6.6 (b), where the constant K_{eff} corresponds to the Darcy flow regime. As expected, the obtained permeability in the IP direction is higher than the one in the TT direction.

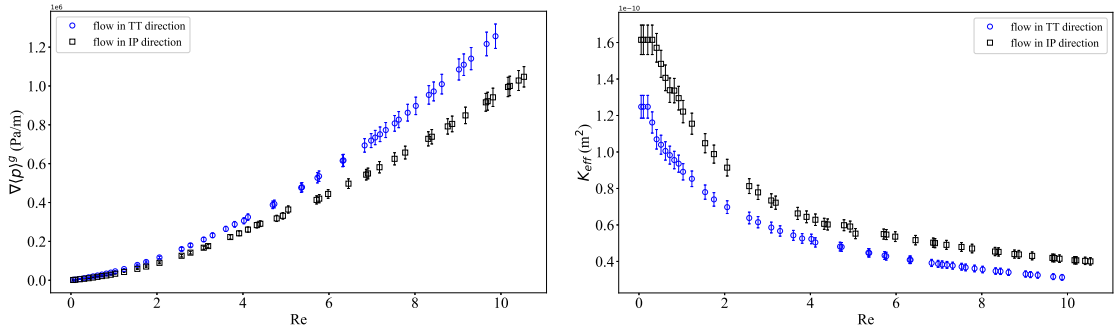

(a) pressure gradient (b) effective permeability

Figure 6.6 – Experimental results measured in IP and TT directions

Fig.6.7 provides a detailed view of the Darcy flow region depicted in Fig.6.6. Initially, we calculate the effective permeability using Eq.6.5, representing permeability within the Darcy regime and subsequently utilize the obtained permeability values to describe the variation of pressure gradient shown in Fig.6.7(a). The pressure gradient demonstrates a linear relationship in the IP direction when the Reynolds number is less than 0.43 and in the TT direction when the Reynolds number is below 0.31. The permeability, K, values for both IP and TT directions are presented in Tab.6.3.

Table 6.3 – Permeability K in IP and TT direction

Flow direction	**Permeability, K (m^2)**	**Limit of Re**
IP	1.615×10^{-10}	0.43
TT	1.248×10^{-10}	0.31

Within the Forchheimer regime, we first substitute K values obtained from Table 6.3 into Eq.6.4, yielding the first coefficient of the polynomial, $\frac{\mu^2}{K\rho d_{cl}}$. The subsequent fitting of experimental data allows us to ascertain the Forchheimer coefficient and the exponent n. This method facilitates describing the intricate relationship between pressure gradient and Reynolds number within the Forchheimer regime. Fig.6.8 presents the variation of pressure gradient with respect to Reynolds number in both the IP and TT directions, along with the curves obtained through data fitting. The values of the Forchheimer coefficient β and exponent n are calculated using the least-squares approximation method and presented in Tab.6.4. First, we use the classic Forchheimer equation with a fixed exponent of 2 to get the Forchheimer coefficient, as shown in Table 6.4's second column, where R^2 denotes the level

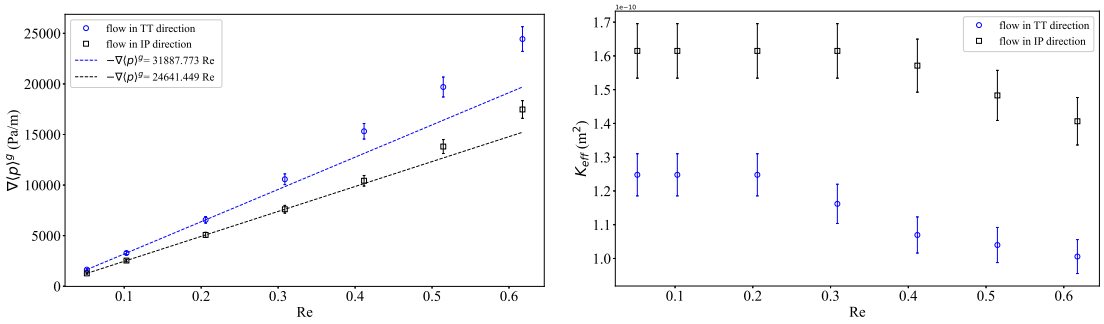

(a) pressure gradient (b) effective permeability

Figure 6.7 – Pressure gradient and effective permeability in Darcy's regime

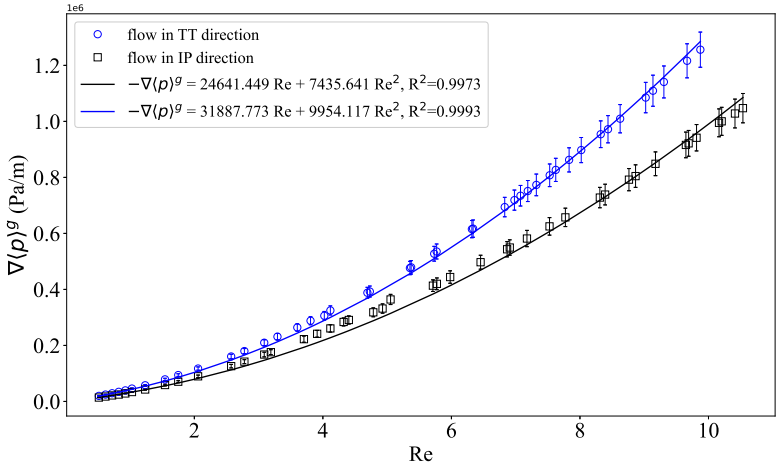

Figure 6.8 – Relationship between pressure gradient and Reynolds number in both the IP and TT directions

.

of fit of the model to the data. Next, we improve the fit by adjusting both the Forchheimer coefficient and the exponent n, with results shown in the third column of the same table. Rather than typically being set as 2, the exponent exhibits minor differences, like Aguilar et al.[71] found in their work with porous rocks. Moreover, the values of β and n are not the same in the IP and TT directions. These disparities arise due to the anisotropy inherent in the sample.

Table 6.4 – Forchheimer coefficient β (1/m) and exponent n in the IP and TT direction

Flow direction	β and n ($n = 2$)	β and n ($n \neq 2$)
IP	1.4948×10^5, 2 ($R^2 = 0.9973$)	2.7015×10^5, 1.73 ($R^2 = 0.9999$)
TT	2.0010×10^5, 2 ($R^2 = 0.9993$)	2.7782×10^5, 1.84 ($R^2 = 0.9999$)

In conclusion, we will proceed to make a simple comparison between the permeability K, the Forchheimer coefficient β obtained in our study, and the data present in Table 6.1. To control for variables, we've opted for the fit results where the exponent is 2. The comparison results are displayed in the table 6.5, where the values of K, were taken directly from our experimental results, specifically $K = 1.615 \times 10^{-10}$ m^2 in the IP direction and 1.248×10^{-10} m^2 in the TT direction and β was calculated based on the corresponding relationship in Table 6.1. The biggest difference between our

Table 6.5 – Comparison of the Forchheimer Coefficient β in the IP and TT direction

Investigators	β (m^{-1})	Remarks
Martin et al. [9]	1.3165×10^4 in IP, 1.4977×10^4 in TT	for packed bed
Petrasch et al. [103]	4.3278×10^4 in IP, 4.9232×10^4 in TT	for porous ceramic
Ahn et al. [194]	9.6157×10^4 in IP, 1.0939×10^5 in TT	for ceramic ablators
Current work	1.4948×10^5 in IP, 2.0010×10^5 in TT	

experiment and the formula in Table 6.1 is when we use the packed bed formula for Calcarb - the results are about ten times apart. When we use the formula for ceramic ablators, the closest material to Calcarb, the results are only about two times apart. However, in this case (ceramic ablators), both calculations remain within the same order of magnitude.

6.4.2 Numerical results

The relationship between the pressure gradient and the flow rate within the Darcy regime was numerically investigated in a previous study by Scandelli et al. [74]. As a crucial material property, the permeability tensor of Calcarb, denoted as $\mathbf{K}$, was calculated. For flows in the Darcy regime (Reynolds number less than 0.5), the value of $\mathbf{K}$ is determined accordingly,

$$\mathbf{K} = \begin{bmatrix} K_{xx} & K_{xy} & K_{xz} \\ K_{yx} & K_{yy} & K_{yz} \\ K_{zx} & K_{zy} & K_{zz} \end{bmatrix}_{x,y,z} m^2 = \begin{bmatrix} 1.561 \times 10^{-10} & 1.391 \times 10^{-11} & 1.021 \times 10^{-11} \\ 1.391 \times 10^{-11} & 1.631 \times 10^{-10} & -5.41 \times 10^{-12} \\ 1.021 \times 10^{-11} & -5.41 \times 10^{-12} & 1.151 \times 10^{-10} \end{bmatrix} m^2 \tag{6.12}$$

A diagonalization procedure is employed to rewrite the permeability tensor K in alignment with the principal axes of rotation. The diagonal matrix $\mathbf{K_{dg}}$ is obtained using the relation $\mathbf{K_{dg}} = \mathbf{P}^{-1}\mathbf{K}\mathbf{P}$,

where $\mathbf{P}$ is change of basis matrix. The values of $\mathbf{K_{dg}}$ and $\mathbf{P}$ are presented in Eq.6.13, with x', y', z' oriented relative to IP, IP, and TT. Fig.6.9 presents the direction of the original coordinates axes x, y, z and the principal axes x', y', and z' (in blue).

$$\mathbf{K_{dg}} = \begin{bmatrix} K_{x'x'} & 0 & 0 \\ 0 & K_{y'y'} & 0 \\ 0 & 0 & K_{z'z'} \end{bmatrix}_{x',y',z'} = \begin{bmatrix} 1.741 \times 10^{-10} & 0 & 0 \\ 0 & 1.491 \times 10^{-10} & 0 \\ 0 & 0 & 1.111 \times 10^{-10} \end{bmatrix} m^2, \mathbf{P} = \begin{bmatrix} -0.6258 & -0.7322 & -0.2686 \\ -0.7790 & 0.6031 & 0.1709 \\ -0.0369 & -0.3163 & 0.9479 \end{bmatrix} \tag{6.13}$$

In Eq.6.13, both $K_{x'x'}$ and $K_{y'y'}$ values correspond to the permeability in the IP direction. However,

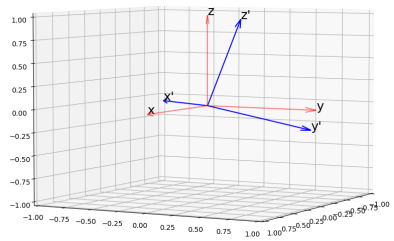

Figure 6.9 – Orientation of the original coordinate axes (x, y, z) and principal axes (x', y', z').

due to the consideration of micro-structural, these two values are not exactly the same.

In this subsection, we first discuss a case involving flow within the Forchheimer regime, showcasing the simulation results and the data processing methodology. Subsequently, we analyze the numerical outcomes obtained at various flow velocities to further elucidate the behavior of the system.

6.4.2.1 Velocity fields and Forchheimer correction tensor

In this particular case, an inlet velocity of 1 m/s is chosen, which corresponds to a Reynolds number of 4.85, indicating that the flow lies within the Forchheimer regime. As discussed in section 6.3.2, the flow velocities for these simulations are set as (1,0,0), (0,1,0), and (0,0,1). Fig.6.10 presents the streamlines within the computational domain, where (a), (b), and (c) respectively correspond to the inlet flow directions along the x, y, and z axes. The streamlines are color-coded based on the velocity magnitude. Fig.6.10 reveals that the maximum gas flow velocity inside the fluid domain can reach values as high as 4.2 m/s, highlighting the complex flow behavior within the porous medium. In each simulation, the pressure gradients $\nabla\langle p\rangle_x^g$, $\nabla\langle p\rangle_y^g$, and $\nabla\langle p\rangle_z^g$ are determined by calculating the average pressure at the interface between the flow and the sample. Simultaneously, the three macroscopic flow velocities, $\langle v_g\rangle_x$, $\langle v_g\rangle_y$, and $\langle v_g\rangle_z$, are obtained by averaging the velocities within the sample. After completing the three simulations, the nine components of the pressure gradients and macroscopic flow velocities can be derived. The next step involves substituting all known values into Eq.6.9 to determine the unknown Forchheimer correction tensor $\mathbf{F}$. In this specific case, the computable terms of the Forchheimer correction tensor $\mathbf{F}$ for the inlet velocities of (1,0,0), (0,1,0) and

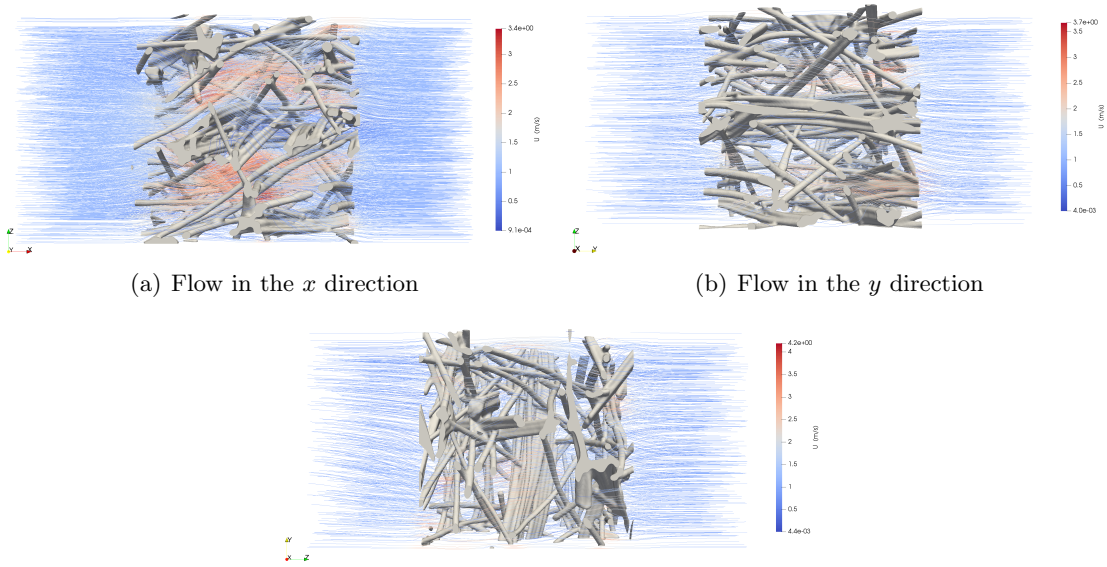

(a) Flow in the x direction

(b) Flow in the y direction

(c) Flow in the z direction

Figure 6.10 – Streamlines visualization in the domain

(0,0,1) are respectively computed as follows:

$$\mathbf{F} = \begin{bmatrix} F_{xx} \\ F_{yx} \\ F_{zx} \end{bmatrix}_{x,y,z} = \begin{bmatrix} 0.901 \\ 0.318 \\ 0.202 \end{bmatrix}, \quad \mathbf{F} = \begin{bmatrix} F_{xy} \\ F_{yy} \\ F_{zy} \end{bmatrix}_{x,y,z} = \begin{bmatrix} 0.308 \\ 0.898 \\ 0.019 \end{bmatrix}, \quad \mathbf{F} = \begin{bmatrix} F_{xz} \\ F_{yz} \\ F_{zz} \end{bmatrix}_{x,y,z} = \begin{bmatrix} 0.413 \\ 0.096 \\ 0.843 \end{bmatrix} \tag{6.14}$$

For each boundary condition, nine components of the tensor $\mathbf{F}$ cannot be obtained. Instead, for a specific flow direction, only three components of the $\mathbf{F}$ tensor can be computed. This restriction results from the non-linear dependency of $\mathbf{F}$ on $\langle \mathbf{v_g} \rangle$. Despite the significant off-diagonal elements, as suggested by the data from Eq.6.14, we still provide reference values for β calculated by the formula $\beta_{ii} = \frac{F_{ii}\mu}{K_{ii}\rho|\langle v_g \rangle|}$, where ii=xx or yy or zz. The values in the xx, yy and zz directions are 0.8452×10^5 m^{-1}, 0.9837×10^5 m^{-1}, and 1.2392×10^5 m^{-1}, respectively. These values, although simplistic, are of the same order of magnitude as the experimental values and thus serve as a rough reference. However, it's worth noting that a more comprehensive approach considering the off-diagonal elements would be necessary for a more accurate comparison.

Now, let's adopt the method proposed by Wang et al.[185], as described in Subsection 6.3.2.2, to directly compute the Forchheimer coefficient tensor using Eq.6.11. we employ the same cases, wherein the inlet gas velocities are respectively set as (1,0,0), (0,1,0), and (0,0,1). The computed value of $\boldsymbol{\beta}$ is found to be

$$\boldsymbol{\beta} = \begin{bmatrix} \beta_{xx} & \beta_{xy} & \beta_{xz} \\ \beta_{yx} & \beta_{yy} & \beta_{yz} \\ \beta_{zx} & \beta_{zy} & \beta_{zz} \end{bmatrix}_{x,y,z} m^{-1} = \begin{bmatrix} 0.915 \times 10^5 & 0.243 \times 10^5 & 0.350 \times 10^5 \\ 0.250 \times 10^5 & 0.889 \times 10^5 & 0.107 \times 10^5 \\ 0.221 \times 10^5 & 0.049 \times 10^5 & 1.183 \times 10^5 \end{bmatrix} m^{-1} \tag{6.15}$$

In the experiment, we obtained the value of $\boldsymbol{\beta}$ as $[1.4948 \times 10^5, 0, 0, 0, 1.4948 \times 10^5, 0, 0, 0, 2.0010 \times 10^5]$

m^{-1} (Table 6.4), whereas, in Eq.6.15, we acquired the full components of tensor $\boldsymbol{\beta}$. In order to compare results Eq.6.15, a diagonalization procedure is necessary to align the tensor with the principal axes of rotation

$$\boldsymbol{\beta_{dg}} = \begin{bmatrix} \beta_{x'x'} & 0 & 0 \\ 0 & \beta_{y'y'} & 0 \\ 0 & 0 & \beta_{z'z'} \end{bmatrix}_{x',y',z'} m^{-1} = \begin{bmatrix} 1.432 \times 10^5 & 0 & 0 \\ 0 & 0.612 \times 10^5 & 0 \\ 0 & 0 & 0.942 \times 10^5 \end{bmatrix} m^{-1} \tag{6.16}$$

Fig.6.11 presents the direction of the original coordinates axes x, y, z and the principal axes x', y', and z' (in blue).

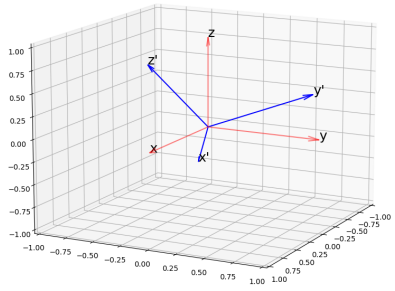

Figure 6.11 – Orientation of the original coordinate axes (x, y, z) and principal axes (x', y', z').

6.4.2.2 Analysis of the pressure drop and Forchheimer correction tensor

In order to extend the numerical computation of the pressure gradient to encompass various fluid velocities $\langle \mathbf{v_g} \rangle$, the Reynolds number is incorporated into the analysis. Fig.6.12 presents the relationship between the pressure gradient components and the Reynolds number for inlet velocities spanning from 0.1 m/s to 10 m/s, corresponding to a Reynolds number range of 0.48 to 48.50, The pressure values obtained from each simulation are depicted using a consistent color scheme. The components $\nabla\langle p \rangle_x^{g1}$, $\nabla\langle p \rangle_y^{g2}$, and $\nabla\langle p \rangle_z^{g3}$ signify the pressure gradient when the inlet flow is aligned with the x, y, and z directions, respectively. The pressure gradient values were acquired from micro-scale simulations for nine values of Re. Within this velocity range, the gas flow exhibits Forchheimer regime behavior. Observations from Fig.6.12 highlight several key points. The pressure gradient components $\nabla\langle p \rangle_x^{g1}$, $\nabla\langle p \rangle_y^{g2}$, and $\nabla\langle p \rangle_z^{g3}$ display a nonlinear behavior as the Reynolds number increases, which can be related to the Forchheimer equation as represented by the fitted curves in Eq.6.17 and Eq.6.18. It should be noted that the differing methodologies in these equations. Eq.6.17 fits only the quadratic coefficient and exponent, keeping the linear term constant, whereas Eq.6.18 fits all terms. Additionally, the pressure gradient component $\nabla\langle p \rangle_z^{g3}$ is notably larger than $\nabla\langle p \rangle_x^{g1}$ and $\nabla\langle p \rangle_y^{g2}$ at the same Reynolds number, indicating the anisotropy of the sample. To further explore the relationship between pressure gradient and Reynolds number in a quantitative manner, we introduce the concept of the Forchheimer term ($\alpha = \mathbf{F} \cdot \langle v_g \rangle$), which provides valuable insights into the flow behavior.

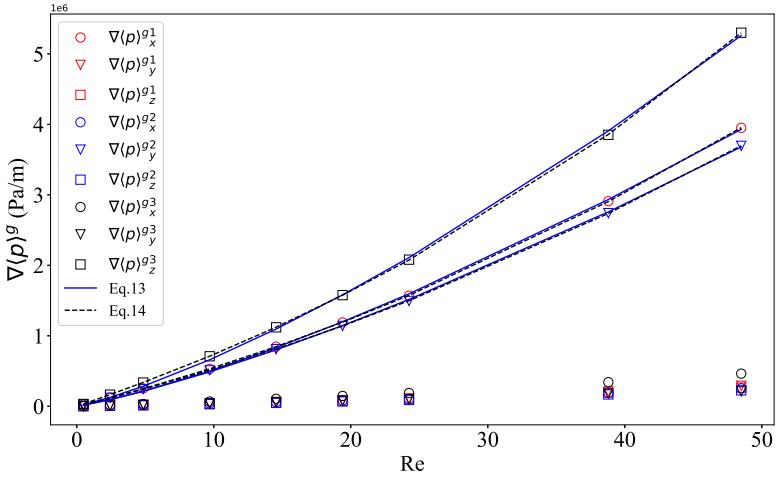

Figure 6.12 – Pressure gradient components of the digitalized Calcarb domain by varying the Re .

$$\begin{cases} \nabla\langle p\rangle^{g1}_x = \frac{\mu^2}{K_{xx}\rho d_{cl}}Re + \frac{\beta\mu^2}{\rho {d_{cl}}^2}Re^n = 25493.8758Re + 9088.99Re^{1.47} \\ \nabla\langle p\rangle^{g2}_y = \frac{\mu^2}{K_{yy}\rho d_{cl}}Re + \frac{\beta\mu^2}{\rho {d_{cl}}^2}Re^n = 24399.7180Re + 9643.5539Re^{1.43} \\ \nabla\langle p\rangle^{g3}_z = \frac{\mu^2}{K_{zz}\rho d_{cl}}Re + \frac{\beta\mu^2}{\rho {d_{cl}}^2}Re^n = 34575.1001Re + 10849.9677Re^{1.49} \end{cases} \tag{6.17}$$

$$\begin{cases} \nabla\langle p\rangle^{g1}_x = 47800.6792Re + 740.9160Re^{1.98} \\ \nabla\langle p\rangle^{g2}_y = 46096.1828Re + 772.4158Re^{1.94} \\ \nabla\langle p\rangle^{g3}_z = 67022.1892Re + 418.0495Re^{2.15} \end{cases} \tag{6.18}$$

The Forchheimer term, α, is the product of the Forchheimer correction tensor $\mathbf{F}$ and Darcy velocity $\langle \mathbf{v_g} \rangle$. As can be derived from Eq. 6.2, this term can also be computed using the following expression:

$$\alpha = -\langle \mathbf{v_g} \rangle - \frac{\mathbf{K}}{\mu} \cdot \nabla\langle p\rangle^g \tag{6.19}$$

In one-dimensional Forchheimer flow, the Forchheimer term is expected to be proportional to the square of the Darcy velocity. To analyze the impact of anisotropy on this term, we first calculated the Forchheimer term using the micro-scale simulation results. Fig.6.13 (a) illustrates all components of the vector α, exhibiting an increasing tendency. The different colors of the dots in Fig.6.13 (a) represent the results of simulations with varying Reynolds numbers, with red, blue, and black dots corresponding to the first, second, and third simulations, respectively. The components α^1_x, α^2_y, and α^3_z denote the Forchheimer term when the inlet flow is aligned with the x, y, and z directions, respectively. Although the values of these three components are higher than the other six, the other components should not be disregarded. For example, the value of α^3_x is approximately 25% of the value of α^3_z. The value of α^1_x, α^2_y, and α^3_z is directly proportional to Re^n, where n is not simply equal to 2, suggesting a more complex relationship between the Forchheimer term and the Reynolds number.

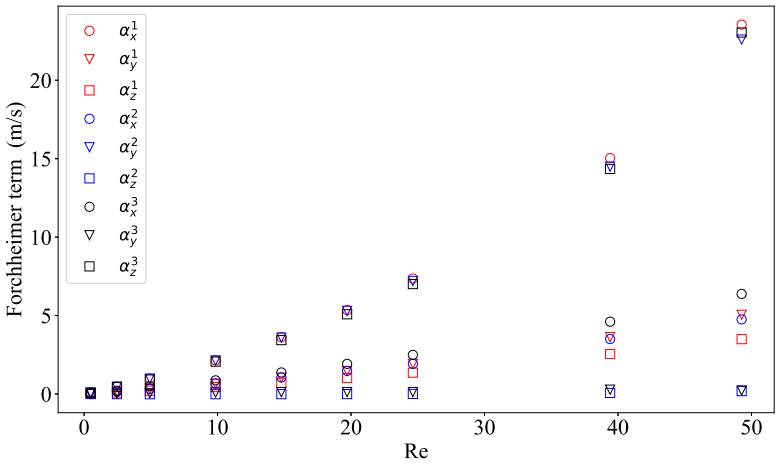

Figure 6.13 – Forchheimer terms estimated from the numerical solution as a function of Reynolds number.

6.4.3 Comparison with Experiment

The strategy for comparing experimental and simulation results focuses on the pressure gradient. In the experiments, we determined the permeability, the Forchheimer coefficient and the exponent in the IP and TT directions by fitting the experimental data using one-dimensional Darcy and Forchheimer equations. In the simulations, we extracted the permeability tensor in the Darcy flow regime. Then, through a transformation of the principal axes, we derived the diagonal permeability tensor components $K_{dg_{x'x'}}$, $K_{dg_{y'y'}}$ and $K_{dg_{z'z'}}$ which correspond to the IP, IP and TT directions in the experimental process. In the Forchheimer flow regime, pressure gradients were obtained.

Fig.6.14 presents a typical comparison of experimental and simulation results within the Darcy flow regime, where the range of Reynolds number in the experiments ranges from 0.05 to 0.50. In this figure, the experimental data in the IP and TT directions are represented by solid blue and dashed black lines, respectively, while the simulation results in the x, y, and z directions, labeled as $\nabla\langle p\rangle^{g1}_x$, $\nabla\langle p\rangle^{g2}_y$, and $\nabla\langle p\rangle^{g3}_z$, are represented by circular, triangular, and square markers. It can be observed that the boundary of the Darcy flow regime for Calcarb, based on numerical results, is around 0.24, with a minor difference between the IP and TT directions. Both simulation and experimental results demonstrate that pressure increases linearly with the Reynolds number when it is below 0.24. Fig.6.14 (b) shows the permeability K remains constant in the Darcy flow regime. The experimental results indicate that the values of K are 1.615×10^{-10} m^2 and 1.248×10^{-10} m^2 in the IP and TT directions, respectively. In the simulations, the corresponding values in the x' or y' (IP) and z' (TT) directions are 1.741×10^{-10} or 1.491×10^{-10} m^2 and 1.111×10^{-10} m^2. The results exhibit a maximum relative difference of around 12.3% ($\frac{1.248-1.111}{1.111}$) within the Darcy flow regime.

Fig.6.15 presents the comparison of experimental and simulation results within the Forchheimer flow regime, where the Reynolds number in the experiments ranges from 0.50 to 10.46. In this figure, the same symbols mentioned earlier are used to represent the respective data points. The data rep-

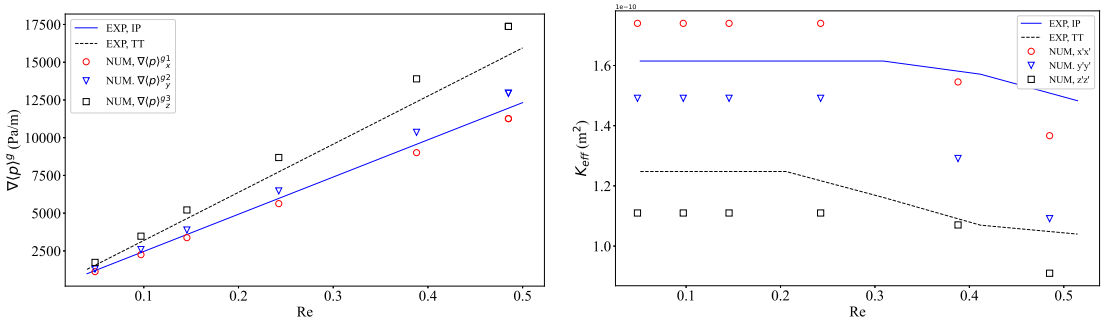

(a) pressure gradient (b) effective permeability

Figure 6.14 – The comparison between numerical and experimental results in the Darcy flow regime.

resenting the experimental correlations are sourced from Table 6.4 (n=2). When comparing values within the Forchheimer flow regime, one can notice that the maximal differences in pressure gradient between simulation and experiment reach up to 64.5% and 68.2% in the IP and TT directions respectively. Given the assumption of one-dimensional flow in the experiments, only the pressure drop in the direction of flow was taken into account. However, in the three-dimensional simulation, the dispersion of flow due to pressure drop in other directions was also considered. This dispersion, occurring in directions other than the main flow, leads to a decrease in pressure drop along the main flow direction, which could result in simulation values being lower than experimental values. Furthermore, as displayed in Fig.6.15, when the Reynolds number is less than 2.4, the difference between the simulation and experimental values is 4.5% and 5.2% in the IP and TT directions, respectively. As the Reynolds number increases, the pressure gradient components in non-main flow directions become more significant, causing the simulated pressure drop along the main flow direction to diverge increasingly from the experimental value.

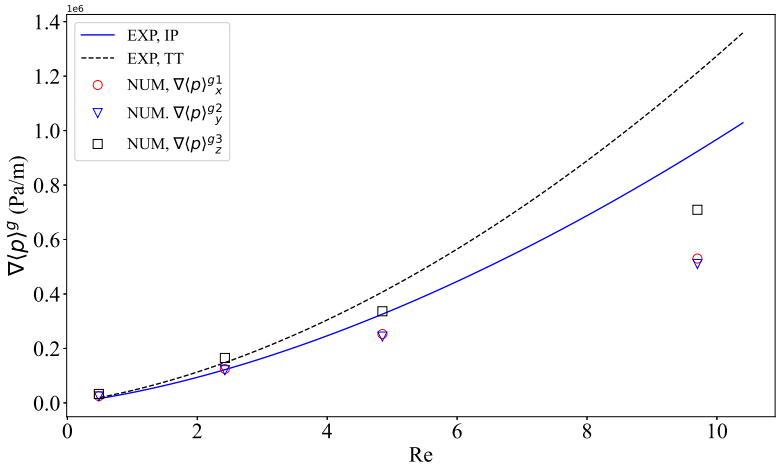

Figure 6.15 – The comparison of numerical and experiment results in the Forchheimer flow regime.

6.5 Conclusion

The objective of this work was to extend micro-scale simulations from the Darcy flow regime to the Forchheimer flow regime and experimentally determine the values of permeability and the Forchheimer coefficient for Calcarb, a carbon fiber preform used as an insulator in TPS applications. To achieve this, we designed an experimental facility to measure the pressure gradient across Calcarb samples in both the Darcy and the Forchheimer flow regimes. Experiments were conducted using nitrogen as the working fluid, for Reynolds numbers ranging from 0.05 to 10.46, and in both in-plane (IP) and through-thickness (TT) orientations. Based on the experimental results, the permeability K, the Forchheimer coefficient β were calculated by fitting the experimental data using one-dimensional Darcy or Forchheimer equations. Concurrently, we computed permeability and pressure gradients from micro-scale numerical solutions, using 3D digital images of Calcarb samples. The numerical model was implemented with finite volumes in PATO. Following permeability calculations, the Forchheimer correction tensor $\mathbf{F}$ was computed and analyzed in terms of fluid velocity.

The results indicated that the limit of the Reynolds number of the Darcy flow regime in Calcarb is around 0.43. Experimental values of permeability are 1.615×10^{-10} m^2 and 1.248×10^{-10} m^2 in the IP and TT directions, respectively. In the simulations, the corresponding values in the principal axes x' or y' (IP) and z' (TT) directions, are 1.741×10^{-10} or 1.491×10^{-10} m^2 and 1.111×10^{-10} m^2. The results exhibit a relative difference of around 12.3% within the Darcy flow regime.

In the Forchheimer flow regime, the experimentally obtained Forchheimer coefficient β had respective values of 1.4948×10^5 m^{-1} in the IP direction, and 2.0010×10^5 m^{-1} in the TT direction. In the simulation process, the values of all the components of the Forchheimer correction tensor $\mathbf{F}$ were not yielded. This is attributed to the fact that the computation method for the permeability tensor $\mathbf{K}$, which involves successively imposing a velocity (or pressure gradient) along the three unit cell directions, becomes inapplicable due to the non-linear dependence of $\mathbf{F}$ on $\langle \mathbf{v_g} \rangle$. Instead, we investigated the relationship between pressure gradient $\nabla \langle p \rangle^g$ and Reynolds numbers Re. $\nabla \langle p \rangle^g$ was presented as a function of Re in the three main directions: x, y, and z. The maximal differences in pressure gradient between simulation and experiment reach up to 64.5% and 68.2% in the IP and TT directions, respectively. This difference could be attributed to several factors. which are: 1) The boundary conditions used to solve permeability may require adjustment due to the influence of inertial flow. 2) The chosen 3D images may not be sufficient to ensure the domain's representativeness. 3) The pressure values obtained in the simulation are oriented along the original x, y, and z axes, which differ from the principal axes. These aspects will be examined in our ongoing work.

Appendix. Results of measurements in IP and TT directions

Table 6.6 – Results of measurements in IP and TT directions

IP				TT			
q_v ($\times 10^{-5}$,m^3/s)	$\langle v_g \rangle$ ($\frac{q_v}{A}$, m/s)	$\Delta\langle p \rangle^g$ (Pa)	Re ($\frac{\rho\langle v_g \rangle d_{cl}}{\mu}$)	q_v ($\times 10^{-5}$,m^3/s)	$\langle v_g \rangle$ ($\frac{q_v}{A}$, m/s)	$\Delta\langle p \rangle^g$ (Pa)	Re ($\frac{\rho\langle v_g \rangle d_{cl}}{\mu}$)
0.083	0.011	25.36	0.053	0.083	0.011	32.82	0.053
0.167	0.021	50.73	0.106	0.167	0.021	65.65	0.106
0.333	0.042	101.45	0.214	0.333	0.042	131.29	0.214
0.500	0.064	152.18	0.309	0.500	0.064	211.53	0.309
0.667	0.085	208.55	0.409	0.667	0.085	306.35	0.409
0.833	0.106	276.18	0.513	0.833	0.106	393.88	0.513
1.000	0.127	349.45	0.615	1.000	0.127	488.71	0.615
1.167	0.149	428.36	0.719	1.167	0.149	583.53	0.719
1.333	0.170	490.36	0.822	1.333	0.170	685.65	0.822
1.500	0.191	569.27	0.925	1.500	0.191	787.76	0.925
1.667	0.212	670.73	1.028	1.667	0.212	919.06	1.028
2.000	0.255	851.09	1.233	2.000	0.255	1152.47	1.233
2.500	0.318	1172.36	1.541	2.500	0.318	1575.53	1.541
2.833	0.361	1409.09	1.744	2.833	0.361	1881.88	1.744
3.333	0.424	1792.36	2.051	3.333	0.424	2348.71	2.051
4.167	0.531	2519.45	2.565	4.167	0.531	3209.41	2.565
4.500	0.573	2840.73	2.770	4.500	0.573	3596.00	2.770
5.000	0.637	3348.00	3.077	5.000	0.637	4194.12	3.077
5.167	0.658	3517.09	3.176	5.333	0.679	4624.47	3.261
6.000	0.764	4447.09	3.694	5.833	0.743	5280.94	3.590
6.333	0.806	4830.36	3.893	6.167	0.785	5762.35	3.787
6.667	0.849	5213.64	4.102	6.514	0.829	6119.76	4.003
7.000	0.891	5675.82	4.309	6.667	0.849	6499.06	4.102
7.132	0.908	5816.73	4.392	7.599	0.968	7760.94	4.676
7.748	0.987	6363.45	4.758	7.661	0.975	7848.47	4.804
7.982	1.016	6634.00	4.915	8.671	1.104	9526.12	5.327
8.183	1.042	7282.18	5.023	8.702	1.108	9577.18	5.353
9.250	1.178	8268.55	5.681	9.283	1.182	10547.29	5.715
9.350	1.191	8398.18	5.757	9.344	1.190	10707.76	5.723
9.685	1.233	8882.91	5.946	10.263	1.307	12341.65	6.306
10.452	1.331	9942.55	6.421	10.232	1.303	12305.18	6.281
11.120	1.416	10866.91	6.832	11.060	1.408	13880.71	6.780
11.187	1.424	10990.91	6.870	11.304	1.439	14376.71	6.994
11.620	1.480	11633.45	7.133	11.457	1.459	14690.35	7.130
12.188	1.552	12501.45	7.485	11.641	1.482	15025.88	7.161
12.588	1.603	13144.00	7.728	11.856	1.510	15463.53	7.301
13.457	1.713	14558.73	8.259	12.193	1.552	16149.18	7.509
13.590	1.730	14772.91	8.342	12.346	1.572	16535.76	7.602
14.190	1.807	15838.18	8.708	12.682	1.615	17250.59	7.921
14.357	1.828	16091.82	8.813	12.988	1.654	17950.82	8.133
14.858	1.892	16971.09	9.123	13.479	1.716	19081.41	8.276
15.625	1.989	18318.18	9.597	13.662	1.740	19438.82	8.417
15.693	1.998	18430.91	9.641	13.968	1.779	20190.12	8.597
15.893	2.024	18831.09	9.759	14.612	1.860	21700.00	8.960
16.460	2.096	19896.36	10.110	14.795	1.884	22188.71	9.084
16.527	2.104	20003.45	10.149	15.070	1.919	22816.00	9.290
16.862	2.147	20561.45	10.355	15.654	1.993	24325.88	9.643
17.062	2.172	20944.73	10.477	15.989	2.036	25120.94	9.745

Chapter 7

Multi-scale investigation of flow and heat transfer coefficients in packed beds at high temperature

Preamble

Authors: S.Liu; A.Ahmadi-Senichault; C.Levet; J. Lachaud;
Affiliations: Arts et Métiers Institute of Technology, Univ. Bordeaux, CNRS, Bordeaux INP, I2M, UMR 5295, F-33400 Talence, France;
Published: No;
Conference: This work has been presented at the 15th Annual International Conference on Porous Media (InterPore2023), 30th May 2023 - Online ;

Abstract

In this study, we investigate the flow and the heat transfer coefficient within randomly packed beds by means of numerical simulations in the local micro-structure and the macro-structure, respectively. For the generation of the local micro-structure, a 3D randomly packed bed filled with sphere particles is constructed by the discrete element method (DEM) software LIGGGHTS. Fully 3D simulations of the gas flow through the packed bed are performed. Numerical tools based on OpenFOAM are used to mesh the geometry in fluid and solid domains. The flow and heat transfer coefficients of the packed beds are calculated based on numerical results. For the simulations in the macrostructure, based on the volume averaging method, a 2D axisymmetric structure is generated to represent the 3D model of randomly packed beds. Numerical tools based on porous material analysis toolbox software PATO are used to solve Forchheimer's flow and the local thermal non-equilibrium (LTNE) model within the packed beds. The effective parameters, that is, the thermal conductivities and heat transfer coefficients, are obtained by carrying out an inverse analysis. The method adopted allows automatic optimization of parameters by coupling the Open Source optimization software Dakota with PATO.

At the micro-scale, the permeability and Forchheimer coefficient are determined, and the critical transition from Darcy flow to Forchheimer flow is observed at a specific Reynolds number. The volumetric heat transfer coefficient exhibits transient behavior, with significant increases observed at higher inlet velocities. The discrepancy between the h_v value obtained by integration of micro-scale results and the one calculated from the inverse analysis is found to be less than 3.8%.

Keywords: Granular media; Permeability; Pore scale; Macro-scale; Experimental validation

7.1 Introduction

Packed bed reactors are widely used in various industrial processes, including reactions, separations, and purification processes [199, 133, 200]. These beds are typically constructed by packing spheres or cylindrical particles in a container [133, 166]. Recently, packed bed has garnered increased attention as a thermal energy storage device. Fluid flow processes in a packed bed can be modeled by using either a micro- or macro-scale approach. Micro-scale models consider pore-scale behavior, including pore heterogeneity and fluid-solid interactions [201, 202, 203]. In contrast, macro-scale models generally treat the packed bed as a homogeneous and isotropic medium, where transfer phenomena are described by averaged equations [68, 204, 205, 206, 207].

In order to bridge micro- and macro-scale models of packed beds, upscaling methods such as the homogenization theory and the volume-averaging technique establish the relationships between variables at different scales. In an equivalent porous continuum model at macro-scale, the value at each point of a macroscopic variable is the volume average value of the corresponding microscopic variable in a representative elementary volume (REV). In macroscopic models, some phenomenological parameters are introduced to characterize the relationships between macroscopic variables. For instance, permeability K, and the Forchheimer coefficient β describe the linear and nonlinear interrelations between pressure drop and velocity for low- and high-speed flows respectively [208, 209]; porosity ε_g, effective thermal conductivity k_{eff} and interfacial heat transfer coefficient h_{sg} characterize the heat transfer process within a packed bed [205]. Several correlations have been developed from experiments such as the Ergun or Kozeny-Carman expressions for pressure drop [166, 210], and Whitaker or Wakao expressions [105, 126] for heat transfer characteristics. Furthermore, by means of numerical methods at the micro-scale, correlations for k_{eff} or h_s have been obtained [133, 166, 211, 212, 132]. However, under some specific conditions, like high temperature and high Reynolds flows, these correlations need to be enhanced to accommodate the substantial changes of the gas properties. Otherwise, there is a possibility that the model may not accurately capture the micro-scale heterogeneity of the porous structure, potentially affecting the reliability of the numerical results. To investigate the pressure drop and heat transfer characteristics of a randomly packed bed at high temperatures, our work employs both micro- and macro-scale approaches and compares the respective features of temperature obtained from these different scales.

To solve a micro-scale problem, the first step is to build a microstructure. Regular structures such as

arrays of square and staggered arrangements of square cylinders have been employed [213, 214]. With the progress of the resolution of computed micro-tomography and computer resources, one can obtain a more realistic microstructure of the packed bed directly by using X-ray Computed Tomography (XCT) scanning [201, 215] or alternatively, generate the packed bed structure by using the discrete element method (DEM) after providing the geometry of a single particle with its diameter d_{par} [200, 166, 211]. According to the obtained microstructure, the global packed bed region consists of the solid and the fluid regions. The velocity and pressure variables only need to be solved within the fluid region using the Navier-Stokes equations. Specifically, for low Reynolds numbers and constant temperature conditions, the fluid is treated as incompressible [166, 132, 74]. However, for high Reynolds numbers or when temperatures vary, the fluid is considered compressible. For the temperature distribution in the packed bed, due to the thermal resistance between particles and gas within the packed bed, a temperature jump occurs across the solid-fluid interface. Therefore, the temperatures of the solid and fluid regions need to be solved separately [132]. To characterize the relative significance of convective heat transfer at the interface compared to conductive heat transfer within the solid, we introduce a dimensionless number, Biot number ($Bi = h_s d_{par}/k_s$). For very small Biot numbers ($Bi \ll 0.1$), heat transfer within the solid can be considered instantaneous. As a result, it is sufficient to solve the heat transfer equation within the fluid region, and the heat transfer within the solid can be neglected.

After obtaining microscopic numerical results, the closure method and the integral method enable to determine various physical quantities corresponding to different macroscopic models. The principle of these two methods is to integrate microscopic-scale variables on solid-fluid interfaces or within the region to obtain macroscopic quantities. The closure method is applicable to periodic unit cells or sufficiently large volume domains that account for all characteristics of the pore structure. The integration method can be applied to diverse geometries. The heat transfer in a packed bed at the macro-scale can be studied using either the local thermal equilibrium (LTE) or local thermal non-equilibrium (LTNE) model [68, 216]. The LTE model assumes that the fluid and solid rapidly reach an equilibrium state thus it only involves one global temperature equation, where the effective conductivity $\mathbf{k_{eff}}$ needs to be determined. The LTNE equation suits the condition where the thermal conductivity of solid and fluid phases exhibit a large difference or heat transfer involves internal heat generation [67, 217]. Therefore it leads to a two-temperature model involving three quantities: gas and solid effective thermal conductivities $\mathbf{k_{g,eff}}$ $\mathbf{k_{s,eff}}$ respectively, and volumetric heat transfer coefficient h_v. In many works, $\mathbf{k_{g,eff}}$ and $\mathbf{k_{s,eff}}$ were straightforwardly calculated as the product of the corresponding porosity and thermal conductivity of the respective phase, as following expressions:

$$\mathbf{k_{g,eff}} = \varepsilon_g k_g \mathbf{I} \qquad \mathbf{k_{s,eff}} = \varepsilon_s k_s \mathbf{I} \tag{7.1}$$

Wakao et al. [126] considered the effect of fluid dispersion in the longitudinal ($||$) and transverse ($\perp$) flow directions and modified the expression of $\mathbf{k_{g,eff}}$ by introducing the product of the Reynolds number and the Prandtl number with a coefficient. Quintard et al. [68] provided a theoretical formulation, stating that $\mathbf{k_{g,eff}}$ is influenced by three factors: thermal conduction, tortuosity, and dispersion, resulting in its anisotropic behavior [68, 72, 30]. For the volumetric heat transfer coefficient h_v, it can

be determined through the integration method, which reads as follows: [218],

$$h_v = \frac{\frac{1}{V}\int_{A_{gs}} k_g \nabla T_g \cdot \mathbf{n}_{gs} dA}{\langle T_s \rangle^s - \langle T_g \rangle^g} \tag{7.2}$$

where V is volume of the global region and A_{gs} is the solid-fluid surface. T_i and $\langle T_i \rangle^i$ denote the point temperature in the i-phase and the intrinsic phase average temperature for the i-phase, $\langle T_i \rangle^i = \frac{1}{V_i}\int_{V_i} T_i dV$, V_i is the volume of the i-phase contained within the volume V. $\mathbf{n_{gs}}$ is the outward unit normal vector, which points from the gas phase towards the solid phase.

The objective of our work is to apply a multi-scale approach to investigate the pressure drop and heat transfer coefficients in a randomly packed bed at high temperatures. To start, we build a 3D randomly packed bed filled with spherical particles via the DEM software LIGGGHTS. Two microscopic models are solved in this packed bed for different situations: the first one is an incompressible flow under constant temperature, characterized by the incompressible Navier-Stokes equations, the solutions are then used to obtain permeability and the Forchheimer coefficient. The second is a transient compressible flow, with high-temperature gas (800K) entering from the inlet, by a model coupling mass and momentum conservation equations for the fluid phase, and energy equations for fluid and solid phases, respectively. Once the temperature field is obtained, h_v can be evaluated by Eq.7.2. Next, in the macroscopic simulation, a 2D axisymmetric structure is designed to mimic the three-dimensional cylindrical structure. The macroscopic governing equations consist of the macroscopic mass and momentum equations and the LTNE model. The effective thermal conductivities and heat transfer coefficients were optimized by using an inverse analysis approach, wherein the governing equations are solved at each iteration to approximate the volume average of the microscopic temperature. The article is organized as follows. In section 7.2, we generate the packed bed structure and present the numerical methods for two microscopic models. In section 7.3, we present the results of micro-scale simulations and investigate the pressure drop at room temperature and the heat transfer coefficient at high temperatures. In section 7.4, the numerical method and results at the macro-scale are presented. It is based on a multi-objective optimization method to minimize errors between the data obtained from the two scales. Some concluding remarks are given in section 7.5.

7.2 Numerical methods at the micro-scale

In this section, we first solve the classical Navier-Stokes equations, assuming constant thermophysical properties, to obtain the pressure drop. This information is then utilized to determine permeability and Forchheimer coefficients. Furthermore, we solve coupled heat and mass transfer equations, considering variable thermophysical properties, to simulate the transient temperature distribution of gas and solid during the heat transfer process. This enables us to determine the heat transfer coefficient. The first subsection outlines the generation of packed beds using the discrete element method (DEM). Subsequently, we introduce the mathematical model and boundary conditions required for solving the flow and heat transfer equations.

7.2.1 Random packed bed generation

To generate a geometric representation of randomly packed beds that accurately reflects the stacking structure, we employed the open-source software LIGGGHTS [219]. This software utilizes the discrete element method (DEM) to simulate the effects of gravity on particles within the packed bed, creating a realistic medium using advanced mathematical functions [220]. Spherical particles are inserted at the top of the tube and fall under the influence of gravity. The software individually tracks each particle's trajectory and collisions, applying Newton's laws of translational and rotational momentum, which account for the possibility of inelastic rebound. The packing process ceases when the kinetic energy of the particles dissipates, and the particles come to rest. Fig. 7.1 presents a 3D view of the randomly packed beds filled with spherical particles. The tube has a diameter of 200 mm and a height of 180 mm, while the spherical particles have a uniform diameter of 16 mm.

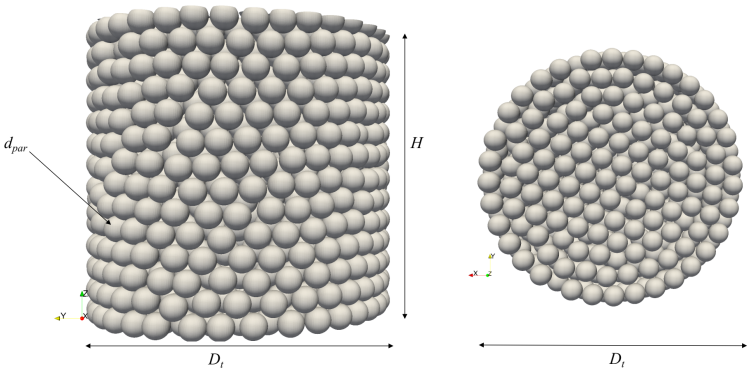

(a) front view of a packed bed

(b) bottom view of a packed bed

Figure 7.1 – Views of the front and the bottom of packed beds with spherical particles.

To validate the accuracy of the generated packed bed model, we calculated the global porosity ε_g and compared it with the classical correlation proposed by Muller [142, 143], which is defined and expressed as follows:

$$\varepsilon_g = 1 - \frac{V_{solid}}{V_{total}} = 0.365 + 0.22/(D_t/d_{par}) \tag{7.3}$$

where V_{solid} and V_{total} represent the volume of spherical particles and the total volume of the packed bed, respectively. This classical correlation applies to randomly packed beds composed of uniformly sized spherical particles. The volume of spherical particles was determined using a ParaView filter (Integrate Variables [221]). The global porosity of the randomly packed bed of spheres was found to be 0.379, while the value calculated from Eq.7.3 was 0.382, resulting in a relative error of 0.7%. These results confirm the reliability and accuracy of the DEM method used in this study for generating randomly packed beds of spheres.

7.2.2 Numerical model

The numerical model shown in Fig. 7.2 consists of a three-dimensional geometry with different regions defined as follows: fluid domains (flow1 and flow2) and a porous domain (packed bed). In the first case, the pressure drop was calculated to determine the permeability and Forchheimer coefficient by solving the classical Navier-Stokes equations. The fluid was assumed to be incompressible in both the fluid and porous domains, and the thermophysical properties of the fluid were assumed to be constant. The permeability and Forchheimer coefficient were then obtained by setting different inlet velocities. In the second case, the coupled heat and mass transfer equations were solved to calculate the heat transfer coefficient. High-temperature air with $T_g = 800$ K was used to heat low-temperature particles with $T_s = 300$ K, and the thermophysical properties of the gas and solid were assumed to be temperature-dependent. Additional details will be discussed below.

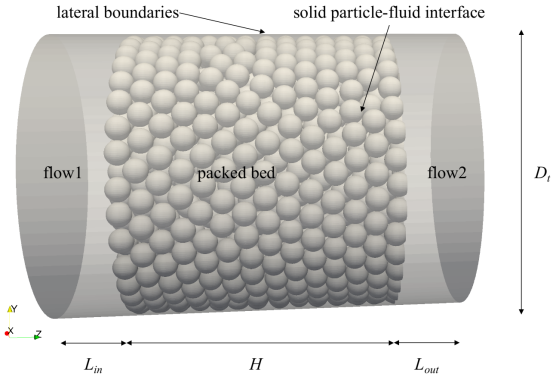

Figure 7.2 – Three-dimensional numerical model of the packed bed.

7.2.2.1 Mathematical model and numerical implementation

For the first case, only the mass and momentum equations were solved. The flow in both the fluid domains (flow1 and flow2) and the porous domain (packed beds) was considered to be transient, incompressible, and without heat transfer. The mass and momentum equations are given by Eq. 7.4:

$$\begin{cases} \nabla \cdot \mathbf{v_g} = 0 \\ \rho_g \left(\frac{\partial \mathbf{v_g}}{\partial t} + \mathbf{v_g} \cdot \nabla \mathbf{v_g} \right) = -\nabla p + \mu_g \nabla^2 \mathbf{v_g} \end{cases} \tag{7.4}$$

where $\mathbf{v_g}$ and p represent the velocity and pressure of the fluid, respectively. ρ_g and μ_g denote the density and dynamic viscosity of the fluid.

For the second case, the transient compressible laminar Navier-Stokes equations and energy equations are used to model the flow domains (flow1 and flow2). In the porous domain (packed beds), heat transfer is modeled using conduction in both phases and convection in the fluid phase. The coupling between the different regions is achieved by ensuring the conservation of mass and continuity of temperatures and heat fluxes at the interfaces. The governing equations for compressible gas flow

at the micro-scale are given:

$$\begin{cases} \partial_t \rho_g + \nabla \cdot (\rho_g \mathbf{v_g}) = 0 \\ \rho_g \left(\frac{\partial \mathbf{v_g}}{\partial t} + \mathbf{v_g} \cdot \nabla \mathbf{v_g} \right) = -\nabla p + \mu_g \nabla^2 \mathbf{v_g} \\ \rho_g c_{p,g} \frac{\partial T_g}{\partial t} + \rho_g c_{p,g} \mathbf{v_g} \cdot \nabla T_g = k_g \nabla^2 T_g \\ \rho_s c_{p,s} \frac{\partial T_s}{\partial t} = k_s \nabla^2 T_s \end{cases} \tag{7.5}$$

where T_g and T_s are respectively the temperatures of the fluid and the solid. $c_{p,i}$ and k_i denote the specific heat at constant pressure and thermal conductivity of the i phase.

Table 7.1 presents the boundary conditions used for the first case, which involves only the fluid domain and includes only pressure and velocity terms. The *fixed value* condition is used to specify a constant value for the inlet velocity. At the solid particle-fluid interface the *no slip* condition is applied to the packed bed domain. At the lateral boundaries, two different kinds of boundary conditions can be applied: *no slip* or *symmetry*, the latter assuming that the domain is a subset of an infinite periodic domain [166]. So we use *no slip* boundary conditions for the lateral boundaries. The pressure boundary condition is set as *zero gradient* to ensure that the pressure gradient perpendicular to the wall is zero. The thermophysical properties of air were evaluated at room temperature (20°C), where the density of air is 1.20 kg/m^3, dynamic viscosity is 1.90×10^{-5} Pa s, and the gas molar constant is 28.96 g/mol. The numerical model was implemented using the Porous material Analysis Toolbox based on OpenFoam (PATO) [92]. The classical Navier-Stokes equations (Eq.7.4) were solved with the *pimpleFoam* solver, which is a combination of the pressure-implicit split-operator (PISO) and the semi-implicit method for pressure-linked equations (SIMPLE) algorithms [196]. Second-order schemes, with flux limiters, were used for spatial discretization.

Table 7.1 – Boundary conditions for gas flow simulation

fluid	inlet	outlet	solid particle-fluid interface	lateral boundaries
$\mathbf{v_g}$	*fixed value*	*zero gradient*	*no slip*	*no slip*
p	*zero gradient*	*fixed value*	*zero gradient*	*zero gradient*

Table 7.2 – Boundary conditions for coupled heat simulation

Region	Initial conditions	Boundary conditions			
fluid		inlet	outlet	solid particle-fluid interface	lateral boundaries
$\mathbf{v_g}$	0 m/s	*fixed value*	*pressureInletOutletVelocity*	*no slip*	*no slip*
p	0 Pa	*fixedFluxPressure*	*fixed value*	*zero gradient*	*zero gradient*
T_g	300 K	*fixed value* (800 K)	*zero gradient*	$k_g \nabla T_g = k_s \nabla T_s$	*zero gradient*
solid		solid		interface	
T_s	300 K	*zero gradient*		$k_s \nabla T_s = k_g \nabla T_g$	

Table 7.2 presents the initial and boundary conditions for the transient heat transfer problem, which includes both the fluid and porous domains. The inlet velocity and outlet pressure for the fluid phase are set to fixed values. The *no slip* boundary condition is applied at the sides and interface to set the velocity to zero. The *fixedFluxPressure* condition is imposed at the inlet to enforce a specific pressure gradient, ensuring that the boundary flux is determined by the specified velocity boundary condition. The thermophysical properties of both the solid (glass) and gas (air) phases are temperature-dependent, and their values are listed in Table 7.3. A multi-block approach is used, where different sets of equations are solved at each time step with appropriate boundary conditions, computed from the mass and energy balances at the interfaces. The equations in the porous and fluid domains are computed using the conjugate heat transfer solver (chtMultiRegionFoam) of OpenFOAM v9. Fluid flow is solved using *pimpleFoam* solver. The equations are solved in series, with appropriate mesh refinement and time steps to ensure that the order of convergence is reached, as described in the section 7.2.2.2.

Table 7.3 – Properties of gas (air) and solid (glass) as a function of temperature

		gas		solid	
T(K)	$c_{p,g}$ ($\mathrm{J\,kg^{-1}\,K^{-1}}$)	μ_g ($\mathrm{kg\,m^{-1}\,s^{-1}}$)	k_g ($\mathrm{W\,m^{-1}\,K^{-1}}$)	$c_{p,s}$ ($\mathrm{J\,kg^{-1}\,K^{-1}}$)	k_s ($\mathrm{W\,m^{-1}\,K^{-1}}$)
290	1010.4	1.909e-05	0.02798	768.75	0.850
340	1013	2.105e-05	0.03091	820.82	0.909
390	1017.5	2.306e-05	0.03401	866.73	0.971
440	1023.9	2.507e-05	0.03719	907.02	1.035
490	1032	2.710e-05	0.04049	942.27	1.105
540	1041.5	2.9135e-05	0.044	973.03	1.177
590	1055.7	3.1198e-05	0.0476	1000.48	1.249
640	1067.6	3.2993e-05.	0.0508	1024.03	1.326
690	1079.8	3.4712e-05	0.0541	1044.78	1.405
740	1092.06	3.6432e-05	0.0574	1063.27	1.486
800	1104.11	3.8156e-05	0.0607	1080.07	1.569

7.2.2.2 Mesh Convergence Analysis

In the first case, only the mass and momentum equations need to be solved for the fluid phase in both fluid and porous domains, and thus only the fluid phase required meshing. In contrast, in the second case, the energy equations for both phases need to be solved separately, which required meshing for both phases. Therefore, we chose to mesh both phases using the OpenFOAM automatic mesher, *snappyHexMesh*, [195]. This tool is a mesh manipulation software that allows users to refine a given background mesh to their desired configuration. The meshing algorithm works through three primary

steps. First, a background mesh is generated, followed by the overlaying of particle surfaces onto the mesh. The algorithm identifies cells intersected by the particle surfaces and subdivides them into four parts, creating mesh refinement near the body surface. Subsequently, mesh points near the body surface are moved to align with the surface, ensuring that the boundary surfaces of the mesh conform closely to the prescribed geometry. The quality of the final mesh depends highly on various parameter settings. Once the parameter configuration process is established, the next step is to perform a mesh independence verification to ensure that the final mesh does not influence the simulation results.

To evaluate mesh convergence, we conducted micro-scale simulations with varying mesh refinement levels, monitoring specific physical quantities. For this analysis, we selected the pressure difference between the inlet and outlet as an appropriate criterion. To incorporate both Darcy and Forchheimer flow regimes [144] into the mesh analysis, three different inlet velocities ($|\langle v_g \rangle|$) corresponding to three different Reynolds numbers ($Re = \rho_g |\langle v_g \rangle| d_{par}/\mu_g$) were chosen. A mesh convergence study was performed, ensuring that the pressure residuals remained below 10^{-6} and velocity residuals below 10^{-8}. The results of the mesh convergence analysis are presented in Fig.7.3. The pressure difference

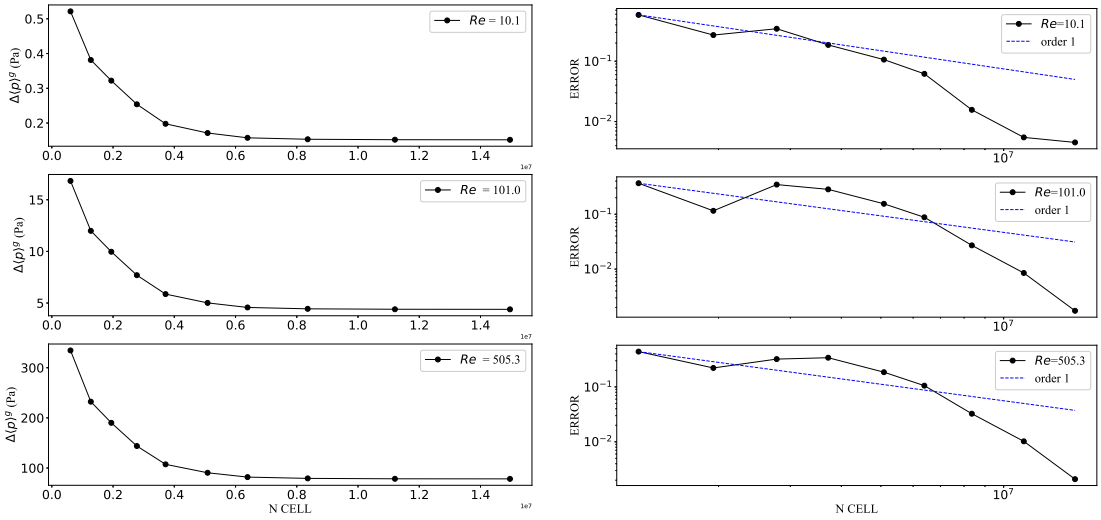

(a) pressure difference

(b) relative error

Figure 7.3 – Mesh convergence analysis of the fluid domain filled with multiple spheres.

between the inlet and the outlet is calculated as the number of cells increases as shown in Fig.7.3 (a). The inlet velocity $|\langle v_g \rangle|$ is 0.01, 0.1, and 0.5 m/s respectively and the corresponding Re is 10.1, 101.0 and 505.3. The behavior of the numerical error is shown in Fig.7.3(b). The error is defined as follows,

$$\text{error} = \frac{\Delta\langle p \rangle^g_{n+1} - \Delta\langle p \rangle^g_n}{\Delta\langle p \rangle^g_{n+1}} \tag{7.6}$$

where the index n denotes the simulation with mesh before refinement. The blue dotted line refers to the first-order slopes. The results suggest that when the number of cells surpasses 11.2 million, the error gradually decreases until it reaches a steady state around 5×10^{-3} for Re=10.1, 8×10^{-3} for Re=101.0 and 1.0×10^{-2} for Re=505.3. Fig.7.4 provides detailed views of the meshed geometry. In

(a) and (b), the red regions represent individual particles, while the blue regions represent the fluid. (c) is an enlarged view of a portion of the particles in (a), showing the refined meshing at the interface between the particles and the fluid. (d) presents the outlet meshing of the structure.

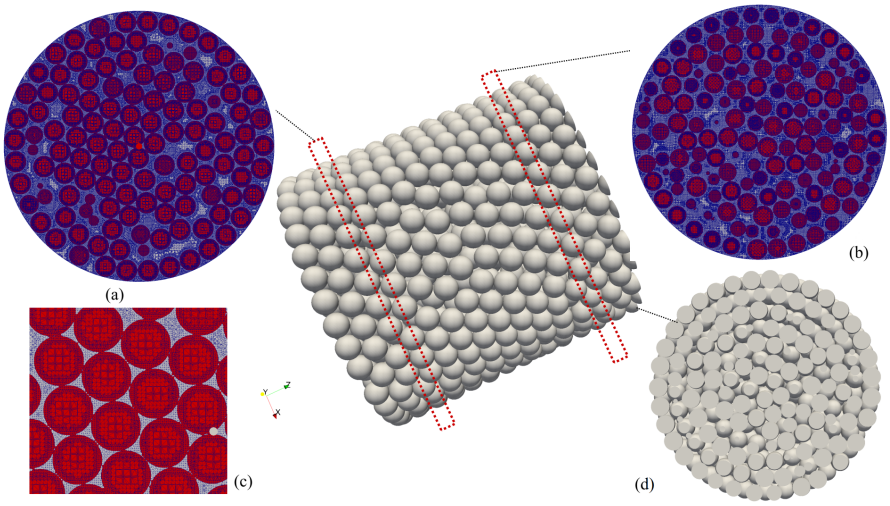

Figure 7.4 – Some details of the meshed geometry: (a), (b) mesh on the two cross-sections, (c) an enlarged view of a portion of the particles, (d) schematic of the structure at the outlet of the porous zone.

7.3 Simulation results at the micro-scale

In this section, we presented the results of two micro-scale simulation cases. In the first case, the inlet velocity of the gas was varied from 0.00001 to 0.5 m/s, resulting in an increase in the Reynolds number from 0.01 to 505.3, and the pressure drop was calculated. Given that the laminar flow limit inside a packed bed typically falls between 500 to 600 [145], this range of inlet velocities is reasonable. In the second case, the same velocity variation was applied, and the temperature distribution inside the packed bed was obtained by solving the governing equations, and the heat transfer coefficient was subsequently calculated.

7.3.1 Pressure drop

To upscale the pore-scale problem in porous media, the homogenization theory [197] or the volume-averaging technique [198] was proposed. The macroscopic model given by Eq.7.7 was demonstrated,

$$\begin{cases} \nabla \cdot \langle \mathbf{v_g} \rangle = 0 \\ \langle \mathbf{v_g} \rangle = -\frac{1}{\mu_g} \mathbf{K} \cdot \nabla \langle p \rangle^g - \mathbf{F} \cdot \langle \mathbf{v_g} \rangle \end{cases} \tag{7.7}$$

where $\langle \mathbf{v_g} \rangle$ and $\langle p \rangle^g$ are the macroscopic pressure and velocity, $\mathbf{F}$ is the Forchheimer correction tensor $(\mathbf{K} \cdot \boldsymbol{\beta})|\langle \mathbf{v_g} \rangle|\rho_g/\mu_g)$, where $\mathbf{K}$ is the permeability tensor, $\boldsymbol{\beta}$ is the Forchheimer coefficient tensor. $\langle \varphi_i \rangle$

and $\langle\varphi_i\rangle^i$ are the superficial and intrinsic phase averages of any quantity φ_i associated with the i-phase, respectively. In this case, we assumed packed beds to be isotropic porous materials. When the flow velocity is small, the second term $\mathbf{F}\cdot\langle\mathbf{v_g}\rangle$ in Eq.7.7 can be neglected, and Darcy's law is validated.

The numerical results for varying Reynolds numbers are illustrated in Fig.7.5. Fig.7.5(a) and (b) display the variations of pressure gradient and effective permeability as a function of Reynolds number, respectively. The effective permeability in one-dimensional flow is calculated using Eq.7.8.

$$K_{eff} = -\langle v_g\rangle \cdot \mu_g \cdot \frac{H}{\Delta\langle p\rangle^g} = -\frac{\mu_g^2}{\rho_g d_{par}} \frac{H}{\Delta\langle p\rangle^g} Re \tag{7.8}$$

In this case, the pressure gradient exhibits a non-linear relationship, and the flow region covers both Darcy and Forchheimer flow regimes, as demonstrated in Fig.7.5 (a). This observation is further supported by Fig.7.5 (b), where the constant K_{eff} corresponds to the Darcy flow regime. For Re less than 10.1, the pressure gradient increases linearly, and the effective permeability K_{eff} remains constant, indicating a Darcy flow regime. For Re higher than 10.1, the pressure gradient increases nonlinearly, accounting for inertial effects. To compute the Forchheimer coefficient β, a rearranged

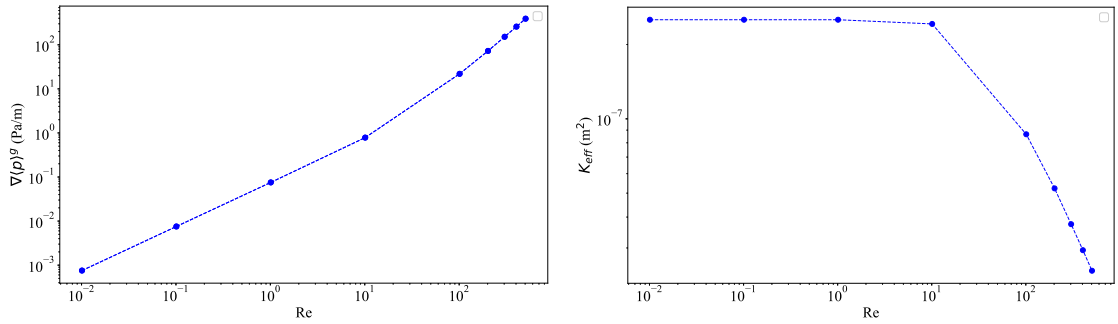

(a) pressure gradient (b) effective permeability

Figure 7.5 – Computed pressure gradient and effective permeability with increasing Reynolds number

form of the Forchheimer equation for one-dimensional flow is presented in Eq.7.9.

$$-\frac{\Delta\langle p\rangle^g}{H} \cdot \frac{1}{\langle v_g\rangle} \cdot \frac{1}{\mu_g} = \beta(\rho_g|\langle v_g\rangle|\frac{1}{\mu_g}) + \frac{1}{K} \tag{7.9}$$

We introduced two new variables, X and Y, $X = \rho_g|\langle v_g\rangle|\frac{1}{\mu_g}$, $Y = -\frac{\Delta\langle p\rangle^g}{H} \cdot \frac{1}{\langle v_g\rangle} \cdot \frac{1}{\mu_g}$, thus given by $Y = \beta X + \frac{1}{K}$, to compute the values of β using the least-squares approximation method, as displayed in Fig. 7.6. The values for both K and β are presented in Table 7.4.

Table 7.4 – Permeability K and Forchheimer coefficient β in packed beds filled with spheres

Permeability, K (m^2)	**Forchheimer coefficient,** β (m^{-1})
2.451×10^{-7}	1.188×10^{3}

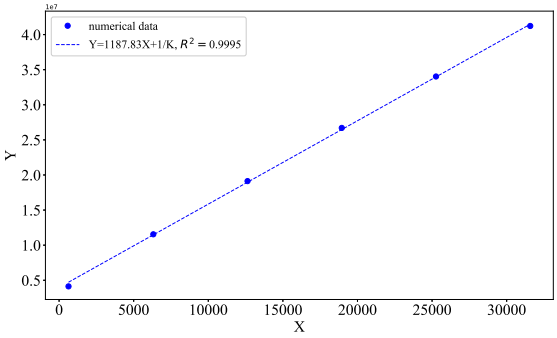

Figure 7.6 – Relationship between terms X (m^{-1}) and Y (m^{-2}).

To validate our simulation results, we have chosen to compare them with the results calculated using the Ergun equation (Eq. 7.10) [165], in which these two parameters are treated as scalars.

$$K = \frac{d_{par}^2 \varepsilon_g^3}{150\varepsilon_s^2}, \qquad \beta = \frac{1.75\varepsilon_s}{d_{par}\varepsilon_g^3} \tag{7.10}$$

where the gas volume fraction (porosity, ε_g) is calculated using the Muller correlation [143], $\varepsilon_g = 0.365 + 0.22/(D_t/d_{par})$. The values of K and β calculated using Eq. 7.10 are 2.51×10^{-7} m^2 and 1.206×10^3 m^{-1}, respectively, with a respective error of 2.44% and 1.52% compared to the simulated values. This indicates that the model used in this work can be used to simulate laminar flow in both the Darcy and the Forchheimer flow regimes.

7.3.2 Volumetric heat transfer coefficient

In this subsection, we start by examining the temperature and velocity distribution within the packed bed at a specific inlet velocity. The impact of the inlet velocity and solid thermal conductivity on the volumetric heat transfer coefficient is then summarized.

7.3.2.1 Temperature and velocity distributions

As a large number of simulations were carried out, a representative case with an inlet gas velocity of 0.1 m/s (Re = 101 at room temperature) was selected to describe the temperature distribution of gas and particles within the packed bed, where the inlet gas temperature was 800 K and the initial temperature of the spherical particles was 300 K, and the internal heat transfer in the spherical particles was considered. To illustrate the velocity and temperature distribution inside the packed beds, we selected three typical cross-sections, as shown in Fig.7.7, where section-1 is located at $y = 0$, section-2 is located at $z = 0.1H$, and section-3 is located at $z = 0.7H$. The packed bed can be further divided into two parts: the spherical solid particles and the fluid region between the particles.

The temperature distribution in section-1 of the randomly packed bed with uniform spheres is presented in Fig.7.8, which was selected at t=1000s to display the temperature distribution due to the transient heat transfer of air. Fig.7.8 (a) shows the overall temperature field of both gas and

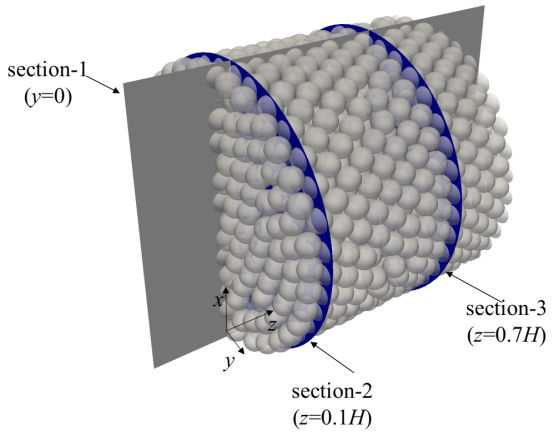

Figure 7.7 – Selected sections in a randomly packed bed of spheres.

solid in the plane, while Fig.7.8 (b) and (c) respectively show the temperature fields of the gas and solid. As shown in Fig.7.8, the temperature distribution in the packed bed is non-uniform. The gas temperature on the left side of the bed reaches up to 790 K, while the gas on the right side remains at room temperature. Similarly, for the solid phase, the solid near the inlet is heated to around 650K, while the solid at the outlet remains at room temperature. To analyze the temperature distribution at the interface between gas and solid and the temperature distribution inside the solid, we selected appropriate positions in Fig.7.8 (a) and (c), magnified the temperature distribution, and plotted temperature contour maps. The results are shown in (d) and (e). In Fig.7.8 (d), the temperature contour intervals are 20 K and it can be seen that the temperature difference between the gas and solid at their interface reaches 30 K, proving that the local gas and solid temperature in the packed bed is not in equilibrium. In Fig.7.8 (e), the temperature of the solid is unevenly distributed within the same sphere with a maximum temperature difference of 30K, indicating that the internal heat conduction of the solid must be considered in this case.

Fig.7.9 provides a complementary analysis to the temperature distribution presented in the previous paragraph. It shows the distribution of gas velocity (v_g), Reynolds number ($Re = \rho_g v_g d_{par}/\mu_g$), and Prandtl number ($Pr = \mu_g c_{p,g}/k_g$) in section-1 of the packed bed. The maximum gas velocity of 0.67 m/s is found in the narrow gaps between the stacked spherical particles (Fig.7.9a), leading to local increases in Reynolds number. The maximum Reynolds number in section-1 is 280, which is a function of gas velocity and thermophysical properties (Fig.7.9b). However, the locations of the maximum Reynolds number do not necessarily correspond to the locations of the largest gas velocity, as the thermophysical properties of air also affect the flow behavior. The Prandtl number varies slightly between 0.691 and 0.7 and can be considered approximately constant throughout the packed bed. These results provide further insight into the complex fluid dynamics and heat transfer phenomena that occur within the packed bed.

Fig.7.10 shows the velocity and temperature distributions in different cross-sections (section-2 and 3) of the randomly packed bed with uniform spheres. It can be observed that the gas velocity distribution is affected by the local structure within the packed beds, which in turn influences the temperature

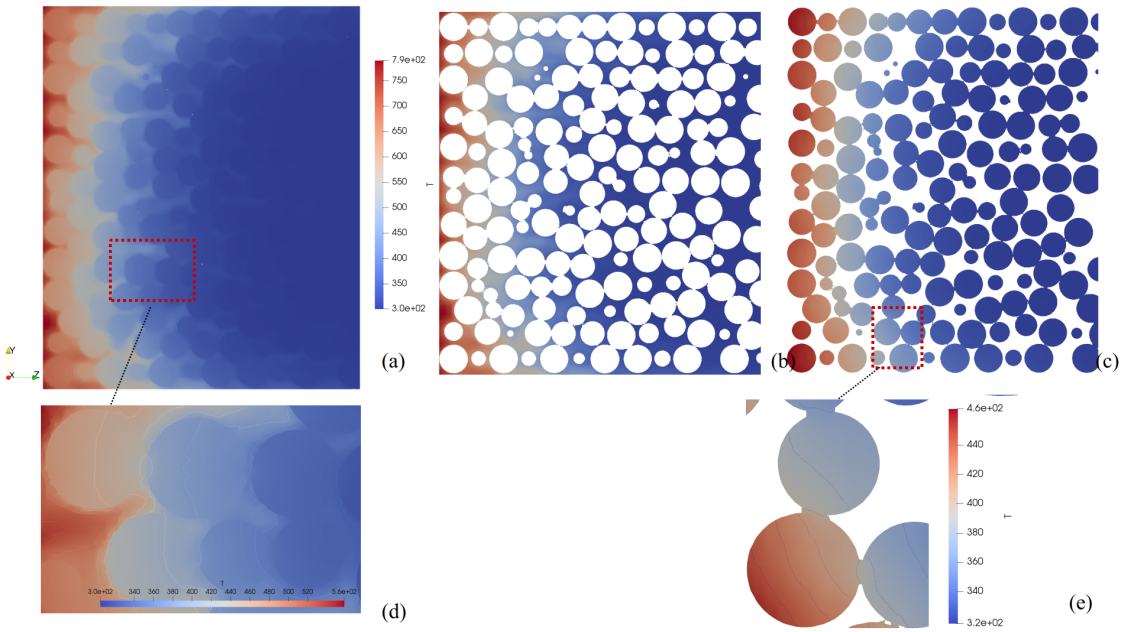

Figure 7.8 – Temperature fields in section-1 of the randomly packed bed (u=0.1m/s, t=1000s). (a) Total temperature field (gas and solid), (b) Gas temperature field, (c) Solid temperature field, (d) Zoomed-in view of the temperature field at the gas-solid interface, (e) Zoomed-in view of the solid temperature field.

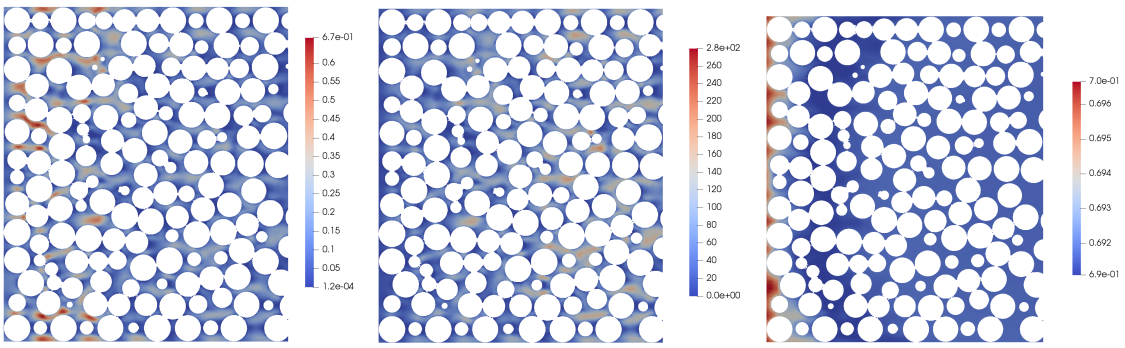

(a) gas velocity (b) Reynolds number (c) Prandtl number

Figure 7.9 – Gas velocity, Reynolds number, and Prandtl number distribution in section-1 of the randomly packed bed with an inlet velocity of 0.1 m/s and a time of 1000 s.

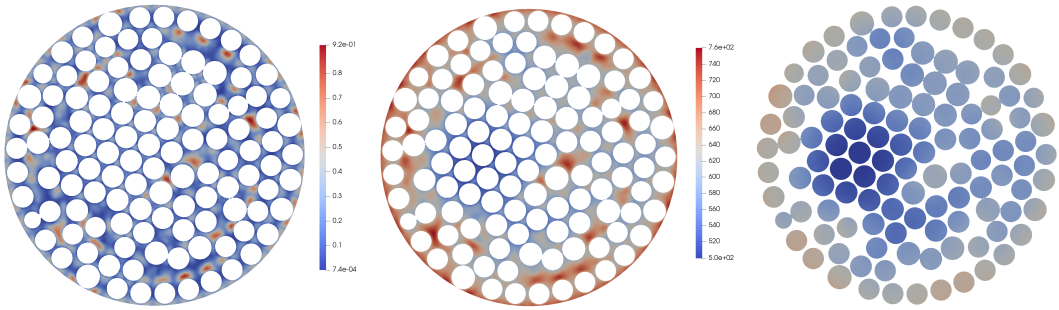

(a) gas velocity in section-2 (b) gas temperature in section-2 (c) solid temperature in section-2

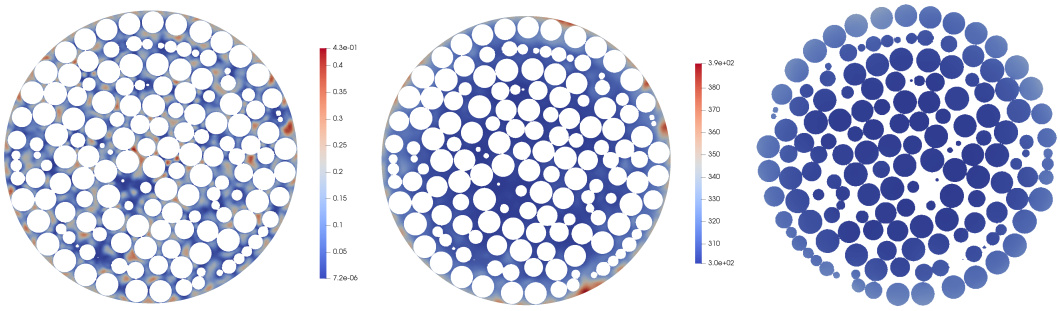

(d) gas velocity in section-3 (e) gas temperature in section-3 (f) solid temperature in section-3

Figure 7.10 – Gas velocity (m/s) and temperature (K) distributions in different sections with an inlet velocity of 0.1 m/s and a time of 1000 s.

distribution of the gas, as shown in Fig.7.10(a). The regions with higher gas velocity correspond to higher gas temperatures in Fig.7.10(b), which further affects the temperature distribution of the solid particles as shown in Fig.7.10(c). Fig.7.10(d), (e), and (f) depict the distributions of gas velocity, gas temperature, and solid temperature in section-3, which exhibit similar distribution patterns as those in section-2. The analysis of internal heat conduction within individual solid particles has been carried out in Fig.7.8 (section-1).

7.3.2.2 Effect of gas velocity

The purpose of this part is to analyze the influence of different inlet gas velocities on the volumetric heat transfer coefficient. First, we obtained the transient average temperature distribution of gas and solid for different inlet gas velocities. Then, by solving Eq. 7.2, we can determine the numerical values of h_v.

Fig. 7.11 presents the average temperature distribution of gas and solid inside the packed bed for different inlet velocities (0.01 to 1 m/s), which are represented by the Reynolds number (at room temperature). The temperature of gas and solid were averaged in the xy plane of the geometry, and their averages were plotted in the z-direction, where z/H=0.1 and 0.7 correspond to section-2 and section-3 shown in Fig. 7.7. Using Fig. 7.11 (c) as an example, we observe a temperature difference ($dT = \overline{T_g} - \overline{T_s}$) of about 28K between the average gas temperature and the average solid temperature in section-2 plane ($z/H = 0.1$), while in section-3 plane ($z/H = 0.7$), this value increases to 39K, where $\overline{T_i}$ is the average temperature of the i-phase in each cross-section, $\overline{T_i} = \frac{1}{S_i} \int_{S_i} T_i dS$, with S_i being the area of the cross-section. These observations strongly suggest the existence of local thermal non-equilibrium (LTNE) during the transient heat transfer process, which is characterized by a temperature difference between the average gas and solid phases in the same plane. Furthermore, our analysis revealed that a higher Reynolds number leads to faster heating of the solid particles.

The volumetric heat transfer coefficient h_v is an important parameter in the analysis of heat transfer in packed beds, and it is influenced by transient changes in thermal conductivity k_g and average temperatures $\langle T_s \rangle^s$ and $\langle T_g \rangle^g$ over time, as defined in Eq. 7.2. Fig.7.12 shows the predicted relationship between the heat transfer coefficient h_v and time for various inlet gas velocities. It is observed that h_v increases with time for all Reynolds numbers, but the rate of increase varies significantly. For low Re corresponding to inlet velocities such as 0.01 m/s and 0.1 m/s, the increase in h_v over time is relatively small, with around 2.7% and 1.5% increases, respectively, and therefore h_v can be regarded as constant. However, for Re of 1010.1, h_v significantly increases with the heat transfer process, with an increase of about 71% from 13529.99 to 23218.36 W/(m^3·K). These findings suggest that Re has a significant impact on the heat transfer coefficient in packed beds, with higher Re resulting in a more significant increase in h_v over time.

7.3.2.3 Effect of solid thermal conductivity

In this part, we investigated the effect of the solid thermal conductivity k_s on the temperature distribution and heat transfer coefficient inside the packed bed. Four different values of k_s (0.1, 1,

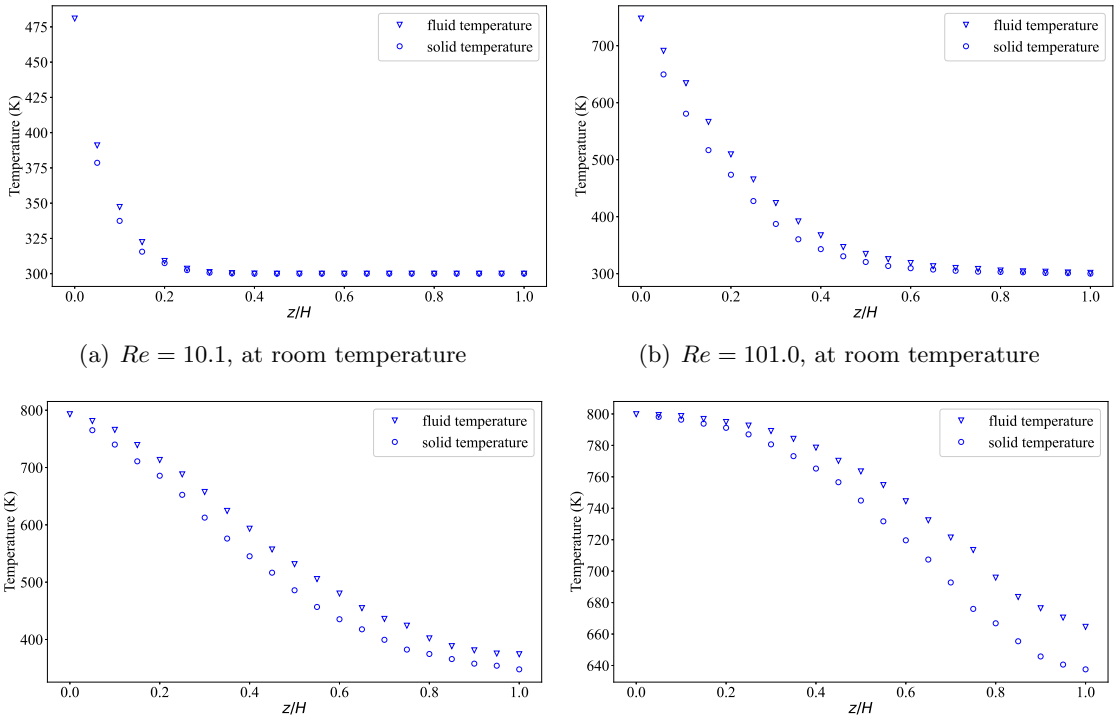

(a) $Re = 10.1$, at room temperature

(b) $Re = 101.0$, at room temperature

(c) $Re = 303.3$, at room temperature

(d) $Re = 1010.1$, at room temperature

Figure 7.11 – Temperature fields comparison between fluid and solid phases at 1000s. The fields are averaged in the xy plane of the packed bed and plotted along the z direction. Different inlet velocities are considered.

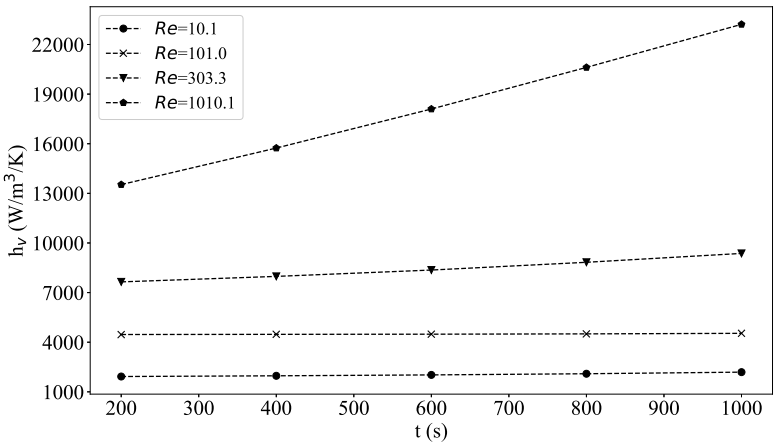

Figure 7.12 – Transient behavior of heat transfer coefficient as a function of time for various inlet velocities.

10, and 100 W/(m·K)) independent of the temperature were considered as a single variable, with a constant value that does not vary with temperature in each simulation.

The inlet gas velocity was set to a constant value of $|\langle v_g \rangle| = 0.3$ m/s (Re=303.3 at room temperature) in all four simulations. Fig. 7.13 displays the solid temperature distribution in section-2 for the different k_s values. Specifically, Fig.7.13(a), (b), (c), and (d) correspond to k_s values of 0.1, 1, 10, and 100 W/(m·K), respectively. The temperature contour intervals were set to 10 K for Fig.7.13(a),

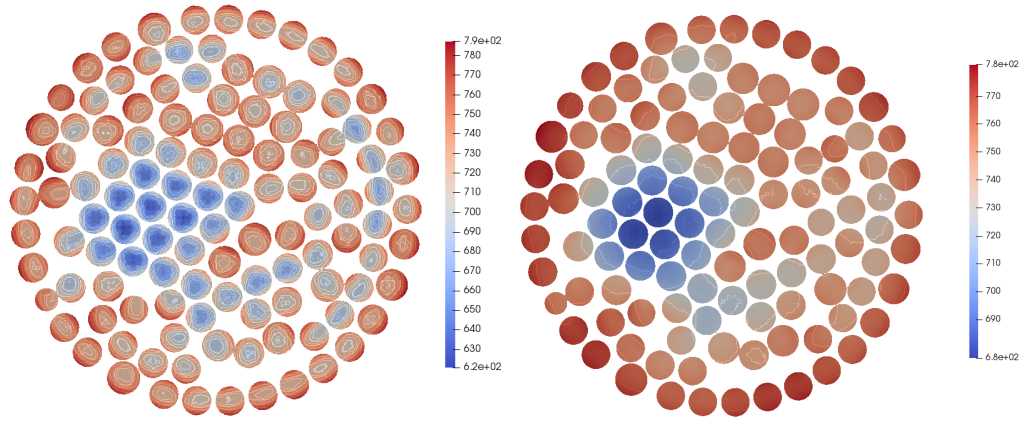

(a) k_s=0.1 W/(m· K) (b) k_s=1 W/(m· K)

(c) k_s=10 W/(m· K) (d) k_s=100 W/(m· K)

Figure 7.13 – Solid temperature distribution at section-2 for various solid thermal conductivity values

(b), and (c), while for Fig.7.13(d), it was set to 5 K. As shown in Fig.7.13(a), the temperature difference from the center of each sphere to the surface is nearly 80 K, indicating significant temperature non-uniformity within individual particles. Similarly, Fig.7.13(b) shows a temperature difference of nearly 20 K. In both (a) and (b) cases, heat conduction within the sphere cannot be neglected. Conversely, in the latter two cases, where k_s values are 10 and 100 W/(m· K), the temperature variation within individual particles is less than 10 K, implying that heat conduction inside the sphere can be neglected. This observation can also be confirmed by Fig.7.13(c) and (d). To explain the temperature

distribution behavior within the particles, the Biot number is introduced.

$$Bi = \frac{h_s d_{par}}{k_s} = \frac{h_v {d_{par}}^2}{6\varepsilon_s k_s} \tag{7.11}$$

where Bi is determined by both the volumetric heat transfer coefficient h_v and the solid thermal conductivity k_s. Note that $h_v = h_s A_s$, where A_s is the specific surface area which can be expressed as $A_s = A_{gs}/V = 6\varepsilon_s/d_{par}$. We first calculate the values of h_v using Eq. 7.2. Then, we analyze the values of the Biot number to further understand the thermal behavior within the particles.

Fig.7.14 presents the time-dependent increase in h_v for packed beds for different solid thermal conductivities, indicating that k_s affects the evolution of h_v. The results show that h_v increases gradually over time for all solid thermal conductivity values, but at a slower rate for lower solid thermal conductivity values. For example, in Fig. 7.14, for a solid thermal conductivity of 0.1 W/(m · K), h_v increases by 12.9% from 4782.11 to 5403.18 W/(m^3·K), while for a solid thermal conductivity of 100 W/(m · K), h_v increases by 27.4% from 7839.24 to 9989.57 W/(m^3·K). Furthermore, an increase in solid thermal conductivity k_s results in a corresponding increase in h_v at a given time.

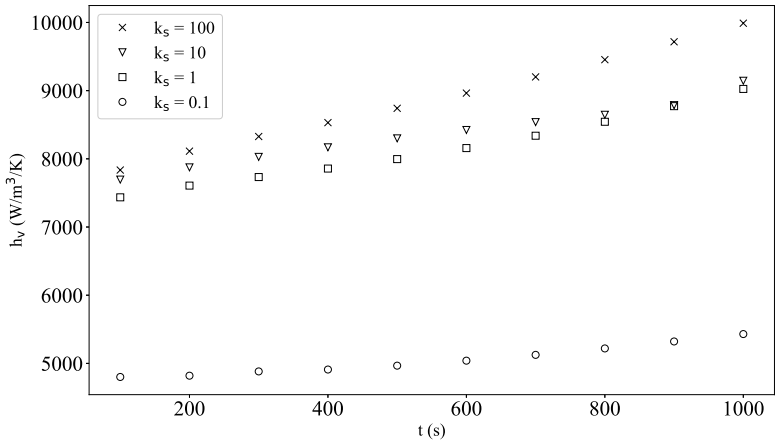

Figure 7.14 – Evolution of volumetric heat transfer coefficient h_v with time for packed beds with different solid thermal conductivities.

The values of h_v obtained from Fig. 7.14 enable the calculation of the corresponding Biot numbers using Eq. 7.11, with h_v values taken from the final time step at $t = 1000$ s. The resulting Biot numbers are 3.72, 0.62, 0.063, and 0.0069, corresponding to increasing k_s values from 0.1 to 100 W/(m · K). These values shed light on the temperature gradient behavior observed within individual particles in Fig. 7.13 (a) and (b), where the Biot number exceeds 0.1. Conversely, the Biot numbers for Fig. 7.13 (c) and (d) are less than 0.1, indicating that the temperature distribution within individual particles can be considered uniform.

7.4 Numerical method and results at the macro-scale

This section aims to validate the effectiveness of the integral method presented in Section 7.3. The verification procedure consists of the following steps: Firstly, a simplified micro-scale geometry is generated, adopting the same porous structure as depicted in Fig.7.2, but excluding the flow1 and flow2 regions. This approach is employed to eliminate the influence of boundary conditions applied at the interface between the flow1 and packed bed regions. The resulting micro-scale model is presented in Fig. 7.15 (a). The volumetric heat transfer coefficient h_v is calculated using the same integral method. Secondly, the macroscopic equations are solved using the derived parameters from the micro-scale simulation, and a comparison is made between the temperature fields in the micro-scale and macro-scale models.

7.4.1 Numerical model

To ensure a consistent comparison between simulation results at the macro and micro scales, it is crucial to maintain identical structures in both simulations. The micro-scale structure, depicted in Figure 7.15 (a), consists exclusively of the packed bed region. In the macro-scale simulation, a two-dimensional axisymmetric numerical domain, as shown in Figure 7.15 (b), is utilized. By maintaining this consistency in structure, accurate and reliable comparisons can be made between the macro and micro scales.

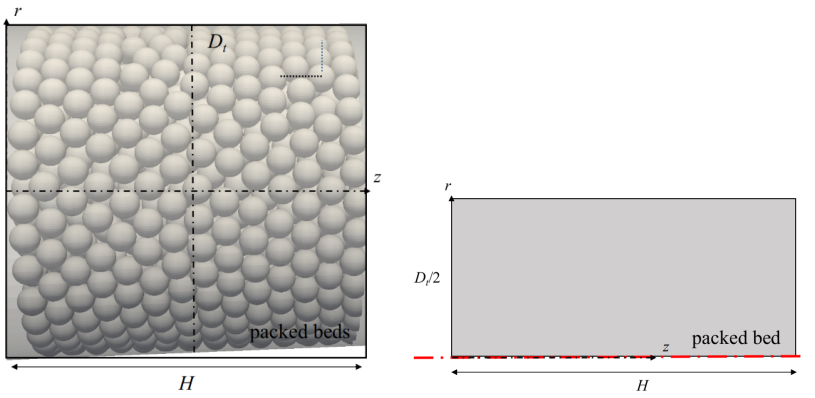

(a) Micro-scale domain (b) Two-dimensional axisymmetric macro-scale domain

Figure 7.15 – Numerical domains at micro and macro-scales

7.4.1.1 Mathematical model and numerical implementation

For the porous domain (packed bed), we employ the LTNE model. The Reynolds number, based on the particle diameter (d_{par}), is defined as $Re = \rho_g |\langle v_g \rangle| d_{par}/\mu_g$, with $|\langle v_g \rangle|$ being the average gas velocity. As mentioned in Section 7.3, the Reynolds number ranges from 10.1 to 1010.1, indicating that the gas flow is in the Forchheimer flow regime. Therefore, we use the Forchheimer equation in

the macroscopic simulation. The averaged governing equations can be expressed as follows:

$$\frac{\partial}{\partial t}\left(\varepsilon_g \frac{M\langle p\rangle^g}{R\langle T_g\rangle^g}\right) + \nabla\cdot\left(-\frac{M\langle p\rangle^g \mathbf{KX}}{R\langle T_g\rangle^g}\cdot\nabla\langle p\rangle^g\right) = 0 \tag{7.12}$$

$$\frac{\partial}{\partial t}\left(\varepsilon_s\rho_s c_{p,s}\langle T_s\rangle^s\right) = \nabla\cdot\left(\mathbf{k_{s,eff}}\cdot\nabla\langle T_s\rangle^s\right) + h_v\left(\langle T_g\rangle^g - \langle T_s\rangle^s\right) \tag{7.13}$$

$$\frac{\partial}{\partial t}\left(\varepsilon_g\rho_g c_{p,g}\langle T_g\rangle^g\right) + \nabla\cdot\left(\rho_g c_{p,g}\langle \mathbf{v_g}\rangle^{\mathbf{g}}\langle T_g\rangle^g\right) = \nabla\cdot\left(\mathbf{k_{g,eff}}\cdot\nabla\langle T_g\rangle^g\right) + h_v\left(\langle T_s\rangle^s - \langle T_g\rangle^g\right) \tag{7.14}$$

where Eq. 7.12 represents the gas mass conservation equation, which is derived from the perfect gas law (Eq. 7.15), mass conservation (Eq. 7.16), and Forchheimer equation (Eq. 7.17). Eq. 7.13 and Eq. 7.14 are the energy equations for the solid and fluid phases, respectively.

$$\rho_g = \frac{M\langle p\rangle^g}{R\langle T_g\rangle^g} \tag{7.15}$$

$$\partial_t\left(\varepsilon_g\rho_g\right) + \nabla\cdot\left(\varepsilon_g\rho_g\langle\mathbf{v_g}\rangle^{\mathbf{g}}\right) = 0 \tag{7.16}$$

$$\langle\mathbf{v_g}\rangle^{\mathbf{g}} = -\frac{1}{\varepsilon_g}(\mathbf{KX})\cdot\nabla\langle p\rangle^g, \quad X_{ij} = \frac{1}{\mu_g K_{ij} + \beta_{ij}\rho_g|\langle v_g\rangle|} \tag{7.17}$$

where the Forchheimer tensor, represented as $\mathbf{X}$, is introduced to simplify the computation process [76]. Considering the packed bed as isotropic allows us to treat $\mathbf{K}$ and $\boldsymbol{\beta}$ as scalars. This implies that $\mathbf{K} = K\mathbf{I}$ and $\boldsymbol{\beta} = \beta\mathbf{I}$, where $\mathbf{I}$ is the identity tensor.

In what follows, $\langle T_g\rangle^g$ and $\langle T_s\rangle^s$ correspond to the gas and solid temperatures in the porous domain (packed bed). The boundary conditions and initial conditions for the system of Eq. 7.13 and 7.14 (LTNE model) are specified in Table 7.5. For the pressure, the *forchheimer Velocity Pressure* condition provides a compressible Forchheimer's velocity condition for pressure. It is derived from a *fixed Gradient* condition, whereas pressure is calculated from the projection of the velocity vector and permeability tensor on the direction of the flow.

Table 7.5 – Initial and boundary conditions of the LTNE model

Region	Initial conditions	Boundary conditions		
packed bed		inlet	lateral boundaries	outlet
$\langle p\rangle^g$	101325 Pa	*forchheimer Velocity Pressure*	*zero gradient*	*fixed value* (101325 Pa)
$\langle T_g\rangle^g$	300 K	*fixed value* (800 K)	*zero gradient*	*zero gradient*
$\langle T_s\rangle^s$	300 K	*zero gradient*	*zero gradient*	*zero gradient*

The numerical model was implemented using the finite volume method in the Porous material Analysis Toolbox based on OpenFOAM (PATO) [77], which is available in open access. For the porous domain, the pressure equation (Eq.7.12) was solved semi-implicitly using first-order schemes in time (Euler) and space (Gauss linear). The pressure gradient term was implicit, while the other terms were explicit. The same approach was used for the energy equations, where the temperature terms were implicit and the other quantities were explicit. The equations were solved in series, with appropriate mesh refinement and time steps to ensure convergence.

7.4.1.2 Physical properties

The parameters mentioned in the averaged governing equations (Eq. 7.12, 7.13, 7.14), including permeability $\mathbf{K}$, Forchheimer coefficient $\boldsymbol{\beta}$ (Eq.7.17), porosity ε_g, gas properties ($\rho_g, \mu_g, c_{p,g}, k_g$), and solid properties ($k_s, c_{p,s}, \rho_s$), were obtained from the micro-scale simulations and are summarized as follows. The values of K and β are listed in Table 7.4, the value of ε_g is 0.379, and the thermal properties of gas and solid are presented in Table 7.3. For the effective parameters, including the effective solid thermal conductivity $\mathbf{k_{s,eff}}$, effective gas thermal conductivity $\mathbf{k_{g,eff}}$, and volumetric heat transfer coefficient h_v, we introduce several dimensionless coefficients, denoted as c_1, c_2, c_3 and f, as defined in Eq. 7.18, to facilitate the optimization algorithm. As presented in the introduction, the value of $\mathbf{k_{g,eff}}$ is influenced by the conductivity, tortuosity and dispersion terms, which exhibit different values in the longitudinal ($||$) and transverse ($\perp$) flow directions [126, 30]. The tortuosity term is typically neglected when compared to the dispersion term [73]. The relationship between the dispersion terms and the thermal properties of the gas follows a similar functional form as proposed by Wakao et al. [126]. Similarly, the modeling of h_v employs the same functional form as suggested by Wakao et al. [105].

$$\begin{cases} \mathbf{k_{s,eff}} = \mathbf{k_{s,con}} + \mathbf{k_{s,tor}} = c_1 \cdot k_s I \\ k_{g,eff,||} = k_{g,con} + k_{g,tor,||} + k_{dis,||} = \varepsilon_g k_g + 0 + c_2 \cdot Re \cdot Pr \cdot k_g = \varepsilon_g k_g + c_2 \cdot d_{par} \cdot |\langle v_g \rangle| \cdot \rho_g \cdot c_{p,g} \\ k_{g,eff,\perp} = k_{g,con} + k_{g,tor,\perp} + k_{dis,\perp} = \varepsilon_g k_g + 0 + c_3 \cdot Re \cdot Pr \cdot k_g = \varepsilon_g k_g + c_3 \cdot d_{par} \cdot |\langle v_g \rangle| \cdot \rho_g \cdot c_{p,g} \\ h_v = (6\varepsilon_s / d_{par}) \cdot (2 + f \cdot Re^{0.6} \cdot Pr^{1/3}) k_g / d_{par} \end{cases} \tag{7.18}$$

where h_v is calculated using the Nusselt number, Nu ($= \frac{h_s d_{par}}{k_g} = \frac{h_v d_{par}^2}{6\varepsilon_s k_g}$), in the following expression: $Nu = 2 + f \cdot Re^{0.6} \cdot Pr^{1/3}$ [105], Prandtl number, Pr, is given by $Pr = \mu_g c_{p,g} / k_g$.

7.4.2 Optimization process and methods

An inverse analysis method was employed to determine the effective parameters by minimizing the errors between the predicted data from micro-scale simulations and the macro-scale results. In the subsequent analysis, T_g and T_s refer to the gas and solid temperatures obtained at the micro-scale, while $\langle T_g \rangle^g$ and $\langle T_s \rangle^s$ represent the gas and solid temperatures obtained at the macro-scale. Additionally, $\overline{T_g}$ and $\overline{T_s}$ denote the average temperatures obtained from the micro-scale simulations. We obtained data sequences, denoted as $\{\overline{T_{g,i}}\}_{i=1}^n$, and $\{\overline{T_{s,i}}\}_{i=1}^n$, which represent the average gas and solid temperatures at different cross-sections indicated by the index i. The cross-sections are evenly spaced at intervals of $0.05H$ along the packed bed, ranging from $z = 0$ to $z = H$ (as presented in Fig. 7.15 (a)). These data sequences were collected at three distinct time points: $t = 300$ s, $t = 500$ s, and $t = 1000$ s, a total of 6 data sequences. The error function S over the six sequences is

$$S = \frac{1}{6} \left(\sqrt{\frac{1}{n} \sum_{i=1}^{n} \left(\frac{\langle T_{g,i} \rangle^g - \overline{T_{g,i}}}{\overline{T_{g,i}}} \right)^2} + \sqrt{\frac{1}{n} \sum_{i=1}^{n} \left(\frac{\langle T_{s,i} \rangle^s - \overline{T_{s,i}}}{\overline{T_{s,i}}} \right)^2} \right)_{t=300s,500s,1000s} \tag{7.19}$$

The minimization of S was performed using the Design Analysis Kit for Optimization and Terascale Applications (DAKOTA) [110]. The local optimization method employed was the Adaptive Non-

linear Least-Squares Algorithm (NL2SOL) [112]. NL2SOL utilizes a quasi-Newton update approach to quickly estimate the optimal value. By approximating the Hessian matrix using a simplification scheme, NL2SOL achieves faster convergence compared to global optimization methods for least squares calculations. An overview of the optimization process is presented in Fig. 7.16. A detailed description of this optimization strategy can be found in the next section.

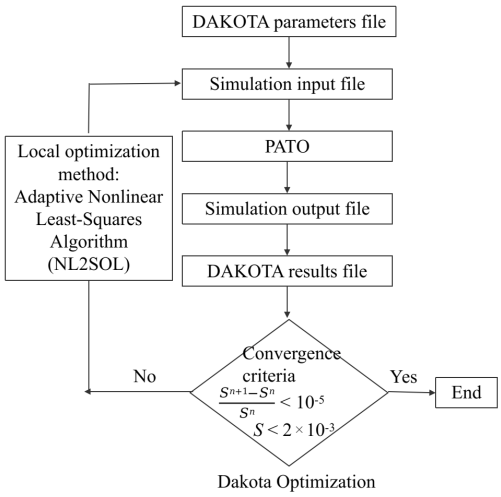

Figure 7.16 – The steps of optimization process

7.4.3 Simulation results at the macro-scale

In this subsection, we present the results of predicted temperatures obtained from micro-scale and macro-scale simulations. Fig. 7.17 provides a comparison between these two scales at three different time points: $t = 300, 500, 1000$ s. The micro-scale results ($\overline{T_g}$ and $\overline{T_s}$) are represented by data points, while the macro-scale results ($\langle T_g \rangle^g$ and $\langle T_s \rangle^s$) are shown as continuous lines. Specific markers and line styles distinguish each time point. The blue color corresponds to the gas phase and the black color for the solid-phase. The procedure for determining the effective parameters is then presented.

Based on the model presented in the subsection 7.4.1.2, there are four parameters to optimize: c_1, c_2, c_3, and f. Studies [73] have indicated that the maximum value of effective gas thermal conductivity in the transverse flow direction, $k_{g,eff,\perp}$, is 0.4 $\varepsilon_g k_g$ when the maximum Peclet number ($Pe = Re \cdot Pr$) is 300 in the packed bed. Similarly, the maximum value of effective gas thermal conductivity in the horizontal direction, $k_{g,eff,||}$, is 250 $\varepsilon_g k_g$ under the same conditions. However, the influence of $k_{g,eff,\perp}$ is relatively small compared to $k_{g,eff,||}$. Therefore, for the subsequent analysis, we set the value of c_3 to zero and focus on optimizing the remaining three parameters: c_1, c_2, and f.

To optimize the parameters, we selected a representative case with an inlet gas velocity of $|\langle v_g \rangle| =$ 1 m/s from our extensive simulations. To determine suitable ranges for the parameters, we consulted the existing literature and sought orders of magnitude. Based on the correlations proposed by Degrot et al. [73] for packed beds, we estimated the dispersion term c_2 to be around 0.31, and the effective

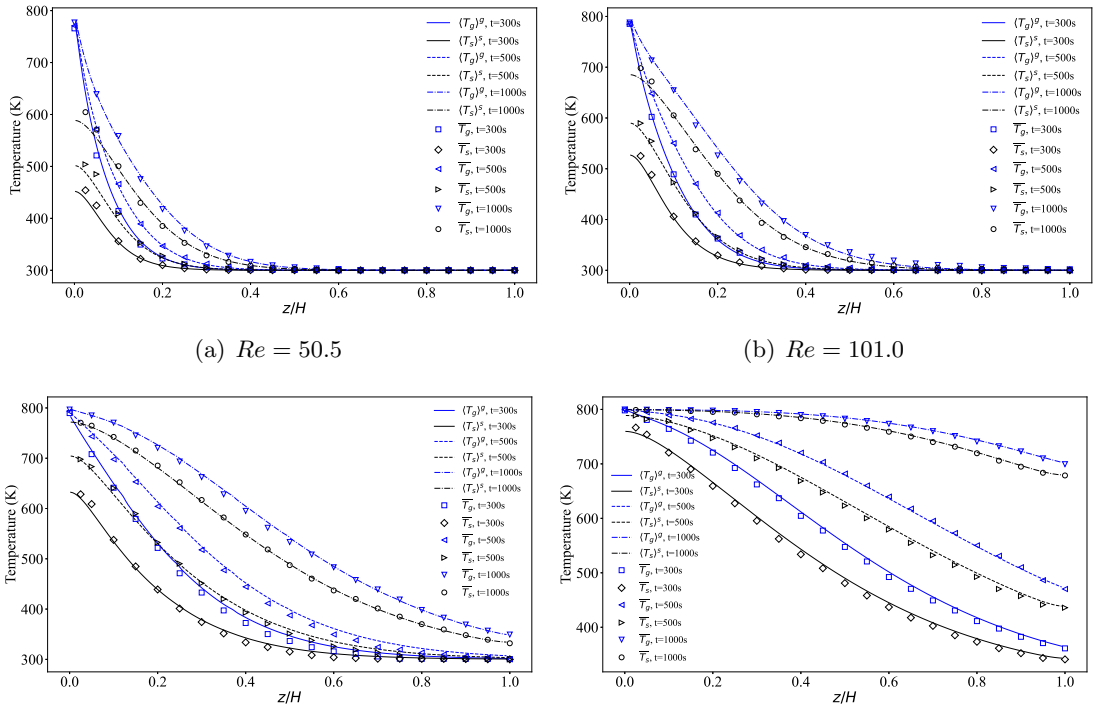

(a) $Re = 50.5$ (b) $Re = 101.0$

(c) $Re = 303.3$ (d) $Re = 1010.1$

Figure 7.17 – Computed temperature field evolution in macro-scale and micro-scale with increasing inlet gas velocity by inverse analysis

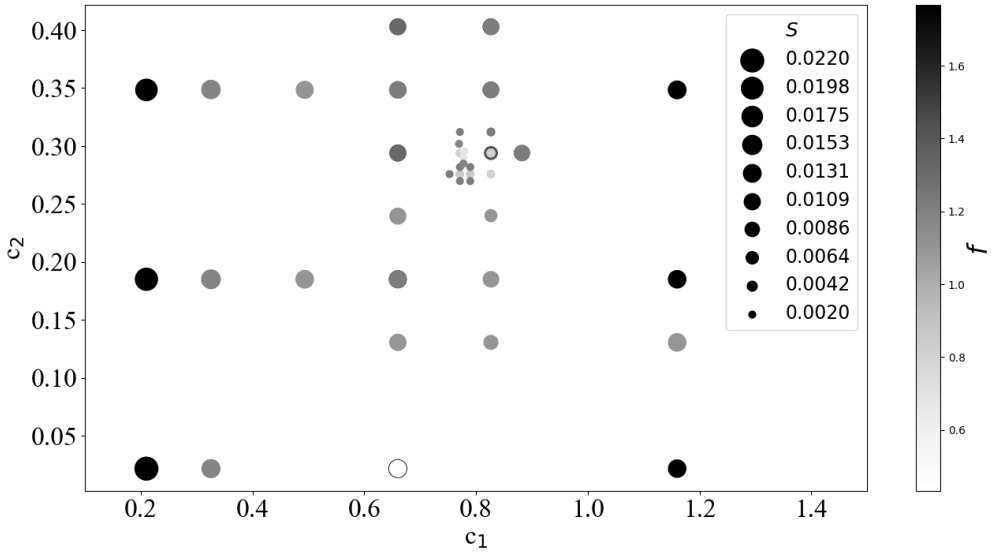

Figure 7.18 – The influence of three variables on the error S, $|\langle v_g \rangle|$=1 m/s

solid thermal conductivity term c_1 was set to a simple form of ε_s, 0.621 for a Peclet number of 300. For the coefficient f, we chose the original form of the Wakao correlation [105] and assumed $f = 1.1$. Taking advantage of the local optimization ability of the NL2SOL algorithm, we defined the following parameter ranges: c_1 from 0.2 to 1.2, c_2 from 0 to 0.5, and f from 0.4 to 1.7. These ranges allow for a comprehensive search for the optimal parameter values. Convergence ($S < 0.002$) was reached after 89 iterations of the local optimization algorithm.

Fig.7.18 presents the impact of the three variables (f, c_1 and c_2) on the error S. The grey scale represents the value of f, while the size of the points corresponds to the magnitude of S. As shown in Fig.7.18, when S is below 0.002, the values of c_1 are concentrated around 0.77 with an uncertainty of $\pm$ 0.03, c_2 concentrates around 0.28 with an uncertainty of $\pm$ 0.04, and f centers around 1.2 with an uncertainty of $\pm$ 0.05. To sum up, when the error S converges to the level of 2×10^{-3}, the ranges of the effective parameters from the optimization solution are given in Table 7.6. When considering the temperature dependency of the gas and solid thermal properties, the coefficient c_1 is not simply equal to the solid phase volume fraction ε_s (0.621) but increases to 0.75. This value is found to be relatively constant across different inlet velocities. The coefficient c_2, which is associated with gas dispersion, shows an increasing trend with higher inlet velocities and is therefore not constant. The coefficient f increases from 1.1 to 1.2 compared to the original Wakao correlation (1.1) [105]. The coefficient c_1, which is related to the solid phase volume fraction ε_s (as shown in Eq. 7.18), is found to increase from 0.621 to 0.75 for Re = 50.5 and 101.0, and 0.77 for Re = 303.3 and 1010.1. This value remains relatively constant across different Re. On the other hand, the coefficient c_2, associated with gas dispersion, shows an increasing trend with higher Re. To gain a deeper understanding, the transient heat transfer coefficient results are now presented.

Fig. 7.19 presents the values of h_v obtained at both the micro and macro scales, along with their

Table 7.6 – The value of $\mathbf{k_{s,eff}}$, $\mathbf{k_{g,eff}}$, f and error S for different gas velocities

Re at t=0 s	50.5	101.0	303.3	1010.1
Re at t=1000 s	9.29-18.18	18.58-38.4	55.75-111.15	185.85-384.21
c_1	0.75±0.03	0.75±0.03	0.77±0.03	0.77±0.03
c_2	0.05±0.005	0.09±0.005	0.28±0.02	0.28±0.04
f	1.1±0.04	1.2±0.05	1.2±0.05	1.2±0.05
$k_{s,eff}$ (W/(m · K))	0.63-1.22	0.63-1.22	0.65-1.25	0.65-1.25
$k_{g,eff,\|\|}$ (W/(m · K))	0.02-0.04	0.04-0.06	0.09-0.13	0.30-0.51
h_v (W/(m^3·K))	3284.11-4378.27	4670.61-6655.13	8019.40-11612.20	15360.04-23166.87

corresponding average temperatures at specific time points. In Fig. 7.19 (a), we plot the transient variation of h_v at different inlet velocities. At the micro-scale, h_v represents the average value over the entire volume, as described by Eq. 7.2. Meanwhile, at the macro scale, where h_v is dependent on time and position within the packed bed, we calculate the average values using the "Integrate Variable" filter in Paraview to obtain the results. The results reveal that the discrepancy between the micro-scale and macro-scale h_v values is less than 3.8%, with the maximum difference occurring at the highest Re. Furthermore, Fig. 7.19 (b) shows the average gas temperature $\langle T_g \rangle^g$ across the entire volume in the macro-scale simulation, providing a comprehensive view of the temperature variations.

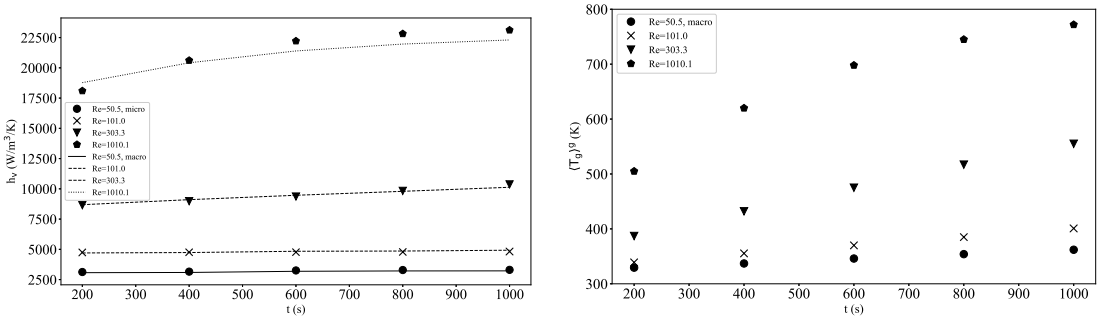

(a) Transient variation of h_v

(b) Aerage local gas temperatures

Figure 7.19 – Transient behavior of volumetric heat transfer coefficient and average local gas temperatures

To further investigate the overall behavior of the temperature in the packed beds, color maps of the simulation results at the macro scale are now presented. Fig.7.20 shows the temperature fields within the packed bed region at 1000 s. It is evident that there is a temperature difference between the local average gas and solid temperatures $\langle T_g \rangle^g$ and $\langle T_s \rangle^s$. The temperature difference ranges from 5 K to 27 K, indicating significant local thermal imbalances between the gas and solid phases. This occurs when the volumetric heat transfer coefficient, h_v, falls within the range of 15360.04-23166.87 W/(m^3·K), suggesting local thermal non-equilibrium.

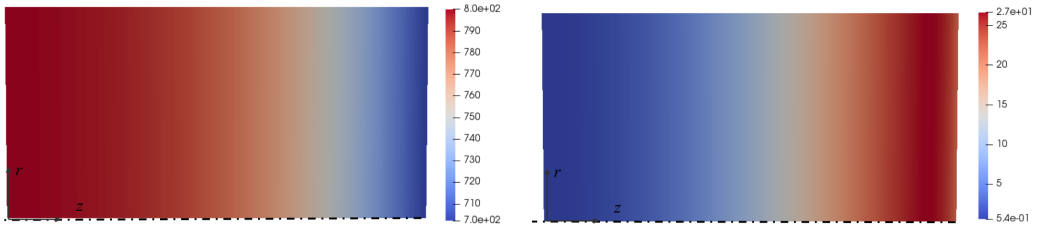

(a) gas temperature $\langle T_g \rangle^g$

(b) temperature difference between gas and solid $\langle T_g \rangle^g$-$\langle T_s \rangle^s$

Figure 7.20 – Macroscopic gas temperature and the difference $\langle T_g \rangle^g$-$\langle T_s \rangle^s$ (K) in the packed bed region

7.5 Conclusion

The objective of this work was to investigate flow and the heat transfer characteristics in a randomly packed bed at high temperatures using a multi-scale approach. The investigation involved simulations at the local micro-scale and at the macro-scale. For the micro-scale simulations, a packed beds model consisting of randomly stacked particles was constructed. The incompressible flow equations were solved to establish the relationship between the pressure drop and flow velocity at room temperature. Subsequently, the compressible flow equations coupled with the energy equation were solved, accounting for the temperature-dependent thermophysical properties of the fluid and solid. The volumetric heat transfer coefficient h_v was calculated using the integration method. The effects of gas velocity and solid thermal conductivity on h_v were discussed. To verify the accuracy of the integration method and obtain effective parameters for the macro-scale simulations, parameter estimations were conducted using numerical inverse analysis. The local thermal non-equilibrium (LTNE) models were employed to investigate heat and mass transfer phenomena. The numerical model was implemented using finite volumes in the Porous material Analysis Toolbox based on OpenFOAM (PATO). The NL2SOL optimization algorithm, a local optimization method, was employed to minimize the error between predicted temperatures obtained from micro-scale and macro-scale simulations. The optimization process was performed using the open-source optimization software Dakota. The results at the micro-scale revealed that at room temperature, the permeability was 2.451×10^{-7} m^2, and the Forchheimer coefficient was 1.188×10^3 m^{-1}. The critical Reynolds number for the transition from Darcy flow to Forchheimer flow was observed at $Re = 10.1$. The volumetric heat transfer coefficient h_v exhibited a transient behavior, but at low inlet velocities (e.g., 0.01 m/s and 0.1 m/s) corresponding to $Re = 10.1$ and 101.0 at room temperature, respectively, h_v could be considered nearly constant. For higher inlet velocities (e.g., 1 m/s) corresponding to $Re = 1001$, h_v increased significantly over time during the heat transfer process. It experienced an increase of approximately 71% from 13529.99 to 23218.36 W/(m^3·K). Additionally, h_v increased as the Biot number (Bi) decreased at the same gas velocity. This further demonstrated that when Bi exceeded 0.1, the temperature distribution within individual particles could not be considered uniform. The comparison between the h_v value obtained by integration of micro-scale results and the one calculated from the inverse analysis revealed a discrepancy of less than 3.8%, with the maximum difference occurring at the highest Re.

This study successfully connected simulations at the micro-scale and at the macro-scale, providing a comprehensive understanding of flow and heat transfer coefficients from a multi-scale perspective.

Bibliography

[1] F. Wang *et al.*, "Thermal performance analysis of porous media receiver with concentrated solar irradiation," *International Journal of Heat and Mass Transfer*, vol. 62, pp. 247–254, 2013.

[2] R. Friberg and W. Blasiak, "Measurements of mass flux and stoichiometry of conversion gas from three different wood fuels as function of volume flux of primary air in packed-bed combustion," *Biomass and Bioenergy*, vol. 23, no. 3, pp. 189–208, 2002.

[3] N. Zamel *et al.*, "Estimating effective thermal conductivity in carbon paper diffusion media," *Chemical Engineering Science*, vol. 65, no. 13, pp. 3994–4006, 2010.

[4] J. Lachaud *et al.*, "A generic local thermal equilibrium model for porous reactive materials submitted to high temperatures," *International Journal of Heat and Mass Transfer*, vol. 108, pp. 1406–1417, 2017.

[5] A. Salim and S. Lim, "Review of recent metamaterial microfluidic sensors," *Sensors*, vol. 18, no. 1, p. 232, Jan 2018.

[6] F. Panerai *et al.*, "Micro-tomography based analysis of thermal conductivity, diffusivity and oxidation behavior of rigid and flexible fibrous insulators," *International Journal of Heat and Mass Transfer*, vol. 108, pp. 801–811, 2017.

[7] J. Lachaud, I. Cozmuta, and N. N. Mansour, "Multiscale approach to ablation modeling of phenolic impregnated carbon ablators," *Journal of Spacecraft and Rockets*, vol. 47, no. 6, pp. 910–921, 2010.

[8] R. A. Beck *et al.*, "Development of the mars science laboratory heatshield thermal protection system," *Journal of Spacecraft and Rockets*, vol. 51, no. 4, pp. 1139–1150, 2014.

[9] A. Martin and I. D. Boyd, "Non-darcian behavior of pyrolysis gas in a thermal protection system," *Journal of Thermophysics and Heat Transfer*, vol. 24, no. 1, pp. 60–68, 2010.

[10] M. Stackpoole *et al.*, "Post-flight evaluation of stardust sample return capsule forebody heatshield material," *AIAA paper*, vol. 1202, pp. 1–7, 2008.

[11] J. Lachaud, I. Cozmuta, and N. N. Mansour, "Multiscale approach to ablation modeling of phenolic impregnated carbon ablators," *Journal of Spacecraft and Rockets*, vol. 47, no. 6, pp. 910–921, 2010.

[12] K. T. Edquist *et al.*, "Mars science laboratory heat shield aerothermodynamics: Design and reconstruction," *Journal of Spacecraft and Rockets*, vol. 51, no. 4, pp. 1106–1124, 2014.

[13] J. B. Meurisse *et al.*, "Multidimensional material response simulations of a full-scale tiled ablative heatshield," *Aerospace Science and Technology*, vol. 76, pp. 497–511, 2018.

[14] M. Mahzari *et al.*, *Development and Sizing of the Mars2020 Thermal Protection System.* AIAA, 2022.

[15] M. Stackpoole *et al.*, "Post-flight evaluation of PICA and PICA-X : Comparisons of the stardust SRC and Space-X Dragon 1 forebody heatshield materials," *10th International Planetary Probe Workshop (IPPW-10)*, vol. June 17-21, 2013.

[16] J. Bouilly and C. Plaindoux, "Asterm: Maturation of a new low density ablative material," in *7th European Workshop on TPS & Hot Structures, ESA/ESTEC*, 2013, pp. 8–10.

[17] R. M. Kendall *et al.*, "An analysis of the coupled chemically reacting boundary layer and charring ablator: Part I," *NASA CR*, vol. 1060, pp. 1–96, 1968.

[18] C. B. Moyer and R. A. Rindal, "An analysis of the coupled chemically reacting boundary layer and charring ablator: Part II," *NASA CR*, vol. 1061, pp. 1–168, 1968.

[19] M. J. Wright *et al.*, "Sizing and margins assessment of the mars science laboratory aeroshell thermal protection system," *Journal of Spacecraft and Rockets*, vol. 51, no. 4, pp. 1125–1138, 2014.

[20] M. Wright *et al.*, "An overview of technology investments in the nasa entry systems modeling project," in *53rd AIAA Aerospace Sciences Meeting*, 2015, p. 1892.

[21] H. Xu *et al.*, "Analytical considerations of local thermal non-equilibrium conditions for thermal transport in metal foams," *International Journal of Thermal Sciences*, vol. 95, pp. 73–87, 2015.

[22] S. Chikh *et al.*, "Analytical solution of non-Darcian forced convection in an annular duct partially filled with a porous medium," *International Journal of Heat and Mass Transfer*, vol. 38, no. 9, pp. 1543–1551, 1995.

[23] A. Shugard and D. Robinson, "A simple model of gas flow in a porous powder compact," Technical Report SAND2014-2858, Sandia National Laboratories, Albuquerque, Tech. Rep., 2014.

[24] W. Lu, C. Zhao, and S. Tassou, "Thermal analysis on metal-foam filled heat exchangers. part i: Metal-foam filled pipes," *International Journal of Heat and Mass Transfer*, vol. 49, no. 15-16, pp. 2751–2761, 2006.

[25] J. Florio Jr *et al.*, "A study of the effects of the assumption of local-thermal equilibrium on the overall thermally-induced response of a decomposing, glass-filled polymer composite," *International Journal of Heat and Mass Transfer*, vol. 34, no. 1, pp. 135–147, 1991.

[26] N. Puiroux, M. Prat, and M. Quintard, "Non-equilibrium theories for macroscale heat transfer: ablative composite layer systems," *International Journal of Thermal Sciences*, vol. 43, no. 6, pp. 541–554, 2004.

[27] N. Puiroux *et al.*, "Macro-scale non-equilibrium heat transfer in ablative layer composite layers," in *8th AIAA/ASME Joint Thermophysics and Heat Transfer Conference*, 2003, p. 3336.

[28] J. Scoggins and H. Hassan, "Pyrolysis mechanism of PICA," in *10th AIAA/ASME Joint Thermophysics and Heat Transfer Conference*, 2010, p. 4655.

[29] H. Scandelli, "Modélisation multi-échelle des milieux poreux réactifs à haute température appliquée aux protections thermique spatiale et à la pyrolyse de la biomasse." Theses, HESAM Université, Oct. 2022. [Online]. Available: https://pastel.archives-ouvertes.fr/tel-04042460

[30] T. Esence *et al.*, "A review on experience feedback and numerical modeling of packed-bed thermal energy storage systems," *Solar Energy*, vol. 153, pp. 628–654, 2017.

[31] M. Hänchen, S. Brückner, and A. Steinfeld, "High-temperature thermal storage using a packed bed of rocks – heat transfer analysis and experimental validation," *Applied Thermal Engineering*, vol. 31, no. 10, pp. 1798–1806, 2011.

[32] G. Alva, Y. Lin, and G. Fang, "An overview of thermal energy storage systems," *Energy*, vol. 144, pp. 341–378, 2018.

[33] R. Anderson *et al.*, "Experimental results and modeling of energy storage and recovery in a packed bed of alumina particles," *Applied Energy*, vol. 119, pp. 521–529, 2014.

[34] ——, "Packed bed thermal energy storage: A simplified experimentally validated model," *Journal of Energy Storage*, vol. 4, pp. 14–23, 2015.

[35] K. Ismail and R. Stuginsky Jr, "A parametric study on possible fixed bed models for pcm and sensible heat storage," *Applied Thermal Engineering*, vol. 19, no. 7, pp. 757–788, 1999.

[36] G. Zanganeh *et al.*, "Design of packed bed thermal energy storage systems for high-temperature industrial process heat," *Applied Energy*, vol. 137, pp. 812–822, 2015.

[37] T. E. Alam *et al.*, "Macroencapsulation and characterization of phase change materials for latent heat thermal energy storage systems," *Applied Energy*, vol. 154, pp. 92–101, 2015.

[38] G. Zanganeh *et al.*, "Packed-bed thermal storage for concentrated solar power – pilot-scale demonstration and industrial-scale design," *Solar Energy*, vol. 86, no. 10, pp. 3084–3098, 2012.

[39] N. Calvet *et al.*, "Compatibility of a post-industrial ceramic with nitrate molten salts for use as filler material in a thermocline storage system," *Applied Energy*, vol. 109, pp. 387–393, 2013.

[40] S. Zunft *et al.*, "Jülich Solar Power Tower—Experimental Evaluation of the Storage Subsystem and Performance Calculation," *Journal of Solar Energy Engineering*, vol. 133, no. 3, 07 2011.

[41] J. Fernengel and O. Hinrichsen, "Influence of material properties on voidage of numerically generated random packed beds," *Chemical Engineering Science*, vol. 233, p. 116406, 2021.

[42] P. E. Burström *et al.*, "Modelling heat transfer during flow through a random packed bed of spheres," *Heat and Mass Transfer*, vol. 54, pp. 1225–1245, 2018.

[43] F. Campuzano, R. C. Brown, and J. D. Martínez, "Auger reactors for pyrolysis of biomass and wastes," *Renewable and Sustainable Energy Reviews*, vol. 102, pp. 372–409, 2019.

[44] B. Peters and C. Bruch, "Drying and pyrolysis of wood particles: experiments and simulation," *Journal of analytical and applied pyrolysis*, vol. 70, no. 2, pp. 233–250, 2003.

[45] W. Guo *et al.*, "Determination of effective thermal conductivity and specific heat capacity of wood pellets," *Fuel*, vol. 103, pp. 347–355, 2013.

[46] S. Pedrazzi *et al.*, "Experimental heat transfer evaluation in a porous media," in *Journal of Physics: Conference Series*, vol. 1868, no. 1. IOP Publishing, 2021, p. 012016.

[47] E. Schröder, A. Class, and L. Krebs, "Measurements of heat transfer between particles and gas in packed beds at low to medium reynolds numbers," *Experimental Thermal and Fluid Science*, vol. 30, no. 6, pp. 545–558, 2006.

[48] J. Ahn and J. J. Kim, "Combustion and heat transfer characteristics inside the combustion chamber of a wood pellet boiler," *Journal of Mechanical Science and Technology*, vol. 28, no. 2, pp. 789–795, 2014.

[49] E. Cardozo *et al.*, "Integration of a wood pellet burner and a stirling engine to produce residential heat and power," *Applied Thermal Engineering*, vol. 73, no. 1, pp. 671–680, 2014.

[50] W. C. Park, A. Atreya, and H. R. Baum, "Experimental and theoretical investigation of heat and mass transfer processes during wood pyrolysis," *Combustion and flame*, vol. 157, no. 3, pp. 481–494, 2010.

[51] H. Khodaei *et al.*, "A cfd-based comparative analysis of drying in various single biomass particles," *Applied Thermal Engineering*, vol. 128, pp. 1062–1073, 2018.

[52] G. Gianfelice and P. Canu, "On the mechanism of single pellet smouldering combustion," *Fuel*, vol. 301, p. 121044, 2021.

[53] R. Mehrabian *et al.*, "A cfd model for thermal conversion of thermally thick biomass particles," *Fuel Processing Technology*, vol. 95, pp. 96–108, 2012.

[54] J. Ahn and H. J. Kim, "Combustion process of a korean wood pellet at a low temperature," *Renewable Energy*, vol. 145, pp. 391–398, 2020.

[55] J. Chaney, H. Liu, and J. Li, "An overview of cfd modelling of small-scale fixed-bed biomass pellet boilers with preliminary results from a simplified approach," *Energy Conversion and Management*, vol. 63, pp. 149–156, 2012, 10th International Conference on Sustainable Energy Technologies (SET 2011).

[56] R. Mehrabian *et al.*, "Multi-physics modelling of packed bed biomass combustion," *Fuel*, vol. 122, pp. 164–178, 2014.

[57] R. van der Lans *et al.*, "Modelling and experiments of straw combustion in a grate furnace," *Biomass and Bioenergy*, vol. 19, no. 3, pp. 199–208, 2000.

[58] C. Mandl, I. Obernberger, and F. Biedermann, "Modelling of an updraft fixed-bed gasifier operated with softwood pellets," *Fuel*, vol. 89, no. 12, pp. 3795–3806, 2010.

[59] W. Yang *et al.*, "Performance analysis of a fixed-bed biomass gasifier using high-temperature air," *Fuel Processing Technology*, vol. 87, no. 3, pp. 235–245, 2006.

[60] C. Ghabi, H. Benticha, and M. Sassi, "Two-dimensional computational modeling and simulation of wood particles pyrolysis in a fixed bed reactor," *Combustion science and technology*, vol. 180, no. 5, pp. 833–853, 2008.

[61] C. H. Bamford, J. Crank, and D. H. Malan, "The combustion of wood. part i," *Mathematical Proceedings of the Cambridge Philosophical Society*, vol. 42, no. 2, p. 166–182, 1946.

[62] J. E. White, W. J. Catallo, and B. L. Legendre, "Biomass pyrolysis kinetics: A comparative critical review with relevant agricultural residue case studies," *Journal of Analytical and Applied Pyrolysis*, vol. 91, no. 1, pp. 1–33, 2011.

[63] J. Villermaux *et al.*, "A new model for thermal volatilization of solid particles undergoing fast pyrolysis," *Chemical Engineering Science*, vol. 41, no. 1, pp. 151–157, 1986.

[64] K. R. G. Burra and A. K. Gupta, "Modeling of biomass pyrolysis kinetics using sequential multi-step reaction model," *Fuel*, vol. 237, pp. 1057–1067, 2019.

[65] C. Di Blasi, "Kinetic and heat transfer control in the slow and flash pyrolysis of solids," *Industrial & Engineering Chemistry Research*, vol. 35, no. 1, pp. 37–46, 1996.

[66] M. Quintard, "Introduction to heat and mass transport in porous media," *Porous Media Interaction with High Temperature and High Speed Flows, Von Karman Institude for Fluid Dynamics, Rhode Saint Genese, Belgium*, 2015.

[67] M. Quintard and S. Whitaker, "One- and two-equation models for transient diffusion processes in two-phase systems," in *Advances in Heat Transfer*, 1993, vol. 23, pp. 369–464.

[68] M. Quintard, M. Kaviany, and S. Whitaker, "Two-medium treatment of heat transfer in porous media: numerical results for effective properties," *Advances in Water Resources*, vol. 20, no. 2-3, pp. 77–94, 1997.

[69] M. Agnaou, D. Lasseux, and A. Ahmadi, "Origin of the inertial deviation from darcy's law: An investigation from a microscopic flow analysis on two-dimensional model structures," *Physical Review E*, vol. 96, no. 4, p. 043105, 2017.

[70] S. Whitaker, "The forchheimer equation: a theoretical development," *Transport in Porous Media*, vol. 25, no. 1, pp. 27–61, 1996.

[71] C. Aguilar-Madera *et al.*, "Computing the permeability and forchheimer tensor of porous rocks via closure problems and digital images," *Advances in Water Resources*, vol. 142, p. 103616, 2020.

[72] M. Kaviany, *Principles of heat transfer in porous media.* Springer Science & Business Media, 2012.

[73] C. T. DeGroot and A. G. Straatman, "Closure of non-equilibrium volume-averaged energy equations in high-conductivity porous media," *International journal of heat and mass transfer*, vol. 54, no. 23-24, pp. 5039–5048, 2011.

[74] H. Scandelli *et al.*, "Computation of the permeability tensor of non-periodic anisotropic porous media from 3d images," *Transport in Porous Media*, vol. 142, no. 3, p. 669 – 697, 2022.

[75] A. Borner, F. Panerai, and N. N.Mansour, "High temperature permeability of fibrous materials using direct simulation monte carlo," *International Journal of Heat and Mass Transfer*, vol. 106, pp. 1318–1326, 2017.

[76] A. M. Amao, "Mathematical model for darcy forchheimer flow with applications to well performance analysis," Ph.D. dissertation, Texas Tech University, 2007.

[77] J. Lachaud *et al.*, "A generic local thermal equilibrium model for porous reactive materials submitted to high temperatures," *International Journal of Heat and Mass Transfer*, vol. 108, pp. 1406–1417, 2017.

[78] H. Scandelli, A. Ahmadi-Senichault, and J. Lachaud, "Two-temperature ablative material response model with application to stardust and msl atmospheric entries," *Aerospace Science and Technology*, vol. 137, p. 108297, 2023.

[79] K. Kamiuto and S. Yee, "Heat transfer correlations for open-cellular porous materials," *International Communications in Heat and Mass Transfer*, vol. 32, no. 7, pp. 947–953, 2005.

[80] A. Fuller *et al.*, "Measurement and interpretation of the heat transfer coefficients of metal foams," *Journal of Mechanical Engineering Science*, vol. 219, no. 2, pp. 183–191, 2005.

[81] X.-l. Xia *et al.*, "Experiment on the convective heat transfer from airflow to skeleton in open-cell porous foams," *International Journal of Heat and Mass Transfer*, vol. 106, pp. 83–90, 2017.

[82] J.-J. Hwang *et al.*, "Measurement of interstitial convective heat transfer and frictional drag for flow across metal foams," *Journal of Heat and Mass Transfer*, vol. 124, no. 1, pp. 120–129, 2002.

[83] X. Fu, R. Viskanta, and J. Gore, "Measurement and correlation of volumetric heat transfer coefficients of cellular ceramics," *Experimental Thermal and Fluid Science*, vol. 17, no. 4, pp. 285–293, 1998.

[84] K. Ando, H. Hirai, and Y. Sano, "An accurate experimental determination of interstitial heat transfer coefficients of ceramic foams using the single blow method," *The Open Transport Phenomena Journal*, vol. 5, no. 1, 2013.

[85] G. Gürüf *et al.*, "Experimental based numerical approach for determination of volumetric heat transfer coefficients of modified graphite foams," *Applied Thermal Engineering*, vol. 174, pp. 115–310, 2020.

[86] S. E. Gustafsson, "Transient plane source techniques for thermal conductivity and thermal diffusivity measurements of solid materials," *Review of scientific instruments*, vol. 62, no. 3, pp. 797–804, 1991.

[87] J. Huang, "Sweating guarded hot plate test method," *Polymer Testing*, vol. 25, no. 5, pp. 709–716, 2006.

[88] A. Rasti, M. Pineda, and M. Razavi, "Assessment of soil moisture content measurement methods: Conventional laboratory oven versus halogen moisture analyzer," *Journal of Soil and Water Science*, vol. 4, no. 1, pp. 151–160, 2020.

[89] H. K. Tran *et al.*, "Phenolic impregnated carbon ablators (PICA) as thermal protection systems for discovery missions," *NASA Technical Memorandum*, vol. 110440, pp. 1–70, 1997.

[90] K. Triantou *et al.*, "Thermo-mechanical performance of an ablative/ceramic composite hybrid thermal protection structure for re-entry applications," *Composites, Part B*, vol. 82, pp. 159–165, 2015.

[91] F. Panerai *et al.*, "Experimental measurements of the permeability of fibrous carbon at high-temperature," *International Journal of Heat and Mass Transfer*, vol. 101, p. 267 – 273, 2016.

[92] J. Lachaud and N. N. Mansour, "Porous-material analysis toolbox based on openfoam and applications," *Journal of Thermophysics and Heat Transfer*, vol. 28, no. 2, p. 191 – 202, 2014.

[93] J. Lachaud *et al.*, "A short review of ablative material response models and simulation tools," in *Proceedings of the 7th European Symposium on Aerothermodynamics, ESA SP-692, ISBN: 978-92-9221-256-8*, L. Ouwehand, Ed., no. 91. Noordwijk, The Netherlands: ESA, 2011, pp. 1–8.

[94] I. Tavman, "Effective thermal conductivity of granular porous materials," *International Communications in Heat and Mass Transfer*, vol. 23, no. 2, pp. 169–176, 1996.

[95] Z. Abdulagatova, I. Abdulagatov, and V. Emirov, "Effect of temperature and pressure on the thermal conductivity of sandstone," *International Journal of Rock Mechanics and Mining Sciences*, vol. 46, no. 6, pp. 1055–1071, 2009.

[96] K.-T. Hsiao and S. G. Advani, "Modified effective thermal conductivity due to heat dispersion in fibrous porous media," *International journal of heat and mass transfer*, vol. 42, no. 7, pp. 1237–1254, 1999.

[97] J. Chevalier and J. Lachaud, "On the effect of the internal gas flow velocity on the thermal conductivity of porous thermal protection systems," in *2nd International Conference on Flight Vehicles, Aerothermodynamics and Re-entry Missions and Engineering*, 2022.

[98] F. Kuwahara, M. Shirota, and A. Nakayama, "A numerical study of interfacial convective heat transfer coefficient in two-energy equation model for convection in porous media," *International Journal of Heat and Mass Transfer*, vol. 44, no. 6, pp. 1153–1159, 2001.

[99] F. E. Teruel, "Entrance effect on the interfacial heat transfer and the thermal dispersion in laminar flows through porous media," *International Journal of Thermal Sciences*, vol. 104, pp. 172–185, 2016.

[100] A. Nakayama, "A note on the confusion associated with the interfacial heat transfer coefficient for forced convection in porous media," *International Journal of Heat and Mass Transfer*, vol. 79, pp. 1–2, 2014.

[101] F. E. Teruel and L. Díaz, "Calculation of the interfacial heat transfer coefficient in porous media employing numerical simulations," *International Journal of Heat and Mass Transfer*, vol. 60, pp. 406–412, 2013.

[102] Z. Wu *et al.*, "Numerical simulation of convective heat transfer between air flow and ceramic foams to optimise volumetric solar air receiver performances," *International Journal of Heat and Mass Transfer*, vol. 54, no. 7-8, pp. 1527–1537, 2011.

[103] J. Petrasch *et al.*, "Tomography based determination of permeability, dupuit–forchheimer coefficient, and interfacial heat transfer coefficient in reticulate porous ceramics," *International Journal of Heat and Fluid Flow*, vol. 29, no. 1, pp. 315–326, 2008.

[104] H. Scandelli *et al.*, "Volumetric heat transfer coefficient: Numerical evaluation and introductory analysis to anisotropic effect," *to appear*, 2022.

[105] N. Wakao, S. Kaguei, and T. Funazkri, "Effect of fluid dispersion coefficients on particle-to-fluid heat transfer coefficients in packed beds: correlation of nusselt numbers," *Chemical engineering science*, vol. 34, no. 3, pp. 325–336, 1979.

[106] L. Younis and R. Viskanta, "Experimental determination of the volumetric heat transfer coefficient between stream of air and ceramic foam," *International Journal of Heat and Mass Transfer*, vol. 36, no. 6, pp. 1425–1434, 1993.

[107] P. Renze and K. Akermann, "Simulation of conjugate heat transfer in thermal processes with open source cfd," *ChemEngineering*, vol. 3, no. 2, p. 59, 2019.

[108] K. Stephan, R. Krauss, and A. Laesecke, "Viscosity and thermal conductivity of nitrogen for a wide range of fluid states," *Journal of physical and chemical reference data*, vol. 16, no. 4, pp. 993–1023, 1987.

[109] F. Torres-Herrador *et al.*, "Determination of heat capacity of carbon composites with application to carbon/phenolic ablators up to high temperatures," *Aerospace Science and Technology*, vol. 108, p. 106375, 2021.

[110] B. M. Adams *et al.*, "Dakota, a multilevel parallel object-oriented framework for design optimization, parameter estimation, uncertainty quantification, and sensitivity analysis: Version 6.15 user's manual," *Sandia Technical Report SAND2020-12495*, 2021.

[111] J. Gablonsky, "Direct version 2.0 userguide technical report," *CRSC-TR01-08, Center for Research in Scientific Computation*, 2001.

[112] J. E. Dennis Jr, D. M. Gay, and R. E. Walsh, "An adaptive nonlinear least-squares algorithm," *ACM Transactions on Mathematical Software (TOMS)*, vol. 7, no. 3, pp. 348–368, 1981.

[113] J. Liu *et al.*, "Experimental study on heat storage and transfer characteristics of supercritical air in a rock bed," *International Journal of Heat and Mass Transfer*, vol. 77, pp. 883–890, 2014.

[114] K. Yang *et al.*, "Theoretical evaluation on the impact of heat exchanger in advanced adiabatic compressed air energy storage system," *Energy Conversion and Management*, vol. 86, pp. 1031–1044, 2014.

[115] H. Mozayeni *et al.*, "Performance study of an advanced adiabatic compressed air energy storage system," *Energy Procedia*, vol. 110, pp. 71–76, 2017, 1st International Conference on Energy and Power, ICEP2016, 14-16 December 2016, RMIT University, Melbourne, Australia.

[116] E. Oró *et al.*, "Review on phase change materials (pcms) for cold thermal energy storage applications," *Applied Energy*, vol. 99, pp. 513–533, 2012.

[117] F. Agyenim *et al.*, "A review of materials, heat transfer and phase change problem formulation for latent heat thermal energy storage systems (lhtess)," *Renewable and Sustainable Energy Reviews*, vol. 14, no. 2, pp. 615–628, 2010.

[118] A. Gil *et al.*, "State of the art on high temperature thermal energy storage for power generation. part 1—concepts, materials and modellization," *Renewable and Sustainable Energy Reviews*, vol. 14, no. 1, pp. 31–55, 2010.

[119] B. Xu, P.-W. Li, and C. L. Chan, "Extending the validity of lumped capacitance method for large biot number in thermal storage application," *Solar Energy*, vol. 86, no. 6, pp. 1709–1724, 2012.

[120] Y. Qu *et al.*, "Heat transfer characteristics of mixed convection in packed beds," *Chemical Engineering Science*, vol. 255, p. 117679, 2022.

[121] T. Schumann, "Heat transfer: A liquid flowing through a porous prism," *Journal of the Franklin Institute*, vol. 208, no. 3, pp. 405–416, 1929.

[122] B. Pomeroy, "Thermal energy storage in a packed bed of iron spheres with liquid sodium coolant," *Solar Energy*, vol. 23, no. 6, pp. 513–515, 1979.

[123] A. Saez and B. McCoy, "Dynamic response of a packed bed thermal storage system—a model for solar air heating," *Solar Energy*, vol. 29, no. 3, pp. 201–206, 1982.

[124] S. Pati *et al.*, "Critical review on local thermal equilibrium and local thermal non-equilibrium approaches for the analysis of forced convective flow through porous media," *Int. Commun. Heat Mass Transf.*, vol. 132, p. 105889, 2022.

[125] X. Ma *et al.*, "Numerical and experimental studies of packed bed thermal energy storage system based on a novel transient energy model," *Energy Science & Engineering*, vol. 11, no. 2, pp. 727–744, 2023.

[126] N. Wakao and S. Kaguei, "Heat and mass transfer in packed bedsgordon and breach science publications," *New York*, 1982.

[127] W. Ranz, "Friction and transfer coefficients for single particles and packed beds," *Chemical Engineering Progress*, vol. 48, pp. 247–253, 1952.

[128] T. Galloway and B. Sage, "A model of the mechanism of transport in packed, distended, and fluidized beds," *Chemical Engineering Science*, vol. 25, no. 3, pp. 495–516, 1970.

[129] J. Yang *et al.*, "Experimental analysis of forced convective heat transfer in novel structured packed beds of particles," *Chemical engineering science*, vol. 71, pp. 126–137, 2012.

[130] M. Naghash *et al.*, "Measurement of convective heat transfer coefficients in a randomly packed bed of silica gel particles using ihtp analysis," *Applied Thermal Engineering*, vol. 106, pp. 361–370, 2016.

[131] M. Nazari *et al.*, "Experimental investigation of heat transfer and second law analysis in a pebble bed channel with internal heat generation," *International Journal of Heat and Mass Transfer*, vol. 114, pp. 688–702, 2017.

[132] V. Sassanis *et al.*, "Numerical determination of the volumetric heat transfer coefficient in fixed beds of wood chips," *Chemical Engineering Journal*, vol. 417, p. 128009, 2021.

[133] F. Augier, F. Idoux, and J.-Y. Delenne, "Numerical simulations of transfer and transport properties inside packed beds of spherical particles," *Chemical Engineering Science*, vol. 65, no. 3, pp. 1055–1064, 2010.

[134] J. Petrasch *et al.*, "Tomography based determination of permeability, dupuit–forchheimer coefficient, and interfacial heat transfer coefficient in reticulate porous ceramics," *International Journal of Heat and Fluid Flow*, vol. 29, no. 1, pp. 315–326, 2008.

[135] A. A. Jalalzadeh-Azar, W. G. Steele, and G. A. Adebiyi, "Heat Transfer in a High-Temperature Packed Bed Thermal Energy Storage System—Roles of Radiation and Intraparticle Conduction," *Journal of Energy Resources Technology*, vol. 118, no. 1, pp. 50–57, 03 1996.

[136] M. Cascetta *et al.*, "A comparison between cfd simulation and experimental investigation of a packed-bed thermal energy storage system," *Appl. Therm. Eng.*, vol. 98, pp. 1263–1272, 2016.

[137] C. Yang and A. Nakayama, "A synthesis of tortuosity and dispersion in effective thermal conductivity of porous media," *International Journal of Heat and Mass Transfer*, vol. 53, no. 15, pp. 3222–3230, 2010.

[138] A. J. van Eekelen and J. Lachaud, "Numerical validation of an effective radiation heat transfer model for fiber preforms," *Journal of Spacecraft and Rockets*, vol. 48, no. 3, pp. 534–537, 2011.

[139] W. Van Antwerpen, C. Du Toit, and P. G. Rousseau, "A review of correlations to model the packing structure and effective thermal conductivity in packed beds of mono-sized spherical particles," *Nuclear Engineering and design*, vol. 240, no. 7, pp. 1803–1818, 2010.

[140] D. Okello, O. J. Nydal, and E. J. Banda, "Experimental investigation of thermal de-stratification in rock bed tes systems for high temperature applications," *Energy Conversion and Management*, vol. 86, pp. 125–131, 2014.

[141] A. Shitzer and M. Levy, "Transient Behavior of a Rock-Bed Thermal Storage System Subjected to Variable Inlet Air Temperatures: Analysis and Experimentation," *Journal of Solar Energy Engineering*, vol. 105, no. 2, pp. 200–206, 05 1983.

[142] S. S. Halkarni, A. Sridharan, and S. Prabhu, "Estimation of volumetric heat transfer coefficient in randomly packed beds of uniform sized spheres with water as working medium," *International Journal of Thermal Sciences*, vol. 110, pp. 340–355, 2016.

[143] G. E. Mueller, "Radial void fraction distributions in randomly packed fixed beds of uniformly sized spheres in cylindrical containers," *Structural Safety*, vol. 72, no. 3, pp. 269–275, 1992.

[144] W. Sobieski and A. Trykozko, "Darcy's and forchheimer's laws in practice. part 1. the experiment," *Technical Sciences/University of Warmia and Mazury in Olsztyn*, 2014.

[145] A. Montillet, "Flow Through a Finite Packed Bed of Spheres: A Note on the Limit of Applicability of the Forchheimer-Type Equation ," *Journal of Fluids Engineering*, vol. 126, no. 1, pp. 139–143, 02 2004.

[146] J. C. Chen and S. W. Churchill, "Radiant heat transfer in packed beds," *AIChE Journal*, vol. 9, no. 1, pp. 35–41, 1963.

[147] B. J. McBride, S. Gordon, and M. A. Reno, "Thermodynamic Data for Fifty Reference Elements," Glenn Research Center, Cleveland, Ohio, NASA TP-3287-REV1, February 2001.

[148] M. Pertermann *et al.*, "Transport properties of low-sanidine single-crystals, glasses and melts at high temperature," *Contributions to Mineralogy and Petrology*, vol. 155, no. 6, pp. 689–702, 2008.

[149] B. Adams *et al.*, "Dakota, a multilevel parallel object-oriented framework for design optimization, parameter estimation, uncertainty quantification, and sensitivity analysis: Version 6.13 user's manual." Sandia National Lab.(SNL-NM), Albuquerque, NM (United States), Tech. Rep., 2020.

[150] A. Olsson, G. Sandberg, and O. Dahlblom, "On latin hypercube sampling for structural reliability analysis," *Structural Safety*, vol. 25, no. 1, pp. 47–68, 2003.

[151] J. C. Helton and F. J. Davis, "Sampling-based methods for uncertainty and sensitivity analysis," Sandia National Lab.(SNL-NM), Albuquerque, NM (United States); Sandia ..., Tech. Rep., 2000.

[152] C. R. Wilke and O. Hougen, "Mass transfer in the flow of gases through granular solids extended to low modified reynolds numbers," *Transactions of the American Institute of Chemical Engineers*, vol. 41, no. 4, pp. 445–451, 1945.

[153] G. Malling and G. Thodos, "Analogy between mass and heat transfer in beds of spheres: contributions due to end effects," *International Journal of Heat and Mass Transfer*, vol. 10, no. 4, pp. 489–498, 1967.

[154] J. D. Acetis and G. Thodos, "Mass and heat transfer in flow of gases through spherical packings," *Industrial & Engineering Chemistry*, vol. 52, no. 12, pp. 1003–1006, 1960.

[155] L. Galloway, W. Komarnicky, and N. Epstein, "Effect of configuration on mass and heat transfer in beds stacked spheres," *Can. J. Chem. Eng*, vol. 135, pp. 139–150, 1957.

[156] H. Khodaei *et al.*, "An overview of processes and considerations in the modelling of fixed-bed biomass combustion," *Energy*, vol. 88, pp. 946–972, 2015.

[157] R. Sikkema *et al.*, "The european wood pellet markets: current status and prospects for 2020," *Biofuels, Bioproducts and Biorefining*, vol. 5, no. 3, pp. 250–278, 2011.

[158] R. Warnecke, "Gasification of biomass: comparison of fixed bed and fluidized bed gasifier," *Biomass and Bioenergy*, vol. 18, no. 6, pp. 489–497, 2000.

[159] G. Souza *et al.*, "Simultaneous heat and mass transfer in a fixed bed dryer," *Applied Thermal Engineering*, vol. 90, pp. 38–44, 2015.

[160] M. Mayerhofer *et al.*, "Experimental investigation of pressure drop in packed beds of irregular shaped wood particles," *Powder Technology*, vol. 205, no. 1-3, pp. 30–35, 2011.

[161] S. Hamidi *et al.*, "Critical review of the local thermal equilibrium assumption in heterogeneous porous media: Dependence on permeability and porosity contrasts," *Applied Thermal Engineering*, vol. 147, pp. 962–971, 2019.

[162] L. Bennamoun and A. Belhamri, "Study of convective heat and mass transfer in a porous media: Application to packed bed drying," *Series Editor: AS Mujumdar*, pp. 532–538, 2006.

[163] V. Sassanis *et al.*, "Numerical determination of the volumetric heat transfer coefficient in fixed beds of wood chips," *Chemical Engineering Journal*, vol. 417, p. 128009, 2021.

[164] F. Yazdanpanah *et al.*, "Airflow versus pressure drop for bulk wood pellets," *Biomass and Bioenergy*, vol. 35, no. 5, pp. 1960–1966, 2011.

[165] S. Ergun, "Fluid flow through packed columns," *Chemical Engineering Progress*, vol. 48, no. 2, pp. 89–94, 1952.

[166] V. Pozzobon, J. Colin, and P. Perre, "Hydrodynamics of a packed bed of non-spherical polydisperse particles: A fully virtual approach validated by experiments," *Chemical Engineering Journal*, vol. 354, pp. 126–136, 2018.

[167] S. Messai *et al.*, "Comparison of 1d and 2d models predicting a packed bed drying," *International Journal for Simulation and Multidisciplinary Design Optimization*, vol. 5, p. A14, 2014.

[168] C. Tremblay, A. Cloutier, and Y. Fortin, "Experimental determination of the convective heat and mass transfer coefficients for wood drying," *Wood Science and Technology*, vol. 34, no. 3, pp. 253–276, 2000.

[169] C. Igathinathane *et al.*, "Simple and inexpensive method of wood pellets macro-porosity measurement," *Bioresource Technology*, vol. 101, no. 16, pp. 6528–6537, 2010.

[170] S. Afshari, S. H. Hejazi, and A. Kantzas, "Pore-level modeling of effective longitudinal thermal dispersion in non-isothermal flows through granular porous media," *Chemical Engineering Science*, vol. 199, pp. 451–462, 2019.

[171] B. J. McBride, *NASA Glenn coefficients for calculating thermodynamic properties of individual species*. National Aeronautics and Space Administration, John H. Glenn Research Center, 2002.

[172] J. B. Scoggins *et al.*, "Mutation++: Multicomponent thermodynamic and transport properties for ionized gases in c++," *SoftwareX*, vol. 12, p. 100575, 2020.

[173] S. Liu *et al.*, "Experimental investigation on the validity of the local thermal equilibrium assumption in ablative-material response models," *Aerospace Science and Technology*, p. 108516, 2023.

[174] J. R. Gaier, "The effects of lunar dust on eva systems during the apollo missions," Glenn Research Center, Cleveland, Ohio, Tech. Rep., 2007.

[175] M. Stackpoole *et al.*, "Post-flight evaluation of stardust sample return capsule forebody heatshield material," in *46th AIAA Aerospace Sciences Meeting and Exhibit*, 2008.

[176] K. T. Edquist *et al.*, "Mars science laboratory heat shield aerothermodynamics: Design and reconstruction," *Journal of Spacecraft and Rockets*, vol. 51, no. 4, pp. 1106–1124, 2014.

[177] J. B. Meurisse *et al.*, "Multidimensional material response simulations of a full-scale tiled ablative heatshield," *Aerospace Science and Technology*, vol. 76, pp. 497–511, 2018.

[178] M. Mahzari *et al.*, "Development and sizing of the mars2020 thermal protection system," in *AIAA AVIATION 2022 Forum*, 2022, p. 3951.

[179] E. Pate-Cornell and R. Dillon, "Probabilistic risk analysis for the nasa space shuttle: a brief history and current work," *Reliability Engineering & System Safety*, vol. 74, no. 3, pp. 345–352, 2001.

[180] J. Lachaud *et al.*, "A short review of ablative-material response models and simulation tools," in *7th aerothermodynamics symposium*, no. ARC-E-DAA-TN3517, 2011.

[181] A. Martin and I. Boyd, "Simulation of pyrolysis gas within a thermal protection system," in *40th Thermophysics Conference*, 2008, p. 3805.

[182] P. Kumar and F. Topin, "Investigation of fluid flow properties in open cell foams: Darcy and weak inertia regimes," *Chemical Engineering Science*, vol. 116, pp. 793–805, 2014.

[183] D. Lasseux, A. A. Abbasian Arani, and A. Ahmadi, "On the stationary macroscopic inertial effects for one phase flow in ordered and disordered porous media," *Physics of Fluids*, vol. 23, no. 7, p. 073103, 2011.

[184] P. Poureslami *et al.*, "Pore-scale convection-conduction heat transfer and fluid flow in open-cell metal foams: A three-dimensional multiple-relaxation time lattice boltzmann (mrt-lbm) solution," *International Communications in Heat and Mass Transfer*, vol. 126, p. 105465, 2021.

[185] X. Wang, F. Thauvin, and K. Mohanty, "Non-darcy flow through anisotropic porous media," *Chemical Engineering Science*, vol. 54, no. 12, pp. 1859–1869, 1999.

[186] M. Hangi, V. Wheeler, and W. Lipiński, "Numerical determination of permeability and forchheimer coefficient in dual-scale porous media," *International Communications in Heat and Mass Transfer*, vol. 122, p. 105089, 2021.

[187] A. G. Straatman *et al.*, "Characterization of Porous Carbon Foam as a Material for Compact Recuperators," *Journal of Engineering for Gas Turbines and Power*, vol. 129, no. 2, pp. 326–330, 2006.

[188] M. D. Innocentini *et al.*, "Prediction of ceramic foams permeability using ergun's equation," *Journal of Materials Research*, vol. 2, pp. 283–289, 1999.

[189] Z. Zeng and R. Grigg, "A criterion for non-darcy flow in porous media," *Transport in Porous Media*, vol. 63, pp. 57–69, 2006.

[190] J. T. Gostick *et al.*, "In-plane and through-plane gas permeability of carbon fiber electrode backing layers," *Journal of Power Sources*, vol. 162, no. 1, pp. 228–238, 2006.

[191] J. Marschall and F. S. Milos, "Gas permeability of rigid fibrous refractory insulations," *Journal of Thermophysics and Heat Transfer*, vol. 12, no. 4, pp. 528–535, 1998.

[192] J. Marschall and M. E. Cox, "Gas permeability of lightweight ceramic ablators," *Journal of Thermophysics and Heat Transfer*, vol. 13, no. 3, pp. 382–384, 1999.

[193] Y.-K. Chen and F. S. Milos, "Effects of nonequilibrium chemistry and darcy—forchheimer pyrolysis flow for charring ablator," *Journal of Spacecraft and Rockets*, vol. 50, no. 2, pp. 256–269, 2013.

[194] H.-K. Ahn, C. Park, and K. Sawada, "Response of heatshield material at stagnation point of pioneer-venus probes," *Journal of Thermophysics and Heat Transfer*, vol. 16, no. 3, pp. 432–439, 2002.

[195] H. Jasak *et al.*, "Openfoam: A c++ library for complex physics simulations," in *International workshop on coupled methods in numerical dynamics*, vol. 1000. IUC Dubrovnik Croatia, 2007, pp. 1–20.

[196] H. G. Weller *et al.*, "A tensorial approach to computational continuum mechanics using object-oriented techniques," *Computer in Physics*, vol. 12, no. 6, pp. 620–631, 11 1998.

[197] C. Mei and J.-L. Auriault, "The effect of weak inertia on flow through a porous medium," *Journal of Fluid Mechanics*, vol. 222, pp. 647–663, 1991.

[198] S. Whitaker, *The method of volume averaging*. Springer Science & Business Media, 2013, vol. 13.

[199] F. Doraia *et al.*, "Packing fixed bed reactors with cylinders: influence of particle length distribution," *Procedia Engineering*, vol. 42, pp. 1335–1345, 2012.

[200] J. Yang *et al.*, "Computational study of fluid flow and heat transfer in composite packed beds of spheres with low tube to particle diameter ratio," *Nuclear Engineering and Design*, vol. 300, pp. 85–96, 2016.

[201] L. Chen *et al.*, "Pore-scale modeling of complex transport phenomena in porous media," *Progress in Energy and Combustion Science*, vol. 88, p. 100968, 2022.

[202] M. Prat, "Recent advances in pore-scale models for drying of porous media," *Chemical engineering journal*, vol. 86, no. 1-2, pp. 153–164, 2002.

[203] A. Parmigiani *et al.*, "Pore-scale mass and reactant transport in multiphase porous media flows," *Journal of Fluid Mechanics*, vol. 686, pp. 40–76, 2011.

[204] J. Bear, J.-M. Buchlin *et al.*, *Modelling and applications of transport phenomena in porous media*. Springer, 1991, vol. 5.

[205] S. A. Mikhailenko and M. A. Sheremet, "Impacts of rotation and local element of variable heat generation on convective heat transfer in a partially porous cavity using local thermal non-equilibrium model," *International Journal of Thermal Sciences*, vol. 155, p. 106427, 2020.

[206] Q. Niu and C. Zhang, "Permeability prediction in rocks experiencing mineral precipitation and dissolution: a numerical study," *Water Resources Research*, vol. 55, no. 4, pp. 3107–3121, 2019.

[207] F. Yazdanpanah, "Permeability of bulk wood pellets with respect to airflow," Ph.D. dissertation, University of British Columbia, 2009.

[208] L. C. Martínez-Mendoza *et al.*, "Numerical study of fluid flow at pore scale in packed bed of spheres and grains to obtain the rev," *Comptes Rendus. Mécanique*, vol. 348, no. 8-9, pp. 769–779, 2020.

[209] A. Faridkhou, M. Hamidipour, and F. Larachi, "Hydrodynamics of gas–liquid micro-fixed beds–measurement approaches and technical challenges," *Chemical engineering journal*, vol. 223, pp. 425–435, 2013.

[210] A. G. Dixon, "Correlations for wall and particle shape effects on fixed bed bulk voidage," *The Canadian Journal of Chemical Engineering*, vol. 66, no. 5, pp. 705–708, 1988.

[211] F. Dorai *et al.*, "Fully resolved simulations of the flow through a packed bed of cylinders: Effect of size distribution," *Chemical Engineering Science*, vol. 129, pp. 180–192, 2015.

[212] J. C. Ferguson *et al.*, "Puma: The porous microstructure analysis software," *SoftwareX*, vol. 7, pp. 81–87, 2018.

[213] A. Nakayama *et al.*, "Heat and Fluid Flow Within an Anisotropic Porous Medium ," *Journal of Heat and Mass Transfer*, vol. 124, no. 4, pp. 746–753, 07 2002.

[214] F. E. Teruel and L. Díaz, "Calculation of the interfacial heat transfer coefficient in porous media employing numerical simulations," *International Journal of Heat and Mass Transfer*, vol. 60, pp. 406–412, 2013.

[215] Z. Nie, Y. Lin, and Q. Tong, "Numerical investigation of pressure drop and heat transfer through open cell foams with 3d laguerre-voronoi model," *International Journal of Heat and Mass Transfer*, vol. 113, pp. 819–839, 2017.

[216] G. F. Al-Sumaily, H. M. Hussen, and M. C. Thompson, "Validation of thermal equilibrium assumption in free convection flow over a cylinder embedded in a packed bed," *International Communications in Heat and Mass Transfer*, vol. 58, pp. 184–192, 2014.

[217] K. Yang and K. Vafai, "Transient Aspects of Heat Flux Bifurcation in Porous Media: An Exact Solution," *Journal of Heat Transfer*, vol. 133, no. 5, 02 2011.

[218] F. Kuwahara, M. Shirota, and A. Nakayama, "A numerical study of interfacial convective heat transfer coefficient in two-energy equation model for convection in porous media," *International Journal of Heat and Mass Transfer*, vol. 44, no. 6, pp. 1153–1159, 2001.

[219] C. Kloss and C. Goniva, "Liggghts–open source discrete element simulations of granular materials based on lammps," *supplemental proceedings: materials fabrication, properties, characterization, and modeling*, vol. 2, pp. 781–788, 2011.

[220] S. Falco, F. De Cola, and N. Petrinic, "A method for the generation of 3d representative models of granular based materials," *International Journal for Numerical Methods in Engineering*, vol. 112, no. 4, pp. 338–359, 2017.

[221] J. Ahrens *et al.*, "36-paraview: An end-user tool for large-data visualization," *The visualization handbook*, vol. 717, pp. 50 038–1, 2005.

Appendix A

introduction

De nombreuses technologies en développement s'appuient sur des matériaux poreux : les échangeurs de chaleur pour les concentrateurs solaires [1], les processus de production de biocarburants [2], les nouvelles générations de stockage d'énergie telles que les piles à combustible et les supercondensateurs [3], les boucliers thermiques pour véhicules spatiaux [4], les capteurs microfluidiques [5] etc. Les ingénieurs chimistes et les chercheurs à la pointe de leurs domaines respectifs et menant l'innovation du $21^{\text{ème}}$ siècle bénéficieraient grandement des développements fondamentaux en matière de transfert de chaleur et de masse dans les milieux poreux pour renforcer les modèles phénoménologiques spécifiques aux applications. Ce travail se concentre sur les écoulements à haute température dans les milieux poreux, qui ont des applications diverses allant de la conception de boucliers thermiques poreux pour les véhicules spatiaux entrant dans l'atmosphère à la simulation de systèmes de stockage d'énergie thermique (TES) en lit compacté. Bien que ces applications puissent différer dans leurs conditions extérieures, d'un point de vue physique, les phénomènes de transfert de chaleur se produisant à l'intérieur des matériaux sont similaires. Plus précisément, ils impliquent des échanges de chaleur entre la structure solide du matériau poreux et le fluide qui s'écoule à travers son réseau de pores. De plus, les lois de conservation régissant le comportement de ces matériaux restent constantes, avec les modèles mathématiques utilisant les mêmes équations pour la masse, la quantité de mouvement, et l'énergie. L'étude des écoulements à haute température dans les matériaux poreux présente un intérêt significatif pour divers domaines, en particulier pour les communautés de l'espace, du stockage de l'énergie et de la biomasse. Pour présenter le problème étudié, commençons par une brève introduction aux trois communautés et un examen de leurs principaux atouts.

A.1 Contexte

Dans la communauté spatiale, la conception de systèmes de protection thermique (TPS) capables de supporter des températures extrêmes est essentielle pour garantir la sécurité et la fiabilité des engins spatiaux et des véhicules hypersoniques [4]. Pour mieux comprendre et prévoir les performances des TPS dans des conditions variées, les experts s'efforcent de créer de nouveaux matériaux et modèles. Dans la communauté du stockage d'énergie, le passage aux sources d'énergie renouvelable a necessite

le développement de systèmes de stockage d'énergie thermique (TES) efficaces, capables de stocker et de fournir de l'énergie au besoin, en particulier en ce qui concerne les sources d'énergie irrégulières comme l'énergie solaire et éolienne. Bien que les systèmes TES à lit compacté constituent une option viable, l'élucidation du transfert de chaleur complexe et de la dynamique des fluides à l'intérieur de ces systèmes continue de poser un défi considérable. Dans la communauté de la biomasse, l'utilisation efficace de la biomasse comme source d'énergie alternative nécessite une compréhension complète des processus de séchage et de pyrolyse qui se produisent à l'intérieur des particules de bois. Ces processus sont fortement influencés par des facteurs tels que le transfert de chaleur, la température et les propriétés des matériaux impliqués.

Cette recherche vise à explorer les subtilités du transfert de chaleur et de masse dans les matériaux poreux, en se concentrant sur ces trois communautés spécifiques qui illustrent l'importance de comprendre ces phénomènes dans différentes communautés. En nous plongeant dans la complexité de chaque communauté, nous cherchons à découvrir des informations fondamentales sur les processus de transfert de chaleur et de masse qui se produisent à l'intérieur des matériaux poreux, ce qui à son tour informera le développement de matériaux et de systèmes avancés pour faire face à la demande mondiale croissante en énergie et en durabilité.

A.1.1 Transfert de chaleur et de masse dans les matériaux TPS

Le TPS est essentiel pour maintenir des températures acceptables à la surface externe des engins spatiaux tout au long des phases de mission, en particulier lors de la rentrée atmosphérique [6, 7, 8]. Les matériaux TPS sont divisés en deux catégories : les matériaux ablatifs et non ablatifs [9]. Une option courante pour le matériau TPS ablatif est une préforme fibreuse poreuse imprégnée d'une résine phénolique. L'ablateur de carbone imprégné de résine phénolique de la NASA (PICA) est un exemple de cette classe de matériau et a été utilisé avec succès dans diverses missions comme Stardust (NASA, 2006) [10, 11], Mars Science Laboratory (NASA, 2012) [12, 13], Mars 2020 (NASA, 2021) [14], et pour les véhicules Dragon (SpaceX, depuis 2012) [15]. L'Agence spatiale européenne et ArianeGroup ont développé ASTERM [16], un matériau ablatif carboné/phénolique de faible densité basé sur le Calcarb, une préforme de fibre de carbone produite en Europe par Mersen. Les matériaux ablatifs protègent les engins spatiaux en utilisant des réactions chimiques pour réduire le flux de chaleur de surface et minimiser la conversion de l'énergie cinétique en énergie thermique. Depuis les années 1950, des modèles détaillés de réponse des matériaux TPS ont été développés, prenant en compte cette physique complexe, avec des progrès significatifs réalisés dans les années 1960 lors de la conception du bouclier thermique Apollo [17, 18]. Des communautés de recherche actives continuent d'affiner et d'adapter ces modèles à de nouvelles générations de matériaux pour réduire les incertitudes de conception [19, 20].

L'utilisation généralisée de matériaux fibreux poreux soulève des questions quant à la validité des hypothèses héritées du passé, telles que l'hypothèse de l'équilibre thermique local, couramment utilisée dans la conception des systèmes de protection thermique. comme l'hypothèse de l'équilibre thermique local (LTE), couramment utilisée dans la conception des TPS. Le transfert de chaleur dans les matériaux poreux peut être étudié sous des hypothèses LTE [4] ou d'équilibre thermique local non équilibré (LTNE) [21, 22, 23, 24]. Dans les modèles LTE, on suppose que les températures moyennes

de la phase solide et de la phase gazeuse sont localement égales, c'est-à-dire à l'intérieur d'un volume élémentaire représentatif donné. Florio [25] et Puiroux [26, 27] ont démontré la validité de l'hypothèse d'équilibre thermique local pour les matériaux à carbonisation dense. Cependant, Scoggins et al. [28] ont montré que l'hypothèse d'équilibre thermique local était invalide pour le PICA, en utilisant des corrélations de la littérature disponibles pour estimer le coefficient de transfert de chaleur entre la phase solide et le gaz s'écoulant à travers les pores [28]. Comme il n'y avait pas de corrélations disponibles pour des matériaux similaires au PICA, Scoggins et al. [28] ont recommandé de réaliser des expériences pour mesurer le coefficient de transfert de chaleur dans les matériaux en fibre de carbone de faible densité. Le choix d'un modèle macroscopique approprié pour décrire avec précision le transfert couplé de chaleur et de masse dans les matériaux TPS reste une question ouverte.

A.1.1.1 Transfert de chaleur et de masse dans les systèmes de stockage d'énergie thermique à lit compacté

Le stockage d'énergie thermique (TES) joue un rôle vital pour exploiter efficacement les sources d'énergies renouvelables, car leur nature intermittente pose des défis à l'approvisionnement en énergie constante [30]. En particulier, les installations de concentration de l'énergie solaire (CSP) peuvent grandement bénéficier du stockage de chaleur pour réduire les coûts globaux du système [31]. Les deux principaux types de TES sont le stockage de chaleur sensible et le stockage de chaleur latente [32]. Le stockage de chaleur sensible augmente la température d'un milieu solide, tandis que le stockage de chaleur latente implique un changement de phase dans le matériau de stockage. Le TES sensible peut être classé en deux catégories : le stockage direct du fluide porteur d'énergie et les systèmes de stockage de chaleur à deux milieux [30, 32]. Les systèmes de stockage direct impliquent généralement un réservoir unique qui maintient le fluide chaud au-dessus du fluide froid. En revanche, les systèmes de stockage à deux milieux utilisent un fluide caloporteur pour transporter la chaleur et un solide ou un liquide supplémentaire pour le stockage de l'énergie [33, 34]. Le TES à lit compacté est une méthode prometteuse pour stocker la chaleur issue du rayonnement solaire, en utilisant l'air comme fluide caloporteur pour transmettre la chaleur à un lit compacté solide.

Dans le cadre d'une comparaison de modèles numériques réalisée dans le TES à lit compacté [35] et résumée par Esence et al. [30], quatre groupes de modèles différents ont été examinés. Ces groupes comprennent les modèles de phase solide continue, qui supposent que le solide se comporte comme un milieu continu plutôt que comme des particules indépendantes. Un autre groupe est le modèle de Schumann, qui néglige la conduction de la chaleur dans la direction radiale à l'intérieur de la phase solide, ainsi que la conduction de la chaleur dans le fluide et l'échange de chaleur entre les particules. Le modèle monophasé suppose que les phases solide et fluide ont des températures transitoires égales. Enfin, le modèle de dispersion concentrique considère un gradient thermique à l'intérieur des particules solides, sans transfert de chaleur entre les particules, ce qui fait que le gradient de température au niveau des surfaces des particules est uniquement dû au transfert de chaleur entre le fluide et le lit. Le choix du matériau de lit est essentiel pour garantir un système de stockage efficace et rentable. Divers matériaux tels que les roches [36], les métaux [37, 38], le béton [38], le sable [39], et les briques [40] ont été utilisés en fonction de l'application. La fonte est populaire pour sa haute densité de stockage

d'énergie, tandis que la pierre ou la brique sont des options plus abordables. De nombreuses études ont été menées sur les méthodes de transfert de chaleur en lit compacté, en tenant compte de facteurs tels que la fraction de vide, les variations de débit [35], les pertes thermiques par les parois [33], la taille des particules, le matériau d'emballage [41], et la température d'entrée du fluide [42].

Pour maximiser l'efficacité de ces systèmes, une analyse énergétique doit être réalisée, qui évalue le stockage de la chaleur et le processus de récupération. Comprendre les principes sous-jacents du TES à lit compacté est essentiel pour concevoir et mettre en œuvre des solutions de stockage d'énergie efficaces pour soutenir l'utilisation croissante des sources d'énergies renouvelables. En améliorant la performance des systèmes de TES à lit compacté, il devient possible de réduire le coût des technologies d'énergie renouvelable et d'accélérer la transition vers un paysage énergétique plus durable et respectueux de l'environnement.

A.1.1.2 Transfert de chaleur et de masse dans la biomasse

Les préoccupations concernant la dépendance aux combustibles fossiles et l'impact du réchauffement climatique ont suscité un intérêt accru pour l'utilisation des ressources renouvelables et des flux de déchets pour la production d'énergie [43]. La biomasse constitue une option attrayante pour les énergies renouvelables et le piégeage du carbone en raison de son caractère durable. durable [44]. Parmi les matières premières de la biomasse, les particules de bois se distinguent comme un choix favorable en raison de leur disponibilité généralisée, de leur rentabilité, et de leurs caractéristiques neutres en carbone [45]. Les phénomènes de transfert de chaleur sont inhérents à plusieurs aspects de l'utilisation de la biomasse, notamment les processus de séchage, de pyrolyse, de combustion, et de gazéification [46, 47, 48, 49]. Pour de petites quantités de biomasse, les particules peuvent être chauffées directement avec un chauffage électrique placé à l'intérieur de l'échantillon ou en utilisant un four externe [45, 50]. Cependant, dans les environnements industriels, le chauffage de grandes quantités de particules de biomasse est nécessaire, nécessitant des solutions alternatives telles que le chauffage des particules dans un conteneur avec un flux de gaz chaud, généralement sous la forme d'un système de lit compacté [47]. Il est essentiel de mieux comprendre le comportement de la conversion thermique pour améliorer l'efficacité des processus et réduire les émissions polluantes. est cruciale non seulement pour améliorer l'efficacité des processus, mais aussi pour réduire les émissions polluantes.

Des chercheurs ont étudié les processus de transfert de chaleur et de masse à l'intérieur d'une seule particule de biomasse, modélisant avec succès la séquence des processus chimiques, y compris le séchage, la pyrolyse, la combustion, et la gazéification du charbon [50, 51, 52, 53, 54]. Les systèmes de lit compacté de biomasse peuvent être modélisés en utilisant soit des approches homogènes (une équation) soit hétérogènes (deux équations) pour modéliser le transfert de chaleur [51, 55, 56]. Le modèle homogène suppose des températures identiques pour les phases gazeuses et solides, appliquant une seule équation de conservation de l'énergie à l'ensemble du système [57]. Le modèle hétérogène, cependant, applique des équations d'énergie séparées à chaque phase [58, 59] et est recommandé pour les lits compactés de biomasse pendant le séchage, la dévolatilisation, et la combustion du charbon. Les processus thermodynamiques impliqués dans les applications de la communauté de la biomasse diffèrent de ceux de la communauté des TES. La biomasse subit des processus physiques et chimiques

complexes, tels que le transfert de chaleur, l'évaporation de l'humidité, et la cinétique de décomposition. Comprendre et optimiser ces réactions pose des défis significatifs [50].

Dans le contexte des particules de bois dans des lits compactés, la pyrolyse est influencée non seulement par la température, mais aussi par les processus de transfert de masse et de chaleur à l'intérieur de la particule de bois. Les produits de la pyrolyse sont généralement classés en trois catégories : le charbon, le goudron et le gaz. La pyrolyse est réalisée dans un environnement sans oxygène à des températures allant de 523 à 873 K, en fonction des caractéristiques de la charge [60]. L'objectif principal de la communauté de la biomasse est de développer un modèle qui explique les processus de séchage et de pyrolyse des particules de bois. Ce modèle permettra d'améliorer l'efficacité et l'efficience de la production d'énergie renouvelable à partir de la biomasse. de la biomasse pour la production d'énergie renouvelable. Bamford et al. [61] ont été les premiers à proposer un modèle de pyrolyse thermique, le processus de pyrolyse est modélisé comme une équation cinétique de premier ordre suivant une loi d'Arrhenius. Au cours des dernières décennies, de nombreux modèles de pyrolyse ont été présentés dans la littérature, comme le résume White et al. [62]. Ces modèles peuvent être catégorisés en trois types principaux: les modèles de réaction globale en une seule étape [63], les modèles en plusieurs étapes [64], et les modèles semi-globaux [65]. Les modèles de réaction globale en une seule étape donnent un aperçu du taux de dévolatilisation des substrats de biomasse. Les modèles en plusieurs étapes impliquent une série de réactions consécutives pour capter la complexité de la cinétique de la pyrolyse de la biomasse. Les modèles semi-globaux simplifient l'analyse en regroupant les produits de la pyrolyse en trois fractions: volatiles, goudrons et charbon.

En résumé, les trois applications et processus discutés impliquant des matériaux poreux abordent différents aspects du transfert de chaleur et de masse. L'étude du transfert de chaleur et de masse dans les matériaux TPS tourne autour de la sélection du modèle macroscopique. Il convient de noter que l'hypothèse largement acceptée d'un équilibre thermique local entre les phases solide et gazeuse dans la conception des TPS a récemment été remise en question par plusieurs chercheurs. Pour y répondre, des modèles à une température (1T) et à deux températures (2T) ont été examinés. D'autre part, l'objectif de l'étude du transfert de chaleur et de masse dans les systèmes TES à lit compact est de développer et de valider un modèle complet à deux équations qui incorpore la conservation de la masse et de la quantité de mouvement dans des conditions de haute température. Ce modèle intègre la conservation de la masse et de la quantité de mouvement dans des conditions de haute température. En outre, la détermination des conductivités effectives et des coefficients de transfert de chaleur est cruciale pour informer le modèle à deux équations. De plus, l'étude du transfert de chaleur et de masse dans la biomasse met en évidence la complexité des processus de pyrolyse de la biomasse. Par rapport aux deux applications précédentes, elle implique un modèle de non-équilibre thermique local avec des réactions chimiques. Malgré leurs applications distinctes, ces processus partagent la caractéristique commune des matériaux réactifs poreux soumis à des températures élevées, qui jouent un rôle critique dans chaque cas.

Un cadre de classification pour les modèles macroscopiques est présenté à la Fig.A.1. Il classe les modèles en deux groupes: ceux sans réactions chimiques et ceux avec des réactions chimiques. Le premier s'applique aux TPS non-ablatifs et au TES, tandis que le second s'applique aux TPS ablatifs

et à la biomasse. Dans les modèles sans réactions chimiques, la conservation de la masse, de la quantité de mouvement et de l'énergie (LTE ou LTNE) est prise en compte pour la phase gazeuse. Dans les modèles avec des réactions chimiques, il faut inclure la conservation de la masse solide et des espèces pour tenir compte du séchage, de la pyrolyse, et/ou des réactions hétérogènes. Par conséquent, la conservation de la masse pour le solide et la conservation des espèces doivent être prises en compte. Comprendre les mécanismes de transfert de chaleur et de masse et les défis posés par les matériaux poreux dans ces applications contribuera à évaluer et à modéliser les échanges de masse, de quantité de mouvement et de chaleur entre une structure solide élastique et réactive interagissant avec un environnement à haute température.

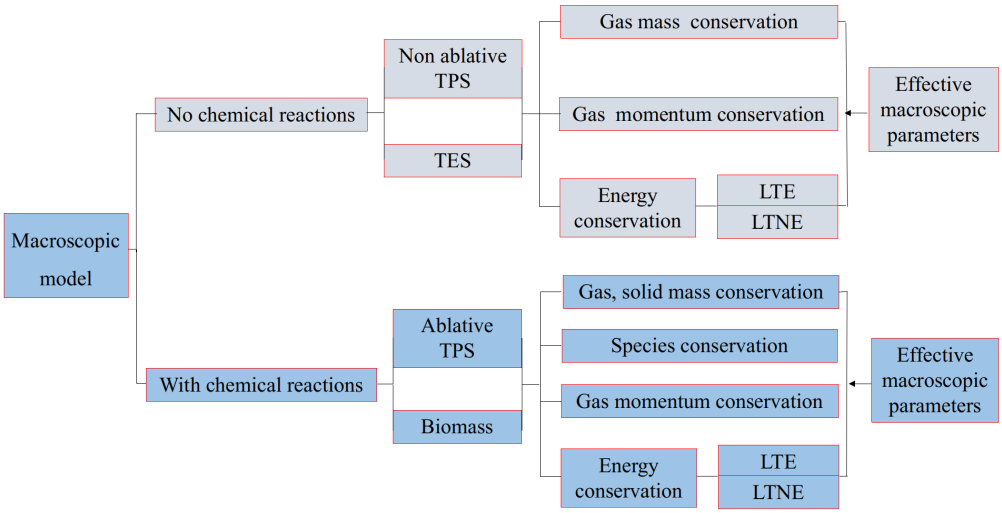

Figure A.1 – Cadre de classification pour les modèles numériques

A.2 Modélisation du transport dans les milieux poreux

Les milieux poreux peuvent être simplement définis comme des structures solides contenant des espaces vides appelés pores. L'interconnexion de ces pores permet la percolation, ou le passage d'un fluide à travers le matériau [21]. Les architectures poreuses peuvent prendre diverses formes, telles que des mousses à cellules ouvertes ou fermées, des feutres de fibres, des agrégats de grains et des alvéoles. Ces matériaux peuvent être trouvés dans la nature (par exemple, éponge, roche, bois) ou être fabriqués par l'homme (par exemple, céramiques, composites de fibres de carbone). Les milieux poreux fabriqués par l'homme peuvent être inspirés de matériaux naturels ou adopter des concepts radicalement différents pour améliorer leurs propriétés. Par exemple, les propriétés mécaniques des composites de fibres de carbone dépassent largement celles du bois. La Fig. A.2 illustre trois matériaux poreux (feutre de fibre de carbone, bois, lit compacté) à la fois à l'échelle micro et macro.

L'échelle macroscopique et l'échelle microscopique sont deux échelles fondamentales utilisées pour décrire les milieux poreux [66]. Une caractéristique multi-échelle représentative est montrée à la

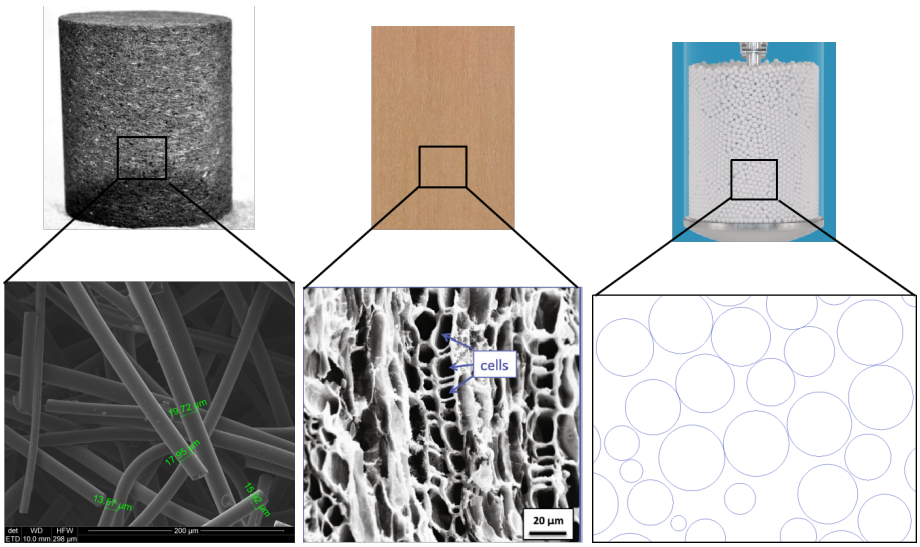

(a) feutre de fibre de carbone (b) bois (c) lit compacté

Figure A.2 – Représentations à l'échelle micro et macro des différents matériaux poreux

Fig. A.3, où la section supérieure illustre l'échelle macroscopique et la section inférieure représente l'échelle microscopique. Au niveau de la micro-échelle, un continuum distinct peut être considéré pour les différentes phases, les phases solides et fluides étant généralement représentées par s et g, respectivement. Les longueurs caractéristiques sont exprimées en l_s et l_g. À l'échelle macroscopique, une représentation efficace est caractérisée par des fluctuations de variables à une échelle de L. La relation entre les niveaux d'échelle peut être décrite comme $l_g << r_0 << L$, où r_0 représente le rayon du volume élémentaire représentatif (REV). Les interactions entre les phases fluide et solide peuvent être expliquées par la mécanique classique fluide-solide et l'échange de chaleur au niveau de l'échelle microscopique. L'échelle microscopique peut être reliée à l'échelle macroscopique via une procédure de mise à l'échelle. Dans les parties suivantes, nous discuterons des équations mathématiques régissant l'échelle microscopique et macroscopique afin de fournir une compréhension plus approfondie des processus se déroulant à l'intérieur des milieux poreux.

A.2.1 Problème de transport à l'échelle microscopique

À l'échelle microscopique, la description du problème de transport est fournie par les équations de Navier-Stokes (continuité et conservation de la quantité de mouvement) et les équations de l'énergie. Ces équations peuvent être écrites sous différentes formes, en fonction des hypothèses faites [67, 68, 69]. Pour présenter ces équations, nous allons classer le système en trois composantes : continuité, quantité de mouvement, et énergie. Nous examinerons chacune de ces composantes individuellement, en présentant leurs formes finales.

On considère le flux monophasique d'un fluide Newtonien incompressible g dans une région macroscopique d'un milieu poreux rigide. Le problème à valeur limite décrivant le processus à l'échelle

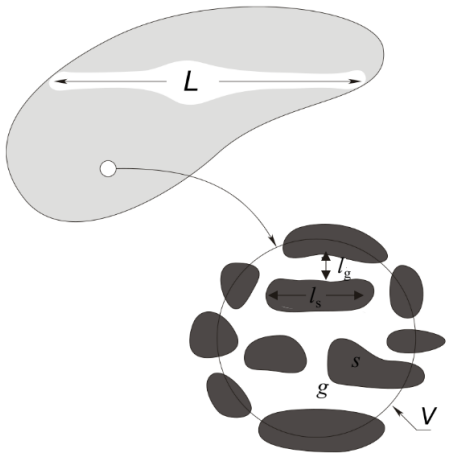

Figure A.3 – Description à deux échelles d'un milieu poreux.

microscopique (poreuse) est donné par les équations classiques de continuité et de bilan de quantité de mouvement

$$\begin{cases} \nabla \cdot \boldsymbol{v}_g = 0 & \\ \rho_g(\dfrac{\partial \boldsymbol{v}_g}{\partial t} + \boldsymbol{v}_g \cdot \nabla \boldsymbol{v}_g) = -\nabla p_g + \rho_g \boldsymbol{g} + \mu_g \nabla^2 \boldsymbol{v}_g & dans\ V_g \\ BC1: \quad \boldsymbol{v}_g = 0 & \text{à } A_{gs} \\ BC2: \quad \boldsymbol{v}_g = \boldsymbol{v}_1(\boldsymbol{x}, t) & \text{à } \partial V_g \\ iC1: \quad \boldsymbol{v}_g(t=0) = \boldsymbol{v}0(\boldsymbol{x}) & dans\ V_g \end{cases} \tag{A.1}$$

où $\boldsymbol{v_g}$ et p_g sont respectivement la vitesse et la pression de la phase gazeuse ; A_{gs} représente la zone d'interface entre la phase gazeuse et la phase solide contenue dans le volume élémentaire représentatif (VER).

L'équation de l'énergie à l'échelle microscopique est donnée comme suit

$$\begin{cases} (\rho\, c_p)_g \dfrac{\partial T_g}{\partial t} + (\rho\, c_p)_g \boldsymbol{v}_g \cdot \nabla T_g = \nabla \cdot (k_g \nabla T_g) & dans\ V_g \\ (\rho\, c_p)_s \dfrac{\partial T_s}{\partial t} = \nabla \cdot (k_s \nabla T_s) & dans\ V_s \\ BC1: \quad T_g = T_s & \text{à } A_{gs} \\ BC2: \quad \boldsymbol{n_{gs}} \cdot k_g \nabla T_g = \boldsymbol{n_{gs}} \cdot k_s \nabla T_s & \text{à } A_{gs} \end{cases} \tag{A.2}$$

où $(\rho c_p)_i$, T_i, k_i, (i=g ou s) sont respectivement la chaleur spécifique de la phase i, la température et

la conductivité thermique. Les conditions aux limites sur A_{gs} sont la continuité de la température et du flux de chaleur à travers l'interface, données comme dans $BC1$ et $BC2$.

A.2.2 Problème de transport à l'échelle macroscopique

Plusieurs méthodologies ont été développées pour augmenter l'échelle des équations à micro-échelle afin d'obtenir des modèles à macro-échelle. pour obtenir des modèles à l'échelle macro. Dans cette section, nous présenterons la méthode de prise de moyenne volumique [67, 66, 70]. Les moyennes de phase superficielle et intrinsèque de toute quantité φ_i associée à la phase i sont respectivement données par

$$\langle \varphi_i \rangle = \frac{1}{V} \int_{V_i} \varphi_i dV \tag{A.3}$$

$$\langle \varphi_i \rangle^i = \varepsilon_i^{-1} \langle \varphi_i \rangle = \frac{1}{V_i} \int_{V_i} \varphi_i dV \tag{A.4}$$

Dans ces relations, V_i est le volume de la phase i contenu dans le volume moyen V qui est un REV du milieu poreux. ε_i est la fraction volumique de la phase i. En utilisant la méthode d'échelonnement, on obtient les équations moyennes suivantes pour la continuité

$$\nabla \cdot \langle \boldsymbol{v}_g \rangle = 0 \tag{A.5}$$

En effectuant le moyennage volumique de l'équation de mouvement du flux monophasé, on obtient l'équation macroscopique suivante

$$\begin{aligned} \frac{\partial \rho_g \langle \mathbf{v}_g \rangle}{\partial t} + \rho_g \langle \mathbf{v}_g \rangle \cdot \nabla \langle \mathbf{v}_g \rangle^g + \nabla \cdot (\rho_g \langle \tilde{\mathbf{v}}_g \tilde{\mathbf{v}}_g \rangle) = \\ -\varepsilon_g \nabla \langle p_g \rangle^g + \varepsilon_g \rho_g \mathbf{g} + \underbrace{\mu_g \nabla^2 \langle \mathbf{v}_g \rangle - \mu_g \nabla \varepsilon_g \cdot \nabla \langle \mathbf{v}_g \rangle^g}_{\text{termes de Brinkman}} + \frac{1}{V} \int_{A_{g\sigma}} \mathbf{n}_{g\sigma} \cdot \left(-\tilde{p}_g \mathbf{I} + \mu_g \nabla \tilde{\mathbf{v}}_g \right) dA \end{aligned} \tag{A.6}$$

où $\mathbf{v}_g$, $\langle \mathbf{v_g} \rangle^{\mathbf{g}}$, et $\tilde{\mathbf{v}}_g = \mathbf{v}_g - \langle \mathbf{v}_g \rangle^g$ sont respectivement la vitesse du gaz dans les pores, la vitesse moyenne de phase intrinsèque, et la vitesse de déviation. $\tilde{p}_g$ est la déviation spatiale de la pression dans la phase gazeuse. À de faibles nombres de Reynolds, l'équation de la quantité de mouvement décrite ci-dessus peut être représentée par l'équation de Darcy, comme le montre ci-dessous

$$\langle \boldsymbol{v_g} \rangle = -\frac{1}{\mu_g} \boldsymbol{K} \cdot (\nabla \langle p_g \rangle^g - \rho_g \boldsymbol{g}) \tag{A.7}$$

Avec l'augmentation du nombre de Reynolds, les termes d'inertie commencent à jouer un rôle dominant. Restant dans un régime laminaire, on doit ajouter un terme d'inertie supplémentaire, à l'échelle macroscopique. Généralement, il peut être écrit comme

$$\langle \boldsymbol{v_g} \rangle = -\frac{1}{\mu_g} \boldsymbol{K} \cdot (\nabla \langle p_g \rangle^g - \rho_g \boldsymbol{g}) - \mathbf{F} \cdot \langle \mathbf{v_g} \rangle \tag{A.8}$$

où $\mathbf{K}$ est le tenseur de perméabilité, $\mathbf{F}$ est le tenseur de correction de Forchheimer, le dernier terme $\mathbf{F} \cdot \langle \mathbf{v_g} \rangle$ est appelé le terme de Forchheimer [71]. Alors que les discussions théoriques ci-dessus suggèrent

l'existence potentielle d'effets d'anisotropie pour les termes de Forchheimer, la pratique de l'ingénierie repose sur des expressions plus simples, en particulier, l'utilisation de l'équation d'Ergun, qui se lit comme suit

$$\langle \boldsymbol{v_g} \rangle = -\frac{1}{\mu_g} \boldsymbol{K} \cdot \left(\nabla \langle p_g \rangle^g - \rho_g \boldsymbol{g} + \rho_g \beta |\mathbf{v}_g| \cdot \langle \mathbf{v}_g \rangle \right) \tag{A.9}$$

où β est le coefficient de Forchheimer (également connu sous le nom de coefficient non-Darcy ou facteur β). Sur la base des données expérimentales recueillies, Ergun a proposé des corrélations pour K et β dans le cas de lits de particules isotropes qui sont encore très populaires dans la pratique de l'ingénierie

$$K = \frac{{d_{par}}^2 {\varepsilon_g}^3}{150 {\varepsilon_s}^2}, \qquad \beta = \frac{1.75 \varepsilon_s}{d_{par} {\varepsilon_g}^3} \tag{A.10}$$

où d_{par} est le diamètre équivalent des particules.

l'homogénéisation des équations énergétiques à l'échelle microscopique conduit aux équations macroscopiques suivantes

$$\begin{cases} \underbrace{\varepsilon_g \left(\rho c_p\right)_g \frac{\partial \langle T_g \rangle^g}{\partial t}}_{\text{accumulation}} + \underbrace{\varepsilon_g \left(\rho c_p\right)_g \langle \mathbf{v}_g \rangle^g \cdot \nabla \langle T_g \rangle^g}_{\text{convection}} = \\ \qquad \underbrace{\nabla \cdot \left[k_g \left(\varepsilon_g \nabla \langle T_g \rangle^g + \frac{1}{V} \int_{A_{g\sigma}} \mathbf{n}_{g\sigma} \tilde{T}_g dA \right) \right]}_{\text{conduction/tortuosité}} - \underbrace{\left(\rho c_p\right)_g \nabla \cdot \left\langle \tilde{\mathbf{v}}_g \tilde{T}_g \right\rangle}_{\text{dispersion}} + \underbrace{\frac{1}{V} \int_{A_{g\sigma}} \mathbf{n}_{g\sigma} \cdot k_g \nabla T_g dA}_{\text{flux interfacial}} \\ \varepsilon_s (\rho c_p)_s \frac{\partial \langle T_s \rangle^s}{\partial t} = \varepsilon_s k_s \nabla^2 \langle T_s \rangle^s + \nabla \cdot \left(\frac{1}{V} \int_{A_{\beta_s}} k_s \widetilde{T}_s \mathbf{n}_{sf} dA \right) + \frac{1}{V} \int_{A_{\beta_s}} k_s \nabla \widetilde{T}_s \cdot \mathbf{n}_{sf} dA. \end{cases} \tag{A.11}$$

où T_i, $\langle T_i \rangle^i$, et $\widetilde{T}_i = T_i - \langle T_i \rangle^i$ sont respectivement la température ponctuelle dans la phase i, la température moyenne intrinsèque de phase pour la phase i, et la déviation spatiale de la température dans la phase i. Les termes traditionnels apparaissant lors du changement d'échelle des flux dans les milieux poreux, c'est-à-dire la dispersion, les effets de tortuosité et les termes d'échange ont été mis en évidence. Le transfert de chaleur dans les matériaux poreux peut soit être étudié en supposant l'ETL (Equilibre Thermique Local), soit l'ETNL (Equilibre Thermique Non-Local). Dans les modèles ETL, on suppose que les températures moyennes des phases solide et gazeuse sont égales, $\langle T \rangle = \langle T_g \rangle^g = \langle T_s \rangle^s$ et la conservation macroscopique de l'énergie s'écrit

$$\left(\varepsilon_g \rho_g c_{p,g} + \varepsilon_s \rho_s c_{p,s}\right) \frac{\partial \langle T \rangle}{\partial t} + \left(\varepsilon_g \rho_g c_{p,g} + \varepsilon_s \rho_s c_{p,s}\right) \langle \mathbf{v_g} \rangle^{\mathbf{g}} \cdot \nabla \langle T \rangle = \nabla \cdot \left(\mathbf{k_{eff}} \cdot \nabla \langle T \rangle \right) \tag{A.12}$$

où le tenseur de conductivité thermique effective est donné par

$$\mathbf{k_{eff}} = \left(\varepsilon_g k_g + \varepsilon_s k_s\right) \mathbf{I} + \frac{k_g - k_s}{V} \int_{A_{gs}} \mathbf{n}_{gs} \mathbf{b}_g dA - \left(\rho c_p\right)_g \left\langle \tilde{\mathbf{v}}_g \mathbf{b}_g \right\rangle \tag{A.13}$$

où la variable de fermeture $\mathbf{b}_g$ est le champ vectoriel qui mappe $\nabla \langle T_g \rangle^g$ sur $\tilde{T}_g$ dans le modèle LTE, $\tilde{T}_g = \mathbf{b_g} \cdot \nabla \langle T_g \rangle^g$. Les modèles LTNE sont nécessaires lorsque les propriétés de transport des différentes phases sont fortement contrastées.

$$\begin{cases} \frac{\partial}{\partial t} \left(\varepsilon_s \rho_s c_{p,s} \langle T_s \rangle^s \right) = \nabla \cdot \left(\mathbf{k_{s,eff}} \cdot \nabla \langle T_s \rangle^s \right) + h_v \left(\langle T_g \rangle^g - \langle T_s \rangle^s \right) \\ \frac{\partial}{\partial t} \left(\varepsilon_g \rho_g c_{p,g} \langle T_g \rangle^g \right) + \nabla \cdot \left(\rho_g c_{p,g} \langle \mathbf{v_g} \rangle^{\mathbf{g}} \langle T_g \rangle^g \right) = \nabla \cdot \left(\mathbf{k_{g,eff}} \cdot \nabla \langle T_g \rangle^g \right) + h_v \left(\langle T_s \rangle^s - \langle T_g \rangle^g \right) \end{cases} \tag{A.14}$$

Une formulation plus détaillée de $\mathbf{k_{s,eff}}$, $\mathbf{k_{g,eff}}$ et h_v dans le modèle LTNE obtenue par la méthode de prise de moyenne volumique est donnée comme suit [72, 68, 73],

$$\begin{cases} \mathbf{k_{s,eff}} = \varepsilon_s k_s \mathbf{I} + \frac{k_s}{V} \int_{A_{gs}} \mathbf{n}_{sg} \mathbf{b_{ss}} dA \\ \mathbf{k_{g,eff}} = \varepsilon_g k_g \mathbf{I} + \frac{k_g}{V} \int_{A_{gs}} \mathbf{n}_{gs} \mathbf{b_{gg}} dA - \rho_g c_{p,g} \langle \tilde{\mathbf{v}}_g \mathbf{b_{gg}} \rangle \\ h_v = \frac{k_g}{V} \int_{A_{gs}} \mathbf{n}_{gs} \nabla s_g dA \end{cases} \tag{A.15}$$

où les variables de fermeture $\mathbf{b_{ii}}$ et s_i sont les champs vectoriels et scalaires qui associent $\nabla \langle T_i \rangle^i$ à $\tilde{T}_i$ dans le modèle LTNE, $\tilde{T}_g = \mathbf{b_{gg}} \cdot \nabla \langle T_g \rangle^g - s_g(\langle T_g \rangle^g - \langle T_s \rangle^s) + ...$, et $\tilde{T}_s = \mathbf{b_{ss}} \cdot \nabla \langle T_s \rangle^s - s_s(\langle T_s \rangle^s - \langle T_g \rangle^g) + ...$ [68].

Dans cette partie, nous avons principalement introduit les équations de masse, de quantité de mouvement et d'énergie aux niveaux microscopique et macroscopique. De plus, nous avons brièvement présenté le processus du changement d'échelle du micro vers le macro. En passant en revue ces problèmes de transport classiques dans les milieux poreux d'un point de vue multi-échelle, nous avons fourni une vue d'ensemble des interactions et des relations entre les différentes échelles dans les phénomènes de transport en milieu poreux. Veuillez noter que cette discussion donne un aperçu général. Des équations plus spécifiques, comme celles pour l'écoulement de fluides compressibles à l'échelle microscopique, et celles traitant des réactions de pyrolyse à l'échelle macroscopique, seront approfondies dans les chapitres à venir.

A.3 Questions de recherche et objectifs

A.3.1 Questions de recherche

L'utilisation de matériaux fibreux poreux dans les TPS a soulevé des questions sur la validité des hypothèses héritées, comme l'hypothèse de l'ELT souvent utilisée dans la conception des TPS. Alors que l'hypothèse de l'ELT a été démontrée comme valide pour les matériaux de carbonisation dense, Scoggins et al. [28] l'ont trouvée invalide pour le PICA, un matériau en fibre de carbone de faible densité. Ils ont recommandé de réaliser des expériences pour mesurer le coefficient de transfert de chaleur dans les matériaux en fibre de carbone de faible densité, car de telles études manquent actuellement dans la littérature. Le problème est encore compliqué car l'écoulement des gaz à travers les milieux poreux modifie également leur conductivité thermique effective par un processus appelé dispersion. **La première question de recherche est donc: étant donné l'utilisation de matériaux en fibre de carbone de faible densité tels que le Calcarb dans les TPS, l'hypothèse de l'ELT est-elle vraie? Sinon, quelle valeur quantifiable les coefficients de transfert de chaleur prennent-ils dans le modèle LTNE ?**

Dans les systèmes de stockage d'énergie à haute température avec lit fixe et écoulement de fluide, les approches traditionnelles supposent un écoulement laminaire et des propriétés de fluide constantes. En général, la résolution de l'équation de l'énergie à l'échelle macroscopique est suffisante. Cependant, l'utilisation de l'air comme moyen de transfert de chaleur dans ces systèmes entraîne des distributions

non uniformes de la température, de la densité du gaz, de la viscosité et de la vitesse dans les lits fixés. Il devient difficile de décrire précisément la distribution de la température en utilisant uniquement l'équation de l'énergie dans ces cas. Il est nécessaire de coupler et de résoudre simultanément les équations de la masse, de la quantité de mouvement et de l'énergie. De plus, il est crucial de déterminer les variables inconnues comme les coefficients de transfert de chaleur et les conductivités thermiques effectives pour les phases fluides et solides en raison des variations significatives des propriétés thermophysiques. **Par conséquent, la deuxième question de recherche est: Comment pouvons-nous modéliser et décrire avec précision la distribution de température non-uniforme dans les systèmes de TES à lit fixe à haute température avec écoulement de fluide, en tenant compte des propriétés thermophysiques variables et de la nécessité de déterminer les coefficients de transfert de chaleur et les conductivités thermiques effectives pour les phases fluides et solides ?**

Le développement de modèles à deux équations pour décrire les processus de transfert de chaleur dans des lits de biomasse, incluant un modèle simplifié sans tenir compte des processus de séchage et un autre prenant en compte la pyrolyse, a soulevé des questions sur la validité de ces approches et la détermination des paramètres effectifs. Alors que des techniques expérimentales comme la méthode transitoire à simple soufflage ont été employées pour estimer des paramètres tels que le coefficient de transfert de chaleur volumétrique h_v, la conductivité thermique effective du solide $\mathbf{k_{s,eff}}$ et la conductivité thermique effective du gaz $\mathbf{k_{g,eff}}$, une compréhension complète de l'influence du contenu en eau sur ces valeurs reste insaisissable. De plus, l'étendue de la divergence entre les modèles qui tiennent compte de l'évaporation de l'eau et ceux qui ne le font pas nécessite encore des investigations supplémentaires. **La troisième question de recherche est donc: Comment le contenu en eau dans des lits de biomasse influence-t-il les paramètres effectifs tels que le coefficient de transfert de chaleur volumétrique, la conductivité thermique effective du solide, et la conductivité thermique effective du gaz? De plus, dans quelle mesure les prédictions diffèrent-elles entre les modèles qui tiennent compte de l'évaporation de l'eau et ceux qui ne le font pas?**

Dans les systèmes de protection thermique (TPS), comprendre les propriétés thermophysiques et les caractéristiques de flux interne de matériaux poreux comme le Calcarb est vital pour simuler avec précision les distributions de température des engins spatiaux lors de la rentrée atmosphérique. Alors que la loi de Darcy peut décrire l'écoulement du gaz dans les milieux poreux, la loi de Forchheimer peut être nécessaire pour capturer adéquatement la complexité du processus d'écoulement dans certains cas. Un défi principal dans l'utilisation de la loi de Darcy ou de Forchheimer est de déterminer la perméabilité inconnue, $\mathbf{K}$, et le coefficient de Forchheimer, β, du Calcarb. Dans un travail précédent, [74] des simulations à l'échelle microscopique ont été réalisées pour résoudre les équations de Navier-Stokes sous l'hypothèse d'écoulement de Darcy, et le tenseur de perméabilité a été prédit sur la base des résultats. La perméabilité a ensuite été comparée avec les valeurs obtenues par Borner et al. [75] en utilisant des méthodes de simulation directe de Monte Carlo, révélant une différence de près de 42%. **La quatrième question de recherche est donc: Quelles sont les valeurs précises de la perméabilité et du coefficient de Forchheimer pour un matériau comme le Calcarb, et l'exposant dans l'équation**

correspond-il à la valeur couramment utilisée de 2 comme le suggère l'équation de Forchheimer? De plus, comment pouvons-nous comparer efficacement les résultats expérimentaux avec les résultats de simulation à l'échelle microscopique pour fournir une explication de l'écoulement de Forchheimer d'un point de vue microscopique?

L'étude de la chute de pression et des coefficients de transfert de chaleur dans empilements aléatoires a soulevé des questions sur la précision des modèles et la nécessité d'une approche multi-échelle complète, qui englobe la microstructure locale et la macro-structure. La méthode des éléments discrets (DEM) a été utilisée pour générer des empilements aléatoires, basées sur la géométrie des particules individuelles. Après la génération, des simulations à la fois à l'échelle microscopique et macroscopique ont été exécutées sur ces structures. Malgré ces progrès, il y a une lacune dans les études qui abordent comment les conditions de haute température affectent les propriétés thermophysiques de l'air et des particules, ce qui influence à son tour les paramètres effectifs tels que les coefficients de transfert de chaleur. Cette complexité est encore exacerbée dans la perspective multi-échelle, où le besoin de données numériques précises pour la validation devient crucial. **La cinquième question de recherche est donc: Comment l'écoulement du fluide et le transfert de chaleur dans les lits compactés sont-ils affectés par les hautes températures par rapport aux conditions de température ambiante? Quelle est l'influence des propriétés thermophysiques des fluides et des solides dans la définition de la chute de pression et des coefficients de transfert de chaleur dans le lit compacté? Enfin, comment pouvons-nous combiner les résultats de simulation à l'échelle microscopique et macroscopique pour déterminer avec précision les paramètres effectifs dans des conditions variables?**

A.3.2 Objectifs

L'objectif global de cette thèse est de contribuer à la compréhension et à la caractérisation du transfert de chaleur et de masse dans les milieux poreux à haute température. L'approche adoptée consiste à concevoir des installations dédiées adaptées aux milieux poreux et aux conditions d'intérêt, à réaliser des expériences entièrement instrumentées, et à effectuer une analyse de données à l'aide de la modélisation numérique de pointe combinée à une optimisation multi-objectifs avancée. Pour apporter une compréhension complète, une analyse théorique - basée sur les développements disponibles dans la communauté de la prise de moyenne volumique - et des simulations numériques à l'échelle des pores seront entreprises pour expliquer et justifier les résultats expérimentaux. Plus précisément, cette approche est appliquée pour aborder les défis et les préoccupations suivants dans le domaine:

1. Enquêter expérimentalement sur la validité de l'hypothèse LTE et contribuer à combler le manque de connaissances en examinant le transfert de chaleur convectif dans des matériaux en fibre de carbone de faible densité comme le Calcarb.
2. Développer et valider un modèle numérique à deux équations pour les conditions de haute température, incorporant la conservation de la masse et de la quantité de mouvement, pour décrire avec précision la distribution de la température dans des lits compactés avec des propriétés non-uniformes. Déterminer les conductivités effectives et les coefficients de transfert de chaleur

nécessaires pour le modèle.

3. Examiner expérimentalement la validité des modèles à deux équations décrivant les processus de transfert de chaleur dans les lits compactés de biomasse avec des teneurs en humidité variables et enquêter sur les effets de l'humidité sur les paramètres effectifs et la divergence entre les modèles qui considèrent l'évaporation de l'eau et ceux qui ne le font pas.
4. Étendre les simulations à l'échelle microscopique de l'écoulement de Darcy à l'écoulement de Forchheimer pour des matériaux poreux comme le Calcarb, tout en déterminant expérimentalement les valeurs de la perméabilité et du coefficient de Forchheimer. Examiner les écoulements dans les deux directions, à travers l'épaisseur (TT) et dans le plan (IP), et enquêter sur la cohérence entre les résultats expérimentaux et numériques.
5. Enquêter sur la chute de pression et les coefficients de transfert de chaleur à l'intérieur des lits compactés au hasard à haute température à travers des simulations à l'échelle microscopique et macroscopique, contribuant finalement à une compréhension plus profonde de ces phénomènes d'un point de vue multi-échelle.

Les contributions numériques de ce projet de doctorat sont mises à disposition en Open Source dans la boîte à outils d'analyse des matériaux poreux basée sur OpenFoam (PATO).

A.4 Plan de la Thèse

Cette thèse est organisée comme le montre la Fig.A.4. Le chapitre 1 a fourni une introduction au

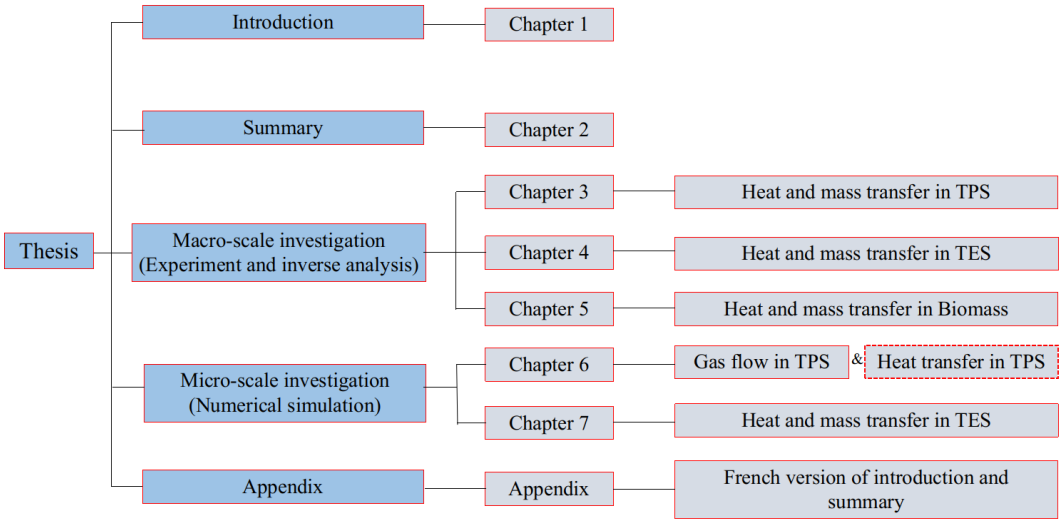

Figure A.4 – Structure organisationnelle de la thèse

contexte de la recherche, couvrant le transfert de chaleur et de masse dans les matériaux TPS, le TES de lit compacté, et la pyrolyse des particules de bois. Ce chapitre a également discuté de la modélisation du transport dans les milieux poreux, abordant à la fois les problèmes à l'échelle microscopique et

macroscopique, et a résumé les questions de recherche et les objectifs que la thèse vise à aborder. Le chapitre 2 présente un résumé de la thèse, y compris la méthodologie de recherche, avec un accent sur les modèle mathématique, le logiciel de simulation numérique, et les approches expérimentales. Ce chapitre fournit également les principaux résultats, qui sont divisés en deux parties, et conclut avec une discussion sur les réalisations de la recherche et les perspectives futures.

Les cinq articles indépendants qui suivent, chacun correspondant à un chapitre séparé, approfondissent les questions de recherche spécifiques et les objectifs mentionnés dans la section 1.3. Les chapitres des articles sont les suivants :

> Chapitre 3 : Investigation expérimentale de la validité de l'hypothèse d'équilibre thermique local dans les modèles de réponse des matériaux ablatifs;
> Chapitre 4 : Investigation expérimentale du transfert de chaleur convectif à l'intérieur des lits compactés au hasard à haute température;
> Chapitre 5 : Validation expérimentale des modèles de transfert de chaleur dans les lits compactés de biomasse : effets de la teneur en humidité;
> Chapitre 6 : Mesures expérimentales et simulations numériques de la perméabilité et du coefficient de Forchheimer pour Calcarb via des images 3D;
> Chapitre 7 : Investigation multi-échelle de la chute de pression et du coefficient de transfert de chaleur à l'intérieur des lits compactés au hasard à haute température.

Ces cinq chapitres sont divisés en deux parties principales en fonction de l'échelle des questions de recherche. La première partie comprend les chapitres 3, 4, et 5, qui se concentrent sur l'investigation à l'échelle macroscopique des caractéristiques de l'écoulement des fluides et du transfert de chaleur dans trois différents matériaux poreux : les feutres de fibre de carbone anisotropes, les matériaux poreux granulaires réguliers, et les matériaux poreux granulaires irréguliers. La deuxième partie comprend les chapitres 6 et 7, qui se concentrent sur l'analyse à l'échelle microscopique de l'estimation numérique des propriétés effectives à l'échelle des pores. Enfin, les annexes de la thèse fournissent une version française de l'Introduction (Chapitre 1) et du Résumé de la Thèse (Chapitre 2), rendant la thèse plus accessible et compréhensible pour les lecteurs francophones.

Appendix B

Synthèse de la Thèse

Ce résumé présente un aperçu de la méthodologie de recherche et synthétise les résultats les plus importants du doctorat.

B.1 Méthodologie de Recherche

La méthodologie de recherche adoptée dans cette thèse repose sur une combinaison d'approches numériques et expérimentales pour répondre aux questions de recherche et aux objectifs présentés au chapitre 1. La première sous-section couvre la description des équations gouvernantes utilisées aux échelles macroscopique et microscopique. L'outil numérique utilisé au cours de cette étude est présenté dans la deuxième sous-section. Dans la dernière sous-section, l'approche expérimentale et les conditions d'essai sont décrites.

B.1.1 Équations gouvernantes

Deux ensembles d'équations sont utilisés pour aborder les questions de recherche à différentes échelles. À l'échelle macroscopique, des équations moyennées sur le volume sont utilisées pour modéliser la conservation de la masse, de la quantité de mouvement et de l'énergie. Pendant ce temps, à l'échelle microscopique, la conservation de la masse, de la quantité de mouvement et de l'énergie est directement capturée par les équations de Navier-Stokes.

B.1.1.1 Équations à l'échelle macroscopique

À l'échelle macroscopique, des équations de conservation de la masse, de la quantité de mouvement et de l'énergie sont introduites pour les modèles d'équilibre thermique local (LTE) et de non-équilibre thermique local (LTNE). Les équations de quantité de mouvement sont décrites en utilisant soit un écoulement rampant, soit un écoulement inertiel en fonction du régime d'écoulement. Pour la première question de recherche, qui est l'investigation expérimentale sur la validité de l'hypothèse d'équilibre thermique local dans les modèles de réponse des matériaux ablatifs, la loi de Darcy avec les équations

LTE et LTNE est utilisée. Pour la deuxième question de recherche, qui est l'investigation expérimentale du transfert de chaleur convectif à l'intérieur de lits en vrac à températures élevées, le modèle de Forchheimer avec les équations LTNE est utilisé. Pour la troisième question de recherche, qui est la validation expérimentale des modèles de transfert de chaleur dans les lits de biomasse sous différents niveaux de teneur en humidité, le modèle de Forchheimer avec les équations LTNE est utilisé. De plus, nous avons amélioré le modèle en incorporant un modèle de pyrolyse. Les différents ensembles d'équations gouvernantes mentionnés sont donnés ci-dessous:

(1) La loi de Darcy avec l'équation LTE

$$\begin{cases} \frac{\partial}{\partial t}\left(\varepsilon_g \frac{M\langle p\rangle^g}{R\langle T\rangle}\right) + \nabla\cdot\left(-\frac{M\langle p\rangle^g}{R\langle T\rangle}\frac{\mathbf{K}}{\mu_g}\cdot\nabla\langle p\rangle^g\right) = 0 \\ \left(\varepsilon_g\rho_g c_{p,g} + \varepsilon_s\rho_s c_{p,s}\right)\frac{\partial\langle T\rangle}{\partial t} + \left(\varepsilon_g\rho_g c_{p,g} + \varepsilon_s\rho_s c_{p,s}\right)\langle\mathbf{v_g}\rangle^{\mathbf{g}}\cdot\nabla\langle T\rangle = \nabla\cdot\left(\mathbf{k_{eff}}\cdot\nabla\langle T\rangle\right) \end{cases} \tag{B.1}$$

où la première équation est la conservation de la masse du gaz écrite en termes de pression du gaz (la vitesse du gaz est substituée par la loi de Darcy) et la deuxième équation est la conservation de l'énergie. La fraction volumique du gaz ε_g est égale à la porosité du milieu poreux. $\mathbf{K}$ et $\mathbf{k_{eff}}$ désignent respectivement les tenseurs de perméabilité et de conductivité thermique effective. $\langle p\rangle^g$ et $\langle\mathbf{v_g}\rangle^g$ sont respectivement la pression moyenne intrinsèque et la vitesse du gaz. $\langle T\rangle$ désigne la température moyenne superficielle du matériau poreux (qui est égale pour les deux phases).

(2) La loi de Darcy avec les équations LTNE

$$\begin{cases} \frac{\partial}{\partial t}\left(\varepsilon_g \frac{M\langle p\rangle^g}{R\langle T_g\rangle^g}\right) + \nabla\cdot\left(-\frac{M\langle p\rangle^g}{R\langle T_g\rangle^g}\frac{\mathbf{K}}{\mu_g}\cdot\nabla\langle p\rangle^g\right) = 0 \\ \frac{\partial}{\partial t}\left(\varepsilon_s\rho_s c_{p,s}\langle T_s\rangle^s\right) = \nabla\cdot\left(\mathbf{k_{s,eff}}\cdot\nabla\langle T_s\rangle^s\right) + h_v\left(\langle T_g\rangle^g - \langle T_s\rangle^s\right) \\ \frac{\partial}{\partial t}\left(\varepsilon_g\rho_g c_{p,g}\langle T_g\rangle^g\right) + \nabla\cdot\left(\rho_g c_{p,g}\langle\mathbf{v_g}\rangle^{\mathbf{g}}\langle T_g\rangle^g\right) = \nabla\cdot\left(\mathbf{k_{g,eff}}\cdot\nabla\langle T_g\rangle^g\right) + h_v\left(\langle T_s\rangle^s - \langle T_g\rangle^g\right) \end{cases} \tag{B.2}$$

où la première équation de l'ensemble représente la conservation de la masse du gaz et est écrite en termes de pression du gaz, la vitesse du gaz étant remplacée par la loi de Darcy. Les deuxième et troisième équations correspondent aux équations de conservation de l'énergie pour les phases solide et fluide, respectivement. $c_{p,i}$ et $\mathbf{k_{i,eff}}$ désignent respectivement la capacité calorifique et le tenseur de conductivité thermique effective de la phase i. $\langle T_i\rangle^i$ et $\langle\mathbf{v_g}\rangle^{\mathbf{g}}$ désignent la température moyenne intrinsèque de phase pour la phase i et la vitesse moyenne intrinsèque du gaz. h_v désigne le coefficient de transfert de chaleur volumique entre le flux de gaz et l'échantillon.

(3) Le modèle de Forchheimer avec les équations LTNE

$$\begin{cases} \frac{\partial}{\partial t}\left(\varepsilon_g \frac{M\langle p\rangle^g}{R\langle T_g\rangle^g}\right) + \nabla\cdot\left(-\frac{M\langle p\rangle^g\mathbf{KX}}{R\langle T_g\rangle^g}\cdot\nabla\langle p\rangle^g\right) = 0 \\ \frac{\partial}{\partial t}\left(\varepsilon_s\rho_s c_{p,s}\langle T_s\rangle^s\right) = \nabla\cdot\left(\mathbf{k_{s,eff}}\cdot\nabla\langle T_s\rangle^s\right) + h_v\left(\langle T_g\rangle^g - \langle T_s\rangle^s\right) \\ \frac{\partial}{\partial t}\left(\varepsilon_g\rho_g c_{p,g}\langle T_g\rangle^g\right) + \nabla\cdot\left(\rho_g c_{p,g}\langle\mathbf{v_g}\rangle^{\mathbf{g}}\langle T_g\rangle^g\right) = \nabla\cdot\left(\mathbf{k_{g,eff}}\cdot\nabla\langle T_g\rangle^g\right) + h_v\left(\langle T_s\rangle^s - \langle T_g\rangle^g\right) \end{cases} \tag{B.3}$$

où la première équation de l'ensemble exprime la conservation de la masse du gaz en termes de pression du gaz, avec la loi de Forchheimer utilisée pour substituer la vitesse du gaz. Les deuxième et troisième équations décrivent les équations de conservation de l'énergie pour les phases solide et fluide, respectivement. Le tenseur de Forchheimer, représenté par $\mathbf{X}$, est introduit pour simplifier le

processus de calcul [76].

$$X_{ij} = \frac{1}{\mu_g K_{ij} + \beta_{ij}\rho_g|\langle v_g\rangle|} \tag{B.4}$$

(4) Modèle de Forchheimer avec équations LTNE et modèle de pyrolyse

Ce modèle offre une représentation numérique des interactions entre un matériau réactif à phases multiples (N_s phases solides) et un mélange de gaz réactif à espèces multiples (N_g éléments/espèces gazeuses) [77, 78]. Le matériau réactif est supposé être rigide, tandis que la phase gazeuse est un mélange compressible et parfait d'éléments/espèces gazeuses. L'eau est modélisée en tant que phase solide statique. Dans la discussion suivante, les équations de pyrolyse, de conservation de la masse, de la quantité de mouvement et d'énergie seront introduites séparément.

Dans le modèle de pyrolyse, nous prenons en compte le fait que le matériau d'intérêt peut être composé de différentes phases, voire sous-phases. Par exemple, les composés principaux des granulés de bois étudiés dans ce travail sont les parois cellulaires du bois (composées de sous-phases de cellulose, hémicellulose et lignine) et l'eau (composée d'eau liée et d'eau libre). Pour aborder cet aspect, nous divisons chaque phase i en $N_{p,i}$ sous-phases. Une sous-phases spécifique, $P_{i,j}$, suit un mécanisme cinétique prédéterminé, entraînant la génération d'une espèce ou d'un élément A_k en fonction des coefficients stœchiométriques $v_{i,j,k}$.

$$P_{i,j} \rightarrow \sum_{k=1}^{N_g} v_{i,j,k} A_k \tag{B.5}$$

Le modèle d'Arrhenius est utilisé pour représenter les réactions de pyrolyse. La progression de la réaction de pyrolyse $\chi_{i,j}$ pour la sous-phase j dans la phase i est définie comme suit :

$$\partial_t \chi_{i,j} = (1-\chi_{i,j})^{m_{i,j}} {T_s}^{n_{i,j}} \mathcal{A}_{i,j} exp(-\frac{\epsilon_{i,j}}{RT_s}) \tag{B.6}$$

où m_{ij} et n_{ij} représentent les paramètres de la loi d'Arrhenius, $\mathcal{A}_{)|}$ est le facteur pré-exponentiel de la loi d'Arrhenius, et ϵ_{ij} est l'énergie d'activation. En combinant les contributions des N_s phases solides, le taux de production total π pour l'espèce k peut être calculé.

$$\pi_k = \sum_{i=1}^{N_s} \sum_{j=1}^{N_{p,i}} v_{i,j,k} \epsilon_{i,0} \rho_{i,0} F_{i,j} \partial_t \chi_{i,j} \tag{B.7}$$

où la fraction volumique initiale, la densité intrinsèque et la fraction massique de la sous-phase j dans la phase i sont représentées par $\epsilon_{i,0}$, $\rho_{i,0}$ et $F_{i,j}$. En additionnant les contributions de tous les éléments et espèces dans le mélange, nous pouvons déterminer le taux de production total de gaz de pyrolyse, Π.

$$\Pi = \sum_{k=1}^{N_g} \pi_k \tag{B.8}$$

Pour toute phase solide donnée i, l'équation de conservation de masse associée caractérisant la phase, l'élément/espèce gazeux et le mélange gazeux peut être écrite de manière concise comme suit :

$$\partial_t(\varepsilon_i \rho_i) = -\pi_i \tag{B.9}$$

En fonction du modèle chimique utilisé dans la phase gazeuse, des espèces pour une chimie à taux fini peuvent être considérées. Dans les cas impliquant une chimie à taux fini, l'équation de conservation pour une espèce générique possédant une fraction massique de y_i peut être exprimée comme suit :

$$\partial_t(\varepsilon_g\rho_g y_i) + \partial_t(\varepsilon_g\rho_g y_i \mathbf{v_g}) + \partial_{\mathbf{x}} \cdot \mathcal{F}_i = \pi_i \tag{B.10}$$

où $\mathcal{F}_i$ représente les flux de masse de diffusion multicomposante efficace pour la i-ème espèce. La bibliothèque Mutation++ est utilisée pour calculer toutes les propriétés thermodynamiques et de transport. Pour le mélange gazeux, la conservation de la masse tient compte du taux de production de pyrolyse comme suit :

$$\partial_t\left(\varepsilon_g\rho_g\right) + \nabla\cdot\left(-\varepsilon_g\rho_g\langle\mathbf{v_g}\rangle^{\mathbf{g}}\right) = -\sum_{i=1}^{N_s}\partial_t(\varepsilon_i\rho_i) = \Pi \tag{B.11}$$

Deux équations de conservation de l'énergie incorporant la pyrolyse sont nécessaires pour représenter les phases solide et gazeuse. Ces équations sont les suivantes :

$$\sum_{i=1}^{N_s}\varepsilon_i\rho_i c_{p,i}\partial_t\langle T_s\rangle^s + \sum_{i=1}^{N_s} h_i\partial_t\left(\varepsilon_i\rho_i\right) = \nabla\cdot\left(\mathbf{k_{s,eff}}\cdot\nabla\langle T_s\rangle^s\right) + h_v\left(\langle T_g\rangle^g - \langle T_s\rangle^s\right) \tag{B.12}$$

$$\begin{aligned}\varepsilon_g\rho_g c_{p,g}\partial_t\langle T_g\rangle^g - \partial_t\left(\varepsilon_g p\right) + \sum_{j=1}^{N_g} h_j\partial_t\left(\varepsilon_g\rho_g y_j\right) + \nabla\cdot\left(\varepsilon_g\rho_g h_g\mathbf{v_g}\right) + \nabla\cdot\sum_{j=1}^{N_g}\mathcal{Q}_j \\ = \nabla\cdot\left(\mathbf{k_{g,eff}}\cdot\nabla\langle T_g\rangle^g\right) + h_v\left(\langle T_s\rangle^s - \langle T_g\rangle^g\right)\end{aligned} \tag{B.13}$$

où h_i et h_j représentent les enthalpies absolues des i-ème et j-ème composants. $\mathcal{Q}_j$ est le transport de chaleur par diffusion effective de l'espèce j.

B.1.1.2 Équations à l'échelle micro

Pour les simulations numériques à l'échelle micro, nous utilisons les équations de Navier-Stokes laminaires transitoires pour modéliser l'écoulement du fluide, sans inclure la conservation de l'énergie pour le fluide. Ceci est appliqué à la quatrième question de recherche, qui implique la dérivation de propriétés effectives. Pour la cinquième question de recherche, l'écoulement du fluide est compressible, et le transfert de chaleur est décrit en utilisant la conduction dans les deux phases et la convection dans la phase fluide. Nous considérons le couplage entre la densité et la température et nous modélisons le système en utilisant les équations de Navier-Stokes laminaires transitoires, incluant la conservation des équations de masse, de la quantité de mouvement et de l'énergie. Les différents ensembles d'équations gouvernantes pour chaque cas considéré sont présentés ci-dessous :

(1) Écoulement incompressible isotherme

$$\begin{cases}\nabla\cdot\mathbf{v_g} = 0 \\ \rho_g(\frac{\partial\mathbf{v_g}}{\partial t} + \mathbf{v_g}\cdot\nabla\mathbf{v_g}) = -\nabla p + \mu_g\nabla^2\mathbf{v_g} \\ \mathbf{v_g} = 0 \qquad \text{à} \quad A_{gs}\end{cases} \tag{B.14}$$

où $\mathbf{v_g}$ et p sont respectivement la vitesse et la pression de la phase gazeuse; A_{gs} représente la zone d'interface entre la phase gazeuse et la phase solide contenue dans la région macroscopique.

2) Écoulement compressible non-isotherme

$$\begin{cases} \partial_t \rho_g + \nabla \cdot (\rho_g \mathbf{v_g}) = 0 \\ \rho_g \left(\frac{\partial \mathbf{v_g}}{\partial t} + \mathbf{v_g} \cdot \nabla \mathbf{v_g} \right) = -\nabla p + \mu_g \nabla^2 \mathbf{v_g} \\ \rho_g c_{p,g} \frac{\partial T_g}{\partial t} + \rho_g c_{p,g} \mathbf{v_g} \cdot \nabla T_g = k_g \nabla^2 T_g \\ \rho_s c_{p,s} \frac{\partial T_s}{\partial t} = k_s \nabla^2 T_s \end{cases} \tag{B.15}$$

où l'équilibre du transfert de chaleur est dérivé dans les phases fluide et solide. La densité du gaz est calculée avec la loi des gaz parfaits :

$$\rho_g = \frac{Mp}{RT} \tag{B.16}$$

Ici, nous considérons que le fluide est non isotherme et compressible. Il est intéressant de comparer les effets de la pression (compressibilité) et de la température (dilatation) sur les variations de densité pour les problèmes qui nous intéressent. Pour ce faire, nous dérivons ρ_g par rapport à T et p, ce qui nous donne une forme différentielle de la densité du gaz :

$$\begin{aligned} d\rho_g &= \frac{\partial \rho_g}{\partial T} dT + \frac{\partial \rho_g}{\partial p} dp \\ &= -\frac{Mp}{RT^2} dT + \frac{M}{RT} dp \end{aligned} \tag{B.17}$$

En substituant l'équation 2.15 et en transformant, nous obtenons :

$$\frac{d\rho_g}{\rho_g} = -\frac{1}{T} dT + \frac{1}{p} dp = -\beta_g dT + \chi_T dp \tag{B.18}$$

où β_g est le coefficient volumétrique de dilatation thermique et χ_T est le coefficient de compressibilité :

$$\beta_g = \frac{1}{V} \left(\frac{\partial V}{\partial T} \right)_p \qquad \chi_T = \frac{1}{V} \left(\frac{\partial V}{\partial p} \right)_T \tag{B.19}$$

Considérons une situation où T est de 300 K. Si la température augmente de 100 K, c'est-à-dire dT = 100 K, alors $\beta_g dT$ devient environ 0.333. Avec p à 101325 Pa et le nombre de Reynolds à 300, une augmentation de la pression dp d'environ 40 Pa (typique des essais avec des billes de verre réalisés dans ce travail) conduit à une valeur de $\chi_T dp$ d'environ 0.000394. En regardant ces nombres, il est clair que $\beta_g dT$ et $\chi_T dp$ diffèrent de trois ordres de grandeur, ce qui est une grande différence. Par conséquent, les effets de compressibilité sont négligeables par rapport aux effets de dilatation thermique dans les conditions des expériences réalisées dans ce travail.

B.1.2 Analyse numérique

Dans cette partie, nous présentons le logiciel utilisé pour les simulations numériques. Le modèle numérique utilisé dans ce travail est basé sur l'outil d'analyse des matériaux poreux basé sur OpenFOAM (PATO), qui est implémenté en tant que module de niveau supérieur en C++ du logiciel de dynamique des fluides computationnelles open-source OpenFOAM. OpenFOAM est un logiciel de dynamique des fluides computationnelles à volumes finis publié par OpenCFD Limited et pris en charge pour les systèmes d'exploitation Unix/Linux. PATO peut être utilisé comme un code de transfert de chaleur de Fourier simple ou inclure des fonctionnalités plus avancées, telles que la décomposition interne (pyrolyse, vaporisation), les interactions chimiques gaz-gaz et gaz-solide (combustion, fissuration, cuisson), le transport d'espèces gazeuses (convection, diffusion) et l'évolution de la morphologie solide (changement de densité interne, ablation de surface). PATO utilise la bibliothèque open-source de thermodynamique, de transport et de chimie Mutation++ produite par l'Institut von Karman pour la Dynamique des Fluides. La figure B.1 donne un aperçu du logiciel PATO.

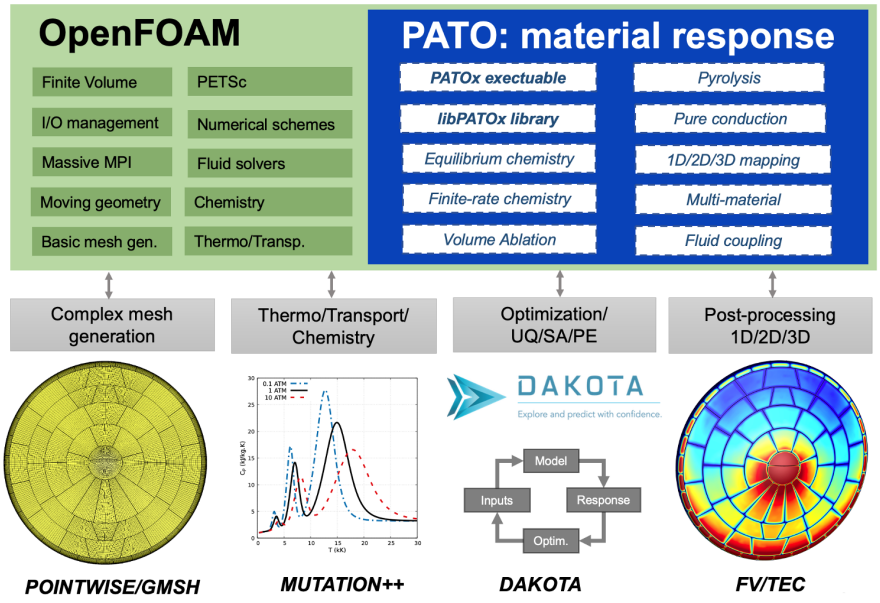

Figure B.1 – Vue d'ensemble du logiciel PATO qui a été mis en œuvre comme un module de haut niveau d'OpenFOAM permettant le couplage à la génération de maillage, la thermo-chimie, l'optimisation et les bibliothèques de post-traitement.

Le travail d'optimisation dans cette thèse a été réalisé à l'aide du Kit d'Analyse de Conception pour l'Optimisation et les Applications à l'échelle Terascale (DAKOTA), qui comprend des modules pour l'analyse de sensibilité et l'optimisation multi-objectifs. Plus précisément, l'échantillonnage hypercubique latin (LHS) a été employé pour l'analyse de sensibilité, tandis que l'optimisation globale a été réalisée à l'aide de l'algorithme DIviding RECTangles (NCSU DIREC) et l'optimisation locale a été réalisée à l'aide de l'algorithme de moindres carrés non linéaires adaptatifs (NL2SOL) pour l'optimisation multi-objectifs. La Figure B.2 montre le schéma du cadre DAKOTA.

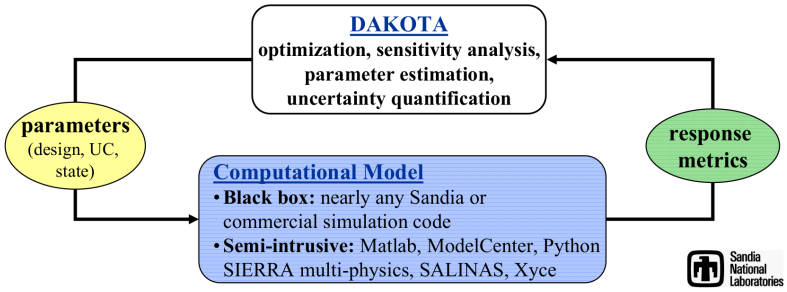

Figure B.2 – Schéma du cadre DAkOTA.

B.1.3 Approche expérimentale

L'approche expérimentale dans cette thèse se concentre sur les processus macroscopiques. Les expériences menées dans ce travail comprennent des mesures de données fondamentales telles que la perte de pression, la conductivité thermique, la porosité et la teneur en humidité, ainsi que la détermination de paramètres effectifs tels que les coefficients de transfert de chaleur volumétrique, les conductivités thermiques effectives et la perméabilité.

Pour déterminer les coefficients de transfert de chaleur volumétrique et les conductivités thermiques effectives, deux approches peuvent être utilisées : une approche à régime permanent [79, 80] ou transitoire [81, 82, 83, 84]. Dans l'approche à régime permanent, un milieu poreux (un échantillon de matériau poreux ou un lit de granulés) est chauffé et maintenu à une température constante, tandis que du gaz froid est envoyé à travers le milieu d'intérêt. La température du gaz est mesurée à l'entrée, à la sortie et éventuellement à l'intérieur du milieu poreux. Le coefficient de transfert de chaleur est déterminé à partir de l'évolution spatiale de la température du gaz. Alternativement, dans l'approche transitoire, un gaz chaud est utilisé pour chauffer un échantillon froid, et l'évolution temporelle de la température du gaz est enregistrée en amont et en aval de l'échantillon. Cette méthode, connue sous le nom de technique du souffle unique transitoire (TSBT) [81, 85], permet de mesurer l'augmentation de température du solide, ce qui fournit une robustesse pour l'analyse inverse. Comme les températures du solide et du gaz varient dans l'espace, leurs conductivités thermiques effectives peuvent être déduites simultanément à l'aide de cette méthode. L'installation expérimentale présentée dans ce travail est basée sur la méthode TSBT.

La mesure de la perte de pression est liée à la perméabilité et au coefficient de Forchheimer de l'échantillon. Pour un échantillon unique de Calcarb, en raison de son anisotropie, les valeurs de perte de pression doivent être mesurées séparément dans les directions du plan (IP) et de l'épaisseur (TT). Pour la mesure de la perte de pression dans les lits de granulés, on fait l'hypothèse d'une variation unidimensionnelle, en négligeant l'anisotropie. Lorsque l'écoulement du fluide correspond au régime d'écoulement de Darcy, la relation linéaire entre la perte de pression et la vitesse est ajustée, et la valeur de perméabilité peut être obtenue. Lorsque l'écoulement du fluide correspond au régime d'écoulement de Forchheimer, la relation non linéaire entre la perte de pression et la vitesse est ajustée, et les valeurs de perméabilité et du coefficient de Forchheimer peuvent être obtenues. Les valeurs critiques séparant les régimes d'écoulement de Darcy et de Forchheimer doivent être déterminées lors de l'expérience.

D'autres données fondamentales, telles que la conductivité thermique de Calcarb, des particules de bois, la porosité et la teneur en humidité, peuvent être obtenues par diverses techniques expérimentales, notamment la technique des sources planes transitoires (Hot Disk, TPS 3500) [86], la méthode de mesure à régime permanent (plaque chaude protégée) [87], la méthode gravimétrique et la méthode de mesure thermogravimétrique (analyseur d'humidité (METTLER TOLEDO, HC103)) [88].

Dans l'ensemble, l'approche expérimentale utilisée dans cette thèse fournit une compréhension complète des propriétés macroscopiques des matériaux étudiés. Cette compréhension est essentielle pour valider les simulations numériques et développer des applications pratiques.

B.2 Résultats Principaux

Cette section donne un aperçu des principaux résultats de la thèse, qui peuvent être divisés en deux parties comme décrit dans la section 1.4. Les conclusions spécifiques et le processus de dérivation pour chaque travail peuvent être trouvés dans les chapitres correspondants.

B.2.1 Première Partie

La première partie de ce travail, présentée dans les chapitres 3, 4 et 5, se concentre sur l'étude des équations de masse, de quantité de mouvement et d'énergie à l'échelle macroscopique.

Les modèles de réponse des matériaux des systèmes de protection thermique (TPS) reposent sur l'hypothèse d'équilibre thermique local (LTE) entre la phase solide et la phase gazeuse. Cette hypothèse a été remise en question et étudiée par plusieurs auteurs, mais une connaissance suffisamment précise des coefficients de transfert de chaleur dans les matériaux TPS faisait défaut pour parvenir à des conclusions définitives. L'objectif du travail présenté dans le chapitre 3 est de contribuer à combler cette lacune en fournissant une revue de la littérature des données disponibles dans d'autres domaines (stockage d'énergie thermique, échangeurs de chaleur) et en réalisant une caractérisation expérimentale de Calcarb, un préformé en carbone commercial utilisé pour la fabrication de systèmes de protection thermique. Le transfert de chaleur au sein de Calcarb a été étudié expérimentalement dans les directions de l'épaisseur (TT) et du plan (IP) pour des nombres de Reynolds de 1 à 4 - représentatifs de l'application TPS - en utilisant la technique du souffle unique transitoire (TSBT). L'estimation des paramètres numériques a été réalisée à l'aide de l'outil Porous material Analysis Toolbox basé sur OpenFoam (PATO) et du Design Analysis Kit for Optimization and Terascale Applications (DAKOTA). Pour effectuer l'estimation des paramètres, un modèle numérique bidimensionnel axisymétrique, comme indiqué dans la Figure B.3, a été construit, comprenant différentes zones identifiées comme suit : flow1 (champ d'écoulement amont), sample (échantillon poreux), flow2 (champ d'écoulement aval), tube (tube en quartz) et thermocouple (thermocouple aval). Une comparaison typique des résultats mesurés et prédits est présentée à la Fig.B.4, où les résultats mesurés sont représentés par des points, et les résultats prédits obtenus en résolvant le modèle de non-équilibre thermique local (LTNE) sont représentés par des lignes pleines et des lignes en pointillés. La température d'entrée du gaz enregistrée, la température de l'échantillon à deux endroits (T2, T5), et la température du gaz

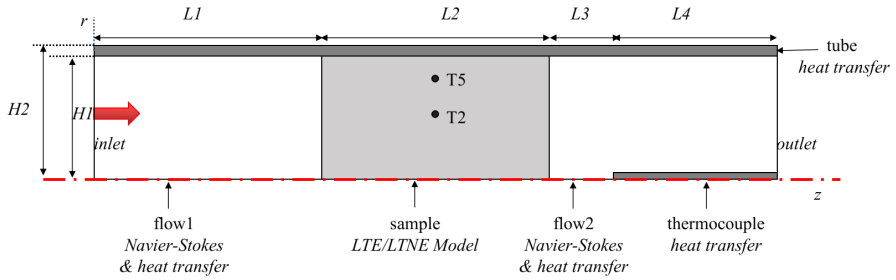

Figure B.3 – Modèle numérique axisymétrique bidimensionnel de la section d'essai

en sortie sont une fonction du temps. Les lignes pleines et en pointillés représentent les températures solides et gazeuses prédites, respectivement. Le coefficient de transfert de chaleur h_v a été estimé être

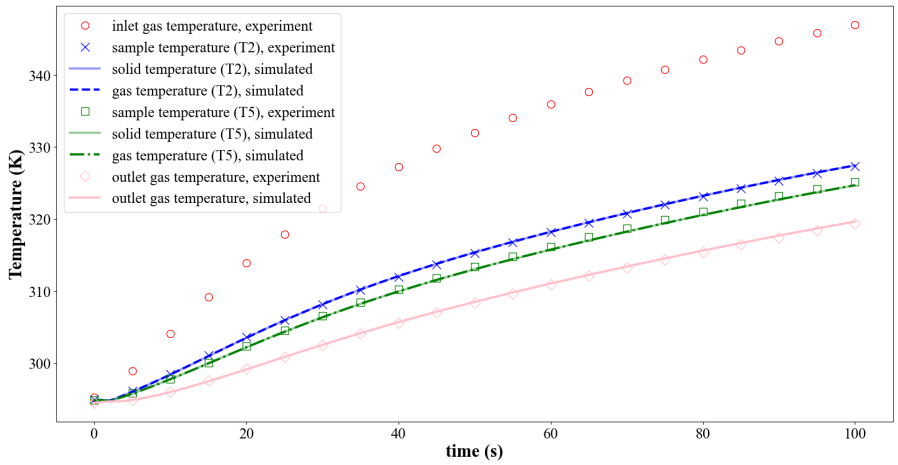

Figure B.4 – La comparaison de la température prédite et mesurée dans la direction TT ($qm = 7.68 \times 10^{-5}$ kg/s).

supérieur ou égal à 10^8 W/(m^3 · K), et l'hypothèse LTE a été démontrée comme étant valide dans les conditions de l'expérience. Les résultats obtenus dans ce chapitre fournissent des informations cruciales pour la validation et l'amélioration des modèles de réponse des matériaux TPS.

Le Chapitre 4 explore le transfert couplé de chaleur et de masse à l'intérieur de lits garnis utilisés pour le stockage d'énergie thermique à hautes températures. Les corrélations traditionnelles de transfert de chaleur ne sont pas suffisantes pour décrire de manière précise les champs de température en raison des distributions non uniformes de température, de densité de gaz, de viscosité et de vitesse à l'intérieur des lits garnis. Une méthode d'analyse inverse expérimentale-numérique a été utilisée pour déterminer les conductivités effectives et les coefficients de transfert de chaleur nécessaires pour informer le modèle d'équilibre thermique local non équilibré (LTNE) dans des conditions de hautes températures. Des expériences ont été menées en utilisant de l'air chaud à différents débits massiques, et un modèle à deux équations intégrant la conservation de la masse et du moment a été mis en œuvre et validé. Une illustration schématique du dispositif expérimental que nous avons développé,

ainsi qu'une vue agrandie de la section d'essai où les positions des thermocouples sont indiquées, sont présentées dans la Fig.B.5. La Fig.B.6 présente une comparaison des résultats mesurés et prédits

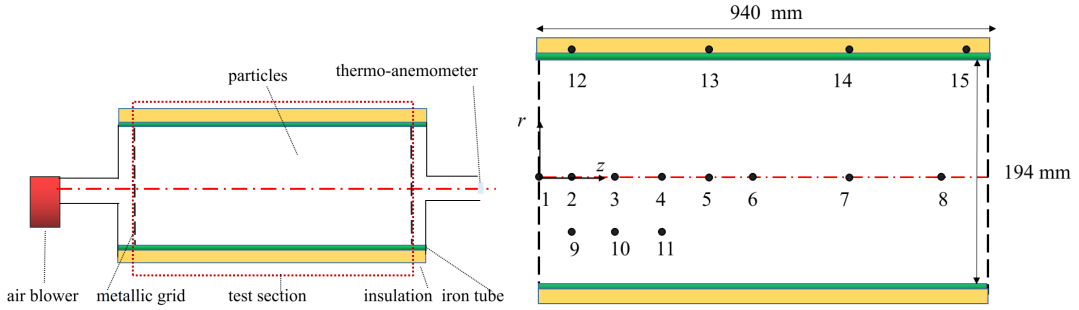

(a) installation expérimentale (b) partie de la section d'essai

Figure B.5 – Schéma du système expérimental et vue agrandie de la section d'essai montrant les numéros d'identification des thermocouples

pour quatre débits massiques, où les résultats mesurés sont représentés par des points, et les résultats prédits obtenus en résolvant le modèle à deux équations sont représentés par des lignes pleines et des lignes en pointillés. Les résultats indiquent que la valeur du coefficient de transfert de chaleur h_v dans le modèle

LTNE est dans l'intervalle de $1.0\times\ 10^4 \sim 2.0\times\ 10^4$ W/(m^3 · K) dans les conditions données. La conductivité thermique de dispersion axiale du gaz a été trouvée environ 4 et 55 fois supérieure à la conductivité thermique du gaz à des nombres de Peclet d'environ 55 et 165, respectivement. De plus, deux corrélations améliorées du nombre de Nusselt ($Nu = 2 + 1.54Re^{0.6}Pr^{1/3}$) et de la conductivité thermique de dispersion axiale du gaz ($k_{dis,||}$=$0.00011Re^{2.49}Pr \cdot k_g$) sont proposées et sont valides pour une gamme de nombres de Reynolds de 58 à 252.

Le Chapitre 5 de ce travail avait pour objectif d'établir un modèle à deux équations pour décrire les processus de transfert de chaleur à l'intérieur de lits garnis de biomasse. Des paramètres efficaces tels que le coefficient de transfert de chaleur volumétrique h_v, la conductivité thermique effective du solide $\mathbf{k_{s,eff}}$ et la conductivité thermique effective du gaz $\mathbf{k_{g,eff}}$ devaient être déterminés. Ces paramètres sont difficiles à obtenir en raison des caractéristiques complexes des particules de biomasse, telles que les configurations géométriques, l'anisotropie, la teneur en humidité et la structure des pores. Pour déterminer ces paramètres, un nouvel équipement expérimental basé sur la technique de souffle unique transitoire a été conçu, et des expériences ont été menées en utilisant de l'air pour chauffer quatre types de matériaux : des granulés de bois humides, des granulés de bois secs, des copeaux de bois humides et des copeaux de bois secs. Pour maintenir une seule variable de teneur en humidité, les vitesses ont été maintenues à des valeurs spécifiques pour chaque matériau. Afin d'éviter la pyrolyse, qui peut présenter des risques de sécurité dans les dispositifs expérimentaux à l'échelle du laboratoire, la température d'entrée maximale a été fixée à 349 K, se concentrant uniquement sur le processus de séchage des lits garnis de biomasse. Les estimations des paramètres ont été effectuées à l'aide d'une analyse inverse numérique. Le modèle numérique a été mis en œuvre à l'aide de volumes finis dans la boîte à outils d'analyse de matériaux poreux basée sur OpenFOAM (PATO). Une méthode d'optimisation locale,

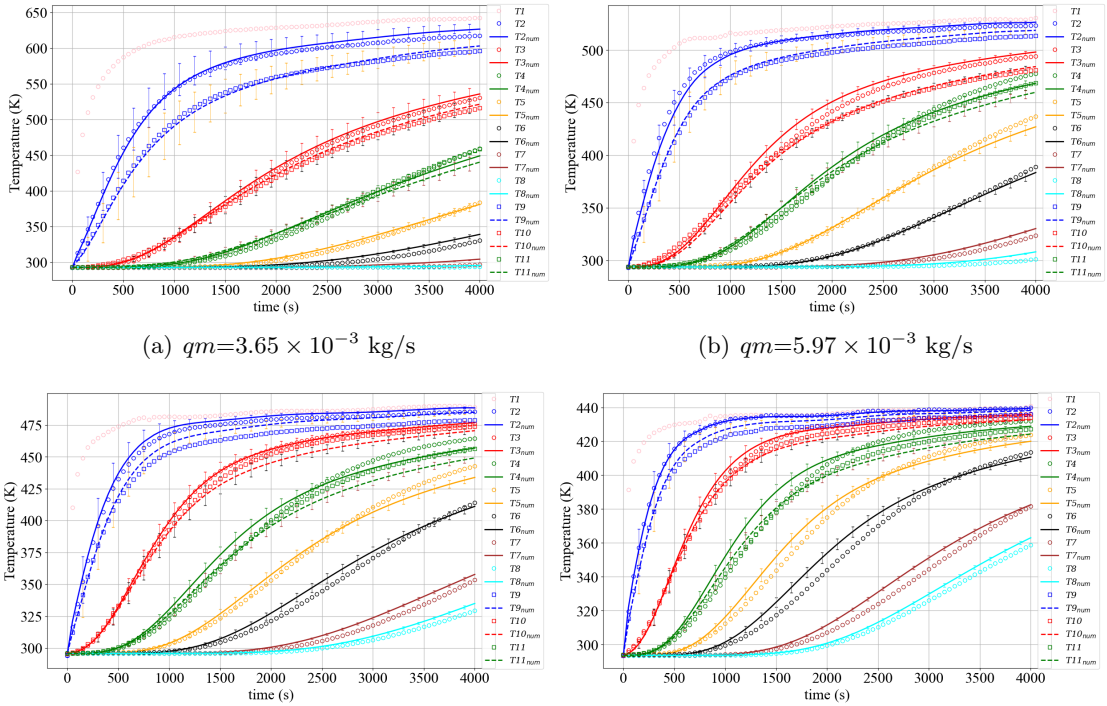

(a) qm=3.65 × 10^{-3} kg/s

(b) qm=5.97 × 10^{-3} kg/s

(c) qm=7.34 × 10^{-3} kg/s

(d) qm=1.02 × 10^{-2} kg/s

Figure B.6 – La comparaison des températures prédites et mesurées avec différents débits massiques

NL2SOL, a été utilisée pour minimiser l'erreur entre les températures mesurées et prédites. Pour effectuer l'estimation des paramètres, un modèle numérique axisymétrique bidimensionnel comme illustré dans la Figure B.7 a été construit, composé de deux régions : lit garni et tube. La Fig.B.8

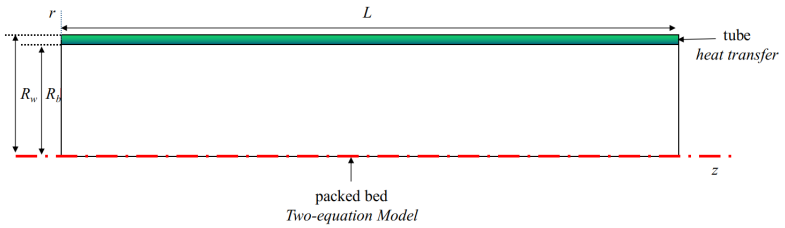

Figure B.7 – Modèle numérique axisymétrique à deux dimensions de la section d'essai

présente la comparaison de la température prédite et mesurée dans les granulés de bois et les copeaux de bois en utilisant le modèle simplifié sans pyrolyse.

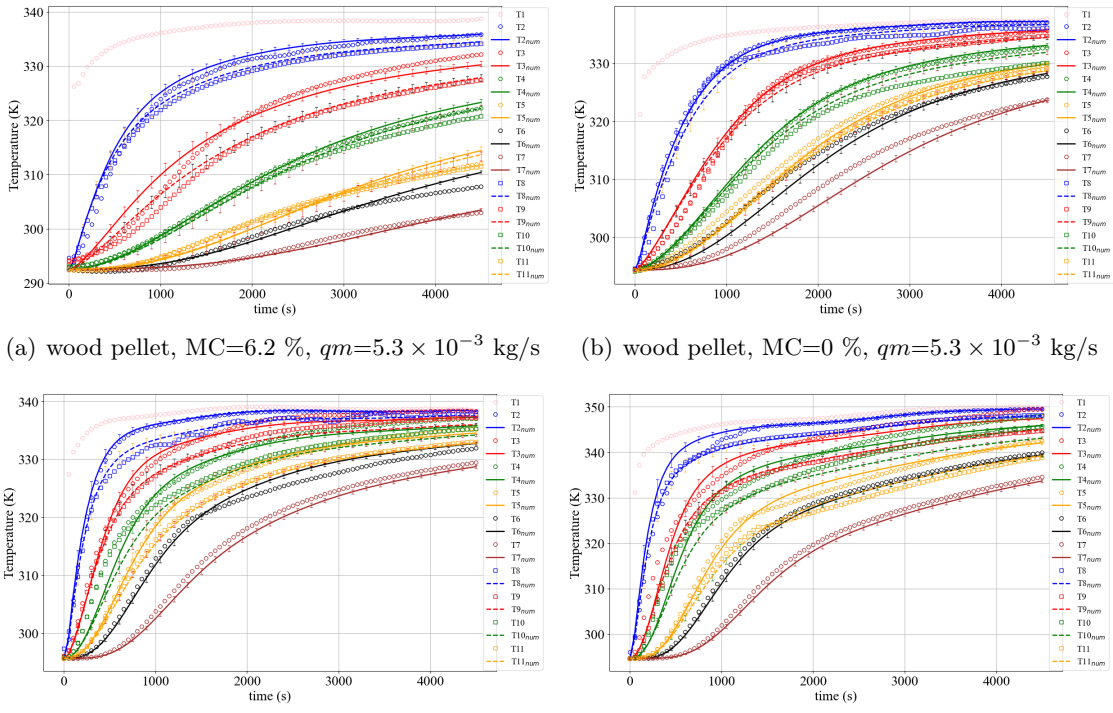

(a) wood pellet, MC=6.2 %, qm=5.3 × 10^{-3} kg/s

(b) wood pellet, MC=0 %, qm=5.3 × 10^{-3} kg/s

(c) wood chips, MC=9.1 %, qm=5.1 × 10^{-3} kg/s

(d) wood chips, MC=0 %, qm=5.1 × 10^{-3} kg/s

Figure B.8 – The comparison of predicted and measured temperature in wood pellets and wood chips.

Les résultats ont révélé que la teneur en humidité affecte significativement le coefficient de transfert de chaleur volumétrique et la conductivité thermique effective dans la plage de test. Le coefficient de transfert de chaleur volumétrique est passé de 13429 à 13850 W/(m^3 K) à 16333 à 16450 W/(m^3 K) dans les mêmes conditions d'écoulement lorsque la teneur en humidité est passée de 6.2% à 0 pour les granulés de bois. Il est passé de 12340 à 12570 W/(m^3 K) à 13924 à 13950 W/(m^3 K) lorsque la

teneur en humidité est passée de 9.1% à 0 pour les copeaux de bois. Comme on peut s'y attendre, l'évaporation de l'eau est responsable d'un effet de blocage à l'échelle des particules.

Ces résultats contribuent à une compréhension plus approfondie des phénomènes de transfert de chaleur et de masse dans les lits garnis de biomasse et peuvent orienter le développement de modèles plus précis pour différentes applications. Ils mettent également en évidence l'importance de tenir compte du dégazage pour les applications de pyrolyse en général, ce qui appelle à une poursuite de ce travail au-delà de la température de séchage.

B.2.2 Deuxième partie

Dans les chapitres 6 et 7, nous étudions les équations de masse, de quantité de mouvement et d'énergie à l'échelle microscopique pour estimer les propriétés effectives des milieux poreux anisotropes non périodiques. Le chapitre 6 se concentre sur la détermination de la perméabilité et du coefficient de Forchheimer, tandis que le chapitre 7 détermine le coefficient de transfert de chaleur volumétrique h_v.

Le chapitre 6 de ce travail se concentre sur les simulations à l'échelle microscopique et l'analyse expérimentale des écoulements de fluide, allant des écoulements lents aux écoulements inertiel, au sein de Calcarb, une préforme en fibres de carbone utilisée comme isolant dans les applications de TPS. Des mesures expérimentales du gradient de pression à travers les échantillons de Calcarb ont été réalisées pour des nombres de Reynolds allant de 0.05 à 10, dans les orientations à la fois dans le plan (IP) et à travers l'épaisseur (TT), et l'azote a été utilisé comme fluide de travail. Les coefficients de perméabilité et de Forchheimer ont été déduits à la fois à partir des données expérimentales et des solutions numériques à l'échelle microscopique basées sur des images numériques en 3D d'un échantillon de Calcarb. Le modèle numérique utilisé pour les simulations à l'échelle microscopique est présenté dans la figure B.9. La figure B.10 présente la variation du gradient de pression en fonction du nombre de Reynolds dans les directions In-Plane (IP) et Through-Thickness (TT) dans les expériences, ainsi que les courbes obtenues par ajustement des données. Les valeurs du coefficient de Forchheimer β et de l'exposant n sont calculées à l'aide de la méthode d'approximation des moindres carrés et présentées dans le tableau B.1. Tout d'abord, nous utilisons l'équation classique de Forchheimer avec un exposant fixe de 2 pour obtenir le coefficient de Forchheimer, comme indiqué dans la deuxième colonne du Tableau B.1, où R^2 représente le niveau d'ajustement du modèle aux données expérimentales. Ensuite, nous améliorons l'ajustement en ajustant à la fois le coefficient de Forchheimer et l'exposant n, avec les résultats présentés dans la troisième colonne du même tableau. Contrairement à la valeur habituelle de 2, l'exposant présente des différences mineures, comme Aguilar et al.[71] l'ont constaté dans leur travail sur les roches poreuses. De plus, les valeurs de β et n diffèrent entre les directions IP et TT en raison de l'anisotropie inhérente de l'échantillon.

La Fig.B.11 présente la comparaison des résultats expérimentaux et des simulations dans le régime d'écoulement de Forchheimer, où le nombre de Reynolds dans les expériences varie de 0.50 à 10.46. Les données représentant les corrélations expérimentales proviennent de la Table B.1. Lorsqu'on compare les valeurs dans le régime d'écoulement de Forchheimer, on peut remarquer que les plus grandes différences de gradient de pression entre la simulation et l'expérience atteignent jusqu'à 64.5%

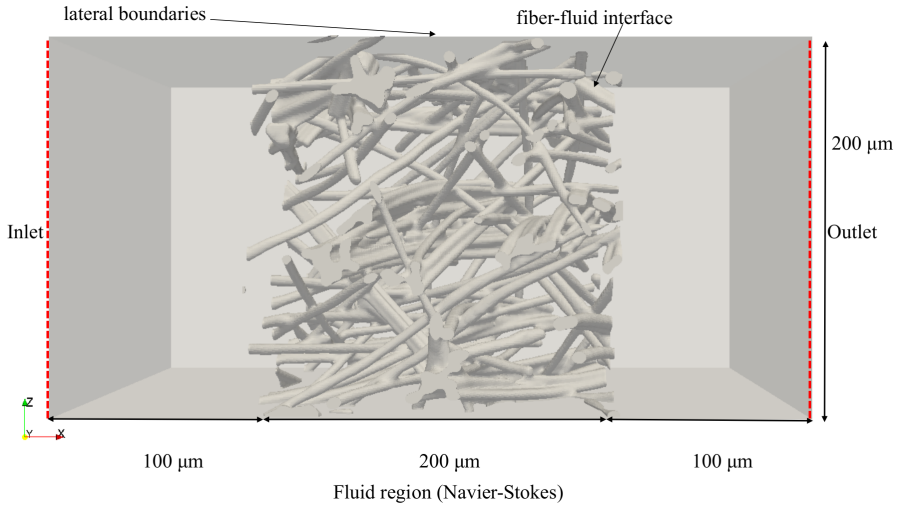

Figure B.9 – Structure numérique tridimensionnelle utilisée dans les simulations à l'échelle microscopique

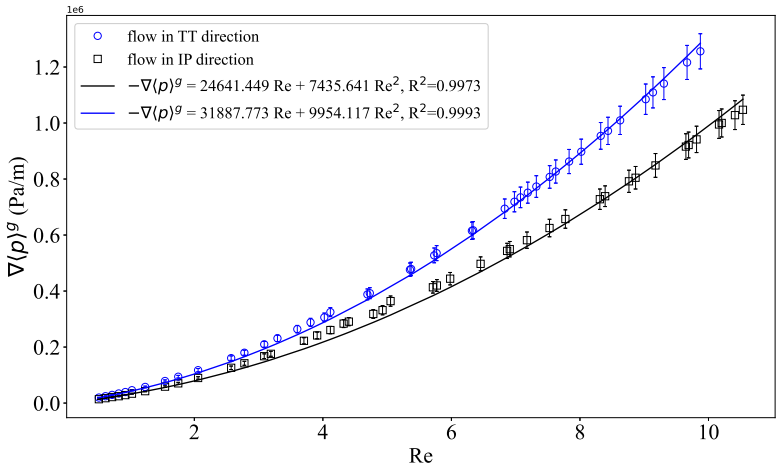

Figure B.10 – La relation entre le gradient de pression et le nombre de Reynolds dans les directions IP et TT dans les expériences

.

Table B.1 – Coefficient de Forchheimer β (1/m) et exposant n dans les directions IP et TT

Flow direction	β and n ($n = 2$)	β and n ($n \neq 2$)
IP	1.4948×10^5, 2 ($R^2 = 0.9973$)	2.7015×10^5, 1.73 ($R^2 = 0.9999$)
TT	2.0010×10^5, 2 ($R^2 = 0.9993$)	2.7782×10^5, 1.84 ($R^2 = 0.9999$)

et 68.2% dans les directions IP et TT respectivement. Étant donné l'hypothèse d'un écoulement

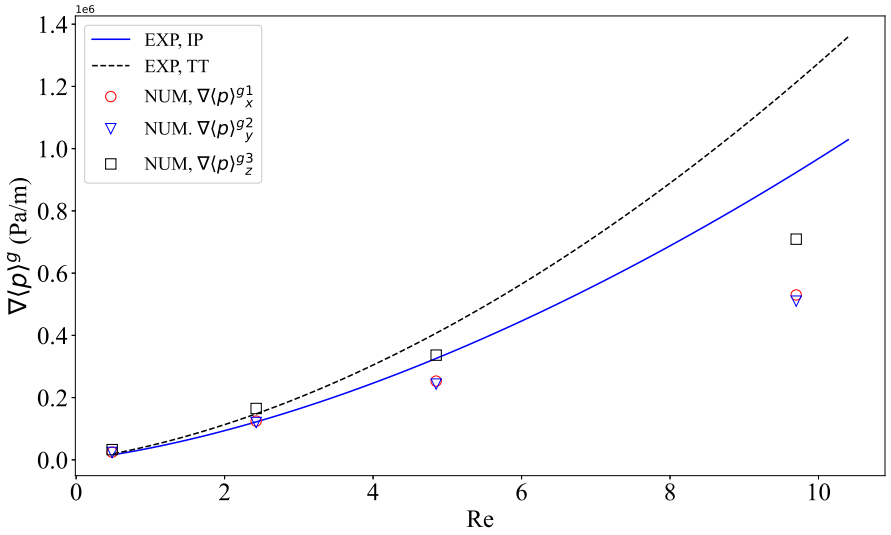

Figure B.11 – Comparaison des résultats numériques et expérimentaux dans le régime d'écoulement de Forchheimer.

unidimensionnel dans les expériences, seule la chute de pression dans la direction de l'écoulement a été prise en compte. Cependant, dans la simulation tridimensionnelle, la dispersion de l'écoulement due à la chute de pression dans d'autres directions a également été prise en considération. Cette dispersion, qui se produit dans des directions autres que l'écoulement principal, entraîne une diminution de la chute de pression le long de la direction de l'écoulement principal, ce qui pourrait conduire à des valeurs de simulation inférieures aux valeurs expérimentales. De plus, comme le montre la Fig.B.11, lorsque le nombre de Reynolds est inférieur à 2.4, la différence entre les valeurs de simulation et les valeurs expérimentales est de 4.5% et 5.2% dans les directions IP et TT, respectivement. À mesure que le nombre de Reynolds augmente, les composantes de gradient de pression dans les directions d'écoulement non principales deviennent de plus en plus importantes, ce qui entraîne une divergence croissante entre la chute de pression simulée le long de la direction d'écoulement principal et la valeur expérimentale.

Le chapitre 7 se concentre sur l'utilisation d'une approche multi-échelle pour étudier la chute de pression et le coefficient de transfert de chaleur dans des lits aléatoirement remplis à des températures élevées. Pour la reproduction de la microstructure locale, un modèle 3D de lits aléatoirement remplis avec des particules sphériques a été développé en utilisant le code LIGGGHTS DEM. Deux modèles microscopiques sont résolus dans ce lit rempli pour différentes situations : le premier modèle concerne un écoulement incompressible à température constante, caractérisé par les équations de Navier-Stokes incompressibles. Les solutions sont ensuite utilisées pour obtenir la perméabilité et le coefficient de Forchheimer. Le second modèle concerne un écoulement transitoire compressible, avec un gaz à haute température (800K) entrant depuis l'entrée, par un modèle couplant les équations de masse et de quantité de mouvement pour la phase fluide, ainsi que les équations d'énergie pour les phases fluide

et solide, respectivement. Une fois le champ de température obtenu, h_v peut être évalué en utilisant une méthode d'intégration (comme indiqué dans l'équation 7.2).

Pour les simulations à l'échelle macroscopique, basées sur les équations moyennées en volume, une structure axisymétrique 2D a été utilisée pour représenter les lits aléatoires remplis en 3D. Des outils numériques basés sur le logiciel PATO (Porous Material Analysis Toolbox) ont été utilisés pour résoudre l'écoulement de Forchheimer et le modèle LTNE (Local Thermal Non-Equilibrium) dans le domaine macroscopique. Les paramètres effectifs, c'est-à-dire les conductivités thermiques et les coefficients de transfert de chaleur, sont obtenus en effectuant une analyse inverse.

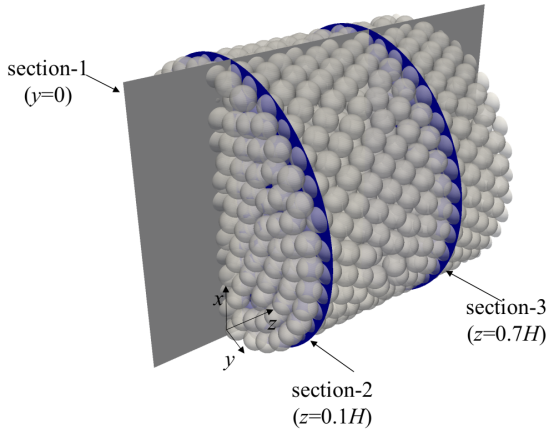

Figure B.12 – Sections sélectionnées dans un lit aléatoire rempli de sphères.

À l'échelle microscopique, trois sections transversales typiques ont été sélectionnées pour illustrer les distributions de vitesse et de température à l'intérieur des lits remplis. Comme le montre la Fig.B.12, la Fig.B.13 présente la distribution de température dans la section-1 du lit aléatoire rempli de sphères uniformes à t=1000s. La méthode adoptée permet une optimisation automatique des paramètres en couplant le logiciel d'optimisation Open Source Dakota avec PATO. La perméabilité et le coefficient de Forchheimer sont déterminés, et la transition critique de l'écoulement de Darcy à l'écoulement de Forchheimer est observée à un nombre de Reynolds spécifique. Le coefficient de transfert de chaleur volumétrique présente un comportement transitoire, avec des augmentations significatives observées à des vitesses d'entrée plus élevées. La différence entre la valeur de h_v obtenue par intégration des champs à l'échelle microscopique et celle obtenue à l'échelle macroscopique par analyse inverse est inférieure à 3.8%.

B.3 Conclusions et Perspectives

B.3.1 Réalisations

De nombreuses technologies en développement reposent sur des matériaux poreux, et des développements fondamentaux en transfert de chaleur et de masse sont essentiels pour les modèles phénoménologiques

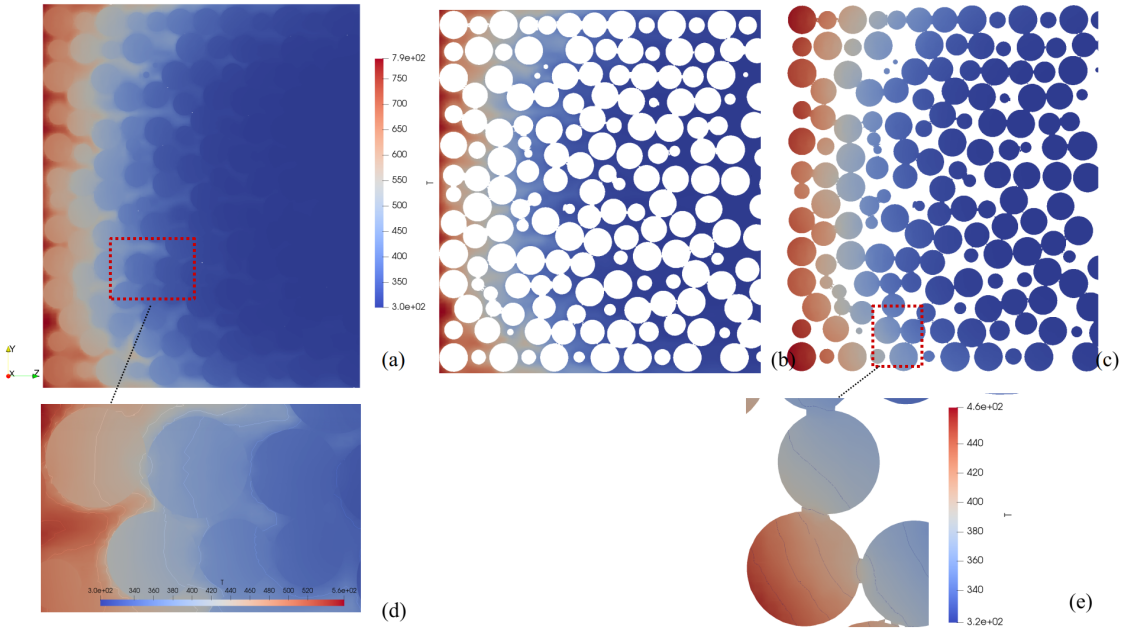

Figure B.13 – Champs de température du gaz et du solide dans la section-1 du lit emballé aléatoirement (u=0.1m/s, t=1000s). a) Température totale (gaz et solide), b) Température du gaz, c) Température du solide, d) Température du gaz et du solide avec ligne de contour dans la boîte rouge, e) Température du solide avec ligne de contour dans la boîte rouge.

spécifiques à chaque application. Dans ce projet de doctorat, l'accent a été mis sur trois applications : le transfert de chaleur et de masse dans les systèmes de protection thermique (TPS), les lits emballés pour le stockage thermique (TES) et la pyrolyse des particules de bois. L'objectif était de développer un cadre numérique générique pour évaluer et modéliser les échanges de chaleur entre la structure solide d'un matériau poreux et le fluide circulant à travers le réseau de pores. Le premier objectif était d'étendre la base de données sur l'écoulement des fluides et le transfert de chaleur dans différents matériaux poreux grâce à des recherches expérimentales. Le deuxième objectif était d'établir et de valider des stratégies numériques en comparant les résultats expérimentaux et les simulations multi-échelles.

La première partie du travail, présentée dans les chapitres 3, 4 et 5, a étudié l'écoulement des fluides et le transfert de chaleur dans trois matériaux poreux différents : les feutres de fibres de carbone anisotropes, les matériaux granulaires de forme uniforme et les matériaux poreux de forme non uniforme. Dans la première application, nous avons examiné expérimentalement le transfert de chaleur convectif dans des matériaux de fibres de carbone à faible densité tels que Calcarb et validé l'hypothèse d'équilibre thermique local (LTE). Les résultats ont montré que l'hypothèse de LTE était valide, car le coefficient de transfert de chaleur estimé h_v était d'au moins 10^8 W/(m^3 · K). Dans la deuxième application, nous avons développé et validé un modèle à deux équations pour les conditions à haute température afin de décrire la distribution de température dans les lits emballés où les propriétés thermophysiques dépendent de la température. Les résultats ont montré que la valeur du coefficient

de transfert de chaleur h_v dans le modèle LTNE variait de $1.0\times\ 10^4$ à $2.0\times\ 10^4$ W/(m^3 · K) dans les conditions données. Nous avons également proposé deux corrélations améliorées pour le nombre de Nusselt et la conductivité thermique du gaz à dispersion axiale pour une gamme de nombres de Reynolds de 58 à 252. Dans la troisième application, nous avons mis en œuvre des modèles à deux équations pour décrire les processus de transfert de chaleur dans les lits emballés de biomasse, avec et sans prise en compte des processus de séchage. Les résultats ont montré que la teneur en humidité affecte significativement le coefficient de transfert de chaleur volumétrique et la conductivité thermique effective dans la plage d'essais. Le coefficient de transfert de chaleur volumétrique a augmenté lorsque la teneur en humidité a diminué pour les granulés de bois et les copeaux de bois. Nous avons constaté que le modèle qui néglige l'évaporation de l'eau entraîne une erreur d'environ dix pour cent sur les coefficients de transfert de chaleur.

La deuxième partie du travail, présentée dans les chapitres 6 et 7, a étudié les propriétés effectives des milieux poreux anisotropes non périodiques à l'échelle microscopique. Nous avons étendu les simulations à l'échelle microscopique du flux de Darcy au flux de Forchheimer et déterminé expérimentalement la perméabilité et le coefficient de Forchheimer pour Calcarb. Les résultats expérimentaux ont révélé que la limite du nombre de Reynolds Re (basé sur le diamètre du cluster) du régime de flux de Darcy dans Calcarb était d'environ 0.43. Les valeurs expérimentales de la perméabilité étaient de 1.615×10^{-10} m^2 (IP) et de 1.248×10^{-10} m^2 (TT), montrant une différence relative de 12.3% par rapport aux simulations. Dans le régime de flux de Forchheimer, le coefficient expérimental de Forchheimer β pour l'équation de Forchheimer a été déterminé comme étant de 1.4948×10^5 m^{-1} (IP) et de 2.0010×10^5 m^{-1} (TT). Bien que la simulation n'ait pas fourni de valeur spécifique pour β ou le tenseur de correction de Forchheimer $\mathbf{F}$ en raison de la dépendance non linéaire de $\mathbf{F}$ sur la vitesse du gaz. Dans la deuxième application, une approche multi-échelle a été utilisée pour étudier l'écoulement et les coefficients de transfert de chaleur dans un lit aléatoirement rempli à haute température. Les résultats à l'échelle microscopique ont révélé qu'à température ambiante, la perméabilité était de 2.451×10^{-7} m^2, et le coefficient de Forchheimer était de 1.188×10^3 m^{-1}. Le nombre de Reynolds critique (basé sur le diamètre des particules) pour la transition du flux de Darcy au flux de Forchheimer a été observé à $Re = 10.1$, où le rapport du diamètre du lit rempli au diamètre des particules était de 12.5. Le coefficient de transfert de chaleur volumétrique h_v a montré un comportement transitoire, mais à de faibles vitesses d'entrée (par exemple, 0.01 m/s et 0.1 m/s) correspondant à $Re = 10.1$ et 101 à température ambiante, respectivement, h_v pourrait être considéré comme constant. Pour des vitesses d'entrée plus élevées (par exemple, 1 m/s) correspondant à $Re = 1001$, h_v a augmenté significativement au fil du temps pendant le processus de transfert de chaleur. Il a connu une augmentation d'environ 71%, passant de 13529.99 à 23218.36 W/(m^3·K). De plus, h_v a augmenté lorsque le nombre de Biot (Bi) a diminué à la même vitesse du gaz. Cela a démontré que lorsque Bi dépassait 0.1, la distribution de température à l'intérieur des particules individuelles ne pouvait pas être considérée comme uniforme. La comparaison entre la valeur de h_v obtenue par intégration des résultats à l'échelle microscopique et celle calculée à partir de l'analyse inverse a révélé une différence inférieure à 3.8%, avec la différence maximale se produisant à la vitesse d'entrée la plus élevée.

B.3.2 Perspectives

Ce travail contribue aux efforts en cours visant à améliorer la compréhension des caractéristiques de transfert de chaleur entre les milieux poreux et les fluides. Dans les paragraphes suivants, les principales perspectives couvertes dans les cinq articles sont présentées dans l'ordre de leurs sujets.

Dans le chapitre 3, une méthode d'analyse inverse a été utilisée pour valider l'hypothèse d'équilibre thermique local (LTE) dans les modèles de réponse des matériaux ablatifs. Le travail a permis d'obtenir une valeur minimale précise pour h_v, mais il n'a pas été possible de déterminer une valeur spécifique pour la conductivité thermique effective du gaz dans les directions transversale et d'écoulement en raison de l'incertitude expérimentale. Une approche potentielle pour des recherches ultérieures consisterait à utiliser la technique du spot laser volant pour étudier le mécanisme de dispersion et déterminer des valeurs spécifiques pour la conductivité thermique effective du gaz dans Calcarb.

Dans le chapitre 4, un modèle à deux équations pour des conditions de haute température, incorporant la conservation de la masse et de la quantité de mouvement, pour décrire avec précision la distribution de température dans les lits emballés, a été implémenté et validé. Cependant, il est important de noter que notre travail actuel se concentre sur le stockage d'énergie thermique sensible. Dans les travaux futurs, notre objectif est d'améliorer le modèle en incorporant des termes de changement de phase, ce qui élargira son applicabilité aux systèmes de stockage d'énergie thermique à changement de phase.

Dans le chapitre 5, un modèle à deux équations décrivant les processus de transfert de chaleur dans les lits emballés de biomasse avec une teneur en humidité variable a été proposé. Pour des raisons de sécurité, l'effet de la pyrolyse des particules de biomasse sur le coefficient de transfert de chaleur n'a pas été étudié, car la température maximale était limitée à 349 K. Dans les travaux futurs, un nouvel équipement expérimental sera construit avec un diamètre de tube plus petit de 60 mm, où l'azote sera utilisé, et la température d'entrée d'azote sera portée à 500°C. En collectant et en analysant la composition des gaz de pyrolyse, le modèle à deux équations sera couplé aux réactions chimiques qui se produisent pendant la pyrolyse.

Dans le chapitre 6, des simulations à l'échelle microscopique du flux de Darcy au flux de Forchheimer pour des matériaux poreux tels que Calcarb ont été réalisées, et les valeurs de perméabilité et de coefficient de Forchheimer ont été déterminées expérimentalement. Cependant, il convient de noter que la procédure utilisée pour le calcul du tenseur de perméabilité, qui consistait à imposer successivement une vitesse (ou un gradient de pression) le long des trois directions de la cellule unitaire pour obtenir le tenseur de perméabilité complet, n'est plus valide ici en raison de la dépendance non linéaire de $\mathbf{F}$ vis-à-vis de $\langle \mathbf{v_g} \rangle$. Dans les travaux futurs, une approche possible consisterait à calculer $\mathbf{F}$ sur une cellule unitaire périodique en résolvant un problème de fermeture tensorielle avec une structure de Navier-Stokes.

Dans le chapitre 7, une approche multi-échelle a été utilisée pour étudier l'écoulement et les coefficients de transfert de chaleur dans un lit emballé aléatoirement à haute température. L'étude a impliqué un écoulement compressible transitoire, où un gaz à haute température (800 K) est entré par l'entrée. Le modèle incorporait les équations de masse et de quantité de mouvement pour la phase fluide, ainsi que les équations d'énergie pour les phases fluide et solide, respectivement. En résolvant le champ de température, le coefficient de transfert de chaleur volumétrique h_v a pu être évalué à l'aide de méthodes d'intégration. Cependant, la détermination de la conductivité thermique effective n'a pas été abordée dans cette étude. Les travaux futurs pourraient consister à calculer la conductivité thermique effective en analysant les distributions de vélocité et de température obtenues à partir de simulations à l'échelle microscopique du lit emballé. Cela pourrait être fait en résolvant un problème de fermeture sur la même géométrie.

Shaolin LIU

Experimental analysis and multiscale modeling of convective heat transfer in porous media in support of the space, energy storage, and biomass communities

Abstract: Numerous emerging technologies rely on porous media, including heat exchangers for solar concentrators, biofuel production processes, new-generation energy storage systems like fuel cells and supercapacitors, and heat shields for space vehicles, to name a few. Modeling transport in porous media requires accounting for the multiple-scale aspects inherent to the structure of porous media. Typical multiple-scale problems may involve several successive scales or at least two scales generally referred to as the micro-scale or pore-scale and the macro-scale or Darcy-scale. Several methodologies based on theoretical analysis have been developed to upscale transport equations from the micro-scale to obtain macro-scale models. This study is built upon these available upscaling techniques and uses various macro-scale models to investigate convective heat transfer in porous media. The accuracy of these macro-scale models is influenced by the macroscopic transport properties, namely porosity, permeability, Forchheimer tensor, effective thermal conductivity, volumetric heat transfer coefficient, etc. While many studies have been conducted on particular macroscopic transport properties, the complexity, addressed in this work, arises from the fact that these parameters are interrelated in the coupled conservation of mass, momentum, and energy equations. The main objective of this thesis is to contribute to the understanding of convective heat transfer in porous media through experimental and numerical studies, to give insight on the choice of the relevant macroscopic models to use and on the determination of the inherent effective or macroscopic properties. In this study, the macroscopic properties are determined using two approaches. The first one consists of the experimental-numerical inverse problem resolution, while the second is based on direct micro-scale numerical simulations. In the first approach, the transient single-blow technique (TSBT) is used to perform experiments on two facilities, designed specifically during this work, with different test section diameters of 1 cm and 20 cm. We study heat transfer by the flow of a hot gas within three different types of porous media: carbon fiber felts, used in Thermal Protection Systems (TPS), packed beds of glass beads, used in Thermal Energy Storage (TES), and packed beds of wood pellets and chips, used as biomass in energy production. We perform a numerical inverse analysis to estimate the quantities of interest using the Porous material Analysis Toolbox based on OpenFoam (PATO) and the Design Analysis Kit for Optimization and Terascale Applications (DAKOTA). In the second approach, the microstructure of the porous media is sought for direct numerical simulation of the flow and heat transfer. For TPS applications, carbon fiber felt is reconstructed using 3D digitalized tomographic images. The permeability and the Forchheimer tensors are then computed by solving the Navier-Stokes equations at the micro-scale. For packed beds of glass beads and wood pellets, a Discrete Element Method (DEM) code is used to generate packings of spheres and cylinders. By solving the coupled Navier-Stokes and energy equations in both fluid and solid phases, the volumetric heat transfer coefficients are determined based on an integration method. This work contributes to the understanding and development of two methods for determining the macroscopic transport properties involved in the macro-scale model, thereby enabling a more accurate study of heat and mass transfer phenomena within porous media. The numerical contributions of the Ph.D. work have been implemented in PATO, which has been released as open source by NASA.

Keywords: Macroscopic simulations, Microscopic simulations, Experimental study, Heat exchange coefficient, Porous materials.